Design Guidelines for Tesla Turbines Based on Comprehensive Theoretical, Numerical and Experimental Investigations

Stefan Günter Klingl, M.Eng.

Vollständiger Abdruck der von der
Fakultät für Luft- und Raumfahrttechnik
der Universität der Bundeswehr München
zur Erlangung des akademischen Grades eines

Doktor-Ingenieurs (Dr.-Ing.)

angenommenen Dissertation.

Gutachter:

1. Univ.-Prof. i.R. Dr. rer. nat. Michael Pfitzner
2. Prof. Dr.-Ing. Stefan Lecheler
3. Univ.-Prof. Dr.-Ing. Hans-Jörg Bauer

Die Dissertation wurde am 5.6.2023 bei der Universität der Bundeswehr München eingereicht und durch die Fakultät für Luft- und Raumfahrttechnik am 11.10.2023 angenommen. Die mündliche Prüfung fand am 17.11.2023 statt.

Abstract

The Tesla turbine is an unconventional type of turbine, invented over 100 years ago by Nikola Tesla. Its rotor consists of several parallel circular disks with small gaps in between. At the outer circumference of the disks, nozzles feed a working fluid into the disk gaps, that travels on a spiral path radially inward to the outlet openings in the centre of the disks. The wall shear stress that the fluid exerts on the disks in circumferential direction drives the rotor.

So far, Tesla turbines are only known to a small research community and are not used industrially. While their efficiency is generally lower compared to conventional bladed turbines, the rotor design is simpler and more cost-efficient. Along with other unique traits, this possibly puts them at an advantage in certain small-scale expander applications, for example in the utilization of waste energy from industrial processes. To provide a basis for comparing and evaluating Tesla turbines, this work summarizes the state of the art of Tesla turbine research and builds upon it with results from analytical modelling, numerical fluid simulation and experiment on a new application-oriented 5 kW Tesla turbine test facility. Practical design guidelines and strategies are provided.

The basis for prediction of Tesla turbine performance is modelling of the spiralling flow inside the flat cylindrical annulus formed by the disk surfaces. A detailed summary of existing analytical solutions, derived from simplified Navier-Stokes equations, is given and two ways of simulating Tesla turbine flow using commercial numerical fluid simulation software are outlined.

For choosing the right modelling approach, some knowledge is necessary about whether the flow inside the disk gap is expected to be laminar or turbulent. Three attempts at locating a theoretical regime boundary through linear stability analysis are summarized. Together with previous experimental results, this allows to predict the flow regimes based on a mass flow parameter and a rotational speed parameter. More insight into the flow and additional validation is provided by results from a new direct numerical simulation.

A comparison between some laminar analytical models of Tesla turbine flow, numerical simulation with turbulence modelling and previous experimental results shows that the analytical models are accurate in the laminar region of the stability map, and some distance beyond the theoretical stability boundary.

The summary and evaluation of modelling approaches is followed by description of a new Tesla turbine test facility, that is used to generate performance maps of a real, application oriented, air-driven Tesla turbine. It is designed to allow modification of some turbine design parameters to evaluate their impact on turbine performance. Different stator designs with one to four nozzles and different nozzle geometries are tried out as well as various rotor configurations with different disk thicknesses, disk spacings, edge geometry and surface roughness. The best turbine performance is achieved for the thinnest disks and the smallest disk spacing, at a power output of over 5 kW and an isentropic efficiency just below 50 %. Some test runs are dedicated to measuring turbine losses, which allow

to qualitatively rank loss mechanisms. Especially for a small ratio of disk spacing to disk thickness, the space between nozzle and rotor is identified as a major source of turbine losses.

The last chapter compiles findings from previous chapters and from literature into advice on some Tesla turbine specific design challenges and chooses and develops a preliminary design strategy. A Tesla turbine model is set up from an analytical rotor model and simplified loss modelling. The outlined design process guides the turbine designer through choosing the major design parameters, for example rotor diameter and disk spacing. Generally, high rotational speed is beneficial for Tesla turbine performance, however the choice of the radial mass flow parameter involves an optimization conflict. Lower mass flow is beneficial for turbine efficiency, but disadvantageous for the ratio of power output to machine size.

Kurzfassung

Die Teslaturbine ist ein unkonventioneller Turbinentyp, der vor über 100 Jahren von Nikola Tesla erfunden wurde. Ihr Rotor besteht aus mehreren parallel angeordneten Scheiben, mit kleinen Spalten dazwischen. Am äußeren Scheibenumfang wird das Arbeitsmedium von Düsen in die Scheibenspalte geführt, wo es sich auf einer Spiralbahn radial einwärts in Richtung der Auslassöffnungen im Zentrum der Scheiben bewegt. Die Wandschubspannung, die das strömende Fluid auf die Scheiben ausübt, treibt den Rotor an.

Bis jetzt sind Teslaturbinen nur einer kleinen Gruppe an Forschern bekannt und werden noch nicht industriell angewendet. Die Effizienz von Teslaturbinen ist allgemein geringer als die von konventionellen beschaufelten Turbinen, der Aufbau des Rotors hingegen ist einfacher und kostengünstiger. Neben anderen einzigartigen Eigenschaften ist die Teslaturbine dadurch in bestimmten Anwendungen möglicherweise von Vorteil, beispielsweise für die Nutzung von Restenergie aus Industrieprozessen. Um eine Basis für den Vergleich und die Bewertung von Teslaturbinen zu schaffen, fasst diese Arbeit den Stand der Technik zusammen und baut darauf auf, mit neuen Ergebnissen aus analytischer Modellierung, numerischer Simulation und Experiment an einer anwendungsorientierten 5 kW Teslaturbine. Praktische Empfehlungen und Strategien zur Auslegung werden bereitgestellt.

Grundlage für die Vorhersage von Leistung und Effizienz einer Teslaturbine ist die Modellierung der Strömung innerhalb des flachen Zylinderringes, der von zwei Scheibenoberflächen begrenzt ist. Existierende analytische Lösungen basierend auf vereinfachten Navier-Stokes Gleichungen werden zusammengefasst und zwei Ansätze zur numerischen Simulation von Teslaturbinenströmung mit Hilfe von kommerzieller Strömungssimulationssoftware wird beschrieben.

Für die Auswahl eines passenden Modellierungsansatzes ist es wichtig, vorab abzuschätzen, ob laminare oder turbulente Strömung vorherrscht. Vorhergehende Studien, die eine theoretische Regimegrenze durch lineare Stabilitätsanalyse lokalisieren, werden zusammengefasst. Zusammen mit vorhergehenden experimentellen Ergebnissen kann das Strömungsregime dadurch über einen Massenstromparameter und einen Drehzahlparameter vorhergesagt werden. Weitere Einblicke in die Strömung sowie zusätzliche Validierung liefern die Ergebnisse einer neuen direkten numerischen Simulation der Turbinenströmung.

Ein Vergleich zwischen einigen laminaren analytischen Modellen der Teslaturbinenströmung, numerischer Simulation mit Turbulenzmodellierung und vorhergehenden experimentellen Ergebnissen zeigt, dass die analytischen Modelle im laminaren Bereich des Stabilitätsdiagrammes zuverlässig sind, sowie eine gewisse Distanz über die theoretische Stabilitätsgrenze hinaus.

Der Zusammenfassung und Evaluierung der Modellierungsansätze folgt eine Beschreibung eines neuen Teslaturbinenprüfstandes, der benutzt wird, um Kennfelder einer realen, anwendungsorientierten Teslaturbine zu erstellen. Der Prüfstand ist darauf ausgelegt, den Einfluss verschiedener Turbinenparameter auf Leistung und Wirkungsgrad zu ermitteln. Es werden verschiedene Statorkonfigurationen getestet, mit einer bis vier Düsen und ver-

schiedenen Düsengeometrien und verschiedene Rotorkonfigurationen mit unterschiedlicher Scheibendicke, Scheibenabstand, Kantengeometrie und Oberflächenrauheit. Die größte Turbinenleistung wird erreicht mit den dünnsten Scheiben und dem kleinsten Scheibenabstand, mit über 5 kW Turbinenleistung und einem isentropen Wirkungsgrad von nahezu 50 %. Einige Testläufe widmen sich der Messung von Turbinenverlusten. Besonders bei einem kleinen Verhältnis von Scheibenabstand zu Scheibendicke ist der Zwischenraum zwischen Stator und Rotor eine große Verlustquelle.

Das letzte Kapitel leitet von den Erkenntnissen der vorhergehenden Kapiteln und aus der Literatur Ratschläge für die Konstruktion von Teslaturbinen ab, und entwickelt eine neue Vorauslegungsstrategie. Ein Teslaturbinenmodell wird zusammengestellt aus einem analytischen Rotormodell und vereinfachter Verlustmodellierung. Die beschriebene Auslegungsstrategie führt den Turbinendesigner durch die Auswahl der wichtigsten Turbinenparameter, z.B. Rotordurchmesser und Scheibenabstand. Hohe Drehzahl ist allgemein vorteilhaft für eine Teslaturbine, die Auswahl des Massenstromparameters geht hingegen einher mit einem Optimierungskonflikt. Ein niedriger Massenstrom ist vorteilhaft für die Turbineneffizienz, gleichzeitig aber von Nachteil für das Verhältnis von Turbinenleistung zu Turbinengewicht.

Contents

List of symbols

Lowercase

a	speed of sound	$\mathrm{m\,s^{-1}}$
b	distance between rotating disk surface and stationary housing surface	m
c_p	specific isobaric heat capacity	$\mathrm{J\,kg^{-1}\,K^{-1}}$
e	area specific turbine power density	$\mathrm{W\,m^{-2}}$
$\boldsymbol{f}$	body force vector	$\mathrm{N\,m^{-3}}$
$\tilde{h}_c$	specific static to static enthalpy drop across the turbine for compressible media	$\mathrm{J\,kg^{-1}}$
$\tilde{h}_{rc}$	estimated specific static to static isentropic rotor enthalpy drop	$\mathrm{J\,kg^{-1}}$
h_c	specific total to static enthalpy drop across the turbine for compressible media	$\mathrm{J\,kg^{-1}}$
h_i	specific total to static enthalpy drop across the turbine for incompressible media	$\mathrm{J\,kg^{-1}}$
h_{rc}	specific total to static enthalpy drop across the rotor for compressible media	$\mathrm{J\,kg^{-1}}$
h_{ri}	specific total to static enthalpy drop across the rotor for incompressible media	$\mathrm{J\,kg^{-1}}$
h	specific enthalpy	$\mathrm{J\,kg^{-1}}$
i	imaginary unit	-
$\dot{m}_g$	radial mass flow through one disk gap	$\mathrm{kg\,s^{-1}}$
$\dot{m}$	turbine mass flow	$\mathrm{kg\,s^{-1}}$
n_d	number of rotor disks	-
n_g	number of rotor disk gaps	-
n_n	number of nozzles	-
n	disk rotational speed	$\mathrm{min^{-1}}$
$\bar{p}_0$	average pressure at the nozzle inlet	bar
$\bar{p}_1$	average pressure at r_1	bar
$\bar{p}_2$	average pressure at r_2	bar
p_{01}	stator pressure drop	bar
p_{02}	turbine stage pressure drop	bar
p_{02max}	maximum possible stage pressure drop	bar
p_{12}	rotor pressure drop	bar
p_{0r}	relative pressure at the stator inlet	bar
p_{2r}	relative pressure at the turbine outlet	bar
p_∞	ambient pressure	bar
p	dimensional pressure	bar

$\boldsymbol{r}$	coordinate vector	m
r_{1min}	minimum allowable disk outer radius	m
r_{2min}	minimum allowable disk inner radius	m
r_1	outer disk radius	m
r_2	inner disk radius	m
r_n	arbitrary reference radius	m
r	radial coordinate	m
s	half the disk spacing	m
t	time	s
$\bar{u}_\phi$	average circumferential velocity (rotating reference frame)	$\mathrm{m\,s^{-1}}$
$\bar{u}_{\phi 1}$	average circumferential velocity at r_1	$\mathrm{m\,s^{-1}}$
$\bar{u}_{\phi 2}$	average circumferential velocity at r_2	$\mathrm{m\,s^{-1}}$
$\bar{u}_r$	average radial velocity	$\mathrm{m\,s^{-1}}$
$\bar{u}_{r1}$	average radial velocity at r_1	$\mathrm{m\,s^{-1}}$
$\bar{u}_{r2}$	average radial velocity at r_2	$\mathrm{m\,s^{-1}}$
$\bar{u}_{rn}$	average radial velocity at r_n	$\mathrm{m\,s^{-1}}$
$\bar{u}_0$	average velocity magnitude at the nozzle inlet	$\mathrm{m\,s^{-1}}$
$\bar{u}_1$	average velocity magnitude at r_1	$\mathrm{m\,s^{-1}}$
$\boldsymbol{u}$	velocity vector	$\mathrm{m\,s^{-1}}$
u_{3max}	maximum allowable velocity magnitude at turbine outlet	$\mathrm{m\,s^{-1}}$
u_ϕ	circumferential velocity (rotating reference frame)	$\mathrm{m\,s^{-1}}$
u_3	velocity magnitude at turbine outlet	$\mathrm{m\,s^{-1}}$
u_r	radial velocity	$\mathrm{m\,s^{-1}}$
u_z	axial velocity	$\mathrm{m\,s^{-1}}$
u	velocity magnitude	$\mathrm{m\,s^{-1}}$
$\dot{v}$	turbine volume flow	$\mathrm{m^3\,s^{-1}}$
$\dot{w}_g$	turbine power output per disk gap	W
$\dot{w}_l$	turbine power loss	W
$\dot{w}$	turbine power output	W
x	placeholder for a dimensional quantity	
x	cartesian x coordinate	m
y	specific turbine power output	$\mathrm{J\,kg^{-1}}$
y	cartesian y coordinate	m
z	axial coordinate	m

Uppercase

A	auxiliary variable for the analytical solution by Breiter and Pohlhausen [1962]	-
B	auxiliary variable for the analytical solution by Breiter and Pohlhausen [1962]	-
C_m	windage loss torque coefficient	-
C	auxiliary variable for the analytical solution by Breiter and Pohlhausen [1962]	-
D_s	Baljé specific turbine diameter	-
$\tilde{E}$	modified nondimensional power density	-
E	nondimensional power density	-
F	auxiliary variable for the analytical solution by Breiter and Pohlhausen [1962]	-

$\tilde{H}_i$	specific nondimensional total to static enthalpy drop across the turbine for incompressible media, including stator losses	-
H_c	specific nondimensional total to static enthalpy drop across the turbine for compressible media	-
H_i	specific nondimensional total to static enthalpy drop across the turbine for incompressible media	-
H_{rc}	specific nondimensional total to static enthalpy drop across the rotor for compressible media	-
H_{ri}	specific nondimensional total to static enthalpy drop across the rotor for incompressible media	-
H	specific nondimensional enthalpy	-
$\mathrm{Im}(\dots)$	imaginary part of ...	-
$\dot{M}_c$	nondimensional turbine mass flow by Whitfield and Baines [1990]	-
$\dot{M}_g$	nondimensional radial mass flow through one disk gap	-
$\dot{M}$	nondimensional turbine mass flow	-
$\mathrm{Max}(\dots)$	maximum value of ...	-
$\bar{P}_0$	average nondimensional pressure at the nozzle inlet	-
$\bar{P}_1$	average nondimensional pressure at R_1	-
$\bar{P}_2$	average nondimensional pressure at R_2	-
$\tilde{P}_{01}$	modified nondimensional stator pressure drop	-
$\tilde{P}_{02}$	modified nondimensional turbine stage pressure drop	-
$\tilde{P}_{12}$	modified nondimensional rotor pressure drop	-
$\tilde{P}$	modified nondimensional pressure	-
P_0^*	local nondimensional pressure at turbine inlet	-
P_0	nondimensional base flow pressure for linear stability analysis	-
P_a^*	nondimensional pressure perturbation amplitude function, local nondimensionalization	-
P_a	nondimensional pressure perturbation amplitude function	-
P^*	local nondimensional pressure	-
P	nondimensional pressure	-
$\mathcal{R}$	turbine degree of reaction	-
Re_{max}	maximum allowable Reynolds number	-
Re^*	local Reynolds number	-
Re	Reynolds number	-
$\mathrm{Re}(\dots)$	real part of ...	-
R_{air}	specific gas constant for air	$\mathrm{J\,kg^{-1}\,K^{-1}}$
R_2	nondimensional inner disk radius	-
R_n	arbitrary nondimensional radial position	-
R_z	average maximum peak to valley surface roughness	m
R^*	local nondimensional radial coordinate	-
R	nondimensional radial coordinate	-
$S_{\phi max}$	maximum nondimensional disk material stress in circumferential direction	-
S_{air}	Sutherland constant for air	K
S_{rmax}	maximum nondimensional disk material stress in radial direction	-

S_ϕ	nondimensional disk material stress in circumferential direction	-
S_r	nondimensional disk material stress in radial direction	-
S	nondimensional disk material stress	-
$\mathcal{T}$	turbine torque	N m
Ta_{max}	maximum allowable Taylor number	-
Ta^*	local Taylor number	-
Ta	Taylor number	-
T^*	local nondimensional time	-
T	nondimensional time	-
$\bar{U}_\phi$	average nondimensional circumferential velocity (rotating reference frame)	-
$\bar{U}_{\phi 1}$	nondimensional average circumferential velocity at R_1	-
$\bar{U}_{\phi 2}$	nondimensional average circumferential velocity at R_2	-
$\bar{U}_r$	average nondimensional radial velocity	-
$\bar{U}_0$	average nondimesional velocity magnitude at the nozzle inlet	-
$\bar{U}_1$	average nondimesional velocity magnitude at R_1	-
$\boldsymbol{U}_0^*$	laminar base flow vector field for linear stability analysis, local nondimensionalization	-
$\boldsymbol{U}_0$	laminar base flow vector field for linear stability analysis	-
$\boldsymbol{U}_a^*$	perturbation amplitude vector for linear stability analysis, local nondimensionalization	-
$\boldsymbol{U}_a$	perturbation amplitude vector for linear stability analysis	-
$\boldsymbol{U}^*$	local nondimensional velocity vector	-
$\boldsymbol{U}$	nondimensional velocity vector	-
$\mathcal{U}_r'$	Fourier transform of fluctuating part of nondimensional radial velocity	-
$U_{\phi a}$	nondimensional circumferential component of velocity amplitude function	-
$U_{\phi 0}^*$	circumferential component of local nodimensional base flow vector field	-
U_{r0}^*	radial component of local nodimensional base flow vector field	-
U_{ra}	nondimensional radial component of velocity amplitude function	-
U_{z0}^*	axial component of local nodimensional base flow vector field	-
U_{za}	nondimensional axial component of velocity amplitude function	-
U_ϕ'	fluctuating part of nondimensional circumferential velocity	-
U_ϕ^*	local nondimensional circumferential velocity (rotating reference frame)	-
U_ϕ	nondimensional circumferential velocity (rotating reference frame)	-
U_τ	friction velocity	-
U_r'	fluctuating part of nondimensional radial velocity	-
U_r^*	local nondimensional radial velocity	-
U_r	nondimensional radial velocity	-
U_z'	fluctuating part of nondimensional axial velocity	-
U_z^*	local nondimensional axial velocity	-

U_z	nondimensional axial velocity	-
U	nondimensional velocity magnitude	-
$\dot{W}_g$	nondimensional turbine power output per disk gap	-
$\dot{W}_l$	nondimensional turbine power loss	-
$\dot{W}$	nondimensional turbine power output	-
X	placeholder for a nondimensional quantity	-
Y	nondimensional specific turbine power output	-
Z^+	axial coordinate in wall-units	-
Z	nondimensional axial coordinate	-

Greek

α_{a1}	flow direction at r_1 (stationary reference frame)	$^\circ$
α_a	flow direction (stationary reference frame)	$^\circ$
α_1	flow direction at r_1 (rotating reference frame)	$^\circ$
α	flow direction (rotating reference frame)	$^\circ$
γ_ϕ^*	local nondimensional circumferential wavenumber	-
γ_ϕ	nondimensional circumferential wavenumber	-
γ_r^*	local nondimensional radial wavenumber	-
γ_r	nondimensional radial wavenumber	-
γ_t^*	local nondimensional temporal wavenumber	-
γ_t	nondimensional temporal wavenumber	-
$\Delta...$	measurement error of ...	
η_c	total to static isentropic turbine efficiency for compressible media	-
η_i	total to static turbine efficiency for incompressible media	-
η_{rc}	total to static isentropic rotor efficiency for compressible media	-
η_{ri}	total to static rotor efficiency for incompressible media	-
η_n	stator efficiency	-
$\tilde{\eta}_c$	static to static isentropic turbine efficiency	-
$\tilde{\eta}_i$	static to static incompressible turbine efficiency including turbine losses	-
$\bar{\vartheta}_0$	average fluid temperature at the nozzle inlet	°C
$\bar{\vartheta}_1$	average fluid temperature at r_1	°C
ϑ_r	Sutherland reference temperature	°C
ϑ	Temperature	°C
κ	heat capacity ratio	-
μ_r	Sutherland reference viscosity	Pa s
μ	dynamic viscosity	Pa s
ν_1	kinemtaic viscosity at r_1	$\mathrm{m^2\,s^{-1}}$
ν_d	Poisson's ratio disk material	-
ν	kinematic viscosity	$\mathrm{m^2\,s^{-1}}$
Π	turbine pressure ratio	-
Π_r	rotor pressure ratio	-
ρ_d	density disk material	$\mathrm{kg\,m^{-3}}$
ρ	fluid density	$\mathrm{kg\,m^{-3}}$
σ_d	disk material stress	$\mathrm{N\,m^{-2}}$
σ_{dmax}	maximum allowable disk material stress	$\mathrm{N\,m^{-2}}$

σ^*	local disk gap aspect ratio	-
σ	disk gap aspect ratio	-
φ_1	geometric rotor inlet angle	$^\circ$
φ_2	nozzle opening angle	$^\circ$
ϕ	circumferential coordinate	rad
$\mathbf{\Omega}$	angular velocity vector	s^{-1}
ω_s	Baljé turbine specific speed	-
ω	angular disk velocity	s^{-1}

Abbreviations

CFD	computational fluid dynamics
CFRP	carbon fibre reinforced polymer
DNS	direct numerical simulation
HAM	homotopy analysis method
MRI	magnetic resonance imaging
ORC	organic Rankine cycle
PTV	particle tracking velocimetry
RANS	Reynolds-averaged Navier-Stokes
RNG	Renormalization group
SAS	Scale adaptive simulation
SST	shear stress transport

Chapter 1

Introduction to Tesla turbines

Invented over 100 years ago, Tesla turbines are a unique type of turbine that, if applied correctly, has the potential to replace conventional turbines in certain applications.

1.1 Operating principle

The Tesla turbine is a friction turbine that converts energy contained in a fluid to mechanical energy, solely through friction between the fluid and the turbine rotor surfaces. In order to maximize contact area between rotor and fluid, the rotor is made up of a series of disks, mounted on a shaft with a small distance in between each of them. One or more nozzles are distributed along the outer circumference of the rotor that feed the working fluid into the thin channels between the disks. The fluid enters the rotor almost tangentially and travels on a spiral-shaped path radially inward towards the exhaust openings in the centre region of the disks. On its way, some of the kinetic energy of the fluid is used up due to viscous friction. This causes a shear force on the surface of the rotor disks that ultimately drives the rotor. Figure 1.1 visualizes this principle.

As for all turbines, the pressurized fluid first enters one or more nozzles, where some of its pressure is used up for acceleration. The nozzles direct the high velocity fluid towards the rotor and inject it into the rotor channels. Throughout the rotor, the pressure continues to decrease as the fluid experiences the natural centrifugal pressure gradient. The direction at which the fluid enters the rotor is neither purely radial nor purely tangential in order

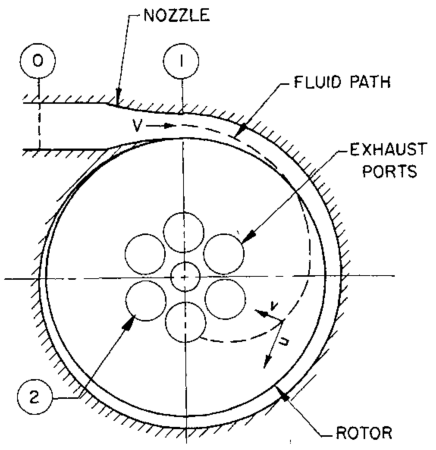

Figure 1.1: Tesla turbine schematic by Beans [1961].

to both create a throughflow in radial inward direction and a flow in the direction of disk rotation. The radial velocity component follows the negative pressure gradient from rotor inlet to outlet and is responsible for the mass flow through the turbine. The tangential component on the other hand is what drives the rotor. The local difference between tangential fluid velocity component and rotor disk surface velocity causes a shear stress in circumferential direction, acting on the disk surface. Taking into account the distance to the axis of rotation and summing up all local contributions across the rotor surfaces, this results in the rotor torque. The turbine shaft in turn transmits the torque to some kind of load, for example an electrical generator. Lastly, after interacting with the rotor, the fluid exits through the outlet openings with some residual kinetic energy and turns towards the axial direction, leaving the turbine through its outlet structures.

Figure 1.2 shows some turbine components. The rotor in this case is made from metal disks, mounted onto a shaft with a shaft nut. There are thin spacing shims in between the disks as to leave narrow gaps between the disks. The first and last disk of the package is thicker to stabilize the rotor. The stator is depicted in figure 1.2b. It consists in this case of four aluminium blocks with four nozzle-shaped openings in between them, that allow the fluid to radially approach the rotor and enter the disk gaps. In the centre of the disks there are five outlet openings, where the fluid exits the rotor in axial direction. Rotor and stator are mounted inside a plenum that is supplied with compressed air. The plenum allows the fluid to distribute evenly around the stator circumference before entering the nozzles. It is depicted in figure 1.2d.

For a Tesla turbine to deliver good performance, it is important to thoughtfully choose rotor and stator geometry. The most important parameters are disk outer radius, outlet radius, disk spacing and disk thickness. For the nozzles, their number and overall shape, especially the nozzle outlet angle, are key to good designs.

This work is strictly focused on Tesla turbines as described so far. It is however theoretically possible to build other types of friction turbines, for example an axial friction turbine, as suggested by Vinha et al. [2016] and Braun et al. [2021]. Radial friction turbines with radially outward flow would be possible as well, but compared to the Tesla turbine, these are of disadvantage and thus very rare. The nozzles would have to be placed in the constricted space in the centre of the rotor and the natural pressure gradient from rotation, that is directed from outer to inner disk radius, would work against the expansion of the fluid. Another advantage of radial inward flow is, that both the disk surface velocity and the fluid velocity in tangential direction decrease towards the outlet. This leads to a more efficient momentum transfer compared to radially outward flow, where the disk surface with increasing velocity would interact with the decreasing tangential fluid velocity component.

Compared to conventional radial and axial bladed turbines, the efficiency of Tesla turbines is generally lower. Nonetheless, they have some unique characteristics, that put them at an advantage in some aspects. There is an ongoing change in the energy market towards different energy sources and more efficient use of energy, that gives rise to new fields of applications for turbines, where the Tesla turbine has potential to compete with or even outperform conventional turbines.

A major advantage of the Tesla turbine concept is its simplicity. In contrast to the complex blade shapes that are required for a bladed turbine rotor, the rotor of a Tesla turbine consists of mere disks that can be manufactured cheaply from sheet stock of any material, for example metals, polymers and fibre reinforced polymers. The diverse choice of rotor materials makes it easier to meet application requirements, for example high temperature, corrosive media, low cost or weight reduction requirements for mobile

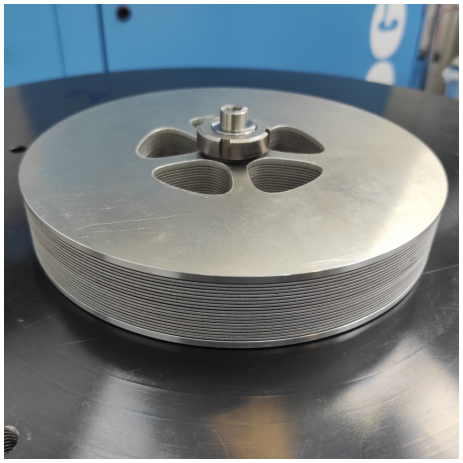

(a) Mounted Tesla turbine rotor with a diameter of 180 mm.

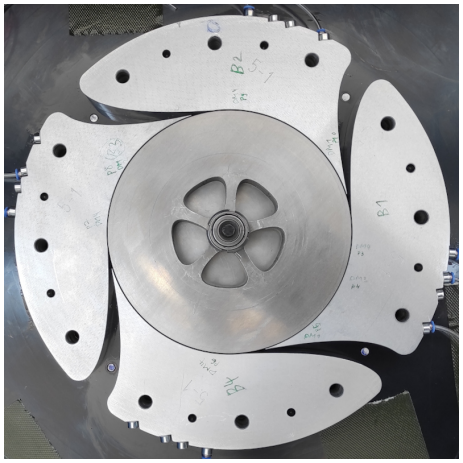

(b) Opened up Tesla turbine. Above view of rotor and stator with four nozzles.

(c) Side view of the rotor.

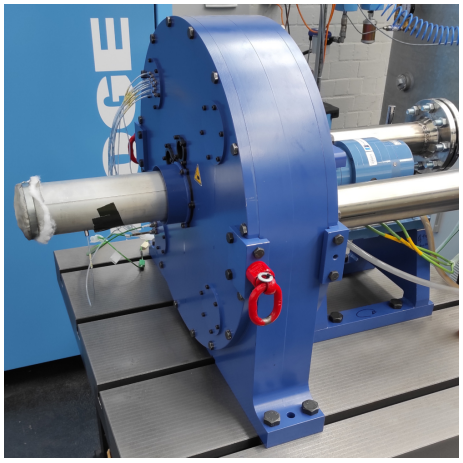

(d) Turbine housing. Compressed air enters from the right and exits towards the left.

Figure 1.2: Tesla turbine components.

machinery. Specialized Tesla turbine designs are possible that are optimized for operation with inhomogeneous media through adapted turbine geometry and wear resistant disk materials. Compared to conventional turbines, the Tesla turbine rotor provides little impact surface for particles and condensation droplets. On top of that, the Tesla turbine design is scalable to a range of power outputs just by adding or removing disks. This would allow a manufacturer to set up a parametric design that can be adapted to a range of turbine power outputs with little or no need to change the design of individual turbine components. Lastly, given a suitable stator design, Tesla turbines are reversible and are worth considering for energy storage applications. The working medium can be compressed in Tesla pump operation and expanded in turbine operation, using the same machine.

1.2 Brief history

The first prototype of a Tesla turbine was patented by Tesla [1913], along with its pump and compressor counterpart, hence the name. Figure 1.3 shows a schematic from the original patent. The invention was originally intended as a competitor to conventional

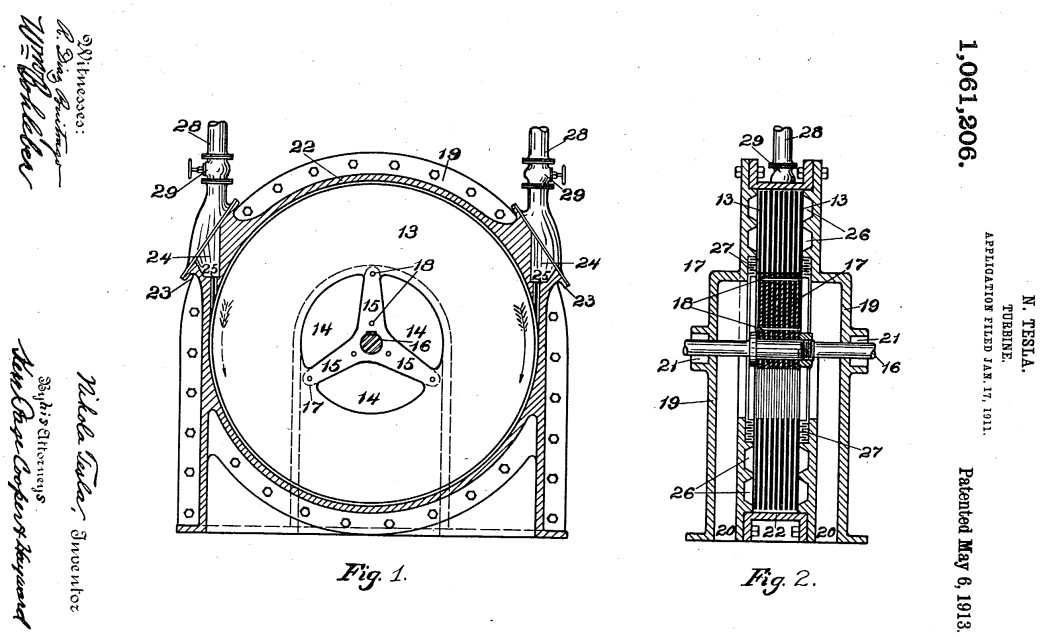

Figure 1.3: Schematic from the original patent by Tesla [1913].

turbines, but to this day, it is not used industrially. For a detailed review of the early history of Tesla turbines, the studies by Armstrong [1952] and Beans [1961] provide very good overviews.

Research interest in Tesla turbines grew after 1950 and persists until today. Over the years, numerous experimental Tesla turbines have been built by researchers and hobbyists. Only a handful of those turbines were large enough to reach power outputs of over 1 kW. The magnitude of the original steam powered prototype that is reported by Scientific American [1911] to have yielded 200 hp, i.e. approximately 150 kW, has so far not been reached again. Already at an early stage of Tesla turbine research, Rice [1965] predicts the Tesla turbine to be a candidate for specialized applications involving exotic fluids and small power outputs. This viewpoint persists until today, where research interest in Tesla turbines is fuelled by the restructuring of the energy sector in the face of global warming and the new challenges to turbine designs that come along with it.

Mathematical modelling of Tesla turbines is a rewarding subject, since the simple annular geometry of the rotor disk interspace allows for major simplifications of the Navier-Stokes equations and derivation of analytical solutions to the rotor flow field. One of the landmark studies in this respect was published by Beans [1961], who was the first to derive an analytical solution using parabolic velocity profile shapes. Breiter and Pohlhausen [1962] first derived a solution from channel flow equations, modified with Coriolis and centrifugal terms. Even in more recent years a new series approach for an analytical solution was found by Batista [2011].

1.3 Possible fields of application

There is no lack in creativity among researchers with regard to possible fields of application for the Tesla turbine. Aside from the main application branches for turbines, for example steam power plants and gas turbines, there are lots of other fields where an expander of some sort is required and the Tesla turbine is a potential candidate. Generally, this is any

application needing a small-scale, low-cost expander, for example in the recovery of waste energy from industrial processes.

One of the largest interest groups in Tesla turbine research is in some way or another connected to organic Rankine cycle (ORC) applications. Talluri [2019] provides a detailed review of Tesla turbines with focus on ORC applications including analytical, numerical and experimental research and compares the Tesla turbine to other expanders. Carey [2010] and Crowell [2009] suggest small scale, solar-powered Rankine cycles using a Tesla turbine as expander. Song et al. [2017] compare different working media for ORC Tesla turbines, while Ji et al. [2019] show that it's possible to recover waste heat from the coolant of a car engine through the use of a Tesla turbine. Baik et al. [2016] describe an experimental Brayton cycle operating on supercritical CO_2 that utilizes a Tesla turbine.

Another idea is to use a Tesla turbine to replace an expansion valve. Aghagoli and Sorin [2020] analyses a heat pump cycle operating on CO_2 and calculate the performance benefit from replacing the expansion valve with a Tesla turbine. Giakoumis et al. [2020] and Niknam et al. [2021] target refrigeration cycles and analyse the interaction of the turbine with a partially condensing vapour. Sheikhnejad et al. [2020] suggest a refrigeration cycle operating on methane that implements a Tesla turbine. Finally, Pfeffer [2020] works on developing a portable integrated turbine and generator system for generation of electrical power from compressed breathing air, carried by divers and firefighters.

Small scale harvesting of water power is another commonly proposed application for Tesla turbines. Andres and Loretero [2019] perform an experimental study on a Tesla turbine with regard to harvesting water energy from agricultural irrigation channels. Zhao et al. [2014] and Raunak et al. [2014] suggest using the Tesla turbine as cheap, small scale water turbine. Krishnan [2015] base their work around small scale water energy harvesting down to millimetre scales, while Hadi et al. [2020] suggest using Tesla turbines to power remote sensors along water networks.

One of the aforementioned benefits of the bladeless design is the minimal interaction between the rotor and inhomogeneities in the fluid. This is why Tesla pumps are also considered for medical applications involving blood. Miller and Fink [1999] show that the stress on blood cells passing through a Tesla pump is small compared to other pump types. Later, Jonsson et al. [2014] were able to power a pacemaker with a Tesla turbine inside the body of a pig.

Navarro-Alarcon et al. [2021] describe another application in the medical field. During magnetic resonance imaging (MRI), mechanical actuators that are made of ferromagnetic materials or generate electromagnetic fields cannot be used. This is why the authors design a pneumatic linear actuator based around a polymer Tesla turbine that doesn't interfere with the MRI-imaging. Nagaraja et al. [2022] describe testing of a tesla Turbine powered prosthesis.

As for another rather exotic application, Han et al. [2021] find a way to use a Tesla turbine in their self-powered ammonia synthesis. They drive the Tesla turbine with nitrogen, which at the same time is an ingredient for the synthesis. The turbine drives a triboelectric generator that feeds a high voltage discharge, which in turn drives the reaction between water and nitrogen to ammonia.

Finally, a unique suggestion is reported in a Russian popular science magazine by Semin [1962]. The author suggests a gas turbine utilizing a bladeless turbine with ceramic disks to account for the high temperatures. The article mentions a prototype from Stainless steel that reaches an efficiency of 41 % at a power output of 10 hp, i.e. approximately 7.4 kW. Deam et al. [2008] perform further analysis with respect to utilizing the Tesla turbine in a gas turbine. They figure that the scaling behaviour down to small sizes is

better than for other turbines.

1.4 Goals and contents

The present work intends to lay out previous findings in Tesla turbine research and further develop the state of the art of Tesla turbine modelling and design. A further goal is to provide an easily accessible basis for the engineer to assess Tesla turbine performance for any given application, benchmark it against other types of expanders and work out a detailed turbine design.

All results reported here are divided into three main categories: Tesla turbine modelling, experiment and design. Chapter 2 summarizes previous research on each of these. After providing basic equations, a wide range of possible approaches to analytically predict the flow field inside a Tesla turbine rotor is laid out. Performance data of existing experimental Tesla turbines is compiled as well as previously established design guidelines. The literature review is followed by chapter 3, which describes two approaches of simulating a Tesla turbine numerically and searches for the laminar-turbulent regime boundary of the Tesla turbine rotor flow. For validation, analytical and numerical modelling of the rotor flow is compared to each other and to previous experimental velocity measurements. The new Tesla turbine test facility, described in chapter 4, is then used for acquisition of performance maps, dependent on various turbine design parameters. Detailed technical specifications are given, along with measurement of various types of losses. Finally, chapter 5 develops a new Tesla turbine preliminary aerodynamic design routine, based on results from previous chapters.

In the course of this work it will become clear, that Tesla turbine technology is well beyond the proof of concept phase and ready to be utilized in industrial applications.

Chapter 2

Previous research on Tesla turbines

Chapter 2 is intended to give an overview of existing literature about Tesla turbines. After introducing basic equations and performance parameters, different methods to mathematically model Tesla turbines are provided. After that, performance parameters of previous experimental Tesla turbines as well as studies about Tesla turbine design are summarized.

2.1 Basic equations

At the core of any Tesla turbine design routine is the modelling of the flow in the narrow channels between the rotor disks. Consider a narrow annulus with imposed vortical throughflow in radially inward direction and corotating walls in axial direction. Figure 2.1 gives a basic overview. The distance between the disks is assumed to be small compared to their radius.

Starting point for analytical investigations are the Navier-Stokes equations. Below, they are given, as derived by Oertel and Prandtl [2017], for an incompressible fluid in rotating frame of reference.

$$\rho\left(\frac{\partial \boldsymbol{u}}{\partial t} + (\boldsymbol{u}\cdot\nabla)\boldsymbol{u} + 2\boldsymbol{\Omega}\times\boldsymbol{u} + \boldsymbol{\Omega}\times(\boldsymbol{\Omega}\times\boldsymbol{r})\right) = \boldsymbol{f} - \nabla p + \mu\Delta\boldsymbol{u} \tag{2.1}$$

$$\nabla\cdot\boldsymbol{u} = 0 \tag{2.2}$$

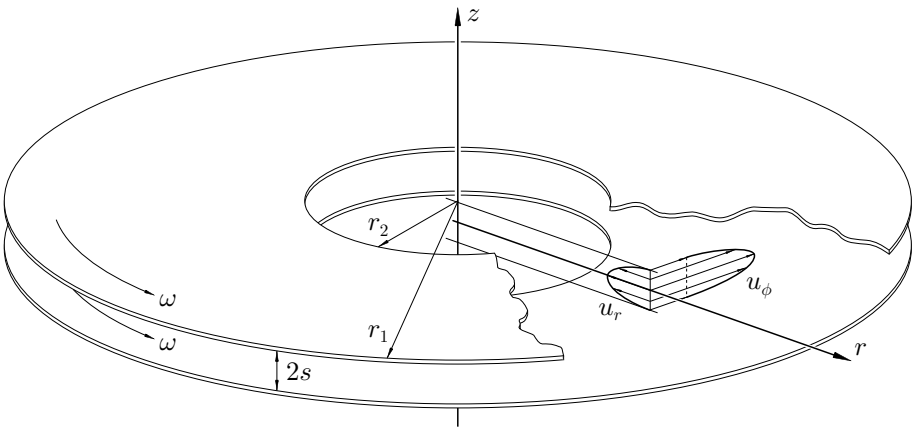

Figure 2.1: Schematic view of the flow setup.

Because of the annular shape of the fluid domain in a Tesla turbine rotor, it is useful to work in a cylindrical coordinate system, using the coordinate vector $\boldsymbol{r} = (r, \phi, z)$ and the velocity vector $\boldsymbol{u} = (u_r, u_\phi, u_z)$. Note that the centrifugal and Coriolis terms are still included, so that u_ϕ describes the circumferential velocity relative to the disk surface. The system rotates with the angular velocity ω around the z-Axis, thus $\boldsymbol{\Omega} = (0, 0, \omega)$.

$$\begin{aligned}\frac{\partial u_r}{\partial t} + \frac{1}{\rho}\frac{\partial p}{\partial r} + u_r\frac{\partial u_r}{\partial r} + \frac{u_\phi}{r}\frac{\partial u_r}{\partial \phi} - \frac{u_\phi^2}{r} + u_z\frac{\partial u_r}{\partial z} - 2\omega u_\phi - r\omega^2 \\ + \nu\left(\frac{u_r}{r^2} - \frac{1}{r}\frac{\partial u_r}{\partial r} - \frac{\partial^2 u_r}{\partial r^2} - \frac{1}{r^2}\frac{\partial^2 u_r}{\partial \phi^2} + \frac{2}{r^2}\frac{\partial u_\phi}{\partial \phi} - \frac{\partial^2 u_r}{\partial z^2}\right) = 0\end{aligned} \tag{2.3a}$$

$$\begin{aligned}\frac{\partial u_\phi}{\partial t} + \frac{1}{\rho r}\frac{\partial p}{\partial \phi} + u_r\frac{\partial u_\phi}{\partial r} + \frac{u_\phi}{r}\frac{\partial u_\phi}{\partial \phi} + \frac{u_\phi u_r}{r} + u_z\frac{\partial u_\phi}{\partial z} + 2\omega u_r \\ + \nu\left(\frac{u_\phi}{r^2} - \frac{1}{r}\frac{\partial u_\phi}{\partial r} - \frac{\partial^2 u_\phi}{\partial r^2} - \frac{1}{r^2}\frac{\partial^2 u_\phi}{\partial \phi^2} - \frac{2}{r^2}\frac{\partial u_r}{\partial \phi} - \frac{\partial^2 u_\phi}{\partial z^2}\right) = 0\end{aligned} \tag{2.3b}$$

$$\begin{aligned}\frac{\partial u_z}{\partial t} + \frac{1}{\rho}\frac{\partial p}{\partial z} + u_r\frac{\partial u_z}{\partial r} + \frac{u_\phi}{r}\frac{\partial u_z}{\partial \phi} + u_z\frac{\partial u_z}{\partial z} \\ + \nu\left(-\frac{1}{r}\frac{\partial u_z}{\partial r} - \frac{\partial^2 u_z}{\partial r^2} - \frac{1}{r^2}\frac{\partial^2 u_z}{\partial \phi^2} - \frac{\partial^2 u_z}{\partial z^2}\right) = 0\end{aligned} \tag{2.3c}$$

$$\frac{u_r}{r} + \frac{\partial u_r}{\partial r} + \frac{1}{r}\frac{\partial u_\phi}{\partial \phi} + \frac{\partial u_z}{\partial z} = 0 \tag{2.4}$$

The corresponding boundary conditions are inlet and outlet boundaries at the outer and inner radius r_1 and r_2 respectively and periodicity in circumferential direction. The walls are fixed at $z = \pm s$ and thus are rotating along with the reference frame.

There is no standardized method for nondimensionalization and naming of nondimensional parameters when analysing Tesla turbines. The following scheme uses a reference radius r_n and half the disk spacing s as radial and axial length scales. Velocities are normalized with $|\bar{u}_{rn}|$ and $|\bar{u}_{rn}|\sigma^*$ respectively, where $\sigma^* = s/r_n$. Throughout this work, uppercase letters are mostly used for nondimensional quantities and lowercase letters for their dimensional counterparts.

$$R^* = \frac{r}{r_n}, \quad Z = \frac{z}{s}, \quad U_r^* = \frac{u_r}{|\bar{u}_{rn}|}, \quad U_\phi^* = \frac{u_\phi}{|\bar{u}_{rn}|}, \quad U_z^* = \frac{u_z}{|\bar{u}_{rn}|\sigma^*}, \quad P^* = \frac{p}{\rho \bar{u}_{rn}^2} \tag{2.5}$$

$\bar{u}_{rn}$ is the average radial velocity at the radius r_n. Absolute values are used for normalization, since the radial velocity is generally negative in the case of Tesla turbine flow. The overbar denotes averaging in z. For any quantity x and its nondimensional counterpart X, at the radial positions r_n and R_n respectively, the averaging can be expressed as:

$$\bar{x}(r_n) = \bar{x}_n = \frac{1}{2s}\int_{-s}^{s} x(r_n, z)\mathrm{d}z \tag{2.6}$$

$$\bar{X}(R_n) = \bar{X}_n = \frac{1}{2}\int_{-1}^{1} X(R_n, Z)\mathrm{d}Z \tag{2.7}$$

This assumes a stationary and axisymmetric flow field, but can be extended naturally to non-axisymmetric and instationary flows. The subscripts 0, 1, 2 and n for any quantity refer to the positions inside the turbine, where 0 stands for the stator inlet, 1 for rotor inlet, 2 for rotor outlet and n refers to an arbitrary radial position inside the rotor.

The circumferential velocity component is deliberately omitted from the normalization, since it is not straight forward to determine, especially in an experimental setting. This is justifiable to some degree because later it will be seen, that the flow sometimes has an asymptotic character where the circumferential velocity component is more determined by the rotational speed of the disks than by the circumferential velocity component at the inlet. It is thus represented by the Taylor number.

Inserting these definitions into equations 2.3 and 2.4 results in three dimensionless parameters that govern the inter-disk flow. A Reynolds number Re^* that is based on radial mass flow, a Taylor number Ta^* based on the disk surface velocity and an aspect ratio σ^*.

$$\mathrm{Re}^* = \frac{s|\bar{u}_{rn}|}{\nu} = \frac{\dot{m}_g}{4\pi r_n \mu}, \quad \mathrm{Ta}^* = \frac{s r_n \omega}{\nu}, \quad \sigma^* = \frac{s}{r_n} \tag{2.8}$$

The nondimensional parameters introduced so far are local parameters, valid only at the radial position r_n. In practice, the space between two rotating disks of course includes a range of values of r_n, from the inner disk radius r_2 to the outer disk radius r_1, and thus a range of Reynolds numbers, Taylor numbers and aspect ratios. The local parameters are useful for prediction of transition and turbulence since the flow is radially inhomogeneous. When applying the parameter scheme to computations and experiments however, it is often more practical to use a global set of parameters with the radial length scale fixed at the outer disk radius r_1. This requires the ratio of inner to outer disk radius R_2 to be introduced as an additional parameter. The set of global variables and parameters can be written as:

$$R = \frac{r}{r_1}, \quad Z = \frac{z}{s}, \quad U_r = \frac{u_r}{|\bar{u}_{r1}|}, \quad U_\phi = \frac{u_\phi}{|\bar{u}_{r1}|}, \quad U_z = \frac{u_z}{|\bar{u}_{r1}|\sigma}, \quad P = \frac{p}{\rho \bar{u}_{r1}^2}, \quad T = \frac{t\ |\bar{u}_{r1}|}{r_1} \tag{2.9}$$

$$\mathrm{Re} = \frac{s|\bar{u}_{r1}|}{\nu} = \frac{\dot{m}_g}{4\pi r_1 \mu}, \quad \mathrm{Ta} = \frac{s r_1 \omega}{\nu}, \quad \sigma = \frac{s}{r_1}, \quad R_2 = \frac{r_2}{r_1} \tag{2.10}$$

According to these definitions, the disk annulus covers the following intervals of local parameters:

$$\mathrm{Re} \le \mathrm{Re}^* \le \frac{\mathrm{Re}}{R_2}, \quad R_2 \mathrm{Ta} \le \mathrm{Ta}^* \le \mathrm{Ta}, \quad \sigma \le \sigma^* \le \frac{\sigma}{R_2} \tag{2.11}$$

Applying the global parameter scheme to the Navier-Stokes equations gives the following set of nondimensional equations:

$$\begin{aligned}
&\sigma\mathrm{Re}\left(\frac{\partial U_r}{\partial T} + \frac{\partial P}{\partial R} + U_r\frac{\partial U_r}{\partial R} + \frac{U_\phi}{R}\frac{\partial U_r}{\partial \phi} - \frac{U_\phi^2}{R} + U_z\frac{\partial U_r}{\partial Z}\right) - 2\sigma\mathrm{Ta}U_\phi - \frac{\sigma\mathrm{Ta}^2}{\mathrm{Re}}R \qquad (2.12a)\\
&\quad + \sigma^2\left(\frac{U_r}{R^2} - \frac{1}{R}\frac{\partial U_r}{\partial R} - \frac{\partial^2 U_r}{\partial R^2} - \frac{1}{R^2}\frac{\partial^2 U_r}{\partial \phi^2} + \frac{2}{R^2}\frac{U_\phi}{\partial \phi}\right) - \frac{\partial^2 U_r}{\partial Z^2} = 0\\
&\sigma\mathrm{Re}\left(\frac{\partial U_\phi}{\partial T} + \frac{1}{R}\frac{\partial P}{\partial \phi} + U_r\frac{\partial U_\phi}{\partial R} + \frac{U_\phi}{R}\frac{\partial U_\phi}{\partial \phi} + \frac{U_\phi U_r}{R} + U_z\frac{\partial U_\phi}{\partial Z}\right) + 2\sigma\mathrm{Ta}U_r \qquad (2.12b)\\
&\quad + \sigma^2\left(\frac{U_\phi}{R^2} - \frac{1}{R}\frac{\partial U_\phi}{\partial R} - \frac{\partial^2 U_\phi}{\partial R^2} - \frac{1}{R^2}\frac{\partial^2 U_\phi}{\partial \phi^2} - \frac{2}{R^2}\frac{\partial U_r}{\partial \phi}\right) - \frac{\partial^2 U_\phi}{\partial Z^2} = 0\\
&\mathrm{Re}\frac{\partial P}{\partial Z} + \sigma^2\mathrm{Re}\left(\frac{\partial U_z}{\partial T} + U_r\frac{\partial U_z}{\partial R} + \frac{U_\phi}{R}\frac{\partial U_z}{\partial \phi} + U_z\frac{\partial U_z}{Z}\right) \qquad (2.12c)\\
&\quad + \sigma^3\left(-\frac{1}{R}\frac{\partial U_z}{\partial R} - \frac{\partial^2 U_z}{\partial R^2} - \frac{1}{R^2}\frac{\partial^2 U_z}{\partial \phi^2}\right) - \sigma\frac{\partial^2 U_z}{\partial Z^2} = 0
\end{aligned}$$

$$\frac{U_r}{R} + \frac{\partial U_r}{\partial R} + \frac{1}{R}\frac{\partial U_\phi}{\partial \phi} + \frac{\partial U_z}{\partial Z} = 0 \tag{2.13}$$

Once a solution to these equations is found, turbine performance parameters can be calculated. For analysing the flow direction, a flow angle α is introduced.

$$\alpha = \arctan\left(\frac{\bar{u}_r}{\bar{u}_\phi}\right) = \arctan\left(\frac{\bar{U}_r}{\bar{U}_\phi}\right) \tag{2.14}$$

The flow angle can also be defined in the non-rotating frame of reference.

$$\alpha_a = \arctan\left(\frac{\bar{u}_r}{\bar{u}_\phi + r\omega}\right) = \arctan\left(\frac{\bar{U}_r}{\bar{U}_\phi + R\ \mathrm{Ta/Re}}\right) \tag{2.15}$$

The specific turbine power outputs y and Y follow from Euler's turbomachinery equation.

$$y = r_2\omega(\bar{u}_{\phi 2} + r_2\omega) - r_1\omega(\bar{u}_{\phi 1} + r_1\omega) \tag{2.16}$$

$$Y = \frac{\mathrm{Ta}}{\mathrm{Re}}\left(R_2\left(\bar{U}_{\phi 2} + R_2\frac{\mathrm{Ta}}{\mathrm{Re}}\right) - \left(\bar{U}_{\phi 1} + \frac{\mathrm{Ta}}{\mathrm{Re}}\right)\right) \tag{2.17}$$

$$y = \bar{u}_{r1}^2 Y \tag{2.18}$$

The fluid energy provided to the turbine rotor can be expressed as specific total to static rotor heads h_{ri} and H_{ri}. For an incompressible medium, as denoted by the subscript i, they can be derived from Bernoulli's principle. The outlet kinetic energy of the fluid is considered lost, so it is omitted from the equations.

$$h_{ri} = \frac{\bar{p}_2}{\rho} - \frac{\bar{p}_1}{\rho} - \frac{\bar{u}_1^2}{2} \tag{2.19}$$

$$H_{ri} = \bar{P}_2 - \bar{P}_1 - \frac{\bar{U}_1^2}{2} \tag{2.20}$$

with

$$h = \bar{u}_{r1}^2 H \tag{2.21}$$

$$u = \sqrt{u_r^2 + (u_\phi + r\omega)^2 + u_z^2} \tag{2.22}$$

$$U = \sqrt{U_r^2 + \left(U_\phi + R\frac{\mathrm{Ta}}{\mathrm{Re}}\right)^2 + U_z^2} \tag{2.23}$$

Using these quantities, rotor efficiency can be calculated from:

$$\eta_{ri} = \frac{y}{h_{ri}} = \frac{Y}{H_{ri}} \tag{2.24}$$

When analysing results involving a compressible medium, the total to static isentropic rotor enthalpy difference h_{rc} and the isentropic rotor efficiency η_{rc} are calculated.

$$h_{rc} = c_p\bar{\vartheta}_1\left(\left(\frac{\bar{p}_2}{\bar{p}_1}\right)^{(\kappa-1)/\kappa} - 1\right) - \frac{\bar{u}_1^2}{2} \tag{2.25}$$

$$\eta_{rc} = \frac{y}{h_{rc}} \tag{2.26}$$

The definitions can be extended to the whole turbine stage simply by swapping out the rotor inlet conditions with the stator inlet conditions, denoted with the subscript 0.

$$h_i = \frac{\bar{p}_2}{\rho} - \frac{\bar{p}_0}{\rho} - \frac{\bar{u}_0^2}{2} \tag{2.27}$$

$$h_c = c_p \bar{\vartheta}_0 \left(\left(\frac{\bar{p}_2}{\bar{p}_0} \right)^{(\kappa-1)/\kappa} - 1 \right) - \frac{\bar{u}_0^2}{2} \tag{2.28}$$

$$\eta_i = \frac{y}{h_i} = \frac{Y}{H_i} \tag{2.29}$$

$$\eta_c = \frac{y}{h_c} = \frac{Y}{H_c} \tag{2.30}$$

The power output of the turbine simply follows from multiplying mass flow and specific power output, where the subscript g indicates quantities with respect to a single disk gap, including two opposing disk surfaces.

$$\dot{w}_g = \dot{m}_g y \tag{2.31}$$

$$\dot{W}_g = \dot{M}_g Y = 4\sigma\pi Y \tag{2.32}$$

with

$$\dot{m}_g = |4rs\pi\bar{u}_r\rho| = 4r_1 s\pi|\bar{u}_{r1}|\rho \tag{2.33}$$

$$\dot{M}_g = |4R\sigma\pi\bar{U}_r| = 4\sigma\pi \tag{2.34}$$

$$\dot{m} = \rho|\bar{u}_{r1}|r_1^2\dot{M} \tag{2.35}$$

$$\dot{w} = \rho|\bar{u}_{r1}^3|r_1^2\dot{W} \tag{2.36}$$

The total turbine power output and mass flows $\dot{w}$ and $\dot{m}$ are obtained by simply multiplying the values per gap with the number of gaps.

2.2 Tesla turbine modelling

2.2.1 Rotor flow

Researchers have come up with many different ways to solve the conservation equations inside the Tesla turbine rotor gap. Herrmann-Priesnitz et al. [2016] distinguish different solution regimes with merged and unmerged boundary layers and map out the regime boundaries with respect to Reynolds number, Rossby number and nondimensional radial inlet velocity. As an example figure 2.2 shows regime boundaries, converted to the present parameter scheme, assuming a small aspect ratio σ. Note that the authors use a constant relative inlet flow angle α_1 across the whole chart. The unmerged boundary layer regime is further divided into entraining and non-entraining flow, depending on the core velocity in the centre region of the channel. Regarding Tesla turbine flow it is desirable to maximize fluid-disk interaction, thus the merged boundary layer regime is the most interesting one. Some of the models in the following sections however also cover the onset of boundary layer separation, which manifests itself in a more and more pronounced inflection point in the velocity profile across the disk gap.

What sets this topic apart from the modelling of conventional radial turbines is the unique rotor geometry along with the shear stress based momentum transfer. The simple

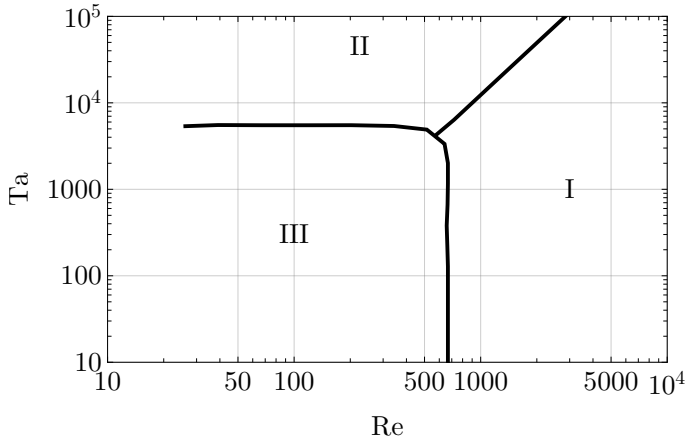

Figure 2.2: Distinction between flow with unmerged entraining (I), unmerged non-entraining (II) and merged boundary layers (III) for $\sigma = 0.001$ and $\alpha_1 = 14.5°$. The figure is based on digitized data from figure 7c by Herrmann-Priesnitz et al. [2016], converted to the present parameter scheme.

annular shape of the rotor channels allows for major simplification of the Navier-Stokes equations and thus efficient modelling of the three-dimensional flow field inside the rotor. The most common assumptions are:

- steady flow
- rotationally symmetric flow
- incompressible fluid
- fully developed flow with no entry and exit effects
- axial velocity component is negligible
- gradients in radial direction are negligible
- terms with small order of magnitude due to small aspect ratio σ are negligible
- imposed velocity profile shapes
- empirical factors such as friction factor

These have been applied by researchers in various combinations with good success. There are fully analytical solutions as wells as hybrid models that combine analytical and numerical methods.

Kármán [1921] famously shows that the flow above a single infinitely large rotating disk can be reduced to a self-similar solution with a velocity profile shape that is dependent only on the disk-normal coordinate. McAlister and Rice [1970] explain, that there is no comparable solution for flow within flat corotating disks. Authors still use approaches that try to decouple the axial and radial dependence of the solutions, but always have to fall back to the more severe simplifications such as negligible axial velocity, imposed velocity profile shapes or neglected nonlinear terms.

The following sections group the available models into categories by their most prominent features, sometimes however the distinction is blurry and models show elements of multiple categories.

2.2.1.1 Friction factor based models

A conceptually easy approach is to simplify the conservation equations through empirical parameters. These can be adapted to both laminar and turbulent flow and even special flow conditions like enhanced wall roughness as proposed by Romanin and Carey [2011]. Each flow regime however requires its own set of calibrated parameters. The first attempt at predicting Tesla turbine performance utilizing this idea is documented by Armstrong [1952] however the particular method is unsuccessful and yields performance predictions off by several orders of magnitude.

Rice [1965] provides a more accurate attempt through solution of a simplified set of conservation equations. They retain some nonlinear inertial terms and approximate the shear force terms through a friction factor. A numerical solution for some example conditions is provided. The author concludes that the model is useful for qualitative analysis of turbine parameters. A friction factor approach that is solvable analytically is developed by Carey [2010].

It remains to be answered how to determine the friction factors, since for the specific case of flow between corotating disks, there is not enough experimental or numerical data available to determine them in advance. To circumvent this, researchers borrow friction factor data from other basic flow configurations. Carey [2010] uses a friction factor based on laminar channel flow, while Song et al. [2018] introduce friction factors from laminar and turbulent pipe flow. In the latter approach, the friction factor is determined locally and thus varies throughout the disk gap, however the model is no longer analytically solvable.

Puzyrewski and Tesch [2010] show that empirical parameters are not limited to friction factors. They develop their own system of equations, simplified through an order of magnitude analysis and integral averaging in the axial direction. The model is analytically solvable, however retains several unknown parameters. These are in turn determined through a CFD simulation. It is yet unclear, how far the operating conditions can deviate from the calibration point while retaining validity of the empirical parameters. At the calibration point however, the agreement between model and CFD computation is shown to be very good.

2.2.1.2 Models with polynomial or power law velocity profiles

The next major category of solutions is based on imposed velocity profile shapes. Beans [1961] and Beans [1966] impose a parabolic shape onto the radial and circumferential velocity component and set the axial component to zero. They derive a simplified set of conservation equations which is analytically solvable in the laminar, incompressible case. They approximate the turbulent regime with a simple mixing length model and a 1/7 power law profile and provide numerical solution for some operating conditions. A comparison between calculated performance data based on those models and their experimental Tesla turbine shows qualitative agreement. Some additional validation is provided by Schosser et al. [2017] and Talluri [2019] who compare their laminar parabolic model to commercial CFD simulation software with good success. The models of Dibelius and Nendl [1973] and Allen [1990] follow the same basic concepts. Euteneuer and Piesche [1978] provide their own, closely related version of the turbulent power law approach.

Sengupta and Guha [2012, 2013] and Guha and Sengupta [2013] develop yet another similar laminar model with parabolic distributions and provide detailed analysis of the results. They break down the order of magnitude of the terms in the momentum equations and a comparison to CFD data shows good agreement. The authors point out an

interesting feature of the flow field, where under certain conditions, the turbine outputs net power even when the tangential fluid velocity at the inlet is smaller than the disk velocity.

To provide an example for the modelling approach based on parabolic velocity distributions, equations 2.12 and 2.13 are simplified by assuming rotationally symmetric flow and by neglecting the axial velocity component as well as terms of order σ^2:

$$\sigma\mathrm{Re}\left(\frac{\partial P}{\partial R}+U_r\frac{\partial U_r}{\partial R}-\frac{U_\phi^2}{R}\right)-2\sigma\mathrm{Ta}\;U_\phi-\frac{\sigma\mathrm{Ta}^2}{\mathrm{Re}}R-\frac{\partial^2 U_r}{\partial Z^2}=0 \tag{2.37a}$$

$$\sigma\mathrm{Re}\left(U_r\frac{\partial U_\phi}{\partial R}+\frac{U_\phi U_r}{R}\right)+2\sigma\mathrm{Ta}\;U_r-\frac{\partial^2 U_\phi}{\partial Z^2}=0 \tag{2.37b}$$

$$\frac{\partial P}{\partial Z}=0 \tag{2.37c}$$

$$\frac{U_r}{R}+\frac{\partial U_r}{\partial R}=0 \tag{2.38}$$

From the axial momentum equation follows, that the pressure is a function of radius only. For the velocities, a parabolic profile shape is imposed:

$$U_r=U_r(R,Z)=\frac{3}{2}\bar{U}_r(R)(1-Z^2) \tag{2.39}$$

$$U_\phi=U_\phi(R,Z)=\frac{3}{2}\bar{U}_\phi(R)(1-Z^2) \tag{2.40}$$

$$P=P(R) \tag{2.41}$$

Again, the overbar indicates integral averaging in Z. The boundary conditions are specified at the outer disk radius as:

$$\bar{U}_r(1)=-1 \tag{2.42}$$

$$\bar{U}_\phi(1)=\bar{U}_{\phi 1} \tag{2.43}$$

$$P(1)=0 \tag{2.44}$$

After inserting the parabolic ansatz, the equations are integrated in Z-direction and the continuity equation can be solved for the radial velocity, then the circumferential momentum equation for the circumferential velocity and finally the radial momentum equation for the pressure. The resulting expression for the pressure is very lengthy and thus not provided here, but it can be obtained using a computer algebra system.

$$\bar{U}_r(R)=-\frac{1}{R} \tag{2.45}$$

$$\bar{U}_\phi(R)=\frac{1}{3R}\left(2\mathrm{Ta}\;\sigma+\left(3\bar{U}_{\phi 1}-3\frac{\mathrm{Ta}}{\mathrm{Re}}-2\mathrm{Ta}\;\sigma\right)\exp\left(\frac{5(R^2-1)}{4\mathrm{Re}\;\sigma}\right)\right) \tag{2.46}$$

Boyack and Rice [1971] demonstrate that it is also possible to use a higher order polynomial expression as velocity profile ansatz. They start from a system of equations that is slightly less simplified. Inserting an nth order polynomial and integrating over Z allows to derive a system of equations by setting the individual coefficients of Z^i with i =0, 1, ..., n to zero. Numerical solutions up to $n = 8$ are provided, which agree well with radial pressure distributions from experimental data. Bassett [1975] and Garrison et al. [1976] extend the approach to compressible flow. Rusin et al. [2022] develop a model with a

sixth-order circumferential velocity profile and a custom W-shaped radial velocity profile, fitted to CFD data. Finally, Romanin [2012] and Romanin and Carey [2011] provide a noteworthy higher-order model that combines elements of the friction factor approach with polynomial velocity profiles. They derive the polynomial order of the velocity profile from the friction factor, where smooth disk surfaces result in a parabolic profile and enhanced roughness increases the polynomial order. The empirical friction factor data in this case originates from channel flow.

2.2.1.3 Asymptotic solutions

The branch of solutions which are referred to as asymptotic is concerned with solutions in which the flow field is independent of the circumferential velocity component at the inlet. The asymptotic solutions only satisfy a mass flow inlet boundary condition, whereas the inlet circumferential velocity is a result. This point of view arises naturally from some simplified forms of the Navier-Stokes equations, which are solvable without any assumptions about the shape of the velocity profile.

The most basic approach, as given by Wollkind and DiPrima [1973], starts from regular Poiseuille flow, driven by a constant pressure gradient in streamwise direction. They add a second equation for the cross-flow velocity component and the Coriolis terms. The resulting pair of linear, second order differential equations with a constant inhomogeneous term in the streamwise momentum equation can be solved analytically. By incorporating the constant pressure gradient into the nondimensionalization, a solution results that is dependent on a single Taylor number and the nondimensional axial coordinate.

Although published earlier, the solution by Breiter and Pohlhausen [1962], originally developed for Tesla pump flow, can be viewed as an extension to this. They add the previously omitted centrifugal term and assume the pressure to be an unknown, radius dependent function.

$$\sigma \mathrm{Re}\, \frac{\partial P}{\partial R} - \frac{\sigma \mathrm{Ta}^2}{\mathrm{Re}} R - 2\sigma \mathrm{Ta}\; U_\phi - \frac{\partial^2 U_r}{\partial Z^2} = 0 \tag{2.47}$$

$$2\sigma \mathrm{Ta}\; U_r - \frac{\partial^2 U_\phi}{\partial Z^2} = 0 \tag{2.48}$$

These equations are related to the basic equations that describe the Ekman boundary layer. They result from equations 2.12 and 2.13 by assuming that the radial and circumferential velocities are functions of Z only, the pressure is a function of R and by setting the axial velocity component to zero. Additionally, all terms that are dependent on some power of the radial coordinate R, except for the centrifugal term, are set to zero.

$$U_r = U_r(Z) \tag{2.49}$$

$$U_\phi = U_\phi(Z) \tag{2.50}$$

$$U_z = 0 \tag{2.51}$$

$$P = P(R) \tag{2.52}$$

Breiter and Pohlhausen [1962] justify the heavy truncation of the Navier-Stokes equations mainly through order of magnitude arguments. The imposed boundary conditions are

no-slip walls, symmetry with respect to $Z = 0$, and a given inlet pressure:

$$U_r(\pm 1) = 0 \tag{2.53}$$
$$U_\phi(\pm 1) = 0 \tag{2.54}$$
$$\left.\frac{\partial U_r}{\partial Z}\right|_{Z=0} = 0 \tag{2.55}$$
$$\left.\frac{\partial U_\phi}{\partial Z}\right|_{Z=0} = 0 \tag{2.56}$$
$$P(1) = 0 \tag{2.57}$$

In equations 2.47 and 2.48, the R and Z-dependent parts of the solution can be solved separately from each other, since the radial coordinate only appears in the inhomogeneous terms. These are combined into a single radius dependent function $F(R)$.

$$F(R) = \frac{\partial P}{\partial R} - \frac{\mathrm{Ta}^2}{\mathrm{Re}^2} R \tag{2.58}$$

With this, the analytical solutions for radial and circumferential velocities can be derived. Note that the radial dependence of the velocities is reintroduced through $F(R)$.

$$U_r(R, Z) = F(R)\frac{\mathrm{Re}}{\mathrm{Ta}}(B\sin(AZ)\sinh(AZ) - C\cos(AZ)\cosh(AZ)) \tag{2.59}$$
$$U_\phi(R, Z) = -F(R)\frac{\mathrm{Re}}{\mathrm{Ta}}(C\sin(AZ)\sinh(AZ) + B\cos(AZ)\cosh(AZ) - \frac{1}{2}) \tag{2.60}$$

with

$$A = \sqrt{\sigma \mathrm{Ta}} \tag{2.61}$$
$$B = \frac{\cos(A)\cosh(A)}{\cos(2A) + \cosh(2A)} \tag{2.62}$$
$$C = \frac{\sin(A)\sinh(A)}{\cos(2A) + \cosh(2A)} \tag{2.63}$$

To solve for the function $F(R)$, an additional equation is set up from mass conservation. From the definition of nondimensional mass flow in equation 2.34 follows:

$$\bar{U}_r = \frac{1}{2}\int_{-1}^{1} U_r(R, Z)\mathrm{d}Z = -\frac{1}{R} \tag{2.64}$$

The negative sign is included, so that the equation is valid for turbine flow, with negative radial velocity. Inserting equation 2.59 into equation 2.64, gives an expression for $F(R)$:

$$F(R) = \frac{4A\ \mathrm{Ta}(\cos(2A) + \cosh(2A))}{R\ \mathrm{Re}(-\sin(2A) + \sinh(2A))} \tag{2.65}$$

The pressure is then calculated from equations 2.58, 2.65 and 2.57.

$$P(R) = \frac{\mathrm{Ta}^2(R^2 - 1)}{2\mathrm{Re}^2} + \ln(R)\frac{4A\ \mathrm{Ta}(\cos(2A) + \cosh(2A))}{\mathrm{Re}(-\sin(2A) + \sinh(2A))} \tag{2.66}$$

There is no more degree of freedom left to satisfy a boundary condition for the circumferential velocity component, as it is fully determined by the Coriolis terms.

Batista [2011] further extends the solution. They retain more terms in their set of conservation equations, including some nonlinear terms and axial velocity. The author

introduces a streamfunction and carefully crafts series expressions for the tangential velocity, the pressure and the streamfunction in terms of the ratio of the aspect ratio σ to the radial coordinate. After inserting these into the conservation equations, a system of equations is derived by equating coefficients of equal powers of R. By solving the equations in sequence for more and more series coefficients, the solution can be calculated to an arbitrary degree. For the third and fourth degree solutions, the author resorts to numerical methods since the expressions get more and more complicated. Again, the method was originally developed for radially outward flow, however the boundary conditions can easily be adapted to turbine configuration. Since the solution process and the solutions themselves are fairly lengthy, they are not given explicitly here. For detailed descriptions, refer to Batista [2011]. The zeroth order solution resulting from this method is identical to the solution above by Breiter and Pohlhausen [1962]. Schosser et al. [2019] introduce an additional degree of freedom into the zeroth order solution of the circumferential velocity to account for an arbitrary inlet angle. This is addressed in the next section.

Singh [2017] describes another linearized model that is related to the solution by Breiter and Pohlhausen [1962]. The authors assign different rotation rates to the disks and naturally, the solution includes the case of corotating disks. In a further study, Singh and Singh [2021] analyse the heat transfer properties of the model flow field.

Matsch and Rice [1968] independently develop an asymptotic solution by using an iterative scheme to generate analytical expressions for the velocities. The scheme is based on a set of integrated momentum equations together with mass flow and symmetry boundary conditions. The degree of simplification of the basic equations is a middle ground between the approaches by Breiter and Pohlhausen [1962] and Batista [2011]. A creeping-flow solution, valid for very small Reynolds numbers, serves as an initial guess and is inserted into the conservation equations to yield a perturbation solution. By repeating the process of inserting improved initial guesses and solving for the perturbation, the accuracy of the solution improves. Analytical expressions up to third order accuracy are given.

Another approach with asymptotic character is given by San'kov and Smirnov [1983]. They introduce a stream function and use series expansion in terms of a dimensionless mass flow and rotational speed parameter to generate a set of differential equations that can be integrated numerically. Again, the generalized case of different rotation rates for the disks is considered. Comparison to an experimentally obtained pressure distribution along the radial direction for the corotating disk case shows good agreement.

2.2.1.4 Further models

Asymptotic solutions are only helpful for the description of real turbine flow when the circumferential velocity component approaches the asymptotic solution fairly quickly after the disk gap inlet. Intuitively this is expected to be the case for flows with low radial mass flow and high rotational speed, in other words, with low Reynolds number and high Taylor number. Models with an imposed velocity profile on the other hand allow for an arbitrary circumferential velocity component at the inlet, but on the downside restrict the shape of the velocity profile.

In order to avoid the restriction of the asymptotic solution, Schosser et al. [2019] build on the zeroth order circumferential velocity solution of Batista [2011] and extend it by multiplication with an unknown radius dependent function. Solving for this function using a boundary condition for the circumferential velocity yields an exponentially decaying perturbation that accounts for the deviation from the asymptotic solution. The solution is compared to experimental data and different numerical solutions. They agree well and it is shown that for some operating conditions, the inlet region in which the flow deviates

from the asymptotic solution can be large.

Another promising method that could yield an accurate analytical solution is the homotopy analysis method (HAM). Das [2015] develops a solution to flow within infinitely large corotating disks with different rotation rates, the method however has yet to be adapted to the Tesla turbine flow configuration.

Finally, there are numerical methods that yield a more accurate model of the flow field. Boyd and Rice [1968] use a custom finite difference method to solve the axisymmetric equations with some order of magnitude assumptions, but keeping most nonlinear terms, the axial velocity component and arbitrary inlet boundary conditions. They show an example case, where the numerical solution quickly approaches the asymptotic solution by Matsch and Rice [1968]. The execution time of the numerical solution at a single set of input parameters is given as 45 min. Considering the jump in computing performance from 1968 to today, a solution could nowadays be obtained in a fraction of that, making the method still viable for investigation of large parameter spaces, presumably more efficient than through conventional fluid simulation software. Felsch and Piesche [1981] describe a very similar approach but include temperature dependent viscosity in their model. They find that the assumption of constant viscosity is reasonable.

2.2.1.5 Condensation and particles

One of the advantages of friction turbomachinery is their tolerance for inhomogeneous media, containing for example particles or droplets. Compared to conventional turbomachinery, there is less interaction between the impurities and the rotor, since there is little attack surface for impacts. There have been attempts to model the behaviour of particles inside the disk gap and their influence on turbine performance.

The earliest models were developed by Truman et al. [1978] for two phase vapour and by Truman et al. [1979] for solid particles. The two models are very similar, except that the vapour model includes a mass transfer between liquid and gaseous phase. Droplets are modelled as spheres that experience a drag force dependent on the velocity difference between the two phases. The model accounts for the second phase through additional conservation equations with omitted pressure and viscosity terms. Some effects, like wall-particle interaction and lift forces, are neglected. The system of equations is solved by a custom, numerical iteration scheme and the authors deduct that only very small particles actually enter the disk gap, while bigger particles are retained due to the centrifugal force acting upon a particle exceeding the drag force. The vapour quality is found to increase throughout the turbine gap.

Talluri et al. [2021] and Niknam et al. [2021] suggest a different approach to treat two phase vapour. They assume that the velocity of the liquid and the gaseous phase is equal and model the effect of the liquid phase by a modified two-phase viscosity and a friction factor. Results are compared to a sophisticated CFD model that includes different vapour particle interactions. The two models agree with each other in the investigated parameter space for an organic working fluid and it is again shown that the vapour quality generally rises throughout the rotor and efficiency improves with rising inlet vapour quality.

2.2.1.6 Disk surface roughness

Another aspect that is special to friction turbomachinery is the role of wall roughness. The implications of increased wall roughness are however not straightforward, since on one hand, momentum transfer is improved, but on the other hand dissipation losses are increased. The easiest way to account for wall roughness in a modelling approach is

through a friction factor model. This is demonstrated by Romanin [2012], Romanin and Carey [2011] and Niknam et al. [2021], utilizing friction factor data from channel and pipe flow.

Another way to model for roughness effects is via fluid simulation software and turbulence models with wall functions dependent on surface roughness. The exemplary comparison by Niknam et al. [2021] between a friction factor model that accounts for enhanced wall roughness and a corresponding CFD approach however give vastly different results.

2.2.1.7 Partial admission

All previously mentioned models have in common that they assume a uniform admission of the disk gap at the outer disk radius, without any blockage due to stator blade tips or any nozzle geometry. In contrast to that, the vast majority of Tesla turbines that have been built so far are partial admission turbines with few or only a single nozzle distributed along the circumference of the rotor. True analytical models for this phenomenon exist only for creeping flow, i.e. very low Reynolds number flow, and potential flow, see Matsch and Rice [1967b] and Matsch and Rice [1967a]. Therefore, for reliable modelling of partial admission effects, one has to fall back to CFD simulations. The irregular velocity distribution in circumferential direction at the rotor inlet due to partial admission inevitably starts to even out with the flow progressing towards the centre of the disks. Because of the asymptotic nature of the flow, this might happen fairly quickly, so that models with assumed uniform admission can still be useful even for partial admission turbines.

2.2.2 Turbine losses

For more accurate predictions of turbine performance, the rotor flow models can be combined with modelling of rotor and stator losses. Generally, the loss mechanisms inside Tesla turbines are similar to those in other turbomachines. Especially the modelling of the turbine components upstream of the rotor can be transferred to Tesla turbines. Gambini and Vellini [2021] provide a collection of modelling approaches for conventional turbomachinery and describe a useful categorization of turbomachinery losses into internal and external losses. They further break down all possible sources of losses in a turbomachine. Applied to Tesla turbines, these are:

- plenum or volute losses
- stator losses
- incidence losses
- passage losses
- windage losses
- leakage losses
- outlet geometry losses
- outlet kinetic energy losses
- bearing losses

Another Tesla-turbine-specific breakdown of losses is provided by Rice [1965].

Losses occur at each component of the turbine. After passing the plenum and the stator, incidence losses occur during the transfer of fluid between stator and rotor. These can in turn be subdivided into several different loss mechanisms. For one, the contraction of cross-sectional area at the rotor inlet, caused by the thickness of the disks, acts as a second nozzle that further accelerates the fluid and generates losses. Talluri [2019] models this by applying an empirical pressure loss correlation for channel flow with an abrupt flow contraction by Idel'chik [1966]. Dibelius and Nendl [1973] introduce a further type of incidence loss into their modelling approach. They set up a simple analytical model for the losses caused by the change from a block velocity profile to a curved channel velocity profile.

After entering the rotor, the fluid continues radially inward and on its way experiences passage losses. These are covered by the rotor flow model. Windage losses on the other hand occur at the outer surfaces of the rotor, in the small clearance between rotor and stationary housing surfaces. The large difference in surface velocities promotes dissipation of energy. Windage losses can be estimated by analysing the flow in the space between a rotating and a stationary disk. This can be modelled analytically, in a similar fashion as the modelling of Tesla turbine rotor flow. Various approaches exist in literature. For rotor-stator flow with radial inward flow, Rohatgi and Reshotko [1974] demonstrate an analytical modelling approach and Poncet et al. [2005] derive modelling parameters from experimental data. In the course of their analysis of losses in Tesla turbines, Krishnan [2015] estimate windage loss through a resistive torque derived from a model of a single enclosed rotating disk by Daily and Nece [1960]. The model gives a torque coefficient for different flow regimes in the rotor stator gap. They distinguish laminar and turbulent flow, each with merged or separated boundary layers. Hu et al. [2017] later extend the analysis for rotor stator flow with radial inflow. Talluri [2019] base their loss analysis of Tesla turbine rotor and stator on existing loss modelling approaches for bladed turbines and implement empirical windage and pumping loss models developed originally for steam turbines. Beans [1961] and Renuke et al. [2019] give empirical analytical fits of experimentally measured windage and bearing friction losses in their experimental Tesla turbines.

In the space between the outer rotor disks and the turbine housing, there is also some fluid bypassing the rotor and exiting through the clearance between rotor and stator, causing leakage losses. Chew [1991] analyses leakage in the space between a rotating and a stationary disk, but, so far, only radially outward flow has been considered.

After exiting the rotor gaps, the fluid has to turn into the axial direction and pass the mechanical outlet structures. This causes additional losses. Renuke et al. [2019] model outlet geometry pressure loss, dependent on a constant empirical parameter, mass flow and density. Lastly, the fluid exits the turbine with a certain residual kinetic energy. Additional, but comparatively small losses stem from bearing friction.

2.2.3 Numerical simulation

Other than custom mathematical models, general-purpose RANS CFD software is a common tool for modelling Tesla turbines. Previous authors employ three-dimensional turbine models of varying complexity for comparison with experimental and analytical results and to analyse the impact of design parameters on turbine performance. A simple approach is to model a sector of a single disk gap with cylindrical in and outflow boundaries, which is particularly suited for comparison with axisymmetric analytical solutions and for covering large parameter spaces, see for example Ciappi et al. [2019], Schosser and Pfitzner [2015]

or Guha and Sengupta [2017]. For more accurate predictions of turbine performance, the single disk gap sector can be extended by a nozzle and the space between nozzle and rotor, including the lateral disk edge. This is demonstrated for example by Jedrzejewski and Lampart [2011] and Renuke and Traverso [2022]. Finally, there are models of full turbines, covering a large part of the turbine circumference and multiple disks, nozzles and the axial rotor-housing interspace. These allow for detailed analysis of leakage losses, windage losses and rotor inflow, see for example Qi et al. [2019c], Rusin et al. [2018b, 2019] or Sengupta and Guha [2018]. Realistic outlet structures are investigated numerically by Qi et al. [2019b] and Rusin [2017].

CFD methods give insight into the flow field that wouldn't be possible with experimental methods. As an example, Guha and Sengupta [2016] break down the individual contributions to the radial pressure distribution inside the disk gap from viscous, inertial, Coriolis and centrifugal terms. Rusin et al. [2018b] use three different turbulence models with their multiple disk Tesla turbine model and find that the RNG k-ε model predicts slightly lower turbine power than k-ω SST and unsteady SST-SAS.

A review of results regarding Tesla turbine design, that were obtained using CFD software, is included in chapter 2.4. Some previous direct numerical simulations that involve some form of rotating disk flow are addressed briefly in the course of the following chapter 2.2.4.

2.2.4 Stability and transition

A major crossroad when modelling a Tesla turbine analytically or numerically is the choice between laminar and turbulent flow modelling. In order to choose the right approach, the turbine designer needs some understanding of the expected flow regime.

Stability of flows involving rotating disks is a wide field of research, as there are many possible configurations with one or two corotating or counterrotating disks, with and without imposed radial flow. Single disk flows can be categorized into Bödewadt, Ekman and von Kármán flows, depending on the rate of rotation of the fluid and the disk. For an overview of instability mechanisms in these basic flows as well as for some types of two disk flows, refer to the summary by Crespo Del Arco et al. [2005]. Especially when the disk spacing is large enough to accommodate separated boundary layers, the instability mechanisms within the two disk flows are closely related to those within the single disk basic flows.

A good starting point for exploration of this field is the flow in a semi-infinite medium above a single rotating disk, also known as von Kármán flow. This flow scenario has seen lots of research and many different tools for analysing stability, transition and turbulence have been applied to it. Appelquist et al. [2018b] describe a direct numerical simulation of turbulent von Kármán flow for two different ranges of Reynolds numbers. They find good agreement with experimental data and strong similarities to turbulent flat plate boundary layer flow. Another recent study on the subject by Appelquist et al. [2018a] describes the intricate transition mechanism in von Kármán flow and points out different transition scenarios dependent on the amplitude of the initial disturbance.

Nishioka et al. [1975] make a similar observation for Poiseuille flow in that transition strongly depends on initial perturbation amplitude. In their experiment, they find nonlinear instability below the critical Reynolds number from linear stability theory, given high enough initial perturbation amplitude.

A known instability phenomenon in von Kármán flow is absolute instability, found by Lingwood [1995] and Lingwood [1997]. Absolutely unstable flow remains in a perturbed state, even when the initial perturbation is no longer present, as opposed to convectively

unstable flow where perturbations only travel downstream and eventually leave the domain of interest. For a more detailed explanation of absolute instability refer to Schmid and Henningson [2001] and Oertel and Delfs [1996]. In contrast to von Kármán flow, nonrotating Poiseuille flow is purely convectively unstable, as shown by Deissler [1987].

A two-disk flow configuration that is directly relevant for many turbomachinery applications is the flow between a rotating and a stationary disk, or the generalized case of disks with different rates of rotation. Among others, Tuliszka-Sznitko and Zielinski [2006], Launder et al. [2010] and Yim et al. [2018] provide detailed analysis through linear stability analysis, large eddy simulation, direct numerical simulation and experimental methods. For large disk spacing and far away from the rotor edge, the flow close to the disks is very similar to von Kármán flow. Still, this flow configuration is generally more unstable than single disk flows and the corotating case, since the relative velocity between the disk surfaces as well as the closed off rotor edge promote instability. The authors find, that under certain conditions, large spiralling arms or vortices form, that can only be captured in a DNS when simulating the full or at least a large part of the rotor circumference. Absolute instability is found as well, however in the configuration simulated by Tuliszka-Sznitko and Zielinski [2006] with relatively large disk spacing, it vanishes as the rotational speed of the two disks approaches each other.

The studies by Murphy et al. [1983] and Singh et al. [1999] are two examples for investigations on laminar and turbulent flow in radial inward direction between stationary disks, also known as sink flow. The authors note that the acceleration actually has a stabilizing effect that can lead to relaminarization of a previously turbulent flow. The opposing scenario featuring corotating disks with no throughflow is analysed, among others, by Randriamampianina et al. [2001], Miura and Mizushima [2007] and Tsai et al. [2007]. Within this kind of flow, non-axisymmetric, instationary, three dimensional flow structures may develop, depending on the radial position and the aspect ratio of the gap.

The specific case of flow stability between narrowly spaced corotating disks with imposed radially inward flow, as found in Tesla turbines, was subject to few experimental and theoretical studies that are summarized in the following two sections. The actual stability boundaries found in these studies will be shown later in section 3.2, in direct comparison to new results from linear stability analysis and direct numerical simulation.

2.2.4.1 Theoretical stability analysis

Linear stability analysis is a tool that reveals unstable, naturally amplified velocity and pressure oscillations that can lead to transition. The basic idea is to perturb a known laminar solution by a Fourier mode and check whether it gets dampened or amplified in time and space. Wollkind and DiPrima [1973] and Flaherty and DiPrima [1978] perform temporal linear stability analysis on the simplified model of Poiseuille flow with added Coriolis terms and omitted centrifugal term, that was previously mentioned in section 2.2.1.3. They find two types of stability limits. One of those essentially corresponds to the same type of instability as found in Poiseuille flow and is relevant for low Taylor numbers. With rising Taylor number, it soon gets overtaken by a cross-flow instability. The authors note that the latter is related to inflection of the velocity profile, which is also the cause of one type of instability of Ekman flow and inviscid, parallel flows in general. For more information on this, refer to Crespo Del Arco et al. [2005] and Schmid and Henningson [2001]. Gusev and Bark [1980] expand the study to higher Taylor numbers.

Mehdizadeh [2010], Mehdizadeh and Oberlack [2010] and Li et al. [2006] investigate the same type of Coriolis modified Poiseuille flow through direct numerical simulation. They run computations for increasing Taylor numbers while keeping the imposed pressure

gradient constant. This causes the perpendicular, Coriolis-induced velocity component to increase and the velocity in the main flow direction to decrease. The authors find that this has a stabilizing effect on the flow. Chesnokov [1984] demonstrate another interesting approach to stability analysis on radially outward flow between corotating disks. They show, that small pressure fluctuations lead to big velocity changes which might lead to instability.

2.2.4.2 Stability experiments

Adams and Rice [1970], Pater [1973] and Pater et al. [1974] use a test facility to establish the limits between laminar, transitional and turbulent flow in Tesla pump and turbine flow. The test facility features a single gap rotor, fed by a nozzle ring at the outer disk radius with a water-ethylene glycol mixture. The rotor is equipped with pressure taps and dye injection taps. Through the transparent upper disk, the researchers are able to determine the flow regime visually as well as measure the flow angle in the laminar regime. Furthermore, radial pressure distributions are measured. The authors provide stability charts in terms of a Taylor number and a nondimensional rotational speed.

Nendl [1973], Nendl [1976] and Dibelius and Nendl [1973] work on a test facility with a single gap rotor and two nozzles supplying the outer disk radius with compressed air. The distance between the disks is just large enough to provide space for a hot-wire velocity probe. Flow regimes are determined through averaged velocity profiles and oscillograms, as well as pressure measurements. Dibelius and Nendl [1973] also mentions a test facility using oil as working medium, however the measurements were impaired by resin deposits on the hot-wire probes.

Velocity measurements through non-intrusive methods allow for even narrower disk spacing in the experimental setup. Schosser [2016] makes use of 3D particle tracking velocimetry (PTV) on a single-gap test rotor with optical access, that is supplied with air by a nozzle ring. Since the velocity measurements are temporally not resolved, flow regimes cannot be identified unambiguously, however the profile shape together with the spread of data points give some impression.

2.3 Tesla turbine experiment

The first Tesla turbine was built and patented by Tesla [1913]. It was powered by steam and had a rotor diameter of 457 mm. Scientific American [1911] reports a power output of up to 149 kW. Armstrong [1952] provides a very early, well documented study on a steam powered Tesla turbine with tapered disk surfaces, which yields 800 W and an isentropic efficiency of 4.32 %. A decade later, Beans [1961] is able to improve isentropic efficiency of their air powered turbine to 23.5 % with a maximum power output of about 2 kW. Rice [1965] further improves the design of his turbine that reaches an isentropic efficiency of 35 % and a maximum power output of about 3 kW. Since then, there were further improvements in terms of efficiency, for example by Lisker et al. [2015] and Renuke et al. [2020]. Table 2.1 gives an overview over some turbine prototypes with reported isentropic efficiencies. Another list of existing Tesla turbines, that includes other efficiency definitions, is gathered by Renuke et al. [2019].

The most unconventional operating media are used by Patel and Schmidt [2002] who drive their turbine with combustion gas from a biomass combustion and Talluri [2019] who uses steam of an organic medium. The turbine by Steidel and Weiss [1976] is different in that the outer disk edge is not circular but has several sawtooth-shaped cutouts. Another

author	medium	rotor diameter $2r_1$ in mm	max. power $\dot{w}$ in W	max.efficiency η in %
Armstrong [1952]	steam	178	826	4.3
Beans [1961]	air	152	1954	23.5
Rice [1965]	air	203	2983	35
Steidel and Weiss [1976]	steam	327	2876	6.7
Patel and Schmidt [2002]	combustion gas	305	3200	11
Lemma et al. [2008]	air	50	225	23.1
Lisker et al. [2015]	steam	175	1400	38
Rusin et al. [2018a]	air	73	71.5	8.9
Renuke et al. [2019]	air	64.5	137	18
Talluri [2019]	R1233zd(E)	216	906	11.3
Renuke et al. [2020]	air	120	>1300	36.5

Table 2.1: Selected performance data of previous Tesla turbines. Maximum power and maximum isentropic efficiency data is usually achieved at different operating points.

rare design feature is found in the turbine by Lisker et al. [2015] who add blade inserts to the outlet region of the disk gap, essentially building a hybrid between friction and bladed turbine. The turbine built by Renuke et al. [2019] has a custom, integrated electrical generator. Very small turbines in the milliwatt power range are assessed by Krishnan [2015]. Further studies that describe small experimental Tesla turbines with power outputs below 100 W are provided by Hoya and Guha [2009], Romanin et al. [2010], Guha and Smiley [2010], Holland [2015], Li et al. [2017], Andres and Loretero [2019], Delaney [2019], Placco and Guimarães [2019], Ji et al. [2019] and Kamran and Manzoor [2020].

2.4 Tesla turbine design

Tesla turbine preliminary design guidelines with focus on organic Rankine cycle (ORC) applications were previously developed by Talluri [2019], with contributions by Talluri et al. [2018] and Talluri et al. [2020]. The authors perform sensitivity analysis on several Tesla turbine design parameters based on their analytical model of the full turbine, including a stator model, a power law rotor model and some loss modelling. They introduce a power density parameter termed "compactness" and define a set of design constraints. A sample design process of an ORC turbine is laid out, consisting of both stator and rotor design. Schosser [2016] provides design charts for some nondimensional turbine parameters and establishes design trends with regard to efficiency and power output. Krishnan [2015] gives some practical design recommendations regarding nondimensional turbine parameters and shows the variation of performance data with rotor outer radius based on a sample design. Alrabie et al. [2017] describe the design process of their cm-scale experimental turbine based on a friction factor rotor model.

Studies that focus on optimizing a single or a few Tesla turbine design parameters are referred to in the next sections where each design feature is treated separately.

2.4.1 Rotor design

2.4.1.1 Disk spacing

Qi et al. [2016] and Qi et al. [2019c] set up a numerical model of a single disk gap of an air-driven Tesla turbine as well as a detailed model of a five-disk turbine with stationary housing walls and different nozzle designs. The simulated rotor disks have a diameter of

100 mm and, in the case of the multiple disk model, a thickness of 1 mm and 2 mm. They run a series of simulations while varying the disk spacing between 0.1 mm and 2 mm over the course of both studies. The authors observe an efficiency optimum for certain values of disk spacing distance, depending on operating conditions and other design parameters. They conclude that too narrow disk channels lead to large internal friction losses as well as high leakage losses from fluid bypassing the rotor. Too wide channels cause velocity profiles with clearly separated boundary layers and losses due to the rotor exit kinetic energy are high.

The experimental comparison by Renuke et al. [2019] covers three different values of disk spacing. They use their air-driven Tesla turbine with multiple nozzles and 0.1 mm thick disks with a diameter of 64.5 mm. Different disk spacings are examined across a range of mass flows and for two different rotational speeds. Turbine performance is lowest for the smallest spacing value of 0.1 mm, while the two larger values 0.2 mm and 0.3 mm give better, rather similar efficiency. Only at low mass flows, the largest spacing is clearly advantageous for efficiency.

2.4.1.2 Disk thickness

As mentioned above, Qi et al. [2019c] use their numerical model of a five-disk Tesla turbine, to compare two different values of disk thickness and come to the conclusion that thinner disks are clearly beneficial for turbine efficiency. Their flow visualizations show that in the course of the sudden contraction upon rotor entry, the flow direction abruptly turns towards the radial direction, which is of disadvantage for torque generation inside the rotor. This effect appears to be more pronounced for thicker disks. Qi et al. [2019c] also analyse a different type of nozzle, where each rotor channel gets provided with its own nozzle channel. With this design, the adversary effect of disk thickness is reduced significantly but the channelled nozzle itself introduces additional losses. This will be further explained in section 2.4.2.1.

The study by Renuke et al. [2019] confirms, that disk thickness needs to be minimized in order to achieve the best possible turbine efficiency.

2.4.1.3 Disk edge geometry

Since the disks have to be able to transfer torque to the turbine shaft, the thickness of the disks cannot be arbitrarily small. Qi et al. [2019a] attempts to reduce the adversary impact of disk thickness by modifying the outer edge of the rotor disks. They use their aforementioned numerical model to compare disk edges with bevelled, circular and elliptic shapes and find that the profiled edges overall increase isentropic turbine efficiency. Using a channelled nozzle however, the positive impact of the disk edge modification is reversed.

2.4.1.4 Disk inner radius

Another main geometry parameter is the radius of the disk outlet. Renuke et al. [2019] use their 64.5 mm diameter disks with differently sized outlet openings distributed around the rotor shaft. The overall diameters of the outlet regions of the disks in their comparison are 20 mm, 25 mm and 30 mm. While a turbine efficiency optimum is found for certain outlet diameter values, depending on the operating conditions, the overall difference in efficiency between the three designs is small. Further lowering the outlet radius however can lead to high losses due to high exit velocity of the working fluid.

2.4.1.5 Disk outlet design

The outlet region of a Tesla turbine rotor poses a design challenge, since the working fluid has to exit the rotor here and at the same time, the disks have to be mechanically connected to the shaft. Three different approaches to this can be found among existing designs. The most common one is to mount the disks to a solid shaft, with multiple outlet openings in the centre region of the disks. This is the simplest approach regarding manufacturing of the rotor. This design is used, among others, by Beans [1961] Rice [1965] and Renuke et al. [2019] within their experimental Tesla turbine designs. One of the drawbacks is the high mechanical load in the centre region of the disks at high rotational speeds, specifically at the bridges in between the outlet openings, which limits disk strength. Furthermore, the flow path of the fluid is disturbed by the outlet geometry and the shaft itself.

An alternative design features a hollow shaft with the outlet openings in the shaft wall, that are accessible from within the disk gaps. This approach was chosen by Schosser [2016] for his single-gap test facility. The downside is that the hollow core and the outlet openings make the shaft mechanically weaker and overall more difficult to manufacture. It has to be ensured, that the shaft is balanced and that it is able to support the disks at high rotational speeds.

A third way is to omit the shaft within the rotor entirely and connect the disks to each other with multiple bolts distributed evenly around the disks. The entire disk package is then mounted to a thick support disk, that is in turn connected to a shaft. This design allows for big circular openings in the disks and an overall unrestricted outlet region, it also opens up the possibility of modifying the outlet region for optimal aerodynamic properties, as demonstrated Talluri et al. [2021]. This concept is applied by Manfrida et al. [2018] and Talluri [2019] in their test facility design. Again there are drawbacks, since the centering of the disks to each other and relative to the shaft requires very high manufacturing precision in order to maintain rotor balance.

Compared to the first design, both the hollow shaft and the one-sided design make it more difficult to place an additional bearing at the outlet side of the rotor, since the exiting fluid essentially has to pass through the bore diameter of the bearing. This requires a big bearing diameter, which lowers its rotational speed limit. A bearing on the outlet side of the rotor is not strictly necessary, however it makes for a more stable design, less vulnerable to vibration.

Regarding outlet losses, Qi et al. [2019b] numerically analyse the flow through a realistic outlet structure with a solid shaft outlet design. It consists of multiple outlet openings in the disks, after which the fluid is redirected to an axial outlet. They compare it to a simplified circular radial outlet and calculate the pressure loss of the outlet structure. For their turbine geometry, featuring relatively thick disks of 1 mm and a spacing distance of 0.5 mm, it is shown that the inner faces of the outlet holes contribute noticeably to torque generation.

A possibility of optimizing the rotor outlet is to vary the outlet opening geometry for each disk within the rotor, with bigger openings towards the turbine outlet. This is briefly mentioned by Lampart et al. [2009], however has yet to be tried out.

2.4.1.6 Number of disks

The number of rotor disks can be used to linearly scale turbine power output and mass flow. The same turbine power output can however be obtained with a small rotor and many disks or a large rotor with few disks. Qi et al. [2023] investigate this by numerically comparing several modelled turbines with the same power output and total mass flow,

but different rotor diameter and number of disks. Due to the smaller impact of leakage losses relative to total mass flow, the rotor with more disks and smaller rotor diameter is preferable in terms of efficiency.

2.4.1.7 Mechanical rotor stability

The rotor of a Tesla turbine is highly stressed due to high rotational speeds. Thus, special attention to disk strength and resistance to vibration of the rotor assembly is necessary. Mechanical load due to high rotational speed can be substantial. Considering a disk with a single circular hole in the centre, the stress inside the disk due to rotation is given analytically by Löffler [1961]. Interestingly, disk thickness does not influence the maximum allowable rotational speed according to their relation, only the disk radii, angular velocity as well as disk material density and Poisson's ratio. Corresponding equations will be given in chapter 5.

Mechanical turbine failure can also occur due to excessive vibration as described by Beans [1961] and Renuke et al. [2020]. At certain operating conditions, the experimental turbines are reported to be rendered unusable because of this. As a remedy, Beans [1961] places additional shims in between the rotor disks, secured by continuous bolts through the rotor.

For analysing behaviour of the rotor disks, Beans [1961] applies an analytical model by Den Hartog [1956] for natural frequencies of a circular disk held at the centre. While this isn't entirely accurate for real rotor disks, it can give a first estimate of critical rotor conditions. More exact predictions of disk strength as well as resonance frequencies of complex rotor assemblies can be obtained numerically. Baginski and Jedrzejewski [2015] and Talluri [2019] demonstrate this using detailed models of their rotor designs. Both studies run computations with ideal and modelled bearing stiffness and conclude that bearing stiffness considerably affects the natural frequencies of the rotor assembly. Niccolini Marmont Du Haut Champ et al. [2022] further explore the impact of bearing stiffness by comparing results from a modelled Tesla turbine rotor with experimental measurement of critical frequencies.

The Tesla turbine rotor can be stabilized by interconnecting the disks with additional bolts and spacing shims. Another common measure to stabilize the rotor assembly and to ensure precise gaps between rotor and housing is to use thick top and bottom disks. This concept is applied by Beans [1961], Talluri [2019], Renuke et al. [2019]. To reduce losses from interaction of the fluid with the lateral faces of the thicker disks, they can be lowered into respective cavities in the housing.

In addition to constructional measures, rotor balancing helps minimize vibration. Pfeffer [2020] devotes special attention to the balancing of their 20 mm diameter Tesla turbine rotor to be able to reach rotational speeds up to $90\,000\,\mathrm{min}^{-1}$. The author describes a balancing concept along with a corresponding measurement setup.

2.4.1.8 Bearings

For a stable operation of the rotor, preloaded bearings are of advantage. Baik et al. [2016] operate a Tesla turbine using supercritical CO_2 as a working medium and they point out, that metal bearings are of disadvantage because the medium dissolves the lubrication of the bearing over time. To alleviate this, the authors switch to ceramic ball bearings.

2.4.2 Stator design

2.4.2.1 Nozzle design

Nozzle design of conventional radial turbines can largely be applied to Tesla turbines. For an overview, see for example Whitfield and Baines [1990] or Gambini and Vellini [2021]. In their Tesla turbine design routine, Talluri [2019] and Talluri et al. [2018] apply some of those methods.

There is one special form of nozzle that can only be found among Tesla turbines. Qi et al. [2019c] and Qi et al. [2019b] coin the term "one-to-one" and "one-to-many" nozzles, where "one-to-one" stands for a nozzle with a channelled structure, similar to the rotor. Each nozzle channel provides fluid to its respective rotor channel. This way, the losses upon transition of the fluid from the nozzle into the rotor decrease and the efficiency penalty of a large ratio of disk thickness to disk spacing is much smaller. The authors show that losses inside the channelled nozzle compared to the unrestricted nozzle are higher, but overall the channelled nozzle reaches a higher maximum turbine efficiency. For channelled nozzles in real-life applications there are additional losses, particularly the losses at the entry into the nozzle channels, as well as losses due to misalignment of the nozzle channels and the rotor channels. The channelled nozzle or "one-to-one" nozzle approach is also found within the experimental test facility of Talluri [2019].

An important design parameter of the nozzle is the geometrical angle at the nozzle exit, which affects the aerodynamic inlet angle into the rotor. Lampart and Jedrzejewski [2011], in the course of their numerical study, compare geometrical inlet angles of 10° and 15° at some selected operating conditions and find that the lower inlet angle, which is closer to the tangential direction, leads to better turbine efficiency.

A turbine parameter related to the inlet flow angle is the ratio between relative tangential fluid velocity to disk surface velocity at the rotor inlet. Qi et al. [2016], in their study of disk spacing with a single disk gap model, analyse the relation between this parameter and isentropic turbine efficiency. Within their parameter space, the ratio leading to optimal efficiency lies approximately between 0 and 0.5. For the lowest analysed disk spacing of 0.1 mm, the optimum ratio even is slightly below zero, which means that the fluid at rotor entry in tangential direction is slightly slower than disk velocity. This configuration however has the overall lowest efficiency compared to larger disk spacings.

2.4.2.2 Number of nozzles

Many existing Tesla turbine designs feature only one or few nozzles instead of a volute or a nozzle ring, which are more common in conventional radial turbines. There are some studies that aim at determining the optimal number of nozzles, but not enough for a conclusive answer to whether Tesla turbines actually perform better with fewer nozzles. Lampart et al. [2009], Jedrzejewski and Lampart [2011] and Lampart and Jedrzejewski [2011] numerically analyse a simplified single disk gap model and a more detailed model including multiple disks and compare turbine performance. They compare one to eight nozzles and tune the throat sections of the nozzles, so that at a designated pressure ratio, the mass flow rate of all nozzle configurations is equal. The overall result is that four nozzles lead to the highest efficiency. On the contrary, Deng et al. [2013] set up another numerical study using a single disk gap model and compare designs with one to eight nozzles across a range of rotational speeds, keeping the turbine pressure ratio constant among the computations. The efficiency is best for one nozzle and decreases with rising number of nozzles.

This seems contradictory at first glance, however it is not entirely appropriate to compare the results from those studies to each other because of the different approaches to choosing operating conditions. The constant pressure ratio approach of Deng et al. [2013] leads to a mass flow that is approximately proportional to the number of nozzles, whereas the mass flow and pressure ratio in the study by Lampart and Jedrzejewski [2011] was kept constant among designs by modifying nozzle geometry. Thus, the studies cover different slices of the turbine performance maps. Since efficiency optima for different nozzle designs might occur at different operating conditions, these slices don't necessarily include the highest possible efficiencies for each nozzle configuration.

An experimental comparison between different numbers of nozzles is described by Renuke et al. [2019]. The authors analyse one and two nozzled operation at different rotational speeds and mass flows, with the two nozzle setup giving an overall better efficiency.

2.4.3 Further design aspects

2.4.3.1 Rotor stator interspace

From the previous considerations regarding disk thickness and disk edge geometry it can be followed, that the space between rotor and stator is a significant source of losses in Tesla turbines. Take for example the visualizations by Qi et al. [2019c], which show that the flow undergoes an abrupt turning upon entry into the rotor. Ntatsis et al. [2019] gives further insight into this through comparison of three numerical calculations with varying spacing between rotor and stator. While the authors point out some mesh dependence issues, a clear trend of higher efficiency with lower spacing between rotor and stator can be observed. Sengupta and Guha [2018] show visualizations of the flow in the space between rotor and stator and find an optimum of their custom efficiency definition for a certain amount of clearance between rotor and stator.

2.4.3.2 Rotor housing interspace

The space between the outer rotor surfaces and the inside of the housing is source of losses from dissipation and leakage. Qi et al. [2019c] use their multi-gap model to analyse the mass flow that bypasses the rotor gaps. They find that for their particular turbine geometry, the interspace swallows more mass flow than a single rotor gap, while producing a lot less torque. Another multiple disk model by Rusin et al. [2019] also shows positive, but very little contribution to torque generation in the space between rotor and housing.

2.4.3.3 Sealing

Measures to minimize leakage are labyrinth seals or other types of contactless seals as found in the turbine designs by Manfrida et al. [2018] and Lisker et al. [2015]. On the drive side, Manfrida et al. [2018] eliminates leakage completely by using a magnetic coupling. Beans [1961] attempts to introduce back pressure into an annular groove in the outer rotor disks for a sealing effect, but reports unsatisfactory results. The author points out, that choosing the distance between outer rotor surfaces and housing requires a trade-off between leakage and windage loss.

2.4.3.4 Diffuser

Talluri et al. [2018] include a modelled diffuser after the rotor outlet into their turbine design methodology. The purpose of the diffuser is to recover some of the kinetic energy

after rotor outlet, that is otherwise lost. They refer to an experimental study by McDonald et al. [1971] that shows a positive impact of flow swirl inside the diffuser on pressure recovery and provides a modelling approach for this. The recent publication by Talluri et al. [2021] shows a Tesla turbine design that has a diffuser shape integrated into the rotor.

2.4.3.5 Condensation and particles

Engelbrecht et al. [2019] and Giakoumis et al. [2020] find a negative influence of condensation droplets on Tesla turbine performance. They predict that only droplets below a certain size are transported radially inward with the main flow direction. As a consequence, they suggest removing as much of the liquid phase from the fluid as possible, before the fluid enters the rotor. Condensation inside the turbine disk gap might also be utilized to improve efficiency, as theorized by Lisker et al. [2017] and Lisker and Hellwig [2017]. The idea is to enforce condensation in the outlet area of the disks through cooling and thus generating a liquid film that helps reduce the outlet velocity. Figueira Júnior et al. [2021] set up an interesting experiment to analyse wear in a pump from abrasive particles in the working medium. They find that the Tesla pump rotor wears less compared to a conventional centrifugal pump rotor. Ferrando et al. [2021] describe a test rig for visualization of two-phase flow inside a static disk gap.

Chapter 3

Modelling and simulation of Tesla turbines

This chapter introduces two examples of numerical modelling of a Tesla turbine through conventional fluid simulation software. Another focus of this chapter lies on determining the flow regime inside the turbine rotor, since this is a prerequisite for choosing an appropriate modelling approach. Finally, some selected analytical approaches are validated by comparing them to numerical and experimental data.

3.1 Numerical simulation

The use of computational fluid dynamics (CFD) software is a modelling approach that circumvents most of the simplifying assumptions of the specialized approaches from section 2.2.1, but comes at higher computational cost. This chapter introduces two ways of simulating a Tesla turbine using ANSYS CFX [ANSYS Inc., 2018], not unlike some of those that were mentioned in chapter 2.2.3 and 2.4. The simplified model consists of a sector of the rotor with axisymmetric inflow. The extended model introduces a nozzle and the small interspace between rotor and stator, which gives more detailed predictions.

3.1.1 Rotor only

The simplified rotor model is a good way to validate analytical results at an early stage of Tesla turbine design. The simulation domain is a 1°-sector of the space between two rotating disks. Figure 3.1 gives a schematic overview.

Bulk inlet velocities are specified at the outer radial boundary. The radial component of the inlet velocity is calculated from a given Reynolds number, domain geometry and estimated inlet kinematic viscosity, the circumferential component is calculated from the radial component and a specified flow angle. At the inner radial boundary, an ambient outlet pressure is specified. The disk surfaces in axial direction are defined to rotate at a certain speed, calculated from a specified Taylor number. Periodicity is imposed at the circumferential boundaries. With this approach, the inlet pressure is a result of the simulation.

The mesh is a structured mesh with a specified number of elements between the disk surfaces, where the height of the elements increases normal to the disk surfaces towards the channel centre with a growth rate of 1.22. Figure 3.2 shows the inlet region of a sample mesh. The shear stress transport (SST) turbulence model is active, results with expected laminar flow are run without turbulence modelling. Variable fluid temperature is taken

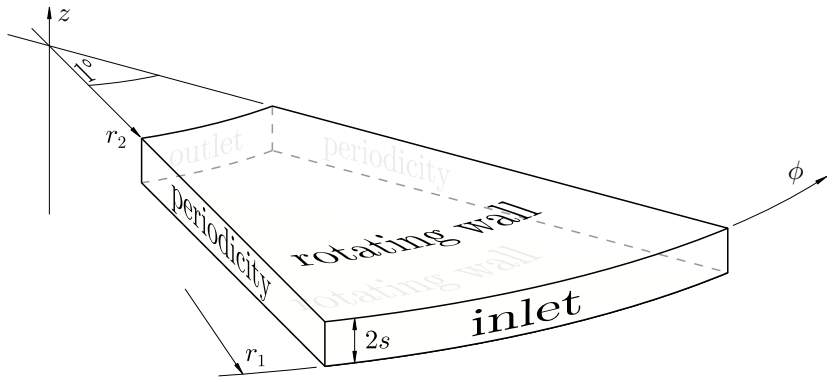

Figure 3.1: Schematic CFD domain for the rotor only case. Not to scale.

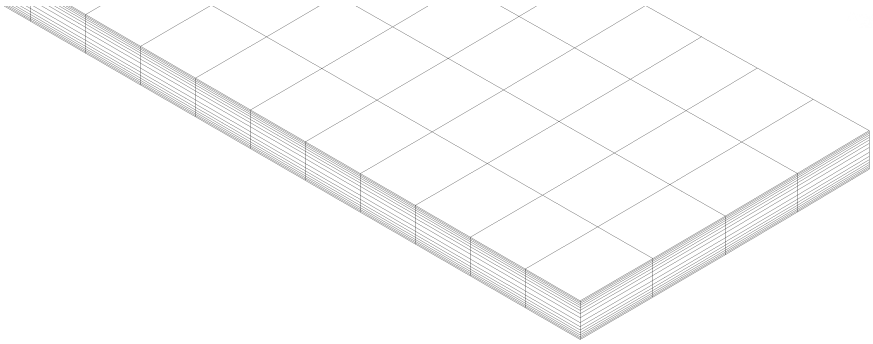

Figure 3.2: Detail view of the inlet region mesh.

into account, starting from a specified temperature at the inlet and with the disk surfaces assumed to be adiabatic. The medium is compressible air, approximated as an ideal gas. As soon as the root-mean-square residuals drop below 10^{-6}, it is assumed that the flow field is fully stationary and the simulation is stopped.

For a mesh independence study, a sample case is set up with the input parameters from table 3.1. These are the conditions with the highest Reynolds and Taylor number encountered in the study in chapter 3.3.2. The dimensions of the domain are fairly large, this is because a larger rotor can cover a larger parameter space in terms of Reynolds number and Taylor number, before the speed of sound limit is reached. This will be further explained in chapter 5. Fully turbulent flow is expected as well as noticeable effects from compressibility due to an inlet Mach number of 0.91. The imposed inlet flow angle is calculated from the nondimensional asymptotic model from equations 2.59, 2.60, 2.65 and 2.66.

As indicator variables for mesh independence, the power output per disk gap and the inlet pressure are chosen. The power output is calculated from the torque, acting on the rotating surfaces with respect to the disk-normal axis, multiplied with angular velocity and scaled up to a full rotor gap.

Figure 3.3 compares meshes with an increasing number of elements. The mesh with 9120 mesh cells is resolved with 15 cells between the disk surfaces. It gives good accuracy, while consuming only about a third of the computing time compared to the largest mesh. The mesh cell closest to the wall has a height of approximately $Z^+ = 30$, thus the near-wall velocity profile is modelled with a wall function. The mesh is shown in figure 3.2 and is chosen for further analysis here and in later chapters. Figure 3.4 shows some streamlines for different Reynolds numbers while leaving Taylor number unchanged. Since domain

parameter		value	
disk outer radius	r_1	1	m
disk inner radius	r_2	0.5	m
disk spacing	$2s$	2	mm
inlet temperature	$\bar{\vartheta}_1$	20	°C
outlet pressure	$\bar{p}_2$	1	bara
Reynolds number	Re	4000	
Taylor number	Ta	10000	
inlet angle	α_{a1}	7.26	°
estimated inlet dynamic viscosity	ν_1	9.8×10^{-6}	$\mathrm{m^2\,s^{-1}}$

Table 3.1: Input parameters for the mesh independence study for the rotor only case.

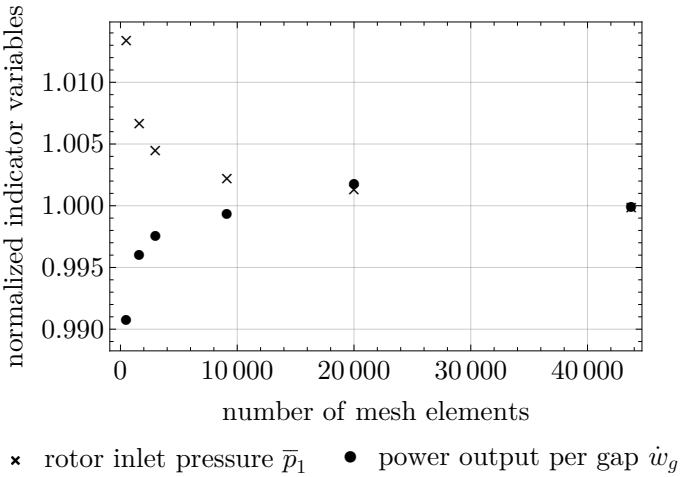

Figure 3.3: Results of the mesh independence study. Variables are normalized with respect to the results from the finest mesh.

geometry remains unchanged and inlet viscosity is almost unchanged, a constant Taylor number in this case is synonymous with constant rotational speed. In comparison, the case with the higher Reynolds number has a higher fluid throughput and almost five times higher output power, however efficiency is only about half of the efficiency of the low Reynolds number case.

3.1.2 Rotor and stator

In a later stage of the design process, when the operating conditions and design of the rotor gap are roughly determined, the simulation can be extended with a stator domain and the rotor-stator interspace. This allows for more accurate performance prediction. The following model is designed after the experimental facility from chapter 4 and will be used to compare experimental and numerical turbine performance and for analysing turbine losses. Figure 3.5 shows a schematic view of the computational domain. Since a four nozzle setup is simulated, a periodic 90°-sector with a single nozzle is sufficient. The domain includes the small clearance between stator and rotor since this is a major source of turbine losses. The lateral edge surface of the disk is included, thus the height of the stator domain is the disk gap height plus the disk thickness.

The medium is, again, compressible air, modelled as an ideal gas with SST turbulence

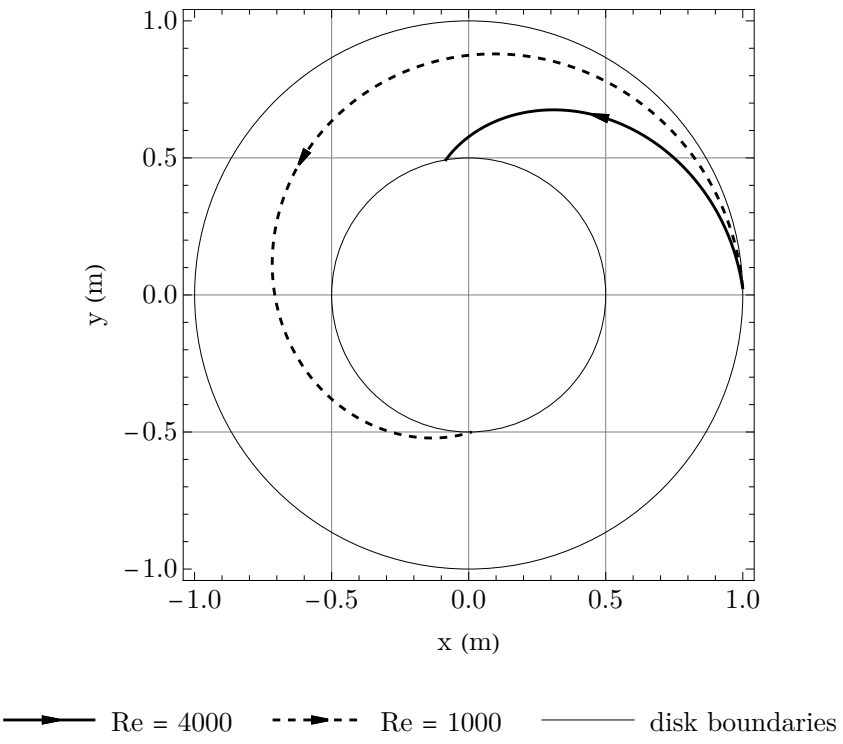

Figure 3.4: Streamlines in a nonrotating frame of reference starting from the centre point of the inlet boundary. Extracted from the rotor only CFD case for two different Reynolds numbers and Taylor number fixed at 10000.

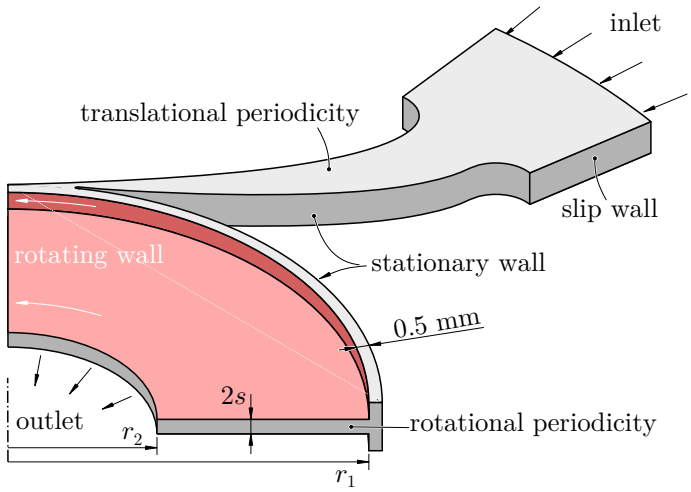

Figure 3.5: Schematic CFD domain for the rotor and stator case. Not to scale.

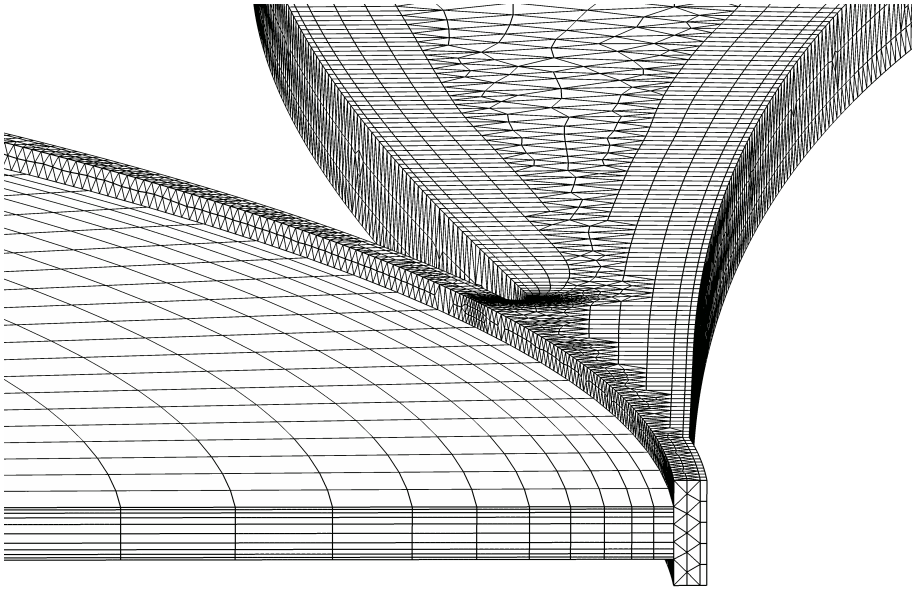

Figure 3.6: Detail view of the mesh at the transition between nozzle and rotor gap.

modelling and variable fluid temperature. The simulation is stopped as soon as the root-mean-square residuals drop below 10^{-6}. Upstream of the stator inlet, there is an inlet region, delimited by slip walls and the radial inlet boundary with a specified inlet mass flow normal to the boundary surface. The side walls of the nozzle and the enclosing cylindrical surface of the rotor are stationary no-slip walls. The axial boundaries of the stator domain are translationally periodic boundaries. The rotor surfaces, coloured red in figure 3.5, are supplied with a wall rotational speed. This includes the edge surface of the disk. At the inner rotor radius, a pressure outlet is located. Finally, rotational periodicity is imposed at the circumferential surfaces of the domain.

The rotor mesh is structured, similar to the rotor only study, the stator and interspace meshes are unstructured with inflation layers at the walls and the rotor-stator interface. See figure 3.6 for a detail view. The mesh in the space between stator and rotor is coarse, with only three layers of cells in radial direction. While this might not be very accurate locally, it is sufficient for the overall results according to the indicator variables of the mesh independence study.

The study is set up in a similar manner as for the rotor only case, for the highest Reynolds number and Taylor number conditions encountered in the experiment in chapter 4. These conditions are summarized in table 3.2. Figure 3.7 summarizes the results of the study. With regard to efficient modelling, the case with 110068 mesh elements is selected for further analysis. It provides good accuracy within 2 % deviation, at about a fifth of the computational cost of the largest case. Figure 3.8 shows a single streamline from the mesh independence study. The Reynolds number and Taylor number calculated from rotor inlet conditions for this case are 506 and 10429 respectively. The Mach number in the domain peaks just after the nozzle at slightly above one.

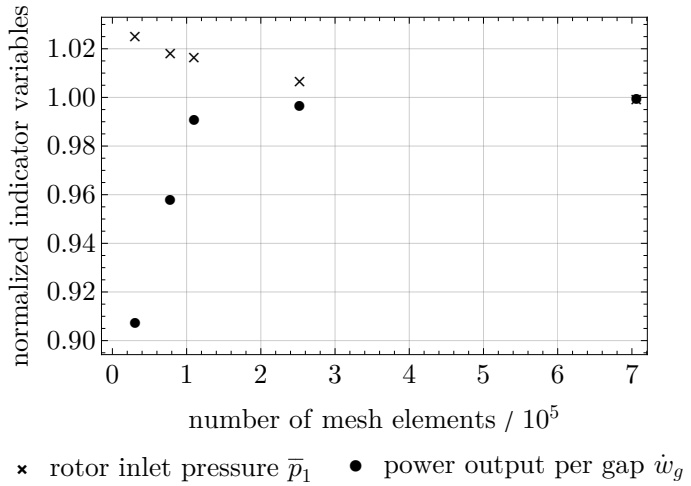

Figure 3.7: Results of the mesh independence study. Variables are normalized with respect to the results from the finest mesh.

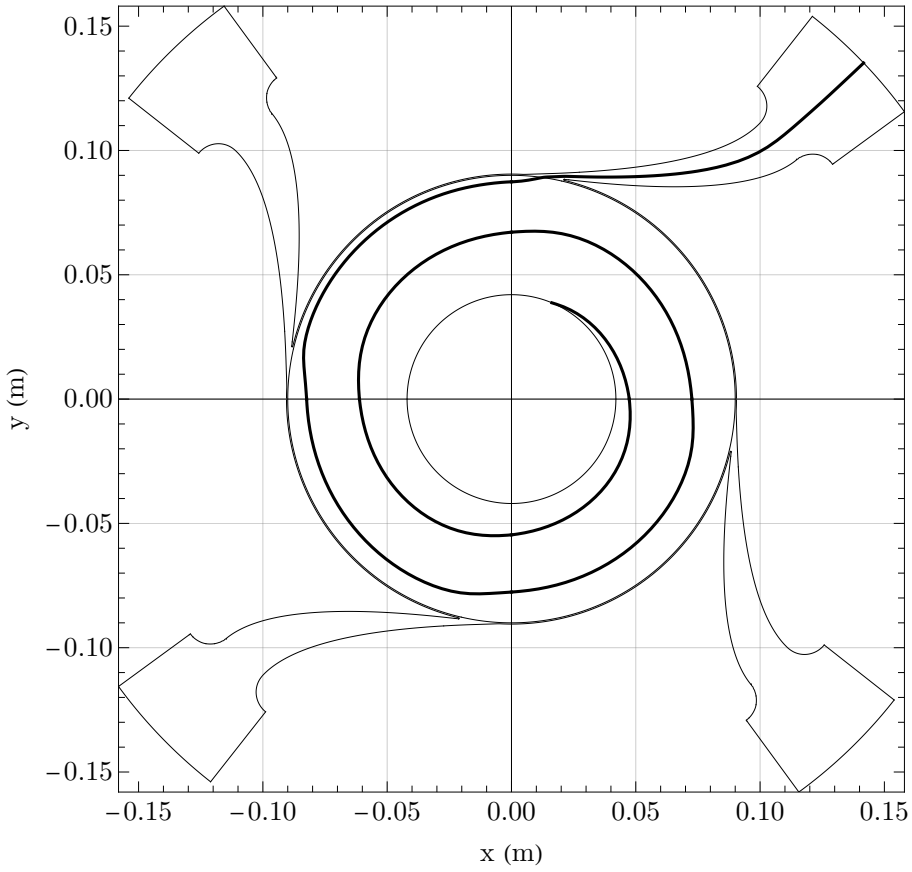

Figure 3.8: A single streamline in a nonrotating frame of reference, starting from the inlet boundary in the rotor stator case.

parameter		value	
disk outer radius	r_1	180	mm
disk inner radius	r_2	42	mm
disk spacing	$2s$	0.8	mm
disk thickness		0.8	mm
inlet temperature	$\bar{\vartheta}_1$	30.4	°C
outlet pressure	$\bar{p}_2$	1.24	bara
inlet mass flow	$\dot{m}_g/4$	2.65	$\mathrm{g\,s^{-1}}$
rotational speed	n	20000	$\mathrm{min^{-1}}$
nozzle configuration		5-8-4	

Table 3.2: Input parameters for the mesh independence study for the rotor and stator case. For an explanation of the nozzle configuration, refer to chapter 4.

3.2 Stability and transition

This section summarizes new results from linear stability analysis and direct numerical simulation that, for the first time, are targeted specifically at Tesla turbine flow. The results were previously published, along with more detailed description of the approaches and results by Klingl et al. [2020, 2022, 2024].

3.2.1 Linear stability analysis

The study by Klingl et al. [2020] is directly aimed at determining flow regime boundaries in Tesla turbine flow. It describes two approaches to linear stability analysis on the laminar solution by Batista [2011] and Schosser et al. [2019]. The authors use a local approach with assumed radial homogeneity and a biglobal approach, with both radial and axial dimensions retained and only circumferential and temporal homogeneity.

The local approach is only valid at a specified radial position and requires a specially designed nondimensionalization, where the Reynolds number is equal to the local nondimensional radial coordinate. This allows to replace occurrences of the radial coordinate in the conservation equations with the Reynolds number. The laminar solution $\boldsymbol{U}_0^* = (U_{r0}^*, U_{\phi 0}^*, U_{z0}^*)$ and P_0^* is then perturbed with a three-dimensional Fourier mode in radius, circumference and time, where the temporal wavenumber γ_t^* has an inverted sign by convention.

$$\boldsymbol{U}^* = \boldsymbol{U}_0^* + \boldsymbol{U}_a^*(Z)\exp(\mathrm{i}(\gamma_r^* R^* + \gamma_\phi^* \phi - \gamma_t^* T^*)) \tag{3.1}$$

$$P^* = P_0^* + P_a^*(Z)\exp(\mathrm{i}(\gamma_r^* R^* + \gamma_\phi^* \phi - \gamma_t^* T^*)) \tag{3.2}$$

$\boldsymbol{U}_a^*$ and P_a^* are Z-dependent amplitude functions, i is the imaginary unit. After inserting the perturbed basic flow into the conservation equations, the terms that only include the base flow can be removed because these, by definition, satisfy the conservation equations and thus, in combination, reduce to zero. In addition, terms that are non-linear in the amplitude functions are removed, since it is assumed that amplification of small perturbations is dominated by linear mechanisms. The resulting equations define an eigenvalue problem that can be solved numerically for the wavenumbers as eigenvalues and the unknown amplitude functions as eigenfunctions.

Klingl et al. [2020] provide real spatial wavenumbers as input parameters, which correspond to spatially neutral oscillations that are neither amplified nor dampened in space. The problem is then solved for complex temporal wavenumbers as eigenvalues. Their real

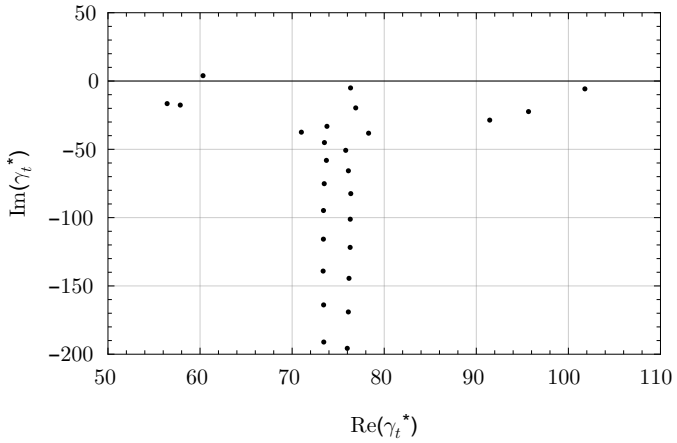

Figure 3.9: Sample temporal eigenvalue spectrum of the $(\gamma_r^*, \gamma_\phi^*) = (145, 290)$ mode from data by Klingl et al. [2020], converted to local nondimensionalization, at $\mathrm{Re}^* = 549$, $\mathrm{Ta}^* = 95.7$ and $\sigma^* = 0.00455$.

parts are related to the frequency of the perturbation, their imaginary parts describe the temporal amplification rates. If the amplification rate is positive, the particular mode is amplified in time and thus unstable. This type of analysis is referred to as temporal stability analysis.

Figure 3.9 shows a sample temporal eigenvalue spectrum from the described approach, with one visible eigenvalue that has a positive amplification rate. The spectrum corresponds to operating conditions close to the stability boundary, so the amplification rate is still quite small. Under these conditions it would take very long for the unstable mode to be amplified enough to have a noticeable influence on the flow field, unless it already has a large amplitude upon entering the domain.

Klingl et al. [2020] apply the local stability approach to a range of Reynolds numbers for virtually constant Taylor number and give amplification rates of various spatial modes. Figure 3.10 shows this as function of local Reynolds number. The lowest Reynolds number for which an unstable eigenfunction can be found is the theoretical critical Reynolds number.

The local approach treated so far assumes homogeneity in radial direction, which is not exactly accurate for radially evolving flows, like the flow inside a Tesla turbine rotor. To accurately represent radial inhomogeneity, the radial direction can be resolved by the amplitude function. Theofilis [2011] calls this approach biglobal linear stability analysis.

$$\boldsymbol{U} = \boldsymbol{U}_0 + \boldsymbol{U}_a(R, Z)\exp(\mathrm{i}(\gamma_\phi \phi - \gamma_t T)) \tag{3.3}$$

$$P = P_0 + P_a(R, Z)\exp(\mathrm{i}(\gamma_\phi \phi - \gamma_t T)) \tag{3.4}$$

This comes at considerably higher computational cost, since a second spatial dimension is introduced into the eigenvalue problem. For solving this, Klingl et al. [2020] employ a numerical method to retrieve excerpts of the eigenvalue spectra in the region of interest. The spectra consist of continuous eigenvalue branches, as opposed to discrete eigenvalues because of the outlet boundary in radial direction. The global nondimensionalization scheme has to be applied, since the method doesn't give information on radial amplification rate. Visual inspection of the eigenfunctions gives however an impression of radial development of the perturbation. Figure 3.11 shows a sample instability. Only the outlet region of the domain is shown, since the perturbation amplitude in the inlet region is very

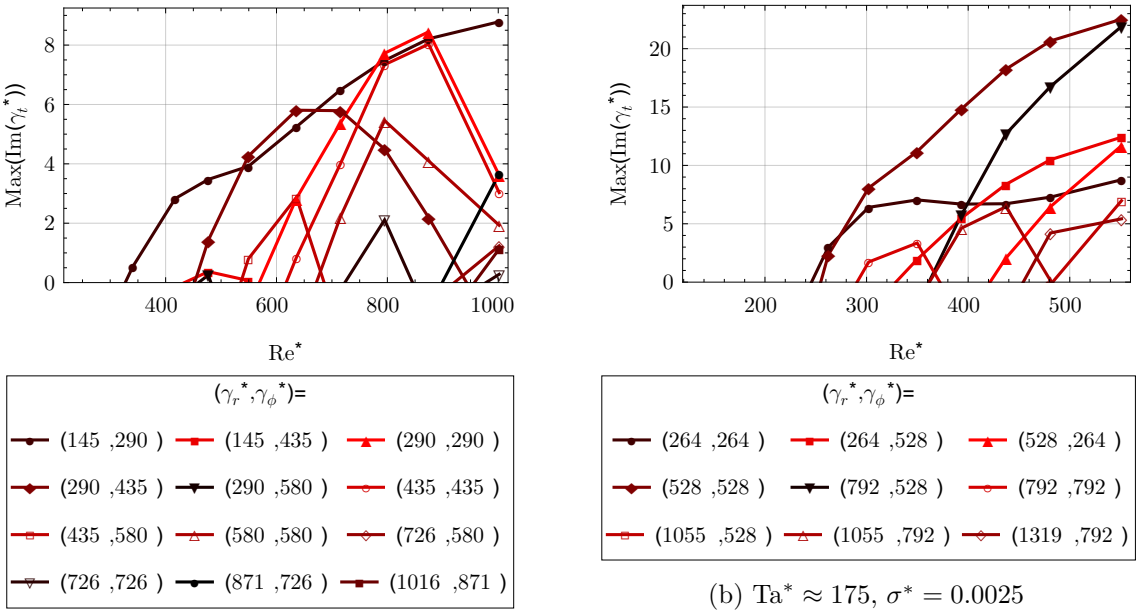

(a) $\mathrm{Ta}^* \approx 96$, $\sigma^* = 0.00455$

(b) $\mathrm{Ta}^* \approx 175$, $\sigma^* = 0.0025$

Figure 3.10: Maximum temporal amplification rates of different spatial modes as functions of local Reynolds number from the local stability analysis by Klingl et al. [2020]. Taylor number slightly varies about ±5 % along the Re^*-axis.

small. This is a consequence of the boundary condition that enforces zero amplitude at the inlet.

The critical Reynolds number for the particular operating conditions analysed by Klingl et al. [2020] is found from the biglobal approach at $\mathrm{Re} = 242$. The local approach on the other hand yields stability limits at global Reynolds numbers of $\mathrm{Re} = 150$ and $\mathrm{Re} = 210$ for the inner and outer analysed radial positions respectively.

Extending the analysis to complex spatial wavenumbers allows for distinguishing convectively and absolutely unstable flow, depending on whether perturbations travel only downstream or upstream and downstream. In a flow that is purely convectively unstable, all perturbations eventually get washed away by the flow and in order for it to remain in a perturbed state, the perturbation source needs to be provided continuously. In contrast

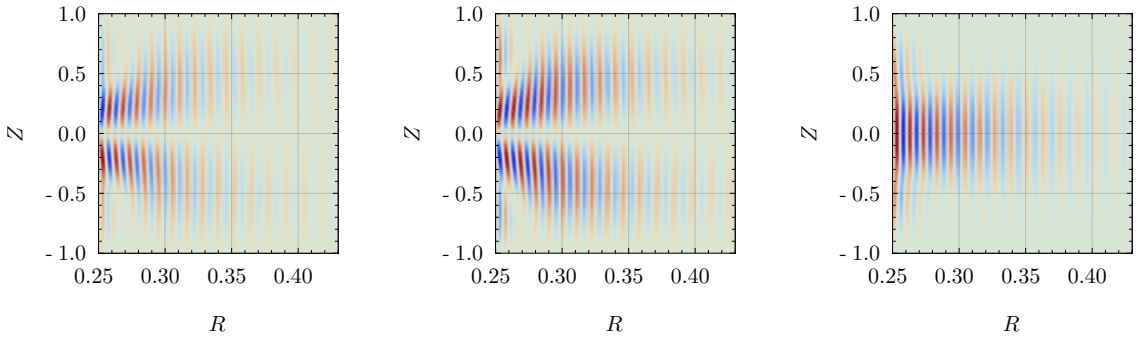

(a) $U_{ra}(R, Z)$ (b) $U_{\phi a}(R, Z)$ (c) $U_{za}(R, Z)$

Figure 3.11: Sample unstable eigenfunction from the biglobal linear stability approach by Klingl et al. [2020] at the global parameters $\mathrm{Re} = 242$, $\mathrm{Ta} = 218$ and $\sigma = 0.002$, with a reference inlet radius of r_1 =125 mm.

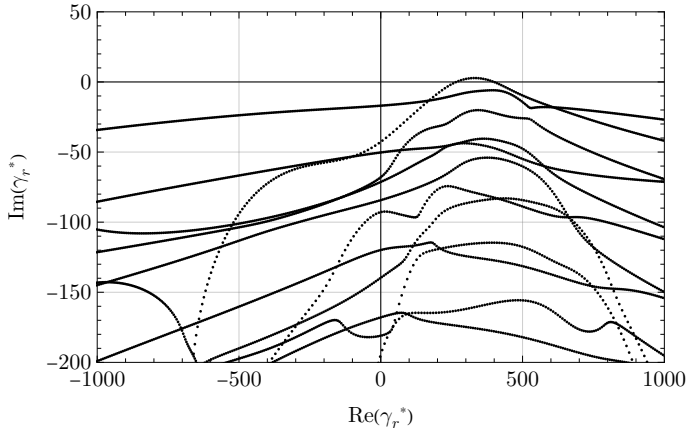

Figure 3.12: Spatial eigenvalue branches resulting from projection of the real axis of the complex temporal wavenumber plane into the complex radial wavenumber plane at $\mathrm{Re}^* = 235$, $\mathrm{Ta}^* = 302$, $\gamma_\phi^* = 468$ and $\sigma^* = 0.00270$.

to that, absolutely unstable flow upholds the perturbed state by itself and only needs a perturbation impulse in time and space as a trigger.

In the search for absolute instability in Tesla turbine flow, Klingl et al. [2022] expand the parameter space of the local linear stability analysis based on the ansatz from equations 3.1 and 3.2, to take complex spatial wavenumbers into account. They find no absolute instability, only convective instability in their analysed parameter space.

The authors search for instabilities by projecting the real axis of the complex temporal wavenumber plane into the complex radial wavenumber plane through the eigenvalue problem. This is achieved by providing real circumferential wavenumbers and real temporal wavenumbers as parameters and solving for the complex radial wavenumbers as eigenvalues. An example of this is displayed in figure 3.12. Each individual point in the chart displays one of the resulting complex radial eigenvalues γ_r^*. The eigenvalues form branches because solutions for many different real temporal wavenumbers are shown at the same time. The x-axis displays the real part of γ_r^*, which corresponds to the radial wavenumber of the oscillation, the y-axis displays the imaginary part, which corresponds to the rate of change in amplitude in radial direction. Equations 3.1 and 3.2 suggest that a positive imaginary part of the radial wavenumber γ_r^* corresponds to increasing amplitude in negative radial direction, which is the direction of flow in this case. Thus, the eigenvalues in figure 3.12 that slightly cross into the positive imaginary part half-plane at $\gamma_r^* \approx 300$ correspond to eigenmodes that increase in amplitude in the downstream direction. In time, these modes are neither amplified nor dampened because of the given real temporal wavenumber. Nevertheless, the existence of similar modes that are amplified in time is implied, provided that the mapping from the temporal wavenumber plane into the radial wavenumber plane is continuous so that moving the given temporal wavenumbers from the real axis into the positive imaginary part half-plane by a small distance leaves the resulting radial eigenvalue spectrum almost unchanged.

The instabilities found this way are of convective nature because absolute instability would require a saddle point formed by two eigenvalue branches from different γ_r^* half-planes, at a temporal wavenumber with positive imaginary part. This was not found by Klingl et al. [2022].

Figure 3.13 visualizes all points in the Re^*-Ta^* plane that are probed by Klingl et al. [2022] for stability. The estimated stability boundary is formed by connecting the unstable

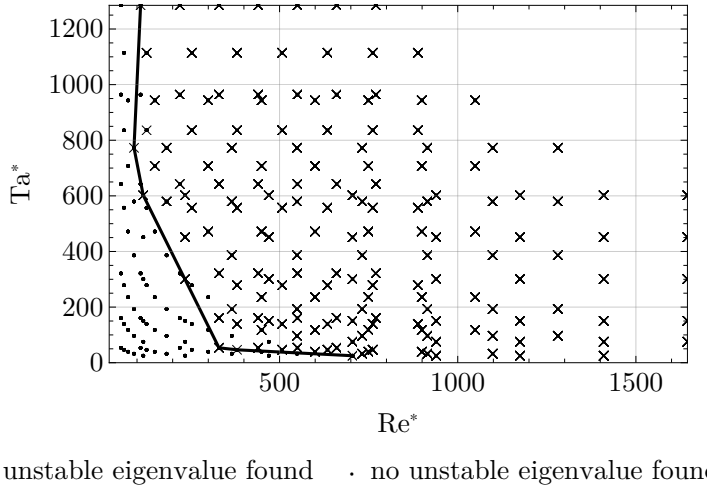

Figure 3.13: Stable and unstable operating conditions found by Klingl et al. [2022] for local aspect ratios between $\sigma^* = 0.00253$ and $\sigma^* = 0.00667$.

points with the smallest Reynolds and Taylor numbers.

Figure 3.14 compares the newly established stability boundary to previous findings from theoretical studies, that were described in section 2.2.4.1. The figure includes the theoretical stability limit for regular Poiseuille flow, which is determined by Orszag [1971] to be 5772.22. The value is multiplied by a factor of 2/3 in order to approximately convert the centreline velocity based Reynolds number to the bulk velocity based definition that is used in the present context. The conversion of the results of Flaherty and DiPrima [1978] and Gusev and Bark [1980] to the present Reynolds and Taylor number definitions is also not straight forward since they use a characteristic velocity based on pressure gradient. To relate this to the presently used nondimensional parameter definitions, a relation is derived from the asymptotic radial velocity solution given in equation 2.59, assuming the function $F(R)$ to be a constant pressure gradient in radial direction and invoking the mass flow condition $\bar{U}_r = -1/R$.

$$\frac{\partial P}{\partial R} = -\frac{4\mathrm{Ta}\sqrt{\sigma\mathrm{Ta}}(\cos(2\sqrt{\sigma\mathrm{Ta}}) + \cosh(2\sqrt{\sigma\mathrm{Ta}}))}{R\ \mathrm{Re}(\sin(2\sqrt{\sigma\mathrm{Ta}}) - \sinh(2\sqrt{\sigma\mathrm{Ta}}))} \tag{3.5}$$

The dashed curves that correspond to the results of Flaherty and DiPrima [1978] show the two types of instability. The Poiseuille instability, originating on the Re*-axis around $\mathrm{Re}^* = 3800$, is overtaken quickly with rising Taylor number by the second type of instability. The chart uses the local definition of Reynolds and Taylor numbers except for the □-symbol, which refers to biglobal results with the outer disk radius as characteristic length. The results generally agree with each other, the remaining inconsistencies are likely due to different modelling assumptions of the approaches, for example the neglected centrifugal term within the model of rotation modified Poiseuille flow.

Results from the stability experiments that were described in chapter 2.2.4.2 are summarized in figure 3.15 and compared to the new theoretical boundary by Klingl et al. [2022]. The two lines by Pater [1973] denote upper and lower bound of observed transitional region, with a global reference radius. The multiple lines by Dibelius and Nendl [1973] denote stability limits found at different radial positions. The experimental axial velocity profiles by Schosser [2016] are labelled as “turbulent looking” when they are, compared to a parabolic profile, visibly flattened in the centre. The results by Dibelius and Nendl [1973] differ noticeably from the other results, which is likely due to the considerably

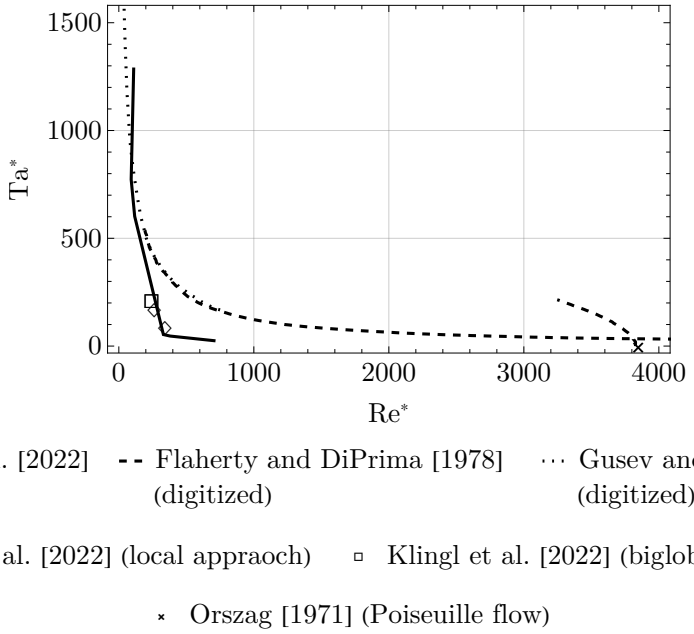

Figure 3.14: Stability curves from theoretical analysis. Unstable modes are present in the region to the top right of the curves.

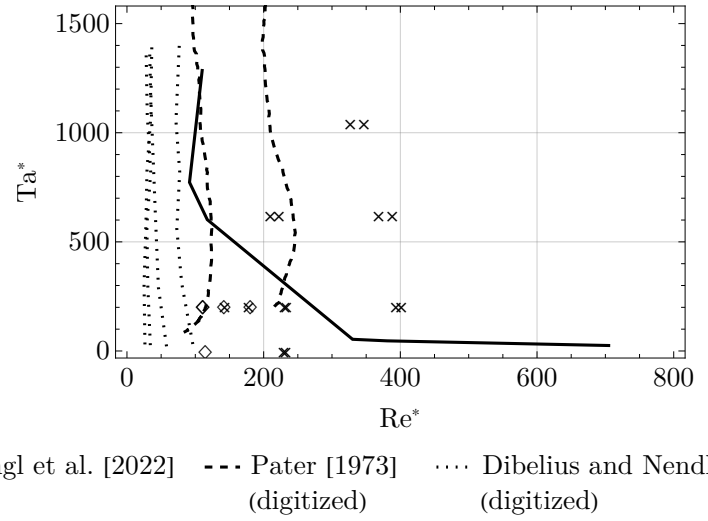

Figure 3.15: Stability boundaries from experiments compared with the theoretical results by Klingl et al. [2022].

higher aspect ratio of their test facility at $\sigma = 0.007$, whereas the other studies work with aspect ratios in the range from $\sigma = 0.00127$ to 0.00270. The chart uses the local Reynolds and Taylor number definitions, except for the results by Pater [1973], which is a global study with no exact information on the radial position of transition. Here the parameters are formed with the outer disk radius. Converting the parameters to the local formulation with respect to the radial position that was actually observed in the experiment would move the boundary towards the lower right of the chart.

Keep in mind, that the occurrence of unstable modes in theory should not lead to

instant transition in practice, as perturbations take time and space to be amplified. If the amplification rate is low, the perturbation might have left the region of interest before it is amplified enough to noticeably influence the flow. Regarding figure 3.15 this means, that the theoretical stability boundary should be located at lower Reynolds and Taylor numbers, compared to the experimental boundaries. Transition in real flows is however not necessarily based on linear instability inside the rotor gap. A possible scenario in a Tesla turbine application is, that the flow approaches the rotor in a turbulent state because of the high flow velocity and comparatively large cross-sectional area at the nozzle outlet. Upon entry into the rotor, the local length scale decreases abruptly and thus the flow gains stability and either laminarizes or stays turbulent.

In conclusion, theoretical and experimental results roughly agree with each other and give the overall impression, that stability is largely independent of Taylor number. The inconsistencies between the studies, that lead to ambiguity in the stability chart, include varying gap aspect ratios and different rotor inlet conditions. Especially the gap aspect ratio is a hidden third dimension of the stability chart.

3.2.2 Direct numerical simulation

Direct numerical simulation (DNS) is a tool that numerically resolves all flow structures without any turbulence modelling. This allows to directly observe unstable oscillations and turbulent structures inside the flow over time. Fourier analysis of the fluid domain allows for verification of the linear stability results. For this purpose, a direct simulation is set up using the open source solver Nek5000 [2019] and used to simulate operating conditions corresponding to transitional and turbulent flow regimes, as shown in figure 3.16. The key input parameters of the two computations are summarized in table 3.3. The study is made possible by a 35 million core hour grant by the Leibniz-Rechenzentrum in Garching, Germany.

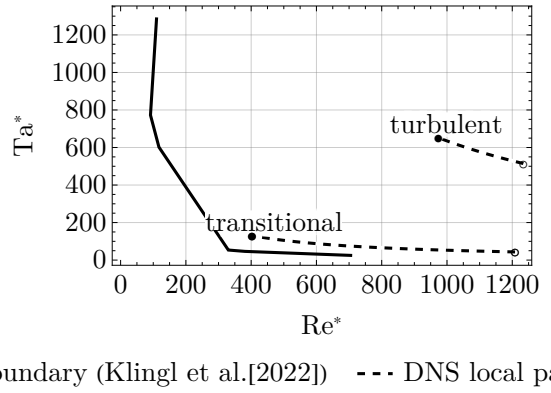

Figure 3.16: Operating conditions used for direct numerical simulation in the stability plane. The stability boundary from linear theory is shown as solid line, the dashed lines indicate the ranges of local parameters covered by the computations, where filled symbols refer to radial position r_1.

This section gives a short summary of the simulation results. For the full study, including detailed descriptions of the simulation setup and postprocessing, a mesh independence study and a full summary of results, for example further Fourier analysis, two-point correlations, energy spectra and friction variables, please refer to Klingl et al. [2024].

The domain for the DNS is a periodic sector of the space between two disk surfaces, as shown schematically in figure 3.1. Its dimensions are chosen, so that the results can be directly compared to the experimental velocity distributions by Schosser [2016]. The

regime		transitional	turbulent	
Reynolds number	Re	403	974	
Taylor number	Ta	131	652	
gap aspect ratio	σ	0.00333	0.00439	
nondimensional outlet radius	R_2	0.467	0.789	
domain size in ϕ-direction		30	3.6	$^\circ$
reference inlet radius	r_1	75	57	mm
reference kinematic viscosity	ν_1	15.04×10^{-6}	11.45×10^{-6}	$\mathrm{m^2\,s^{-1}}$
mesh element resolution	$r \times \phi \times z$	$480 \times 347 \times 6$	$648 \times 171 \times 27$	

Table 3.3: DNS operating conditions.

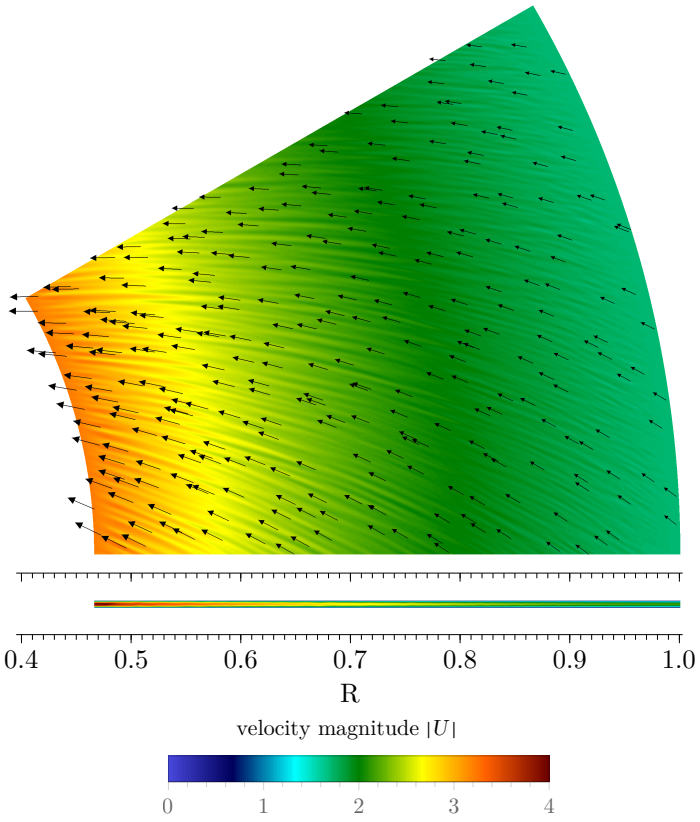

Figure 3.17: Velocity magnitude and flow direction on a plane at 75 % domain height in Z (top) and velocity magnitude at $\phi = 0$ (bottom), both at a fixed point in time.

domain is resolved with a regular mesh of spectral elements, where each element is resolved internally with a polynomial order of seven in all three spatial dimensions.

In a small section of the domain, right after the inlet boundary, there is an artificial random body force acting in Z-direction to disturb the flow and trigger oscillations. The forcing consists of a superposition of radial and circumferential modes in a certain range of wavenumbers, each with the same amplitude and a random phase shift. The strength of the forcing can be adjusted. For the transitional operating point, it is set to be small to be able to observe the downstream development of the oscillations, for the turbulent operating condition the forcing is large to trigger turbulence as quickly as possible.

Shortly before the outlet, all fluctuations are dampened away to avoid reflections at the outlet boundary. The inlet boundary and initial conditions are calculated from a laminar

analytical solution with parabolic velocity profiles. The given flow direction at the inlet is a result of extrapolation from the experimental velocity measurements.

The transitional operating conditions are simulated in a 30°-sector of the rotor circumference. Figure 3.17 shows velocity magnitude and flow direction on two-dimensional slices through the domain. The flow oscillations that develop from the inlet perturbation are visible. For the visualization, the strength of the inlet forcing is increased, otherwise the oscillations would be almost invisible in relation to velocity magnitude. The to-scale ϕ-normal slice that is shown in the lower part of the figure visualizes the small aspect ratio of the gap.

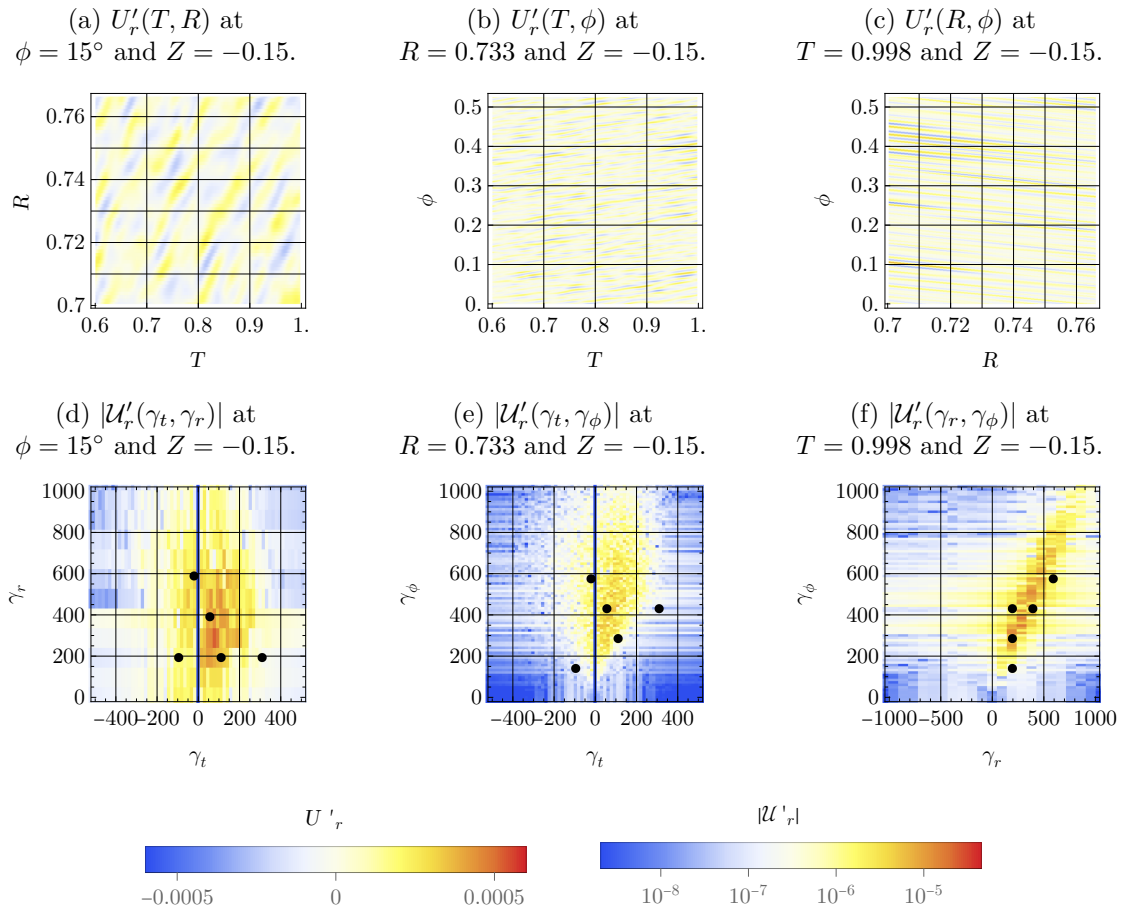

Figure 3.18: Fourier analysis of the fluctuating component of radial velocity U'_r at the transitional operating conditions. The black dots are unstable modes found in the local linear stability analysis by Klingl et al. [2020].

The flow field is subjected to discrete Fourier transform on two-dimensional slices through the domain in time and space, resulting in spectral maps that can be compared to unstable modes found in linear stability analysis. Figure 3.18 shows some selected excerpts of the flow domain in space and time together with their respective Fourier transforms. Note the small amplitude of the velocity oscillation compared to velocity magnitude in figure 3.17. Only the analysis of the radial velocity component is shown, since the other components and the pressure have a similar spectral structure. The independence of the results from mesh resolution, domain size and perturbation strength was checked. Unstable modes from the local linear stability analysis with the same operating conditions and geometry are shown as black dots. The radial extent of the slices is restricted to a

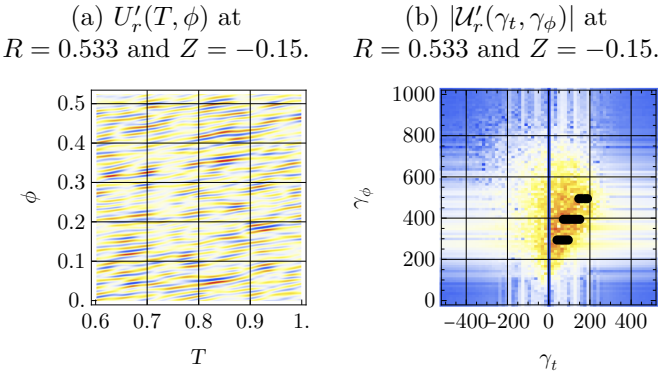

Figure 3.19: Fourier analysis of the fluctuating component of radial velocity U_r' during the transitional simulation. The black dots are unstable modes found in the biglobal linear stability analysis by Klingl et al. [2020]. For the colour scales see figure 3.18.

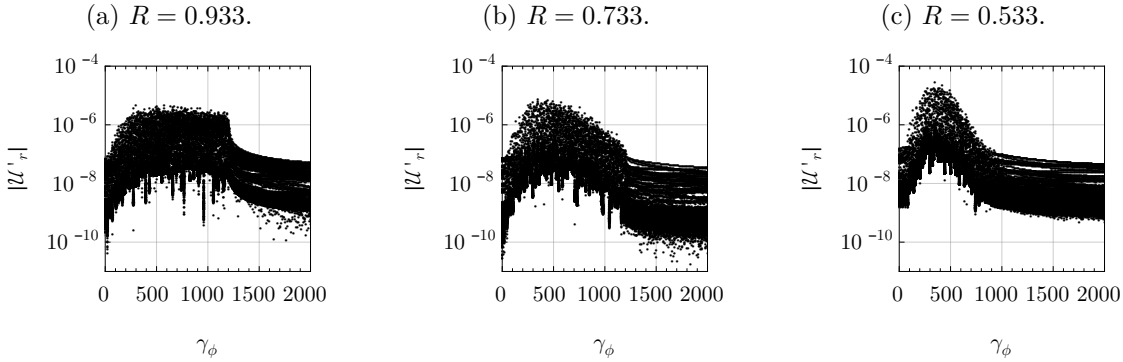

Figure 3.20: Radial development of perturbation amplitude during the transitional simulation. The charts show the two-dimensional Fourier transform of T-ϕ-slices at $Z = -0.15$ and different radial positions. The slices cover a timespan from $T = 0.6$ to $T = 1$. Temporal wavenumbers are not distinguished.

short section surrounding the point of the local analysis at $R = 0.733$. In terms of spatial wavenumbers, the linear stability results coincide with the hotspots in the spectral maps, the temporal wavenumbers deviate to some degree for certain modes.

A similar comparison of results is shown in figure 3.19, but this time with unstable modes from the biglobal linear stability approach. The results agree and now, the temporal wavenumbers are modelled correctly as well.

Figure 3.20 gives insight into the radial, downstream development of the oscillations. In the first chart for $R = 0.933$, which is close to the inlet boundary, a broad spectrum of modes up to wavenumbers of approximately $\gamma_\phi = 1200$ is present in the flow. This stems from the artificially imposed perturbation. Further downstream, most modes are dampened and only a small section between approximately $\gamma_\phi = 200$ and $\gamma_\phi = 600$ is amplified.

The fluctuating velocity components at one point in time are shown figure 3.21. They consist of a superposition of many modes, but the general structure of the high-frequency content is comparable to the unstable eigenfunction from theoretical analysis, shown in figure 3.11.

For the simulation of turbulent operating conditions, the computational cost is much higher and thus the domain only covers 3.6° of the rotor circumference and is also shorter

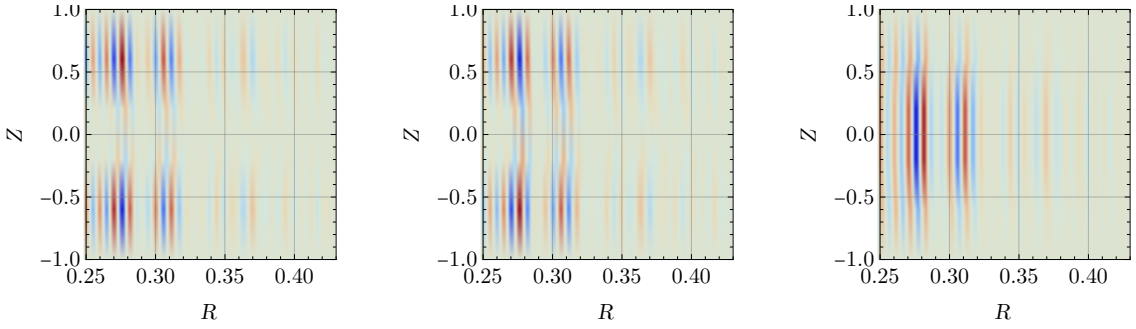

(a) $U'_r(R, Z)$ (b) $U'_\phi(R, Z)$ (c) $U'_z(R, Z)$

Figure 3.21: Fluctuating part of the velocity components at one point in time for the transitional operating conditions from direct numerical simulation. The reference length for nondimensional radius is changed to r_1 =125 mm to allow direct comparison with figure 3.11.

in radial direction. Figure 3.22 shows axial and circumferential slices of the domain. The radial development of the flow can be made out, where the fluid flows from right to left, entering the domain in a laminar state, after which strong oscillations are enforced, which in turn break down into a chaotic looking velocity field.

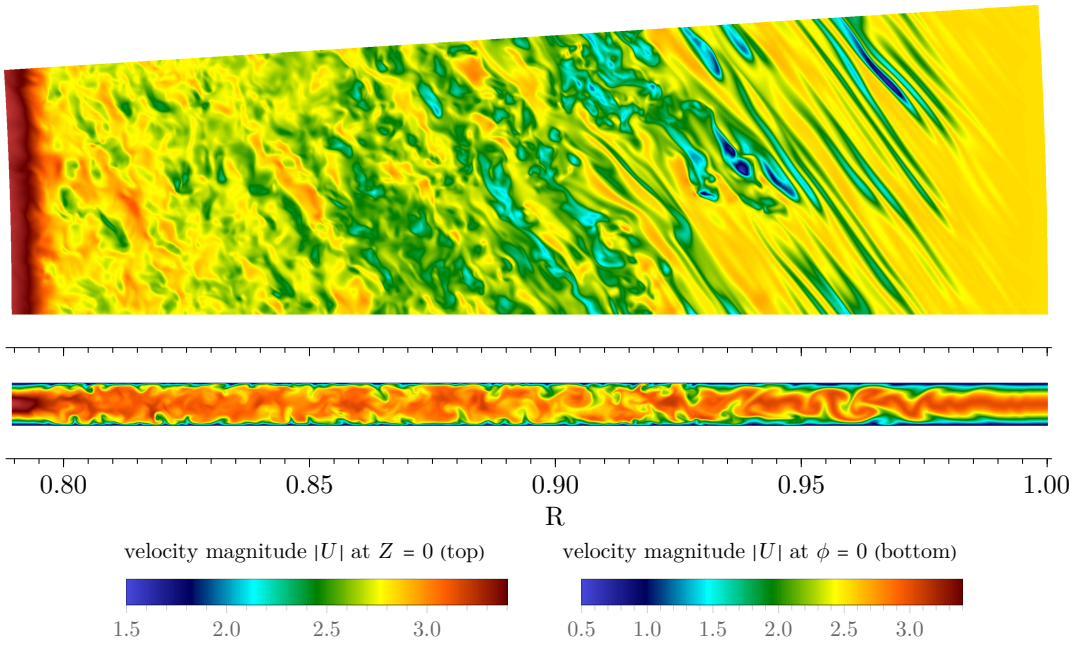

Figure 3.22: Velocity magnitude at the planes $Z = 0$ (top) and $\phi = 0$ (bottom) at one point in time during simulation of turbulent operating conditions.

The turbulent simulation is run over a period of simulation time, in which the domain could be crossed more than 20 times in radial direction at average fluid velocity. During this period, averages and statistics of the velocity field are collected. The comparison in figures 3.23 and 3.24 shows average and instantaneous radial and circumferential velocity profiles at a radial position close to the outlet boundary and compares them with experimental data and a corresponding simulation from the rotor-only CFD approach with turbulence modelling using ANSYS CFX. The profiles from experiment and DNS agree very well. The circumferential velocity component from the commercial CFD simulation

slightly deviates, even though the inlet mass flow and flow direction are matched to the DNS. This is due to the mismatch in inlet velocity profile shapes. While the DNS is supplied with parabolic profiles, the rotor-only CFD results are based on a default block inlet profile. A new run of the latter with a custom parabolic inlet velocity profile shape leads to better agreement, as shown by figure 3.25. The radial velocity component from figure 3.23a is virtually unaffected by this.

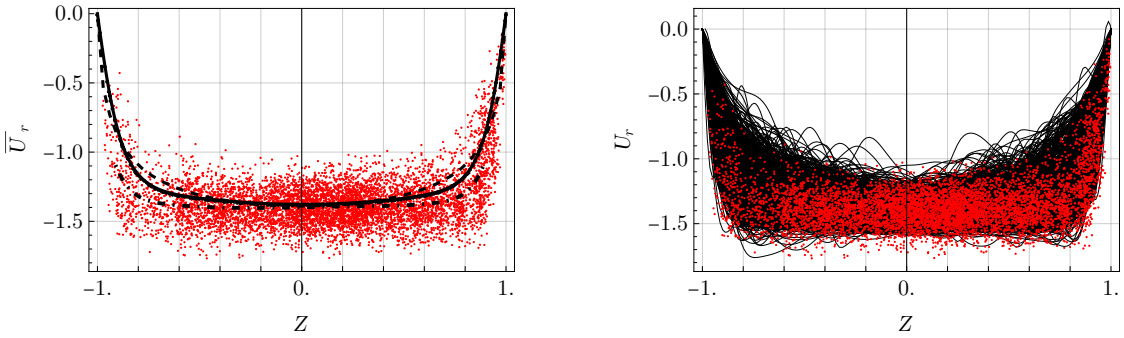

(a) Comparison of experimental data and average velocities.

(b) Comparison of experimental data and instantaneous velocity profiles from DNS.

DNS RANS SST experiment polynomial fit experiment

Figure 3.23: Comparison of turbulent temporal average radial velocity profiles at r =47 mm (R = 0.825). Experimental data was recorded by Schosser [2016].

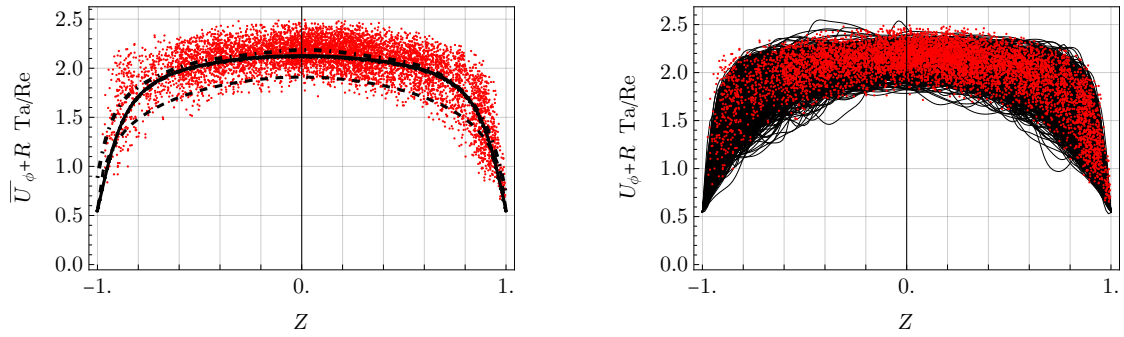

(a) Comparison of experimental data and average velocities.

(b) Comparison of experimental data and instantaneous velocity profiles from DNS.

DNS RANS SST experiment polynomial fit experiment

Figure 3.24: Comparison of turbulent temporal average circumferential velocity profiles in a stationary reference frame, at r =47 mm (R = 0.825). Experimental data was recorded by Schosser [2016]. R Ta/Re is the nondimensional disk surface velocity.

Figure 3.26 shows the average velocity magnitude profile in wall units on a logarithmic length scale, along with analytical log-law approximations. The corresponding friction Reynolds number is 118. The chart also shows the mesh resolution near the wall, with the closest mesh point lying at $Z^+ = 0.466$.

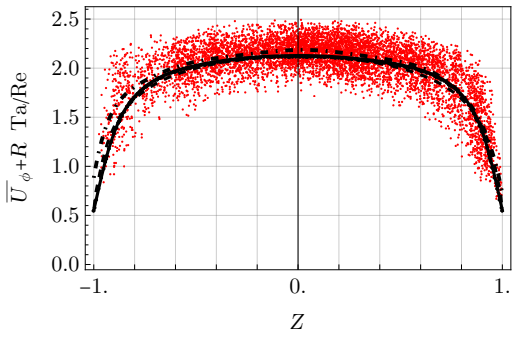

Figure 3.25: Modified version of figure 3.24a with the inlet velocity profile shape in the RANS CFD matched to the DNS.

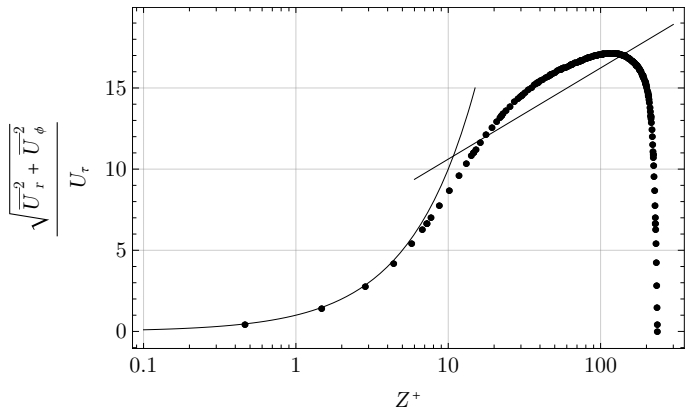

Figure 3.26: Average velocity magnitude from DNS at r =47 mm (R = 0.825), normalized with the friction velocity U_τ. The solid lines are $U^+ = Z^+$ and $U^+ = \frac{1}{0.41}\ln(Z^+) + 5$ [Schlichting and Gersten, 2017].

3.3 Model validation

The findings from stability analysis help distinguishing laminar and turbulent flow, but in the transitional region, the distinction is blurry. It is yet unclear, how far beyond the stability boundaries the turbine parameters can progress, before the predictions by the laminar analytical models become too inaccurate. To clear this up, this section concludes the chapter about modelling and simulation of Tesla turbines by checking the validity of different modelling approaches. Four selected analytical models are compared to experimental data by previous authors. After that, the region of validity is roughly outlined in terms of Reynolds and Taylor number by comparison with CFD results. The analytical models that are selected for the comparison are summarized in table 3.4.

name	character	equations	reference
Beans	parabolic velocity profiles	2.45, 2.46	Beans [1961]
Breiter	asymptotic	2.59, 2.60, 2.65, 2.66	Breiter and Pohlhausen [1962]
Batista	asymptotic up to second order		Batista [2011]
Pfitzner	asymptotic with inlet correction		Schosser et al. [2019]

Table 3.4: Selected models for comparison to experimental data.

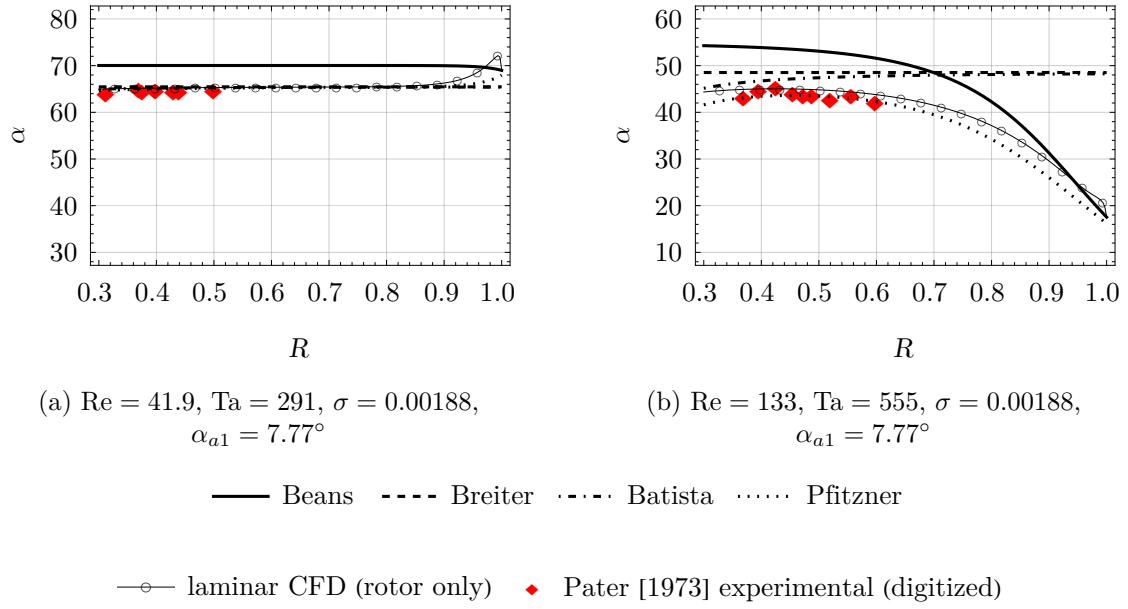

(a) Re = 41.9, Ta = 291, $\sigma = 0.00188$, $\alpha_{a1} = 7.77°$

(b) Re = 133, Ta = 555, $\sigma = 0.00188$, $\alpha_{a1} = 7.77°$

Figure 3.27: Comparison of modelled and experimental flow angle α in the rotating frame. The experimental data points were digitized from figures 24 and 32 by Pater [1973].

3.3.1 Validation through experiment

Experiments that directly measure the flow field in a corotating disk gap are a rare but valuable source of validation for analytical and numerical modelling. So far, there have been some attempts to experimentally capture velocity and pressure distributions inside a corotating disk gap, that resembles Tesla turbine applications. These studies allow for pointwise validation of theoretical models.

For the following comparison, the experimental results by Pater [1973] and Schosser [2016] are used. They were briefly described before in chapter 2.2.4.2. Figure 3.27 shows a comparison between the flow angle measurements by Pater [1973] and the computed flow angles from analytical models and CFD. The experimental values were visually determined by the researchers from photographs of ink trails in the fluid. Only laminar operating conditions were examined, because otherwise, the ink trails were not distinct enough. Since the ink is assumed to mainly stay in the centre plane between the disks, the modelled flow angle displayed in the charts is not computed using average velocities, as given in equation 2.14, but with velocities in the centre plane of the channel at $Z = 0$. The results are compared with the rotor only CFD model from section 3.1.1, without turbulence modelling. For the CFD simulation, the Reynolds number, Taylor number, gap aspect ratio and inlet flow angle are matched to the conditions of the experiments, the dimensional outer disk radius as well as the medium is however unchanged from table 3.1, only the disk spacing is adapted to match the gap aspect ratio of the experimental facility and the outlet radius is decreased to 0.2 m. Similarly, figure 3.28 compares pressure measurements over radius between models and experiment.

The models agree with each other, only the prediction from the Beans-model with the assumed parabolic velocity profile is slightly off for the flow angle. In terms of the pressure, the asymptotic solution by Breiter and Pohlhausen [1962] deviates at small radii in figure 3.28b. Figure 3.27b apparently shows non-asymptotic conditions, where the asymptotic models deviate at large radii and approach the other data slowly towards the outlet. For

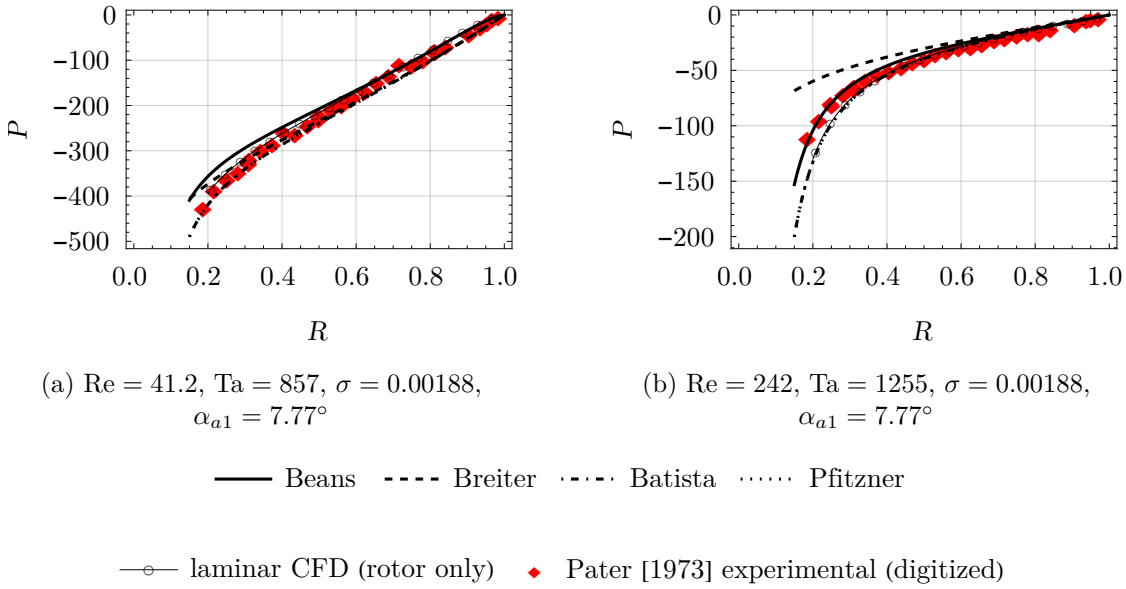

(a) Re = 41.2, Ta = 857, $\sigma = 0.00188$, $\alpha_{a1} = 7.77°$

(b) Re = 242, Ta = 1255, $\sigma = 0.00188$, $\alpha_{a1} = 7.77°$

Figure 3.28: Comparison of modelled and experimental dimensionless pressure P. The experimental data points were digitized from figures 46 and 51 by Pater [1973].

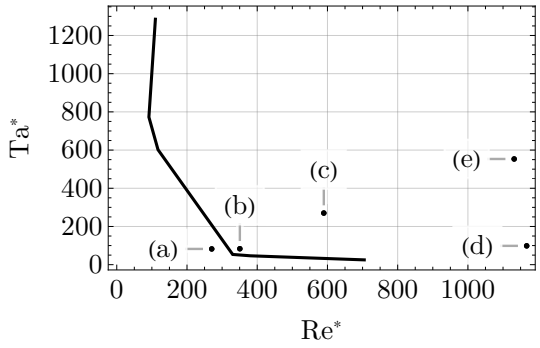

Figure 3.29: Local Reynolds and Taylor numbers for the velocity profiles from figure 3.30. Letters refer to the respective subfigure. The theoretical stability boundary by Klingl et al. [2022] is shown again for reference.

the operating conditions in figure 3.27a, this happens much quicker since the Reynolds number is lower and the flow direction at the inlet is already almost asymptotic.

The PTV measurements by Schosser [2016] were already compared to analytical and numerical models by Schosser et al. [2019] and Klingl et al. [2020]. For completeness, the same is repeated here for selected datasets. Figure 3.30 shows the gathered velocity profiles, figure 3.29 visualizes the selected operating conditions relative to the theoretical stability boundary by Klingl et al. [2022]. As expected, analytical models and experimental data agree better, the lower Reynolds and Taylor numbers are. In figures 3.30d, 3.30e, the deviation in the circumferential velocity component between some analytical models and experiment grows very large. CFD data overall agrees well with the experimental data. In accordance with figure 3.29, turbulence modelling is active, except for points (a) and (b). The inlet angle is assumed to be 21.3°, which is an estimate obtained from simulation results by Schosser et al. [2019]. This is a source of uncertainty, because the actual inlet flow angle varies with the operating conditions.

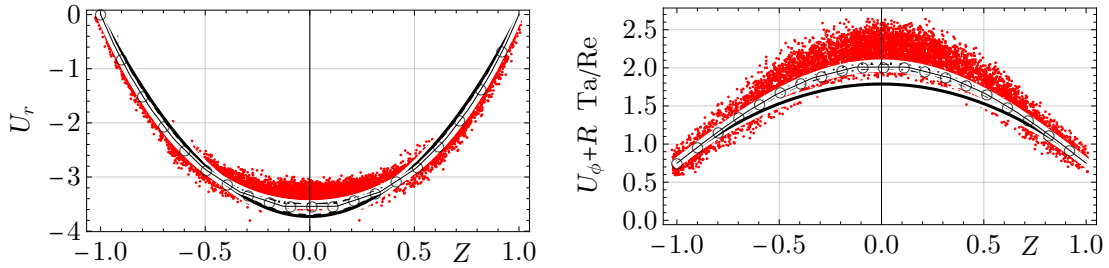

(a) Re = 109, Re* = 270, Ta = 204, Ta* = 82, $R = 0.40$, $\sigma = 0.002$, $\alpha_{a1} = 21.3°$.

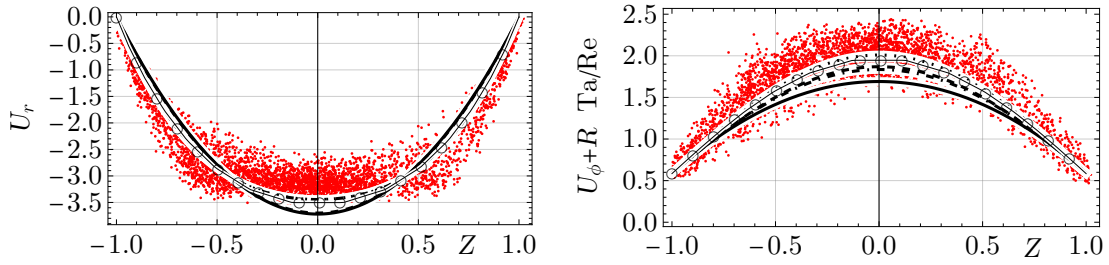

(b) Re = 141, Re* = 351, Ta = 206, Ta* = 83, $R = 0.40$, $\sigma = 0.002$, $\alpha_{a1} = 21.3°$.

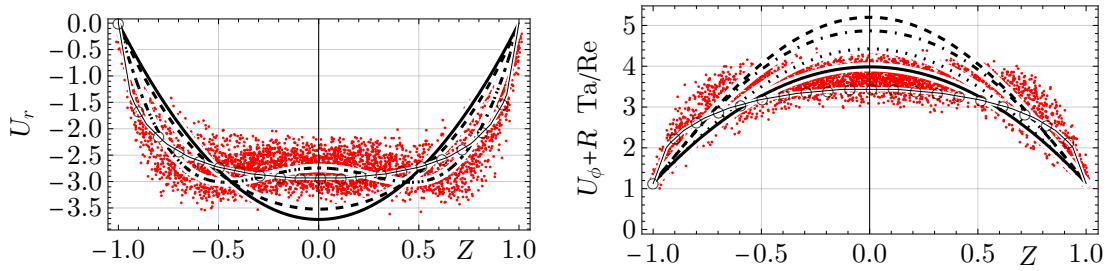

(c) Re = 238, Re* = 590, Ta = 670, Ta* = 270, $R = 0.40$, $\sigma = 0.002$, $\alpha_{a1} = 21.3°$.

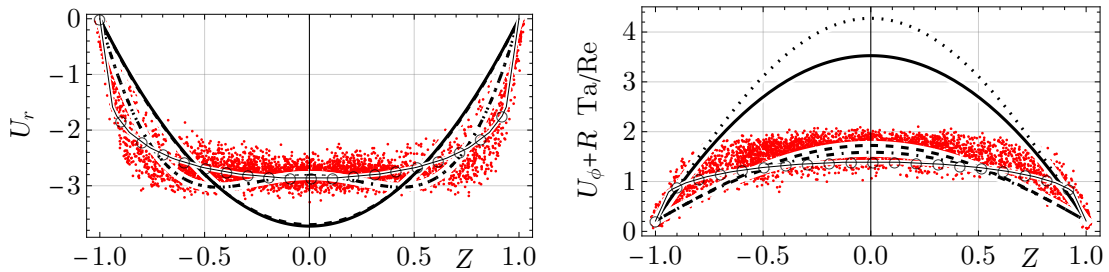

(d) Re = 470, Re* = 1167, Ta = 244, Ta* = 98, $R = 0.40$, $\sigma = 0.002$, $\alpha_{a1} = 21.3°$.

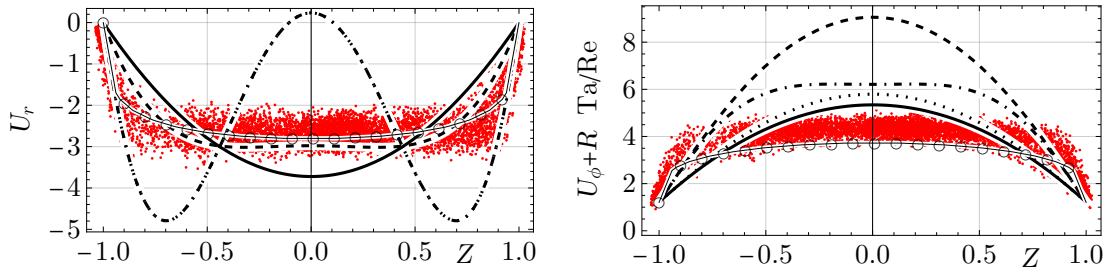

(e) Re = 456, Re* = 1132, Ta = 1374, Ta* = 553, $R = 0.40$, $\sigma = 0.002$, $\alpha_{a1} = 21.3°$.

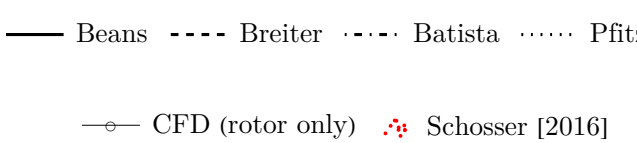

Figure 3.30: Comparison between measured and modelled velocity profiles. Circumferential velocity is given in a stationary reference frame, where R Ta/Re is the nondimensional disk velocity.

3.3.2 Numerical validation of laminar analytical models

To check the validity of the models over a larger parameter space, this section compares analytical models from table 3.4 to the simplified numerical model of rotor flow from section 3.1.1. To keep it simple, the gap aspect ratio and the nondimensional outlet radius are kept fixed throughout the study at $\sigma = 0.001$ and $R_2 = 0.5$. Furthermore, the inlet angle α_{a1} is fixed to the asymptotic inlet angle, determined at each point in the Re-Ta-plane from the solution by Breiter and Pohlhausen [1962]. The disk outer and inner radius, disk spacing, inlet temperature and outlet pressure are unchanged from table 3.1 in the CFD simulation. The medium is still compressible air. Turbulence modelling is on for Reynolds numbers greater than 100. Reynolds numbers and Taylor numbers are varied between approximately 10 to 4000 and 10 to 10000 respectively, on a regular grid with approximately 200 points in total in the logarithmic Re-Ta-plane. For the particular rotor geometry used in the CFD study, compressibility effects from inlet Mach numbers bigger than 0.3 are expected only in the far upper right region of the plot, approximately for both Reynolds numbers bigger than 300 and Taylor numbers bigger than 3000.

Figure 3.31 compares the incompressible formulation of rotor efficiency η_{ri} (see equation 2.24) from the analytical models with the compressible formulation η_{rc} (see equation 2.26) from CFD results. Nondimensional power output per gap $\dot{W}_g$ from equation 2.32 across the models is displayed in figure 3.32.

Additionally, the stability boundary by Klingl et al. [2022] is shown, but keep in mind that the stability boundary uses the local formulation of Reynolds number and Taylor number. Converting the stability boundary to the global system would move it towards the upper left of the chart, by multiplying Reynolds number and dividing Taylor number with the nondimensional radial coordinate R. The figures show, that the analytical models are still useable past the theoretical stability boundary. Efficiency predictions from the analytical models start to deviate in the region where Reynolds numbers are greater than 100 and Taylor numbers are greater than 1000. The analytical nondimensional power output is accurate approximately up to Reynolds numbers of 300. For the highest efficiency, the parabolic model by Beans [1961] deviates to a small degree from the other models and the CFD results.

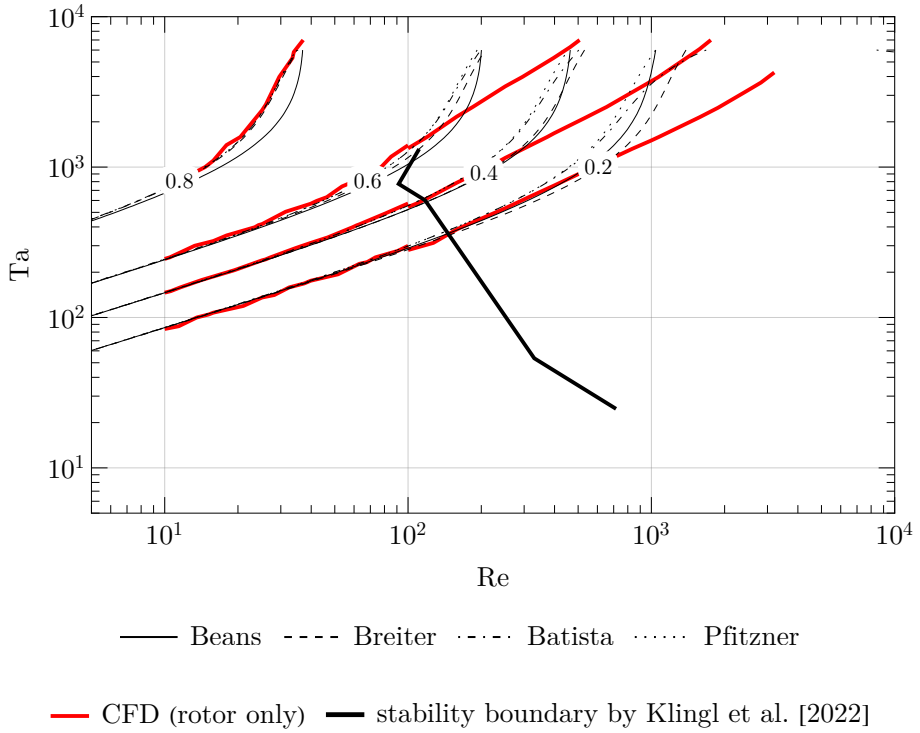

Figure 3.31: Lines of constant rotor efficiency for comparison. The CFD results use the compressible formulation η_{rc}, the analytical models use the incompressible formulation η_{ri}. The theoretical stability Boundary by Klingl et al. [2022] is shown.

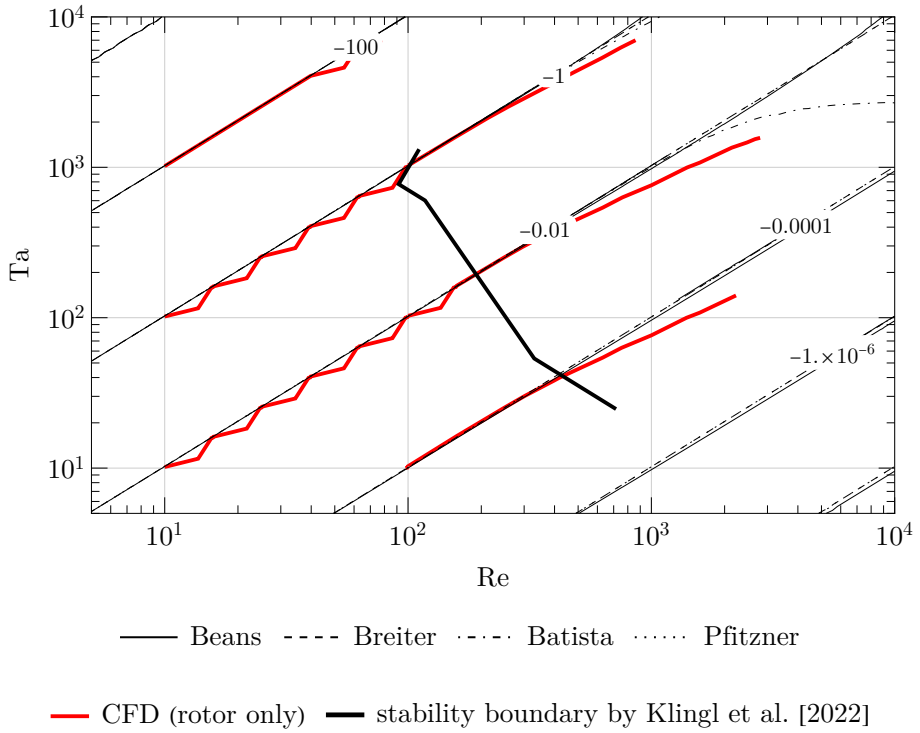

Figure 3.32: Lines of constant nondimensional power output $\dot{W}$ from simplified CFD and analytical models. The theoretical stability Boundary by Klingl et al. [2022] is shown.

Chapter 4

Experimental study of Tesla turbine performance

This chapter provides parameter studies from a new application oriented test facility, featuring an air-driven Tesla turbine with a maximum measured power output of more than 5 kW. Results are given in terms of power output and efficiency, depending on mass flow and rotational speed. Turbine losses are analysed through measurements and CFD analysis.

4.1 Test facility description and specifications

The new Tesla turbine test facility consists of a supply system for compressed air and a turbine test bench. The Tesla turbine itself is designed to allow for easy exchange of rotor and stator components. Turbine power is dissipated by a water-cooled eddy current brake. For measurement of some types of turbine losses, the eddy current brake can be replaced with a motor. Measurement equipment and data acquisition hardware is set up to document performance parameters, pressures and temperatures. Figure 4.1 shows an overview of the test facility and figure 4.2 a pipe layout schematic. The heater wasn't in use for all test runs reported here. The following sections give a detailed description of the turbine itself, specifications all remaining test facility equipment can be found in appendix A.

4.1.1 Turbine housing

The machined steel turbine housing has a diameter of 660 mm and is mounted on a 760 kg cast iron test table. The lids are circular and can be disassembled using a manually operated crane. They have removable caps for introducing cables and tubes from the measuring equipment into the housing. Three 36 mm diameter windows give some visual access to the rotor edge. The rotor and the nozzle segments are mounted between one of the lids and a mounting plate inside the housing. Figures 4.3, 4.4, 4.5 and 4.6 show photos and schematics of the setup. The housing acts as a plenum chamber and is supplied with air by two pipes with a diameter of approximately 80 mm. The inlet pipes are large enough so that the kinetic energy of the fluid in the pipes is negligible, even for the highest encountered flow rates. Incoming air flows around the mounting plate and enters the nozzles radially. The turbine outlet is connected to a short section of pipe with an attached silencer, consisting of porous damping materials. Near the outlet opening, there is an adjustable labyrinth seal (see also figure 4.13) that is set with the help of a feeler

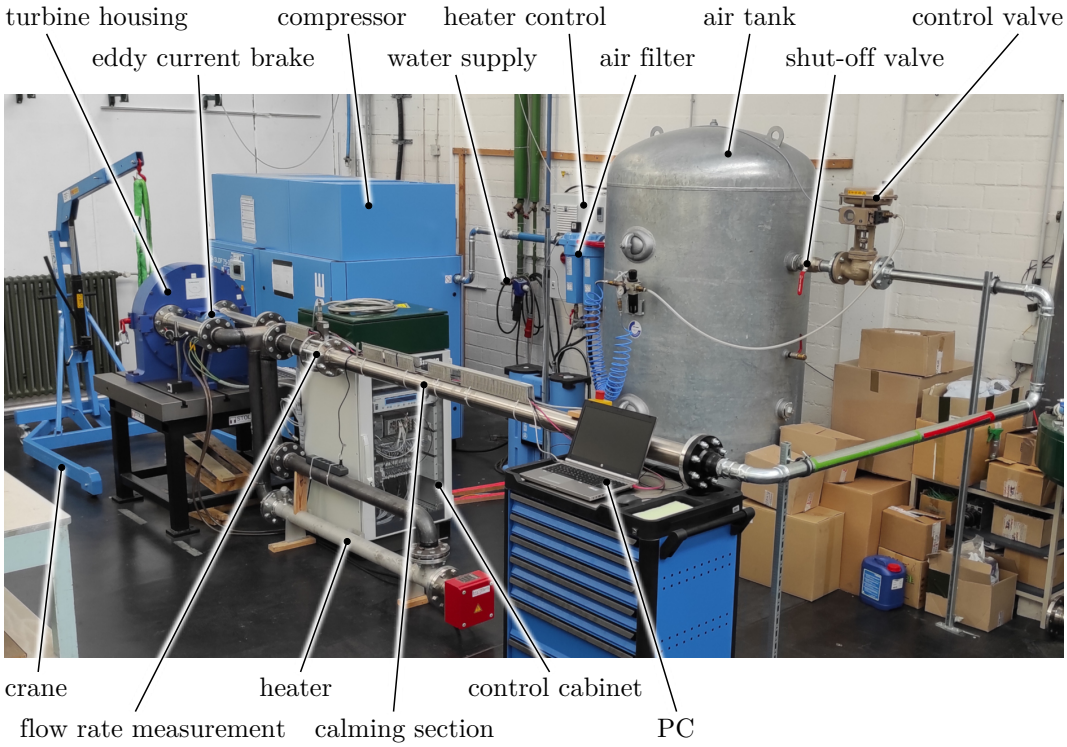

Figure 4.1: Test facility overview.

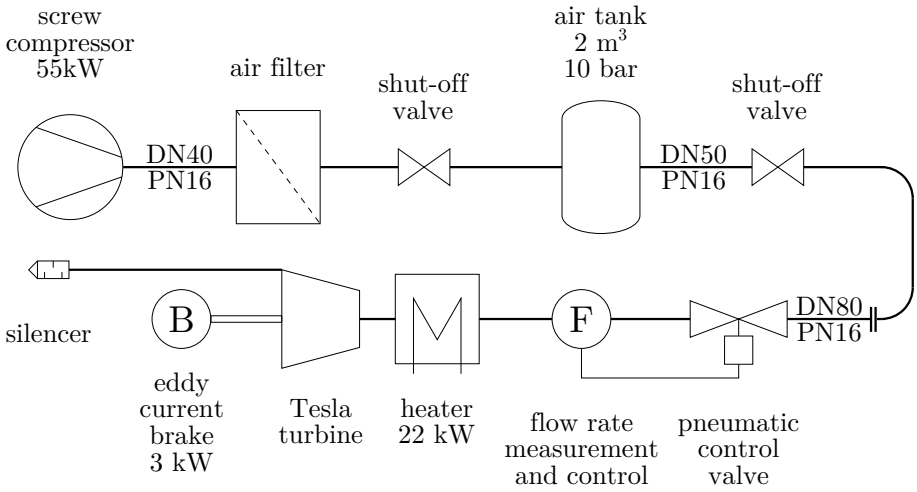

Figure 4.2: Pipe layout of the test facility.

gauge to a residual gap of approximately 0.2 mm between the first rotating disk and the housing. On the other side, towards the eddy current brake, the turbine shaft passes through the housing. Air leakage on this side is mostly sealed off by the contactless seals of the bearings.

4.1.2 Turbine stator

The turbine stator consists of four exchangeable aluminium nozzle segments that form up to four nozzles of varying geometry. Some of the nozzle segments are fitted with pressure taps that can be connected to measuring tubes. Figures 4.7 and 4.8 show some nozzle

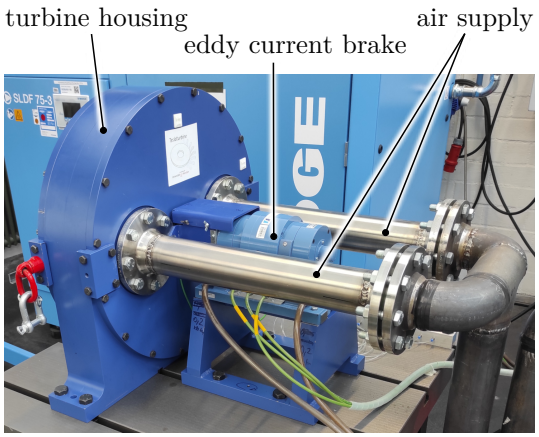

Figure 4.3: Test bench back view.

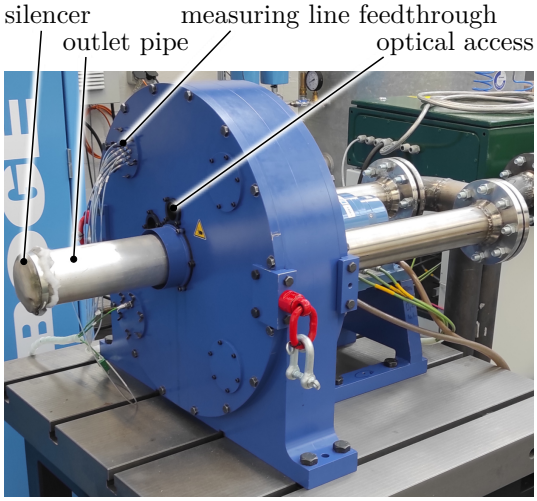

Figure 4.4: Test bench front view.

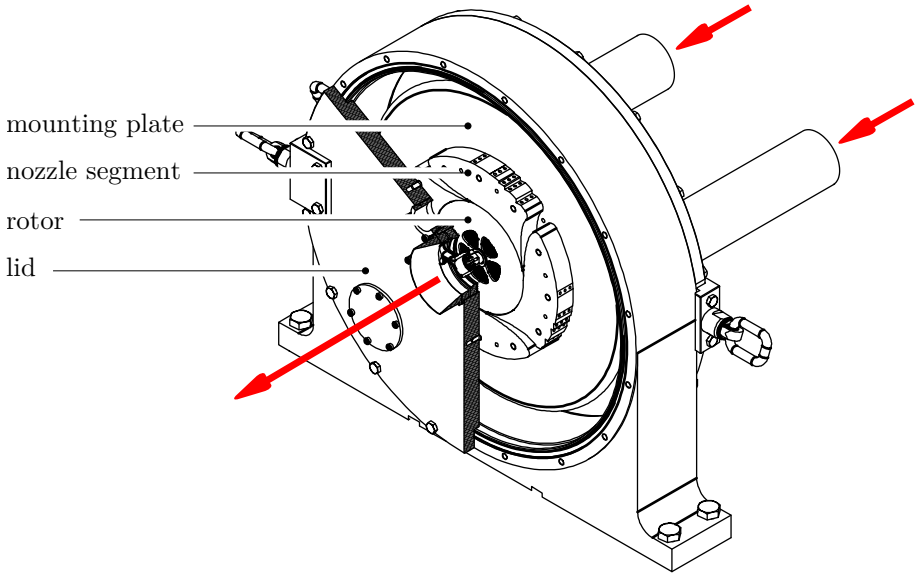

Figure 4.5: Cut open view of the turbine housing with red arrows indicating air flow direction.

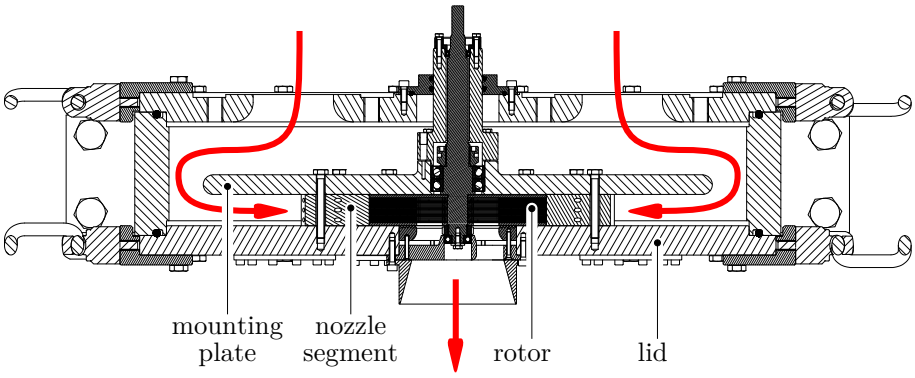

Figure 4.6: Horizontal slice of the turbine housing with red arrows indicating air flow direction.

segments. Rotor and nozzle segments mounted to the mounting plate are displayed by figure 4.18. The nozzles are centered relative to the rotor with dowel pins and fixed by screws that connect the mounting plate, the nozzle segments and the lid. The housing design allows for different heights of nozzle segments, nevertheless, all nozzle segments used in this study have the same height of 32 mm and the number of rotor disks is adjusted accordingly. The surfaces of the nozzle segments that are in contact with the mounting surfaces of the housing are precision ground for flatness and parallelity and are coated with oil prior to assembly to ensure an airtight fit.

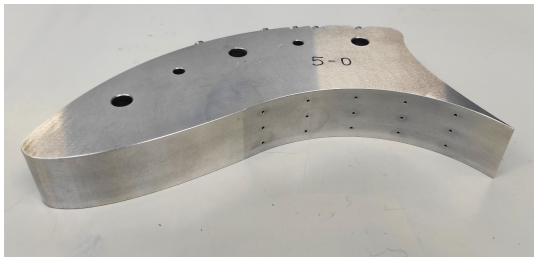

Figure 4.7: Nozzle segment front view with 1 mm pressure taps.

Figure 4.8: Some nozzle segments.

4.1.3 Turbine rotor

Figures 4.9, 4.10, 4.11 and 4.12 show impressions of the turbine rotor, which consists of a hardened steel shaft with the disk package mounted to it. The first and last disk of the package act as stabilizers and have a thickness of 3 mm. For the inner disks, three thicknesses are available: 0.8 mm, 0.5 mm and 0.2 mm. All disks have an outer diameter of 180 mm. The fluid outlet is formed by 5 central openings with an overall enclosing diameter of about 84 mm. Two types of outlet opening shapes with minor differences between them are used. The axial clearance between the rotor and the inner housing surfaces is between 0.5 mm and 2 mm, depending on the rotor configuration. The radial clearance to the stator segments is 0.5 mm, see also figure 4.10 and 4.29.

Figure 4.9: Rotor disk package mounted to the shaft.

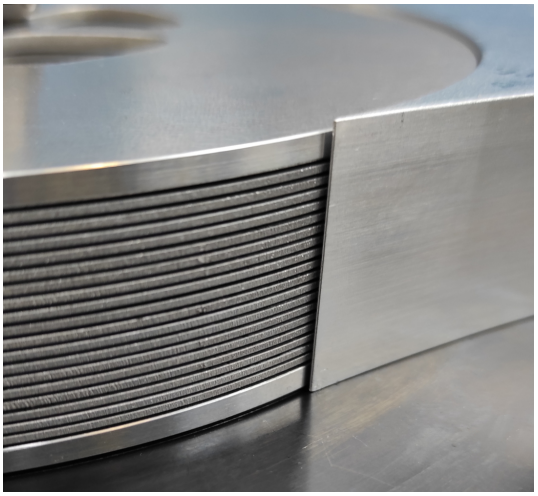

Figure 4.10: Closeup view of the clearances between the rotor, a nozzle segment and the mounting plate.

Figure 4.11: Side view of the rotor with some spacing dents visible between the disks.

Figure 4.12: Some rotor disks.

The material of the thick outer disks is aluminium (EN AW-5754), the thin inner disks consist of either aluminium (EN AW-5754 or EN AW-6082) or steel (1.4016). With the help of finite element strength analysis through Autodesk inventor [Autodesk, 2022], the maximum permissible rotational speed was decided to be $20\,000\,\mathrm{min}^{-1}$ for the aluminium disks and $18\,000\,\mathrm{min}^{-1}$ for the steel disks. The disks are mounted to the shaft with shims in between them to set the disk spacing and held in place with a single shaft nut. The shims in the centre are however not enough to keep a constant disk spacing, since thin sheet metal disks are never perfectly flat. Therefore, a specialized tool is used to imprint small dents with the exact height of the desired disk spacing into the disks. Each disk has 10 dents with a diameter of about 4 mm each, distributed equally along a diameter of 160 mm. The dents are slightly shifted for every other disks as to not overlap them. The spacing dents are visible in figures 4.11 and 4.12. Other than regulating the disk spacing, the dents also stabilize the rotor. Trial runs without dented disks were stopped prematurely due to excessive vibration.

As for the bearings, there are two lightly preloaded FAG angular contact spindle bearings in place, with a rated maximum rotational speed of $28\,000\,\mathrm{min}^{-1}$. These are denoted with “main bearing” in figure 4.13. In addition to that, there are two smaller, axially floating deep groove ball bearings to support the shaft on either end against vibration, denoted with “outlet side bearing” and “drive side bearing” in figure 4.13. All bearings are equipped with contactless seals and grease lubrication.

4.1.4 Data postprocessing

Text files with all gathered measurement data are processed using Wolfram Mathematica [Wolfram Research, Inc., 2022]. The custom postprocessing tool iterates through the data and looks for intervals in time, where mass flow and rotational speed vary less than $\pm 2\,\mathrm{g\,s}^{-1}$ and $\pm 30\,\mathrm{min}^{-1}$ respectively for at least one minute. All other data is discarded. Sectors with a turbine output power of 200 W or less are discarded as well, because the relative measurement error grows very large in the region of small power output. All measured values are then averaged over the one minute or longer intervals and further parameters are calculated from the averaged data, for example efficiency and pressure ratio. Within the calculations, the fluid properties shown in table 4.1 are assumed to be constant. Air

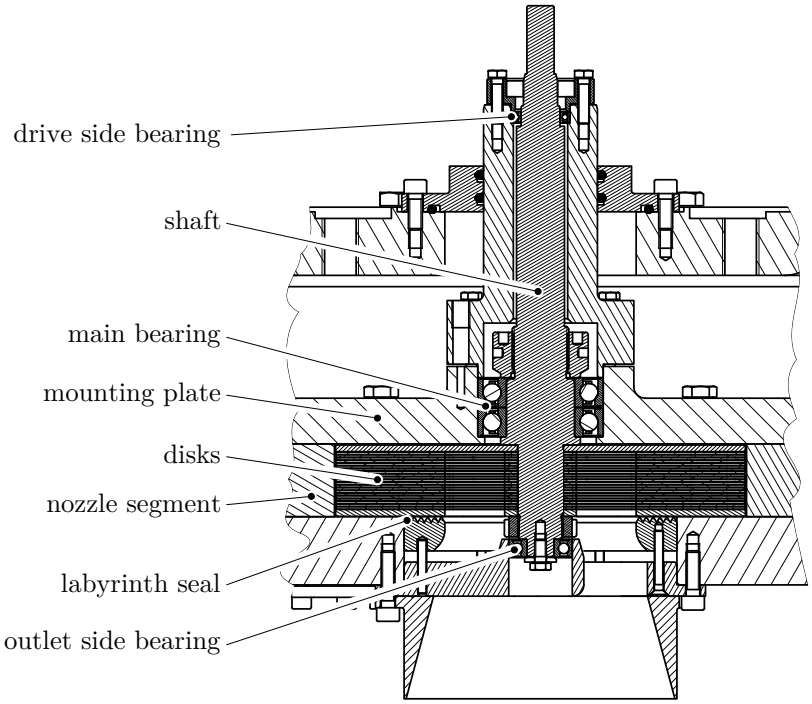

Figure 4.13: Detail cut view of assembled rotor and bearings.

densities are calculated from ideal gas law, viscosity is determined through equation 4.1, which is referred to as Sutherland formula by Schlichting and Gersten [2017].

$$\mu(\vartheta) = \mu_r \left(\frac{\vartheta}{\vartheta_r}\right)^{\frac{3}{2}} \frac{\vartheta_r + S_{air}}{\vartheta + S_{air}} \tag{4.1}$$

property		value	
heat capacity ratio	κ	1.4	
isobaric heat capacity	c_p	1006.1	$\mathrm{J\,kg^{-1}\,K^{-1}}$
specific gas constant	R_{air}	287.1	$\mathrm{J\,kg^{-1}\,K^{-1}}$
Sutherland constant	S_{air}	110	K
Sutherland reference temperature	ϑ_r	291.15	K
Sutherland reference viscosity	μ_r	18.108	µPa s

Table 4.1: Constant fluid properties used for postprocessing.

The power output $\dot{w}$ of the turbine is calculated from torque $\mathcal{T}$ and rotational speed n.

$$\dot{w} = \omega\mathcal{T} = 2\pi n\mathcal{T} \tag{4.2}$$

The definition of experimental turbine efficiency is equivalent to equation 2.30, however it is calculated from measured power output rather than calculated specific power output. Additionally, turbine inlet kinetic energy is neglected.

$$\tilde{h}_c = c_p \bar{\vartheta}_0 \left(\left(\frac{\bar{p}_2}{\bar{p}_0}\right)^{(\kappa-1)/\kappa} - 1 \right) \tag{4.3}$$

$$\tilde{\eta}_c = \frac{\dot{w}}{\dot{m}\tilde{h}_c} \tag{4.4}$$

An approximate degree of reaction $\mathcal{R}$ can be calculated from a measured rotor inlet pressure p_1 as follows:

$$\tilde{h}_{rc} = c_p \bar{\vartheta}_0 \left(\left(\frac{\bar{p}_2}{\bar{p}_0} \right)^{(\kappa-1)/\kappa} - \left(\frac{\bar{p}_1}{\bar{p}_0} \right)^{(\kappa-1)/\kappa} \right) \tag{4.5}$$

$$\mathcal{R} = \frac{\tilde{h}_{rc}}{\tilde{h}_c} \tag{4.6}$$

Turbine inlet pressure $\bar{p}_0$ and temperature $\bar{\vartheta}_0$ are measured inside the plenum, directly behind the small lids, indicated with "measuring line feedthrough" in figure 4.4. Turbine outlet pressure $\bar{p}_2$ is measured inside the outlet pipe, which is also visible in figure 4.4. The rotor inlet pressure is measured at several circumferential positions at the rotor inlet using the pressure taps in the nozzle segments that are visible in figure 4.9. Throughout this chapter, the term rotor inlet pressure, denoted with the symbol $\bar{p}_1$, refers to a weighted average between all the inlet pressure measurements.

For comparison with other turbines, mass flow is also displayed in nondimensional form, as suggested by Whitfield and Baines [1990]. $\dot{M}_c$ is the ratio between measured turbine mass flow and the mass flow through and opening of radius r_1 at the speed of sound and turbine inlet conditions.

$$\dot{M}_c = \frac{\dot{m}\sqrt{R_{air}\bar{\vartheta}_0/\kappa}}{\bar{p}_0 \pi r_1^2} \tag{4.7}$$

4.1.5 Measurement uncertainty

Table 4.2 summarizes maximum measurement errors for directly measured quantities. The errors account for the accuracy of the sensors themselves and, where applicable, the accuracy of the sensor output voltage measurement. Additional sources of uncertainty during operation of the test facility are variations in the clearances between rotor and housing due to slightly varying rotor heights and adjustment of the labyrinth seal, as well as possibly inconsistent bearing lubrication conditions.

quantity		maximum error	
pressure	Δp	± 0.056	bar
temperature	$\Delta\vartheta$	± 2	°C
torque			
turbine operation	$\Delta\mathcal{T}$	± 15	mN m
loss measurement	$\Delta\mathcal{T}$	± 5	mN m
rotational speed			
turbine operation	Δn	± 250	min^{-1}
loss measurement	Δn	± 100	min^{-1}
mass flow	$\Delta\dot{m}$	± 2.3	$\mathrm{g\,s}^{-1}$

Table 4.2: Summarized maximum measurement errors for directly measured quantities.

The error of calculated quantities can be determined by propagation of maximum uncertainty and depends on the particular operating conditions as well as the sensor measurement errors. For example, the maximum measurement errors of output power and efficiency can be calculated as:

$$\Delta\dot{w} = \left| \frac{\partial \dot{w}}{\partial \mathcal{T}} \right| \Delta\mathcal{T} + \left| \frac{\partial \dot{w}}{\partial n} \right| \Delta n \tag{4.8}$$

$$\Delta\tilde{\eta}_c = \left|\frac{\partial\tilde{\eta}_c}{\partial\mathcal{T}}\right|\Delta\mathcal{T} + \left|\frac{\partial\tilde{\eta}_c}{\partial n}\right|\Delta n + \left|\frac{\partial\tilde{\eta}_c}{\partial\vartheta_0}\right|\Delta\vartheta_0 + \left|\frac{\partial\tilde{\eta}_c}{\partial\dot{m}}\right|\Delta\dot{m} + \left|\frac{\partial\tilde{\eta}_c}{\partial p_{0r}}\right|\Delta p_{0r} + \left|\frac{\partial\tilde{\eta}_c}{\partial p_{2r}}\right|\Delta p_{2r} + \left|\frac{\partial\tilde{\eta}_c}{\partial p_\infty}\right|\Delta p_\infty \quad (4.9)$$

To improve accuracy of the calculated turbine pressure ratio, which is one of the input parameters for turbine efficiency, the measured absolute pressures are divided into ambient and relative pressure. Ambient pressure is measured at startup of the facility for each test run, and taken from the pressure sensor for $\bar{p}_2$, which has the best agreement with a DPI 740 handheld ambient pressure measuring device. The measurement error for the ambient pressure is assumed to be the maximum uncertainty of the sensor, so $\Delta p_\infty = \pm 0.056\,\text{bar}$. The error of the relative pressure measurement is determined by a calibration process to be $\Delta p_{0r} = \Delta p_{2r} = \pm 0.02\,\text{bar}$. For details on the calibration, see appendix A.4. With this method, the uncertainty of a single pressure measurement grows larger compared to using the measured absolute pressures directly, since the errors of ambient pressure measurement and relative pressure measurement add up. The uncertainty of calculated pressure ratios however decreases, since the ambient pressure uncertainty has a much smaller impact on the pressure ratio than the relative pressure uncertainty.

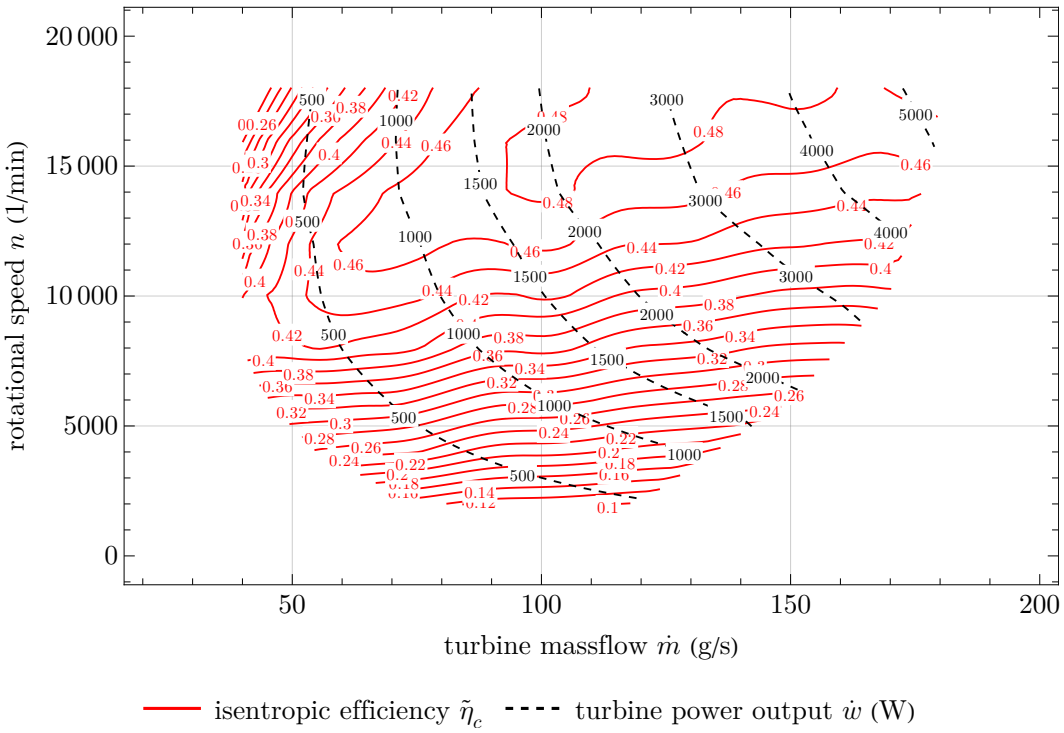

Figure 4.14: Turbine performance map at 5-8-4 nozzle configuration and a rotor with 64 0.2 mm thick disks and two 3 mm end disks with a spacing of 0.2 mm between the disks.

4.2 Experimental results

The performance of the turbine design with the highest measured power output of 5376 W is shown in figure 4.14, along with a visualization of maximum measurement uncertainty in figure 4.15. The underlying data points are spaced evenly at approximately $5\,\text{g}\,\text{s}^{-1}$ and $2000\,\text{min}^{-1}$ in the $\dot{m}$-n-plane. Operating conditions at every single data point were

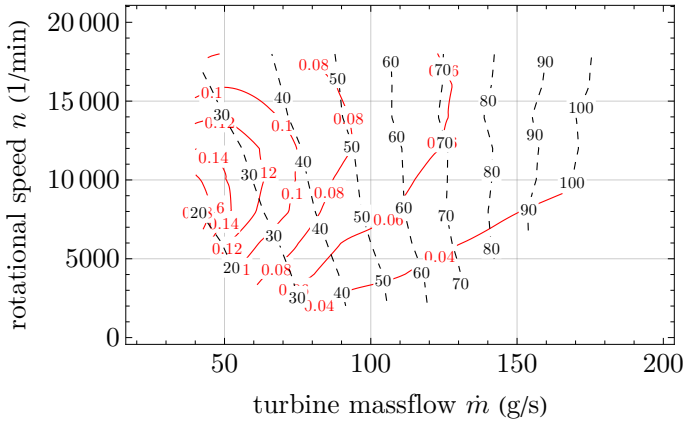

Figure 4.15: Maximum absolute measurement error of efficiency and turbine power output, corresponding to figure 4.14.

quantity		value	max. error	
rotational speed	n	18000	±250	min^{-1}
mass flow	$\dot{m}$	179	±2.3	$\mathrm{g\,s}^{-1}$
efficiency	$\tilde{\eta}_c$	0.486	±0.04	-
power output	$\dot{w}$	5376	±103	W
turbine inlet pressure	$\bar{p}_0$	2.77	±0.056	bara
turbine inlet temperature	$\bar{\vartheta}_0$	28.2	±2	°C
average rotor inlet pressure	$\bar{p}_1$	1.762	±0.056	bara
turbine outlet pressure	$\bar{p}_2$	1.262	±0.056	bara
turbine outlet temperature	$\bar{\vartheta}_2$	-0.97	±2	°C
pressure ratio	Π	2.22	±0.1	-
degree of reaction	$\mathcal{R}$	0.391	±0.03	-
Reynolds number	Re	132		-
Taylor number	Ta	1896		-
disk gap aspect ratio	σ	0.00111		
number of disk gaps	n_g	65		

Table 4.3: Performance data at the operating conditions with highest turbine power output.

kept constant for at least 5 min. See appendix A.8 for a detailed description of the test procedure. Table 4.3 summarizes some performance parameters for the operating point with the highest recorded power output of $\dot{w}$ =5376 W. The highest recorded efficiency of 0.488 % is encountered at different operating conditions with a lower power output of 2890 W. All other measured performance maps are listed in appendix B.

Figures 4.16 and 4.17 can be compared to turbine performance maps that are commonly found in turbomachine literature, for example by Whitfield and Baines [1990]. They are based on the same data as displayed in figure 4.14 and show the nondimensional mass flow and isentropic turbine efficiency as functions of pressure ratio and rotational speed.

The following sections give detailed analysis of the gathered performance data with respect to some rotor and stator geometry parameters and of turbine loss measurements.

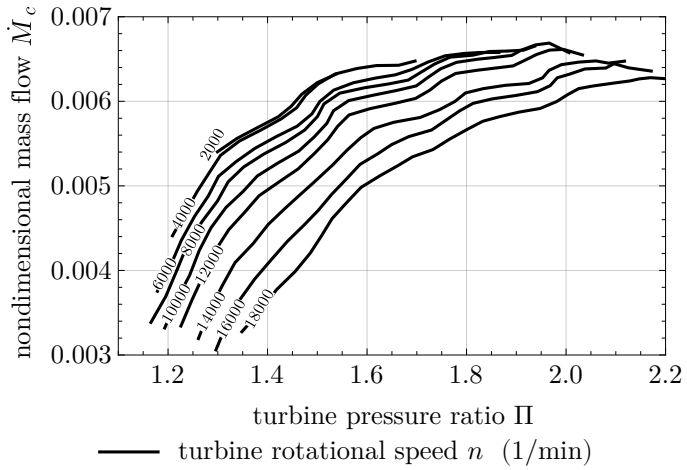

Figure 4.16: Nondimensional turbine mass flow (see equation 4.7) as function of turbine pressure ratio and rotational speed, based on the same data as displayed in figure 4.14.

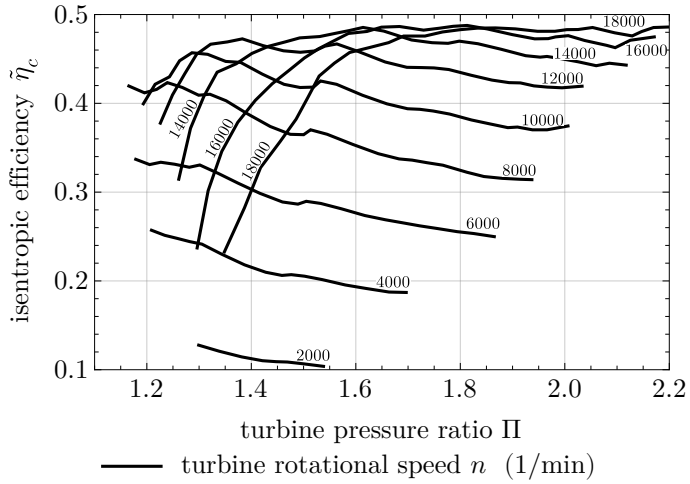

Figure 4.17: Isentropic turbine efficiency as function of turbine pressure ratio and rotational speed, based on the same data as displayed in figure 4.14.

4.2.1 Stator design study

The first thing to be analysed is the stator geometry. There are four different nozzle shapes available, each varying in geometric nozzle outlet angle, opening width and overall shape. Figure 4.18 gives an overview over all used nozzle configurations. The naming scheme is based on two geometry parameters and the number of nozzles, according to φ_1-φ_2-n_n, where φ_1 is the angle between the nozzle wall and a tangent at the rotor inlet, φ_2 is the opening angle and n_n is the number of nozzles. See figure 4.19 for clarification. As an example, 5-8-4 means $\varphi_1 = 5°$, $\varphi_2 = 8°$ and $n_n = 4$. The nozzle shape is designed to guide the fluid as smoothly as possible from the radial direction into the rotor entry direction, while simultaneously reducing cross-sectional area. A systematic aerodynamic optimization of nozzle shape has not yet been performed. Note however that for each φ_1-variant, the overall nozzle shape is different (see figure 4.18). Throughout the nozzle study, the rotor consists of 24 aluminium disks with a thickness of 0.8 mm and two 3 mm thick end disks with a spacing of 0.2 mm between the disks.

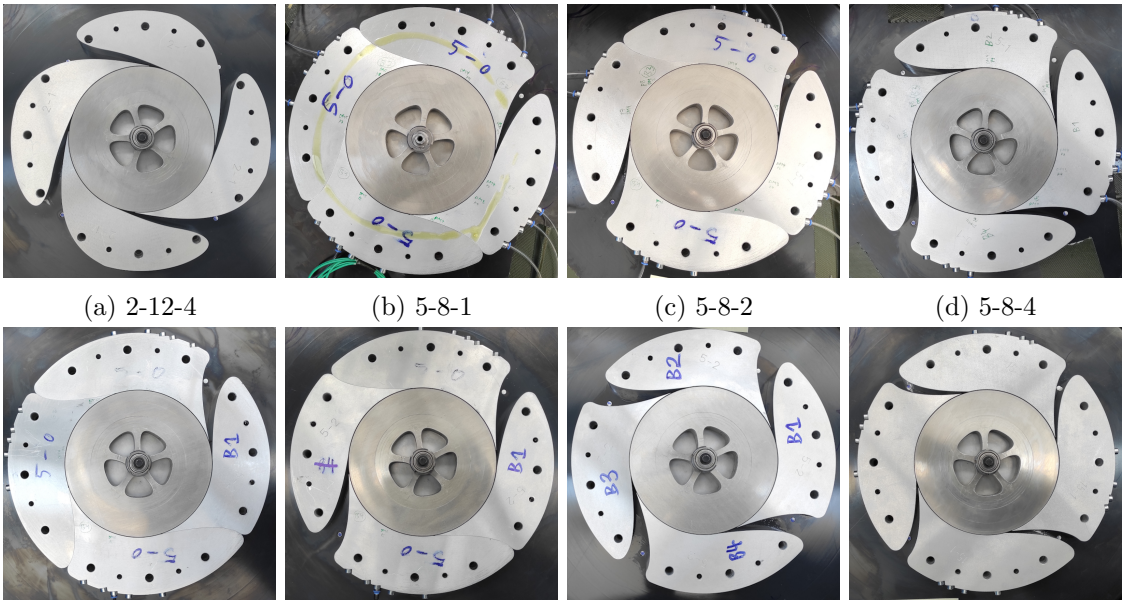

(a) 2-12-4 (b) 5-8-1 (c) 5-8-2 (d) 5-8-4

(e) 5-12-1 (f) 5-12-2 (g) 5-12-4 (h) 15-5-4

Figure 4.18: All examined nozzle configurations.

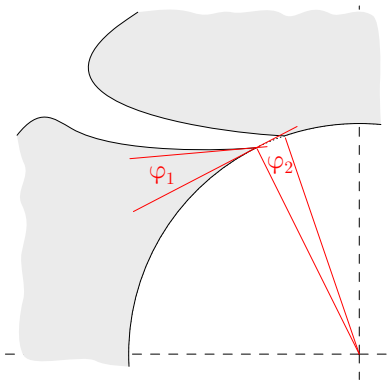

Figure 4.19: Nozzle Parameters.

4.2.1.1 Nozzle shape

Figure 4.20 compares the isentropic efficiency produced by all four nozzle shapes, each with a nozzle count of four. The curves show efficiency as a function of measured turbine power output divided by the number of disk gaps. Rotational speed varies within the figure, since only the maximum achieved efficiency across the whole range of rotational speeds is shown. The 5-8-4 design stands out with the best performance across the whole range of power output with a maximum efficiency of about 0.32.

4.2.1.2 Nozzle number

The 5-8 and 5-12 geometries are examined with a nozzle count of one, two and four. Figure 4.21 shows the comparison. Again, maximum achieved efficiency is shown as a function of power output per disk gap, across the examined range of rotational speeds. For both designs, a turbine with a single nozzle performs significantly worse than with two and four nozzles. Between two and four nozzles, the four nozzle setup performs slightly better

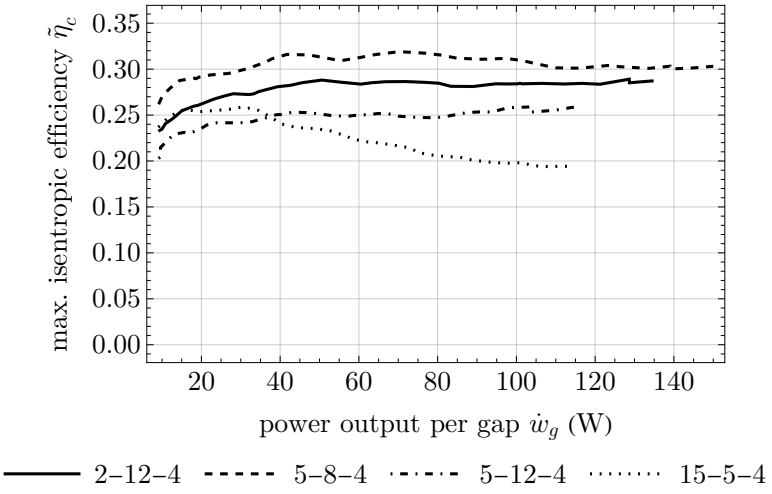

Figure 4.20: Influence of nozzle geometry on isentropic efficiency as a function of power output per disk gap. Only data for 4 nozzles is shown. The curves show the maximum achieved efficiency across all examined rational speeds for each nozzle setup.

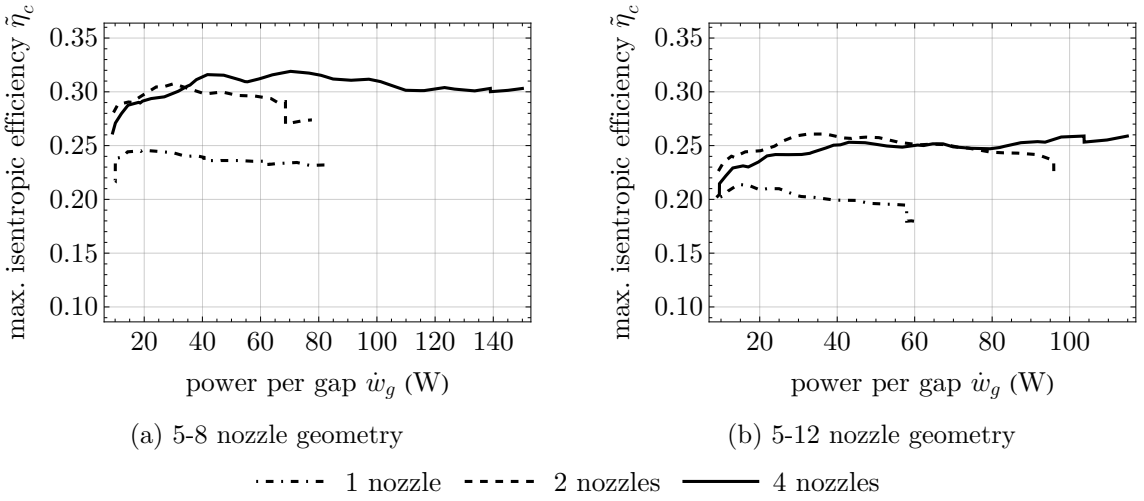

(a) 5-8 nozzle geometry

(b) 5-12 nozzle geometry

Figure 4.21: Influence of nozzle count on isentropic efficiency as a function of power output per disk gap. The curves indicate the maximum achieved efficiency across all examined rotational speeds for each nozzle setup.

most of the time, while also allowing for a higher air throughput and therefore a higher maximum power output.

4.2.2 Rotor design study

A further test campaign is aimed at optimizing the rotor design. It will be seen, that the rotor setup which was used in the nozzle study is not ideal for turbine performance. The rotor parameters to be analysed in this section are disk thickness, disk spacing, disk surface roughness and disk edge geometry. In total, nine thickness and spacing combinations are analysed, as shown in figure 4.22. Additionally, disks with bevelled outer edges and roughened surface finish are tested for three different disk spacings each. The disk material is aluminium for disk thicknesses of 0.8 mm and 0.5 mm and steel for 0.2 mm thickness. All rotor test runs are conducted using the 5-8-4 nozzle configuration which proved to

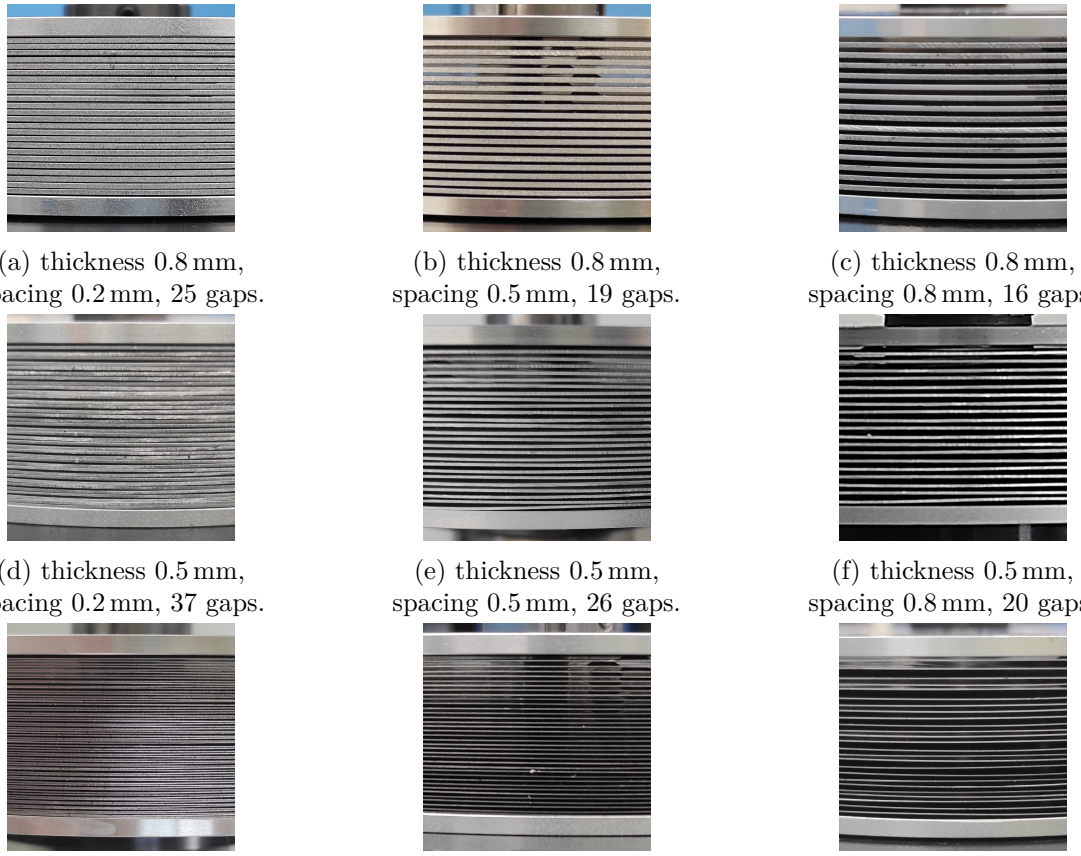

(a) thickness 0.8 mm, spacing 0.2 mm, 25 gaps.

(b) thickness 0.8 mm, spacing 0.5 mm, 19 gaps.

(c) thickness 0.8 mm, spacing 0.8 mm, 16 gaps.

(d) thickness 0.5 mm, spacing 0.2 mm, 37 gaps.

(e) thickness 0.5 mm, spacing 0.5 mm, 26 gaps.

(f) thickness 0.5 mm, spacing 0.8 mm, 20 gaps.

(g) thickness 0.2 mm, spacing 0.2 mm, 65 gaps.

(h) thickness 0.2 mm, spacing 0.5 mm, 36 gaps.

(i) thickness 0.2 mm, spacing 0.8 mm, 26 gaps.

Figure 4.22: All examined disk spacing and thickness configurations.

yield the highest turbine efficiency so far.

4.2.2.1 Disk thickness and spacing

Figure 4.23 compares turbine efficiency and power output per disk gap for all disk thickness and spacing configurations. Smaller disk thickness has a universally positive impact on efficiency. The optimum for disk spacing appears to shift towards a larger value for larger disk thickness. This suggests, that the ratio of disk spacing to disk thickness can significantly impact turbine performance. The maximum power output per disk gap increases with growing disk spacing. This is mainly because the rotor height is kept constant and rotors with larger disk spacing have fewer disk gaps, while the maximum analysed mass flow is approximately equal for all analysed rotor designs, as it is mainly limited by the air supply.

4.2.2.2 Disk edge geometry

To further assess the negative impact of disk thickness, some of the 0.8 mm aluminium disks are modified with a 15° bevel at the outer disk circumference, see figure 4.24. For easier manufacturing, the bevel is only applied to one side of the disk. Figure 4.25 gives a comparison between the modified and unmodified disks for all three disk spacing values, using the 5-8-4 nozzle configuration. The edge modification considerably improves effi-

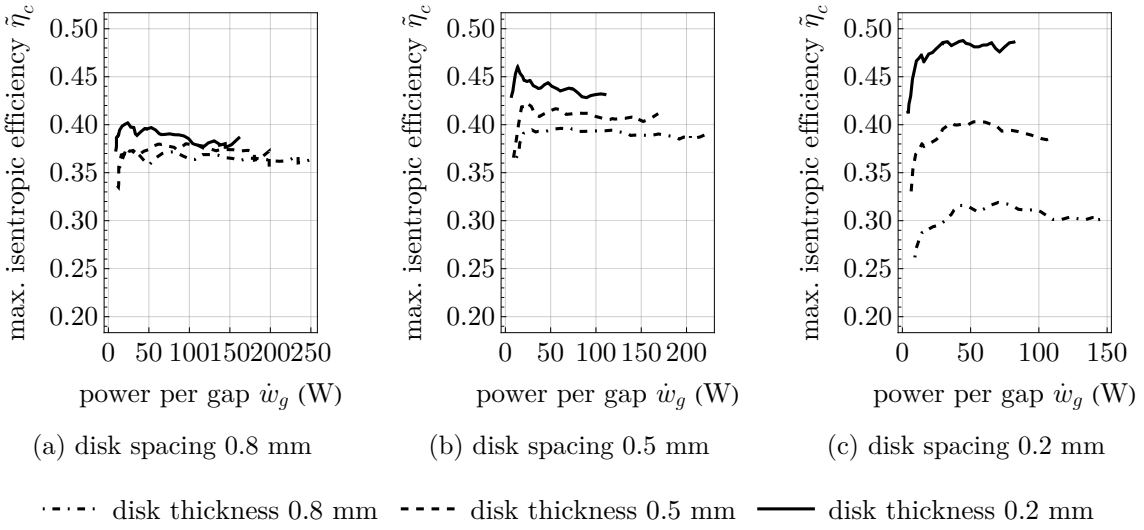

Figure 4.23: Comparison of maximum achieved efficiency for different disk thickness and spacing configurations in dependence of power output per disk gap, across all examined rotational speeds.

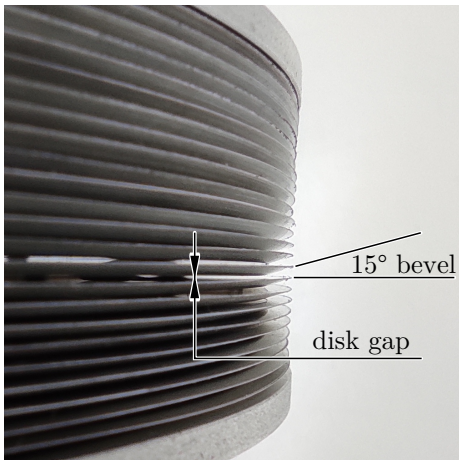

Figure 4.24: Detail view of the rotor inlet with bevelled disk edges.

ciency for the smallest disk spacing and has little to no impact for the other two spacing values.

4.2.2.3 Disk surface finish

For a further test run, the 0.5 mm aluminium disks are roughened on both sides by hand, using a lathe and coarse sandpaper. This results in a rough surface with small concentric grooves. Since the process is done by hand, there is some variation in the resulting surface roughness. A measurement of some disks with a Mahr MarSurf PS 10 roughness measuring device with a PHT 100 probe gives roughness values varying between R_z =10 µm and R_z =30 µm, while the untreated disks range between R_z =3 µm and R_z =10 µm.

Figure 4.26 gives the comparison between roughened and smooth disks. While there appears to be a impact on efficiency, the difference falls within the measurement uncertainty. For the largest power output per disk gap, the efficiency difference between smooth and rough disks is smaller than 0.02, compared to a maximum absolute uncertainty of 0.03

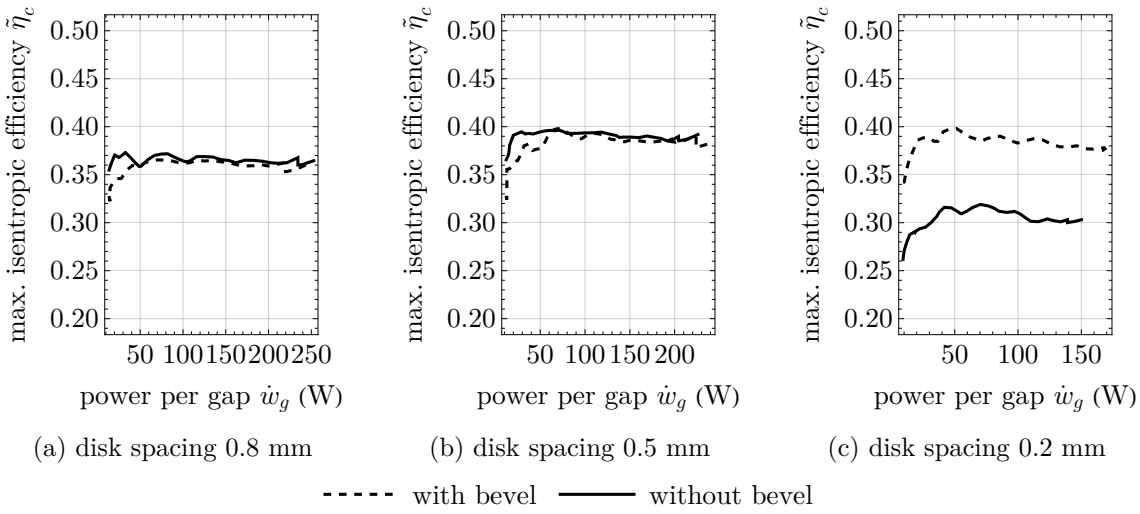

Figure 4.25: Comparison of maximum achieved efficiency for different disk outer edge geometry in dependence of power output per disk gap, across all examined rotational speeds.

to 0.04.

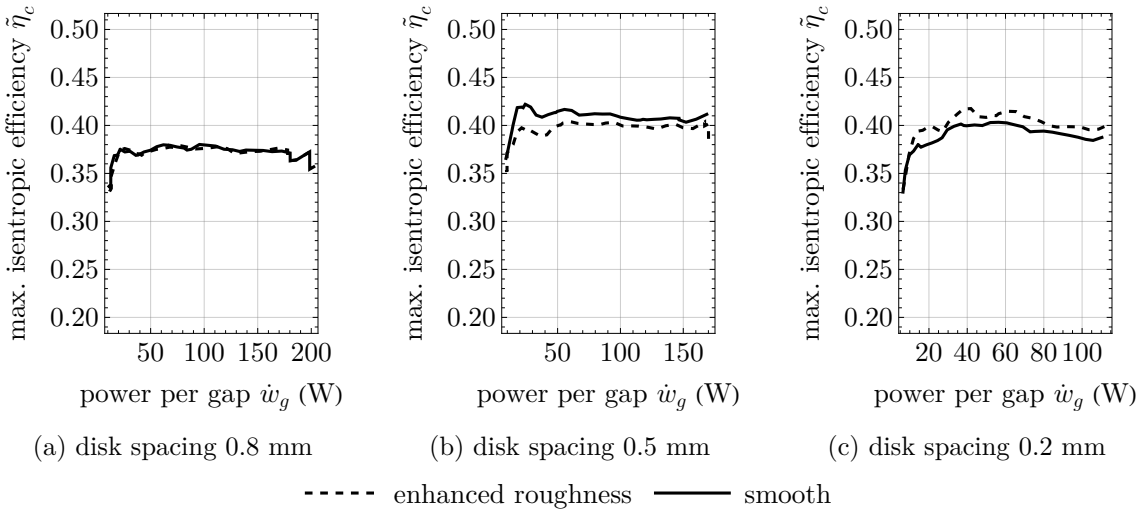

Figure 4.26: Comparison of maximum achieved efficiency for different disk surface roughness in dependence of power output per disk gap, across all examined rotational speeds.

4.2.3 Rotor inlet pressure

Rotor inlet pressure is measured at several circumferential positions, using the pressure taps in the nozzle segments (see figure 4.7). Eight selected pressure taps are connected to sensors. All shown measurements in figure 4.27 are from pressure taps at half the stator height, at 16 mm from the top and bottom housing walls. The placement of the mass flow labels on the constant mass flow lines in figure 4.27 corresponds to the circumferential location of the respective pressure tap and the labels are connected with straight lines. The light red bars indicate the location of the nozzle exits. Additionally, the location of nozzles and pressure taps is visualized in figure 4.28 for 5-8-4 nozzle configuration. Only data for 18 000 min^{-1} is shown, since the overall shape of the pressure distributions

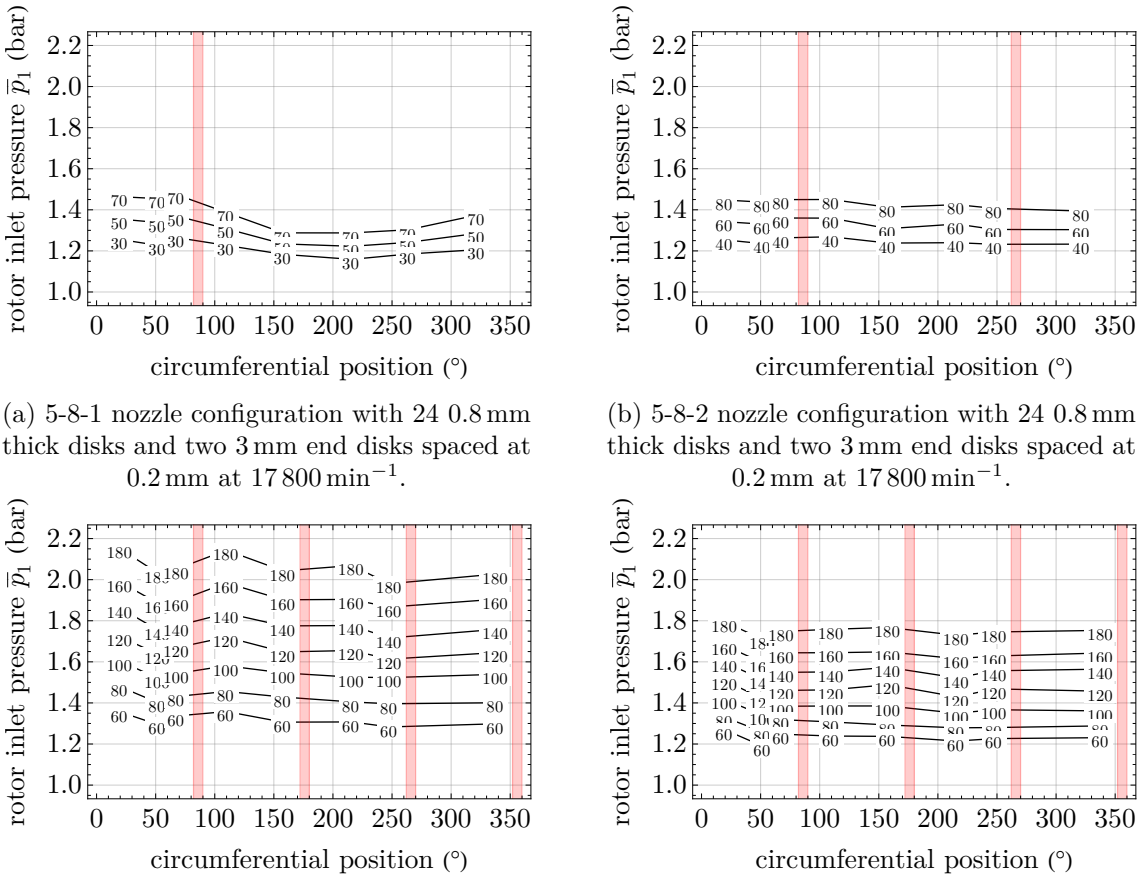

(a) 5-8-1 nozzle configuration with 24 0.8 mm thick disks and two 3 mm end disks spaced at 0.2 mm at 17 800 min^{-1}.

(b) 5-8-2 nozzle configuration with 24 0.8 mm thick disks and two 3 mm end disks spaced at 0.2 mm at 17 800 min^{-1}.

(c) 5-8-4 nozzle configuration with 24 0.8 mm thick disks and two 3 mm end disks spaced at 0.2 mm at 18 000 min^{-1}.

(d) 5-8-4 nozzle configuration with 64 0.2 mm thick disks and two 3 mm end disks spaced at 0.2 mm at 18 000 min^{-1}.

Figure 4.27: Measured rotor inlet pressure distributions with lines of constant mass flow for selected nozzle and rotor configurations. The light red bars indicate the position and width of the nozzle exits. The direction of rotation is from right to left towards decreasing circumferential position.

is largely independent of rotational speed. Data for one, two and four nozzles with 5-8 geometry from the nozzle study is shown, as well as data with 4 nozzles of 5-8 geometry with the more optimal rotor configuration of 0.2 mm thick disks, spaced at 0.2 mm. As expected, the measurements show an uneven pressure distribution for the single nozzle case. For two and four nozzles, the distribution evens out, with some remaining fluctuation between the nozzles.

4.2.4 Losses

For the loss measurements, a motor is mounted in place of the eddy current brake to drive either a solid rotor dummy or the shaft alone. Leakage mass flow is measured as well as power consumption through a torque and rotational speed transducer. Note that the leakage mass flows are very small and the mass flow meter is operated at the lower end of its measuring range, thus the maximum measuring error of $\pm 2.3\,\mathrm{g\,s^{-1}}$ has a relatively big impact on the leakage measurement. There are other uncertainties, for example bearing friction, which is dependent on the lubrication conditions that presumably

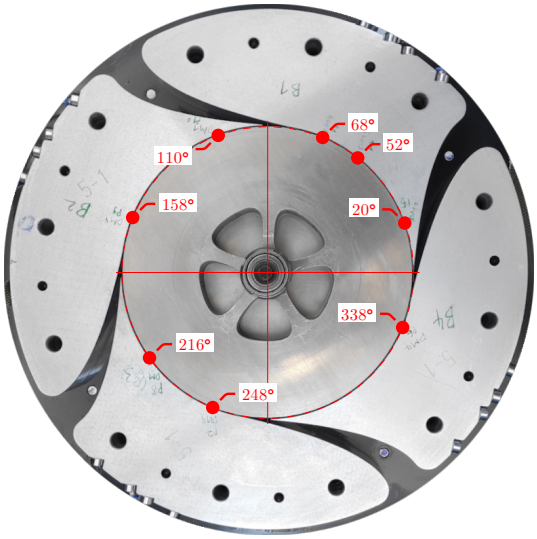

Figure 4.28: Circumferential position of the utilized rotor inlet pressure taps.

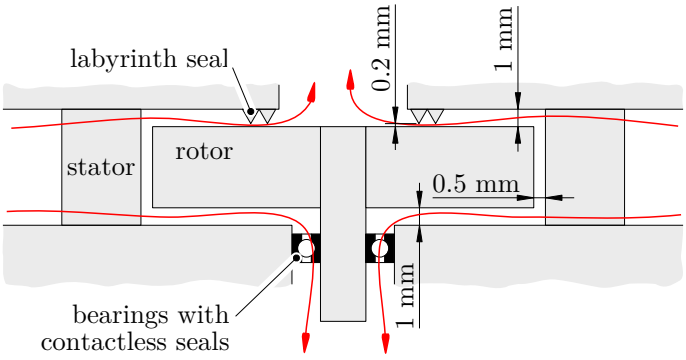

Figure 4.29: Possible paths of leakage flow around the turbine rotor in red with approximate gap widths.

change over time. Other than that, it is not exactly clear whether the flow between rotating and stationary turbine parts is the same for the solid rotor dummy and an actual rotor during turbine operation. This is mainly because during the leakage and windage loss measurements, the fluid lacks kinetic energy at the nozzle outlet due to the small leakage mass flows. Still, the loss measurements give an impression of order of magnitude of the respective losses and help direct optimization efforts towards the most impactful loss types.

4.2.4.1 Leakage

The experimental Tesla turbine employs a fairly low-cost approach to sealing, with adjustable labyrinth seal at the outlet side and no dedicated seal at the drive side, only the contactless sealing disks of the bearings. See figure 4.29 for a visualization of the possible paths of the leakage flow.

For the leakage measurement, the rotor dummy spins at rotational speeds up to $15\,000\,\mathrm{min}^{-1}$ and mass flows of up to $10\,\mathrm{g\,s}^{-1}$ in steps of $2\,\mathrm{g\,s}^{-1}$ are imposed. The leakage test runs can be matched to actual turbine operating points under the assumption that the same rotor pressure ratio Π_r, i.e. the ratio between rotor inlet and outlet pressure, leads to the same leakage conditions. Figure 4.30a displays measured leakage mass flows. They appear to be approximately proportional to rotor pressure ratio.

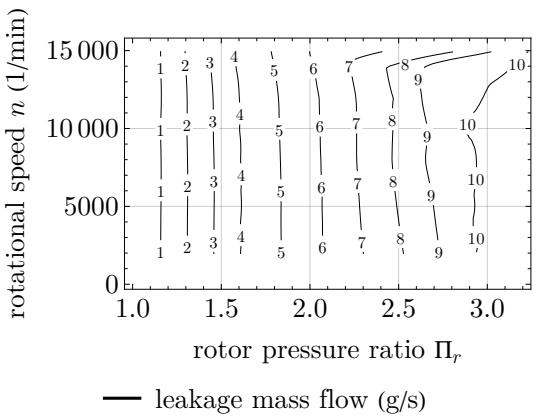

(a) Measured leakage mass flow depending on rotational speed and rotor pressure ratio.

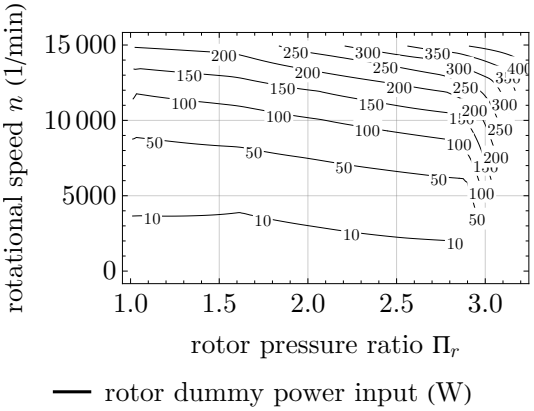

(b) Power required to spin the solid rotor dummy depending on rotational speed and rotor pressure ratio.

Figure 4.30: Rotor dummy test run results.

The highest measured rotor pressure ratio across all turbine test runs is approximately 1.7. Comparing this to figure 4.30a, the leakage mass flow during turbine operation should not exceed about $5\,\mathrm{g\,s^{-1}}$. For comparison, in the case with 65 disk gaps that was previously shown in figure 4.14, the maximum measured air mass flow per disk gap is about $2.7\,\mathrm{g\,s^{-1}}$, so the leakage in this case would be approximately two times the mass flow per disk gap.

4.2.4.2 Friction

Two types of friction losses can be measured. The bearing loss, by spinning the shaft without rotor, and the windage and bearing loss by spinning the shaft together with the solid rotor dummy. Figure 4.31 shows the measured losses from spinning the shaft alone. The measurement is conducted twice, with used main bearings with many hours of previous runtime, and with brand new main bearings. Compared to the turbine power output of some kilowatts, the bearing friction losses are very small. The power requirement

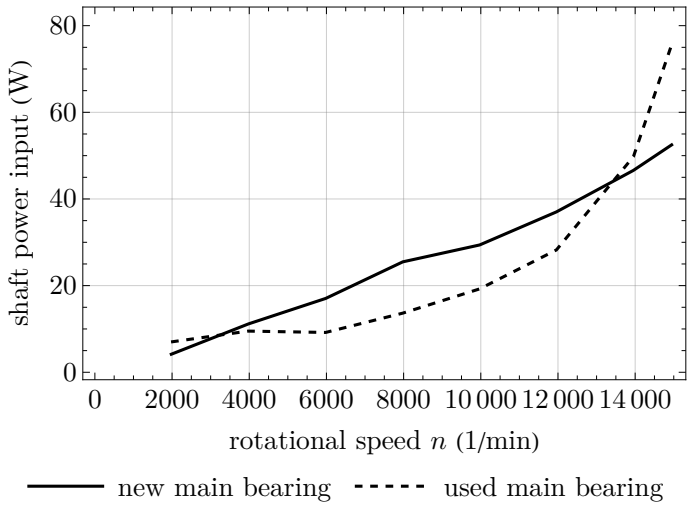

Figure 4.31: Power required to spin the shaft without any rotor for a set of new main bearings and a set that has seen many hours of use.

for spinning the rotor dummy includes both bearing friction and windage losses. The measurements are displayed in figure 4.30b. Friction losses show a primary dependence on rotational speed and a secondary dependence on rotor pressure ratio. Only rotor dummy test results for four nozzles with 5-8 geometry are shown, since there is no noticeable difference to measurements with two nozzles.

4.3 Comparison between numerical and experimental results

To further analyse the inner workings of the turbine, three high efficiency operating conditions at different rotational speeds are simulated using the detailed CFD approach from section 3.1.2. The input parameters are summarized in table 4.4. It is assumed, that the leakage through one of the two rotor-housing gaps is equal to the mass flow per disk gap, so the mass flow per gap in the CFD simulation is calculated from the turbine mass flow divided by the number of disk gaps plus two, which in this case is 67.

run		C1	C2	C3	
outer disk radius	r_1	90	90	90	mm
inner disk radius	r_2	42	42	42	mm
disk spacing	$2s$	0.2	0.2	0.2	mm
turbine mass flow	$\dot{m}$	179	125	101	$\mathrm{g\,s^{-1}}$
mass flow per gap	$\dot{m}_g$	2.68	1.86	1.51	$\mathrm{g\,s^{-1}}$
rotational speed	n	18000	16000	14000	$\mathrm{min^{-1}}$
inlet temperature	$\bar{\vartheta}_1$	28.2	28.4	30.7	°C
outlet pressure	$\bar{p}_2$	1.26	1.13	1.08	bara

Table 4.4: CFD input parameters.

run		C1		C2		C3		
		CFD	exp.	CFD	exp.	CFD	exp.	
turbine power output	$\dot{w}$	5869	5376	3263	2890	2152	1916	W
power output per gap	$\dot{w}_g$	90.3	82.7	50.2	44.5	33.1	29.5	W
efficiency	$\tilde{\eta}_c$	0.521	0.486	0.536	0.488	0.535	0.485	-
stator inlet pressure	$\bar{p}_0$	2.93	2.77	2.12	2.01	1.79	1.71	bara
rotor inlet pressure	$\bar{p}_1$	1.64	1.76	1.37	1.44	1.25	1.29	bara
rotor inlet temperature	$\bar{\vartheta}_1$	-8.68		-0.44		6.69		°C
rotor inlet total temperature	$\bar{\vartheta}_1 + \frac{\bar{u}_1^2}{2c_p}$	25.9	25.4	26.5	25.7	29.09	28.4	°C
rotor outlet temperature	$\bar{\vartheta}_2$	-12.7	-0.97	-3.65	4.90	5.09	11.7	°C
Reynolds number	Re	117	132	82.8	92.0	67.3	73.9	-
Taylor number	Ta	1934	1896	1396	1366	1089	1061	-
average rotor inlet angle	α_{a1}	2.65		2.93		2.98		°

Table 4.5: Comparison between simulation results and experiment.

Some CFD results, together with their experimental counterparts, are listed in table 4.5. Overall the predictions from the simulation are accurate, the power output and efficiency are slightly overestimated because inlet pressure in the simulation settles at a higher value than measured in the experiment and also windage and bearing losses have to be subtracted from the numerical power output prediction. The rotor inlet temperature is measured at the nozzle outlet, approximately in the centre of the stream, so the measured

rotor inlet temperature resembles the total temperature. The mismatch in outlet conditions is presumably due to the fact that simulation results are taken just before the fluid exits the disk gap, whereas in the experiment, the conditions are measured downstream of the turbine outlet structures, in the outlet pipe before the silencer.

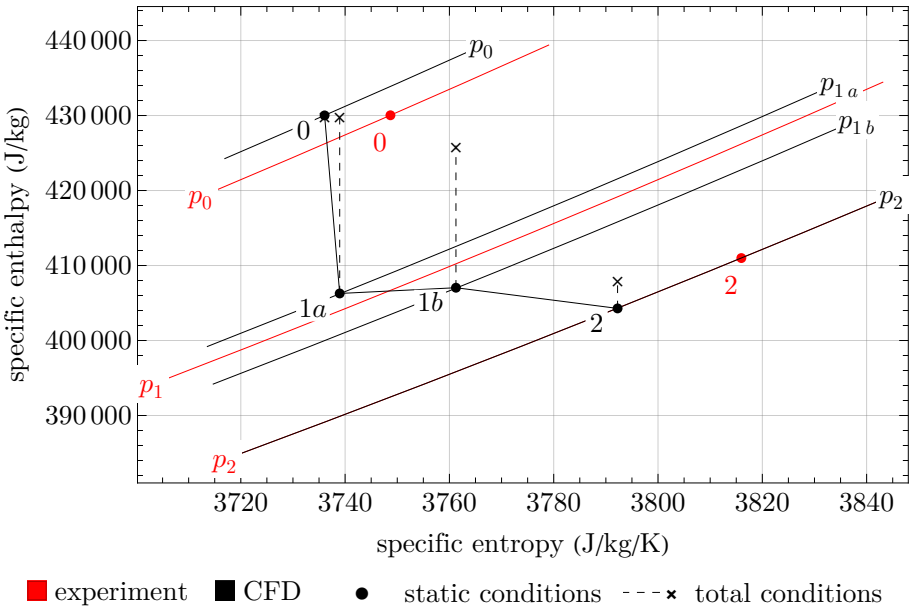

Figure 4.32: Entropy-enthalpy chart for the C3-operating point. The $1a$ and $1b$ conditions refer to conditions shortly before exiting the nozzle and shortly after entering the rotor, calculated from surfaces at radii of 91 mm and 89 mm respectively.

The C3-operating conditions are analysed further with respect to turbine losses. Figure 4.32 shows an entropy-enthalpy chart. The positions $1a$ and $1b$ are introduced to visualize the conditions shortly before the fluid exits the nozzle and shortly after it enters the rotor. The disk surfaces between stations $1a$ and $1b$ mainly include the lateral edge surfaces and contribute to turbine power output, which is why there is a small loss in total enthalpy between those states.

Figures 4.33 and 4.34 break down the turbine losses from experimental measurements and simulation results. The total available power from isentropic enthalpy drop across the turbine is bigger for the CFD results because of the slightly higher turbine inlet pressure, but the overall distribution of losses is consistent. The chunk labelled with "other losses" includes stator, interspace, rotor and outlet kinetic energy loss, all of which couldn't be measured directly in the experiment. For the CFD results however, stator, interspace and rotor losses can be exactly determined from differences in enthalpy drop between the simulated conditions 0, $1a$, $1b$ and 2 and the respective conditions in a theoretical, completely isentropic reference turbine 0, $1as$, $1bs$ and $2s$, that operates across similar pressure levels. Thus, stator, interspace and rotor loss are calculated from $(h_0 - h_{1as}) - (h_0 - h_{1a})$, $(h_{1as} - h_{1bs}) - (h_{1a} - h_{1b})$ and $(h_{1bs} - h_{2s}) - (h_{1b} - h_2)$ respectively.

4.4 Conclusions regarding turbine design

In summary, findings by previous authors regarding turbine design that were cited in chapter 2.4 were confirmed and extended. As expected, thinner disks proved to be always preferable in terms of achievable turbine efficiency. For disk spacing there is an optimum

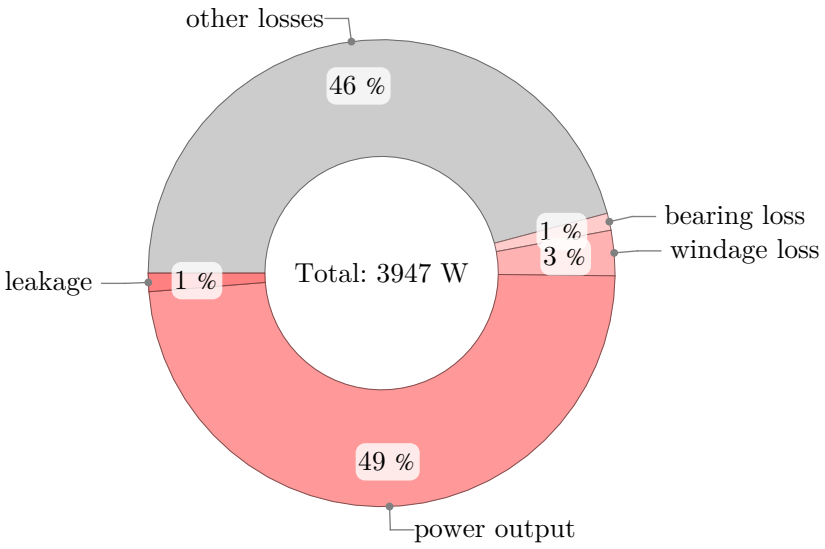

Figure 4.33: Breakdown of turbine losses from experiment. The given total available power corresponds to $\dot{m}\tilde{h}_c$.

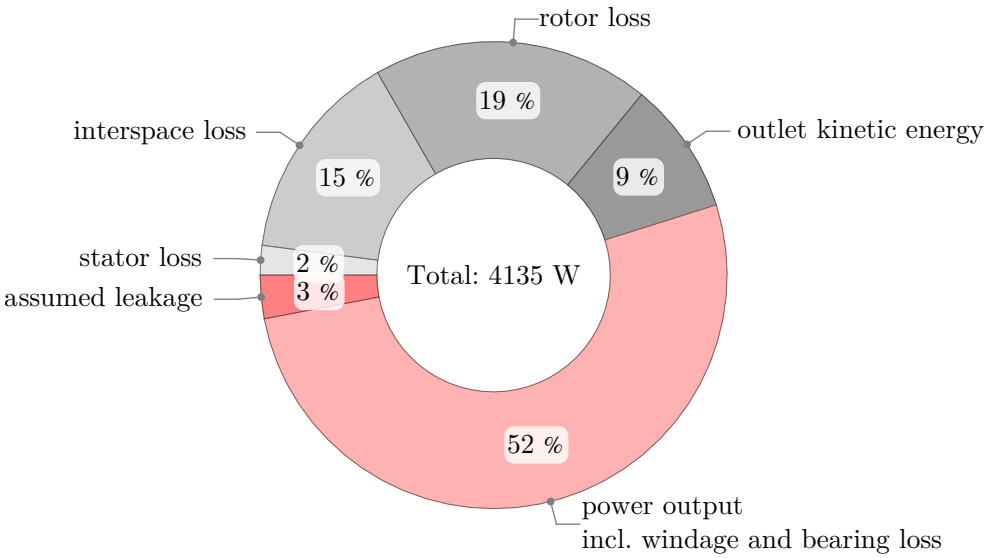

Figure 4.34: Breakdown of turbine losses from CFD. The given total available power corresponds to $\dot{m}\tilde{h}_c$.

that is dependent on disk thickness, as there appears to be an efficiency penalty when the ratio of disk thickness to spacing distance gets large. Specifically in figure 4.23 it can be seen, that for 0.5 mm thick disks, the disk spacing of 0.5 mm performs best, whereas for 0.2 mm thick disks, a 0.2 mm spacing yields better efficiency. It is possible, that further reduction of disk spacing would further improve efficiency for the thinnest disks.

With increasingly thinner disks and smaller disk spacing, it becomes however difficult to maintain an even disk spacing. From figure 4.22 it can be seen that this is already difficult for the 0.2 mm spacing.

Disk edge profiling overall improves turbine efficiency, however the effect is only observed for the largest ratio of disk thickness to spacing. Thus, regarding turbine design, it is preferable to reduce disk thickness rather than shaping the disk edges since the additional step in manufacturing the disks adds cost and can negatively affect rotor balance if the edge profile is inconsistent.

For disks with enhanced surface roughness, no significant difference in turbine performance was found. The roughness might have to be increased even further to cause a measurable impact. This is a challenge in terms of manufacturing, because the roughness that can be obtained from sanding is limited, and sandblasting does not work in this case because it deforms the thin disks. Structuring the disk surface by etching would however be possible.

Just as in previous Tesla turbine experiments, rotor vibration was an issue when disks were merely mounted to the shaft with no additional measures to stabilize the rotor. Excessive vibration effectively prohibited operation above certain rotational speeds. In order to circumvent this, a new method that introduces precise dents into the disks was developed and employed with good success. The dents do not prevent the disks from being pushed apart at very high mass flows and rubbing on the inner housing surface, the advantage is however, that they stabilize the rotor while adding no additional weight to the disks that could possibly affect rotor balance and disk load.

Regarding the stator, nozzles with a geometrical nozzle outlet angle of 5° perform better than 2° and 15°-versions. The overall nozzle shape was different for the three variants, so it is not clear yet whether the impact on turbine performance is purely caused by the difference in nozzle outlet angle. The setup with four nozzles gave a higher efficiency optimum than the two and one nozzle setups. The efficiency increase from two to four nozzles however is much smaller than from one to two nozzles. This suggests an efficiency saturation above a certain number of nozzles.

Chapter 5

A new approach to Tesla turbine preliminary design

Preliminary turbine design requires a computationally inexpensive model for estimating turbine performance parameters over a wide range of input parameters. Suitable rotor flow modelling approaches and Tesla turbine specific loss models from chapter 2 can be combined with stator modelling from conventional radial turbine design methods. In this chapter, a basic step by step design routine is outlined, based on an analytical laminar rotor flow model. Stator design and loss modelling are only roughly implemented, in favour of a detailed optimization of rotor design parameters. The routine can be modified by the turbine designer to account for other modelling approaches and application specific constraints and requirements. Along the way, some general design guidelines are derived that help estimating suitable Tesla turbine design parameters, before implementing a detailed design routine. Design predictions are put to the test by comparison with numerical simulation and actual experimental Tesla turbine performance and examples are provided for water and air turbines.

5.1 Turbine selection

To help decide whether to choose a Tesla turbine over any other type of expander, it is helpful to compare them using the system originated by Baljé and summarized by Gambini and Vellini [2021]. It introduces specific speed and specific diameter as nondimensional design parameters. These normalize rotor diameter and rotational speed with volumetric fluid throughput $\dot{v}$ and isentropic static to static enthalpy difference $\tilde{h}_c$.

$$\omega_s = \omega \frac{\dot{v}^{1/2}}{\tilde{h}_c^{3/4}} \tag{5.1}$$

$$D_s = 2r_1 \frac{\tilde{h}_c^{1/4}}{\dot{v}^{1/2}} \tag{5.2}$$

Figure 5.1 locates the highest efficiency Tesla turbine performance map from the experiment, previously shown in figure 4.14, in the Baljé design chart, relative to the radial turbine efficiency contours by Gambini and Vellini [2021]. The efficiency optimum of the experimental Tesla turbine is located in the upper left region of the radial turbine contours, towards volumetric expanders. Presumably, one of the reasons for the shift is that the experimental turbine is a partial admission turbine. Another similar categorization of Tesla turbines is provided by Fiaschi and Talluri [2019] and Renuke and Traverso [2022], who also locate a Tesla turbine in the Baljé chart, based on modelled performance data.

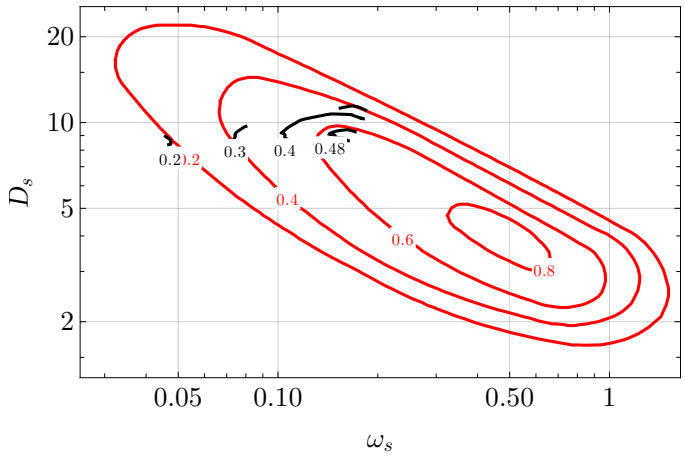

Figure 5.1: Lines of constant turbine efficiency, as a function of specific speed and specific diameter. Comparison between Tesla turbine experiment from chapter 4 and the radial turbine Baljé chart, digitized from figure 2.9 by Gambini and Vellini [2021].

5.2 Optimization goals

Two major optimization goals for turbine designs across all applications are high efficiency and high power density. In other words, to convert the highest possible fraction of the available energy contained in the working fluid to mechanical energy, using a machine that is as small, lightweight and inexpensive as possible. These objectives contradict each other and a suitable trade-off has to be found. Comparing two machines with the same power output, the more efficient machine tends to be larger, with lower relative velocity between fluid and disk. Larger machines also come with a natural efficiency benefit from smaller clearances between rotating and stationary turbine parts, relative to machine size. On the contrary, machines with high power density are smaller with a higher relative velocity between disk and fluid.

To quantify turbine power output relative to its size, a power density parameter is introduced. It is defined as the ratio of output power to one-sided disk surface area.

$$e = \frac{n_g y \ \dot{m}_g}{n_d \pi (r_1^2 - r_2^2)} \tag{5.3}$$

Strictly speaking, there is always one more disk than disk gaps. For a large number of rotor disks however, the extra disk can be neglected. So, assuming $n_g \approx n_d$, dimensional and nondimensional power density can be expressed as:

$$e = \frac{y \ \dot{m}_g}{\pi (r_1^2 - r_2^2)} \tag{5.4}$$

$$E = \frac{4\sigma Y}{1 - R_2^2} \tag{5.5}$$

with

$$e = \rho |\bar{u}_{r1}^3| E \tag{5.6}$$

Power density has to be analysed in the dimensional parameter space, since it is a dimensional quantity by nature and two turbines with the same nondimensional power density

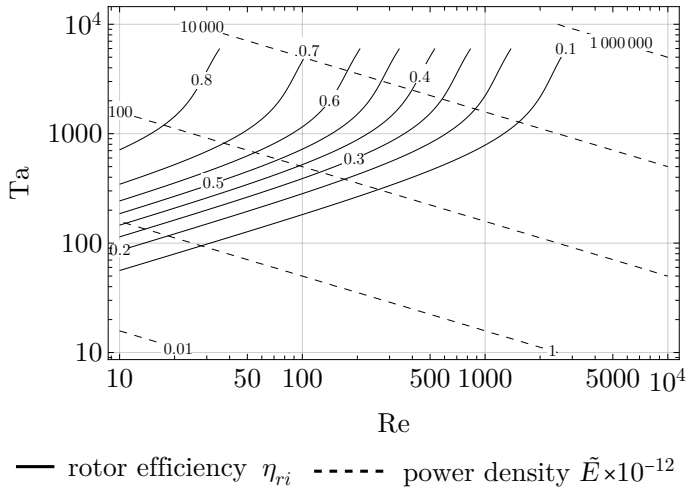

Figure 5.2: Lines of constant rotor efficiency and constant power density from the asymptotic solution by Breiter and Pohlhausen [1962] for $R_2 = 0.5$ and $\sigma = 0.001$.

can have different dimensional energy densities. The definition of nondimensional power density E given so far is not ideal for optimization since it makes the dimensional power density a function of the rotor inlet velocity u_{r1}. Comparing power densities by this definition across the dimensionless parameter space is essentially the same as comparing turbines with the same rotor inlet velocity and variable turbine geometry, which is rather unintuitive. A better way to express nondimensional power density is to introduce a new normalization, so that dimensional power density becomes a function of rotor outer radius. Optimizing by this quantity gives the machine with the highest power density for fixed rotor outer radius.

$$\tilde{E} = \frac{4\mathrm{Re}^3 Y}{\sigma^2(1 - R_2^2)} \tag{5.7}$$

with

$$\tilde{E} = \frac{\mathrm{Re}^3}{\sigma^3} E \tag{5.8}$$

$$e = \frac{\rho\nu^3}{r_1^3}\tilde{E} \tag{5.9}$$

For establishing some basic design trends with regard to Reynolds and Taylor number, incompressible rotor efficiency from equation 2.24 and power density $\tilde{E}$ from above is now calculated based on the analytical expressions for velocities and pressure from the asymptotic model by Breiter and Pohlhausen [1962], given in equations 2.59, 2.60, 2.65, 2.66. Inserting the analytical expressions into the rotor efficiency definition gives a rather complicated expression, however visualizing it reveals a simple structure. There is an upper efficiency plateau for low Reynolds number and high Taylor number and a transition into a lower plateau on the opposite side of the map. Figure 5.2 shows this for estimated values of R_2 and σ. Changing these estimates within physical boundaries affects the transition region from high to low efficiency, but the overall structure remains the same.

For $\mathrm{Re} \to 0$, the analytical expression for efficiency simplifies by l'Hospital's rule to

$$\lim_{\mathrm{Re}\to 0} \eta_{ri} = 2\frac{1 - R_2^2}{2 - R_2^2} \tag{5.10}$$

This is the upper limit for rotor efficiency in terms of the analytical model.

Regarding power density, inserting the analytical expressions for velocities and pressure from the asymptotic model results in very simple relations:

$$e = 4\rho\ r_1 s|\bar{u}_{r1}|\omega^2 = \frac{\omega^2 \dot{m}_g}{\pi} \tag{5.11}$$

$$E = 4\sigma \frac{\mathrm{Ta}^2}{\mathrm{Re}^2} \tag{5.12}$$

$$\tilde{E} = \frac{4}{\sigma^2}\mathrm{Ta}^2\mathrm{Re} \tag{5.13}$$

Thus, power density from the asymptotic model is proportional to mass flow and to the square of angular velocity. For fixed rotor geometry and fluid, this directly translates to Reynolds number and the square of Taylor number.

The optimization goals can now be formulated in terms of nondimensional parameters. High efficiency Tesla turbines are characterized by high Taylor number and low Reynolds number. Energetically dense machines require high Taylor number as well, but combined with high Reynolds number. Consequently, the trade-off between efficiency and power density manifests itself in the choice of Reynolds number of the turbine design. For machines with the same geometry and working fluid, this means that the more efficient machine has a lower radial mass flow and the high power density machine has a higher radial mass flow, whereas high rotational speed is advantageous for both efficiency and power density.

In real turbines, the positive effect of high rotational speed on turbine efficiency is counteracted to some degree by windage and bearing friction losses, which scale with rotational speed. On top of that, the inlet angle cannot be arbitrarily small, which has a potentially big impact for high efficiency and low power output machines. Also, for operating conditions above a certain threshold in terms of Reynolds number and Taylor number, the analytical model is not valid any more, as was shown in chapter 3.3.2.

5.3 Modelling approach

The turbine model that is at the core of the design routine is an individual choice of the turbine designer, dependent on available application requirements, tools and resources. The design routine that is outlined here uses the asymptotic analytical model by Batista [2011], together with the inlet angle correction by Schosser et al. [2019]. Compared to other models, it is based on fewer simplifying assumptions. Some validation is provided in section 3.3 through comparison with numerical and experimental data. In the parameter region with high rotor efficiency, the model gives accurate predictions. To keep it simple, modelling of the stator is condensed into a single estimated total pressure loss parameter η_n. It is defined as the ratio between dynamic pressure at the rotor inlet and the static pressure difference between stator inlet and outlet, neglecting dynamic pressure at the stator inlet. This can be replaced with a more sophisticated stator model from turbomachinery literature.

$$\eta_n = \frac{\rho_1 \bar{u}_1^2}{2(\bar{p}_0 - \bar{p}_1)} \tag{5.14}$$

To model the adverse impact of high rotational speed on efficiency, the windage loss model by Daily and Nece [1960] is integrated into the routine. Their empirical torque coefficient for flow regime III is used, which assumes turbulent flow with merged boundary layers in

the space between outer rotor surfaces and housing. The windage loss model allows to calculate a power loss $\dot{w}_l$, that is dependent on rotational speed, disk geometry and fluid.

$$\dot{w}_l = C_m \frac{1}{2} \rho \omega^3 r_1^5 \tag{5.15}$$

$$C_m = \frac{0.08}{(b/r_1)^{1/6} (\mathrm{Ta}/\sigma)^{1/4}} \tag{5.16}$$

From this, under the assumption that the distance between rotating and stationary surfaces, denoted by b, is equal to the disk spacing $2s$, the nondimensional power loss can be expressed as:

$$\dot{W}_l = 0.0356359 \, \frac{\mathrm{Ta}^{11/4} \, \sigma^{1/12}}{\mathrm{Re}^3} \tag{5.17}$$

Other types of turbine losses are neglected for now. The windage loss and the stator efficiency are incorporated into the incompressible efficiency formulation, which will be used as a performance parameter in the design procedure.

$$\tilde{H}_i = \bar{P}_2 - \bar{P}_1 - \frac{\bar{U}_1^2}{2 \, \eta_n} \tag{5.18}$$

$$\tilde{\eta}_i = \frac{\dot{M}_g Y + (\dot{W}_l / n_g)}{\dot{M}_g \tilde{H}_i} \tag{5.19}$$

5.4 Comparison between design model and experiment

To verify the design model, results are compared to an experimental performance map. Figure 5.3 shows the computed incompressible efficiency from the design model with the measured compressible efficiency $\tilde{\eta}_c$ from the most efficient turbine configuration from the experiment in chapter 3. Experimental Reynolds and Taylor numbers are calculated using fluid properties from ideal gas law and Sutherland formula, using the measured average rotor inlet pressure and a rotor inlet temperature calculated from isentropic expansion from measured turbine inlet conditions to rotor inlet pressure. The absolute inlet angle is estimated from the numerical simulation from chapter 4.3 to be 3°. As expected, the modelled efficiencies are overestimated due to the limited loss modelling. Furthermore the efficiency optimum seems to be shifted towards the upper right, but considering the large degree of simplification in the model, the results agree very well.

5.5 Preliminary design procedure

The following design procedure combines the Tesla turbine design trends from turbine modelling with mechanical and aerodynamical limits of turbine operation, for example the rotational speed limit of the disks due to disk strength and the speed of sound limit for fluid velocities. In the course of the design process, the turbine designer selects all nondimensional turbine parameters plus one dimensional parameter, in this case the outer disk radius r_1, so that the turbine is fully defined in both dimensional and nondimensional parameter space.

Figure 5.4 gives a basic outline of the design procedure. It starts out by gathering application specific fluid data, as well as estimating the turbine design parameters R_2, α_{a1}, σ, the number of disk gaps n_g and stator efficiency η_n. Taking into account some physical limits, Reynolds number, Taylor number and disk outer radius are then selected

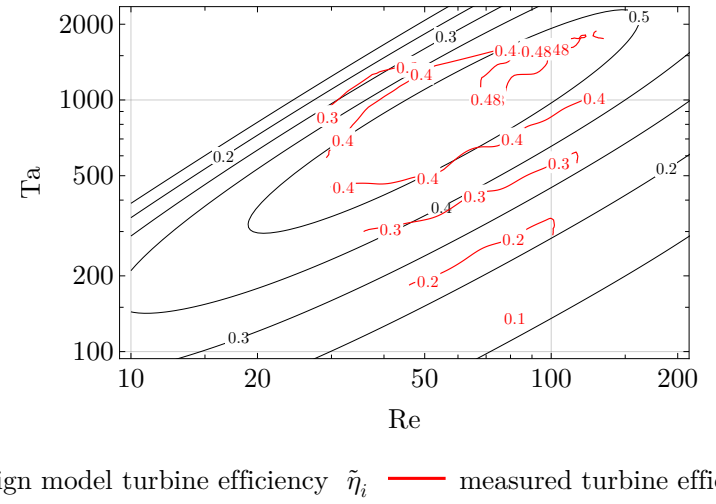

Figure 5.3: Comparison of modelled and measured turbine efficiency. The design parameters of the test facility turbine are $R_2 = 0.467$, $\sigma = 0.00111$, $\alpha_a = 3°$ and $n_g = 65$. The estimated stator efficiency is $\eta_n = 0.8$.

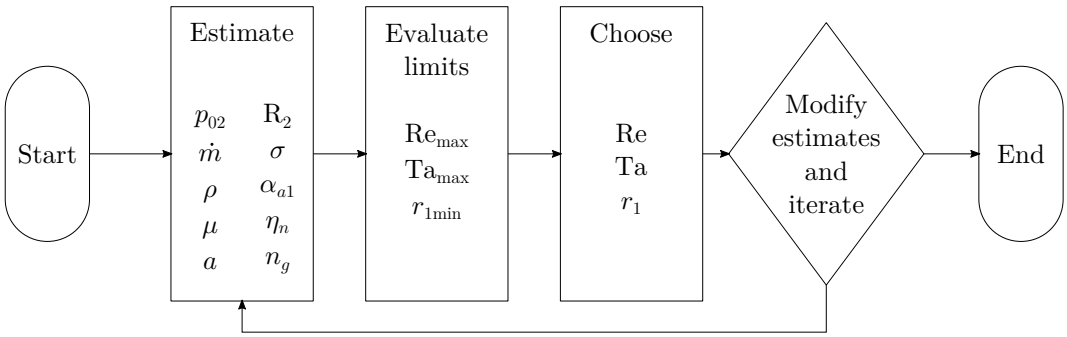

Figure 5.4: Basic structure of the design procedure.

with regard to optimal power density and efficiency. Based on the selected parameters, the previous estimates are refined and the process starts from the beginning until a suitable design is found.

5.5.1 Estimate

The first step of the design routine is to define input parameters based on the application requirements. This means deciding on a fluid, as well as estimating total available fluid mass flow and pressure drop p_{02} across the turbine. If the application calls for a certain turbine power output, the turbine mass flow has to be estimated. For the sample designs in the following sections, the fluid data from table 5.1 is utilized, as well as disk material data in table 5.2.

medium		air	water	
density	ρ	1.19	998	$\mathrm{kg\,m^{-3}}$
dynamic viscosity	μ	18.2×10^{-6}	1002×10^{-6}	$\mathrm{Pa\,s}$
speed of sound	a	343	1482	$\mathrm{m\,s^{-1}}$

Table 5.1: Sample fluid data at 20 °C and 1 bara for use in section 5.5.

material		aluminium EN AW-5754 H14	carbon fibre reinforced polymer	
density	ρ_d	2700	1500	$\mathrm{kg\,m^{-3}}$
Poisson's ratio	ν_d	0.3	0.1	-
stress limit	σ_{dmax}	190	900	MPa

Table 5.2: Sample material data for use in section 5.5. The values for aluminium are from Wittel et al. [2017], the values for carbon fibre reinforced polymer are estimates based on Jin et al. [2018].

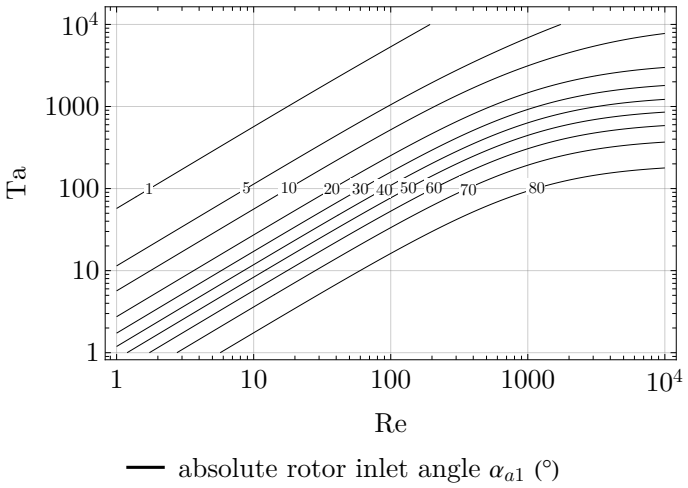

Figure 5.5: Lines of constant rotor inlet angle from the asymptotic model by Breiter and Pohlhausen [1962] for $R_2 = 0.5$ and $\sigma = 0.001$.

Additionally, some of the output parameters of the design routine have to be estimated beforehand, since it's an iterative procedure. This concerns the rotor gap aspect ratio σ, the nondimensional outlet radius R_2, the rotor inlet angle in a nonrotating reference frame α_{a1}, the number of disk gaps n_g and the stator efficiency η_n. For definitions refer to chapter 2.1. As starting point for air and water turbines, the following estimates for the rotor geometry are appropriate:

$$\sigma \approx 0.001 \tag{5.20}$$

$$R_2 \approx 0.5 \tag{5.21}$$

As for the inlet angle α_{a1}, the flow angle from the asymptotic solution at the rotor inlet is a good guideline, although it's not necessarily the ideal angle in terms of performance goals for the turbine. Figure 5.5 visualizes the asymptotic absolute rotor inlet angle for the estimated values of R_2 and σ. In the high efficiency region, the inlet angle is fairly small, thus a value of

$$\alpha_{a1} \approx 3^\circ \tag{5.22}$$

might be a good starting estimate for the design routine. Additionally, stator efficiency and number of disk gaps are estimated as:

$$\eta_n \approx 0.8 \tag{5.23}$$

$$n_g \approx 50 \tag{5.24}$$

5.5.2 Evaluate limits

As a second step, mechanical and aerodynamical limits to turbine operation are gathered. The following limits are sufficient to choose a turbine design, however application specific requirements might be translated into additional or modified limits.

Rotor inlet Mach number For compressible fluids, the upper bound for the fluid velocity at rotor inlet is determined by the Mach number. The absolute inlet fluid velocity is required to stay below the speed of sound.

$$\sqrt{u_{r1}^2 + (u_{\phi 1} + r_1\omega)^2} < a \tag{5.25}$$

$$\sqrt{u_{r1}^2 + \left(\frac{u_{r1}}{\tan(\alpha_{a1})}\right)^2} < a \tag{5.26}$$

from this the limit for the radial inlet velocity follows, which can be translated into a limit for the Reynolds number Re_{max}.

$$|u_{r1}| < \frac{a}{\sqrt{1 + \frac{1}{(\tan(\alpha_{a1}))^2}}} \tag{5.27}$$

$$\mathrm{Re} < \frac{a\sigma r_1}{\nu\sqrt{1 + \frac{1}{(\tan(\alpha_{a1}))^2}}} = \mathrm{Re}_{max} \tag{5.28}$$

Using the estimates for a, σ, α_{a1} and ν from the previous chapter, this limit can be evaluated as a linear function of the disk outer radius r_1.

Disk strength As previously explained, high rotational speed is desirable for a Tesla turbine, however the disk material only tolerates this to a certain degree. The aforementioned analytical model for the stress distribution inside a disk with a single circular hole in the centre, given by Löffler [1961] is an easy way to estimate the rotational speed limit due to disk strength. At given disk geometry, material and rotational speed, the radial and tangential stresses are functions of the nondimensional radial position R.

$$S_r = \frac{3 + \nu_d}{8}\left(1 + R_2^2 - \frac{R_2^2}{R^2} - R^2\right) \tag{5.29}$$

$$S_\phi = \frac{3 + \nu_d}{8}\left(1 + R_2^2 + \frac{R_2^2}{R^2} - \frac{1 + 3\nu_d}{3 + \nu_d}R^2\right) \tag{5.30}$$

$$S = \sqrt{S_r^2 + S_\phi^2} \tag{5.31}$$

with

$$\sigma_d = \rho_d\ \omega^2 r_1^2 S \tag{5.32}$$

Analysing the function S_r across the disk from for $R = R_2$ to $R = 1$ reveals that it reduces to zero at the boundaries and that it has a maximum for $R = \sqrt{R_2}$, where it assumes the value

$$S_{rmax} = S_r(\sqrt{R_2}) = \frac{3 + \nu_d}{8}(1 - R_2)^2 \tag{5.33}$$

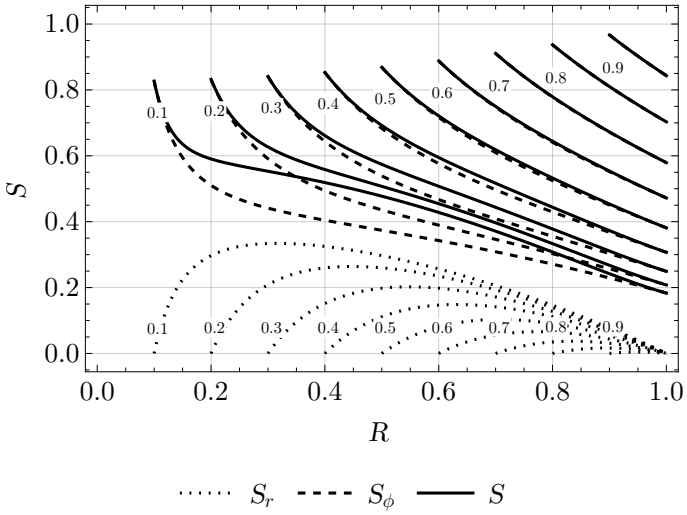

Figure 5.6: Nondimensional stress distribution inside the rotor disk for $\nu_d = 0.3$. The curve labels indicate different values of R_2.

The distribution of the tangential stress S_ϕ on the other hand is a strictly decreasing function across the disk and thus has its maximum value at the inner disk radius R_2, which equates to

$$S_{\phi max} = S_\phi(R_2) = \frac{3+\nu_d}{8}\left(2 + R_2^2\left(1 - \frac{1+3\nu_d}{3+\nu_d}\right)\right) \tag{5.34}$$

Visualizing the stress distribution inside the disk for different nondimensional disk inner radii, figure 5.6 reveals that the maximum disk stress is always at the inner radius R_2 and is purely in tangential direction. The chart is based on an estimated Poisson's ratio ν_d that is valid for most metals, the conclusions remain unchanged for Poisson's ratios of polymers, ceramics and other materials.

Comparing the maximum stress inside the disk with the maximum tolerable stress of the disk material σ_{dmax}, allows deriving a limit for the disk surface velocity at the outer disk radius $r_1\omega$.

$$\sigma_{dmax} > \rho_d\, \omega^2 r_1^2 S_{\phi max} \tag{5.35}$$

$$r_1\omega < \sqrt{\frac{\sigma_{dmax}}{\rho_d S_{\phi max}}}, \quad \text{for } r_1 > 0 \tag{5.36}$$

This can be translated into a limit for Taylor number, which again is a linear function of r_1.

$$\mathrm{Ta} < \frac{r_1\sigma}{\nu}\sqrt{\frac{\sigma_{dmax}}{\rho_d S_{\phi max}}} = \mathrm{Ta}_{max} \tag{5.37}$$

Model limitations To take into account the limitations of the modelling approach itself, a second set of limits for Reynolds and Taylor number is set up. These can be estimated from the comparison in section 3.3.2 between analytical and numerical modelling. Interpreting the chart generously, the model gives accurate efficiencies when either Reynolds number is smaller than 200 or Taylor number is smaller than 2000.

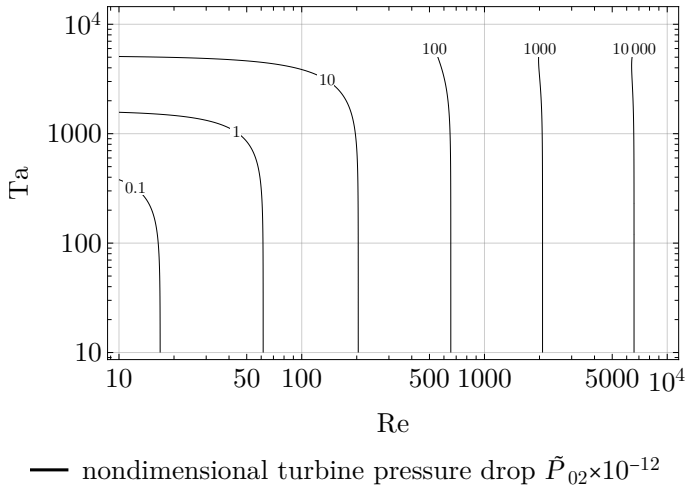

Figure 5.7: Lines of constant nondimensional pressure drop $\tilde{P}_{02}$ for $R_2 = 0.5$, $\sigma = 0.001$, $\alpha_a = 3°$ and $\eta_s = 0.8$.

Pressure drop Another limiting factor in terms of Reynolds and Taylor number is the pressure drop that is available to the turbine. Similar to the treatment of power density before, it is helpful to introduce a new dimensionless pressure $\tilde{P}$ that compares the pressure among turbines with the same rotor outer diameter and fluid. This way, dimensional pressure becomes a function of rotor outer radius.

$$\tilde{P} = \frac{\mathrm{Re}^2}{\sigma^2} P \tag{5.38}$$

$$p = \frac{\rho \nu^2}{r_1^2} \tilde{P} \tag{5.39}$$

The pressure drop is divided into a rotor pressure drop p_{12} and nozzle pressure drop p_{01}. The rotor pressure drop follows from the rotor flow model, whereas the nozzle pressure drop is derived from the dynamic pressure at rotor inlet, divided by stator efficiency.

$$p_{02} = \bar{p}_0 - \bar{p}_2 \tag{5.40}$$

$$p_{12} = \bar{p}_1 - \bar{p}_2 \tag{5.41}$$

$$p_{01} = \bar{p}_0 - \bar{p}_1 = \frac{1}{\eta_n} \frac{\rho \bar{u}_1^2}{2} \tag{5.42}$$

and in nondimensional form

$$\tilde{P}_{02} = \tilde{P}_0 - \tilde{P}_2 \tag{5.43}$$

$$\tilde{P}_{12} = \tilde{P}_1 - \tilde{P}_2 \tag{5.44}$$

$$\tilde{P}_{01} = \tilde{P}_0 - \tilde{P}_1 = \frac{1}{\eta_n} \frac{\bar{U}_1^2}{2} \tag{5.45}$$

Figure 5.7 gives the distribution of the modified dimensionless pressure across the Re-Ta-plane for the previously estimated turbine parameters. Using this chart, together with fluid data and a value for r_1, the available pressure drop from the application can be matched to a set of Reynolds and Taylor number that leads to as high as possible isentropic turbine efficiency.

Turbine outlet Mach number The last limit concerns the velocity of the fluid that exits the rotor. Since all the fluid has to pass through the outlet opening of the last disk, the outlet diameter has to be as large as possible to minimize outlet losses. The outlet velocity follows from:

$$u_3 = \frac{\dot{m}}{\rho r_2^2 \pi} \tag{5.46}$$

Setting an upper limit for u_3 and using the estimated value for R_2 leads to a lower limit for the rotor outer radius r_1.

$$r_{2min} = \sqrt{\frac{\dot{m}}{\rho u_{3max} \pi}} \tag{5.47}$$

$$r_{1min} = \frac{r_{2min}}{R_2} \tag{5.48}$$

The maximum allowable outlet velocity u_{3max} has to be estimated. For compressible fluids it can be set to a fraction of the speed of sound, for incompressible media, the pressure drop in pipe flow based on the pipe friction factor is a way to estimate a suitable outlet velocity. In a real turbine, the outlet geometry is restricted due to some necessary mechanical features, so the real outlet velocity will be higher than the estimate based on R_2.

5.5.3 Choose

Based on the gathered information, the turbine parameters Re, Ta and r_1 can now be selected according to the optimization goals. Figure 5.8 visualizes turbine efficiency and power density from the turbine model based on the parameter estimates. Earlier, in figure 5.2, which was based on the asymptotic model, the efficiency optimum was located in the upper left of the chart. This is no longer the case due to the fixed inlet angle and the included windage loss. Instead, an efficiency optimum forms around a Taylor number of 1000 and Reynolds number just below 100. The chart is based on nondimensional parameters only, so it is valid for all fluids with negligible compressibility at the estimated values for σ, R_2, α_{a1}, n_g and η_n.

The maximum achievable pressure drop across the turbine stage is achieved at the biggest possible Reynolds and Taylor number. The previously derived limits for these are linear functions of the disk outer radius r_1, but it turns out that the maximum achievable dimensional pressure drop at those limits is only weakly affected by r_1. To visualize this, figure 5.9 gives the turbine stage pressure drop at the Reynolds and Taylor number limit for the parameter estimates as a function of r_1.

The process of choosing Reynolds number, Taylor number and outer disk radius is itself an iterative procedure. It starts out by setting the outer disk radius to the minimum allowable radius r_{1min}. From this, the Reynolds and Taylor number limits can be calculated, as well as the stage pressure drop at those limits. This gives the turbine with the highest possible power density. To give some design examples, some sample boundary conditions are given in table 5.3. These result in a minimum outer disk radius r_{1min} of 0.0397 m and 0.0652 m for air and water, respectively. From this, the Reynolds and Taylor number limits can be calculated. They are given in table 5.4. For the water turbine, the limits are so large, that they don't affect the design decision.

To guide the process of choosing operating conditions, figure 5.10 visualizes the limits together with an isobar at the design pressure drop. For the air turbine, the highest

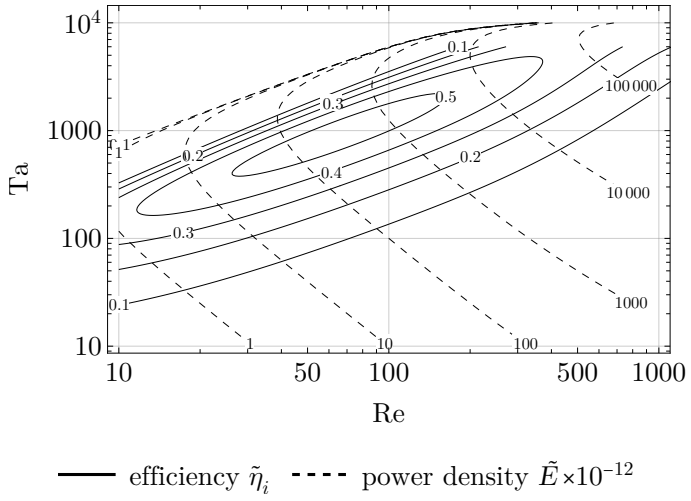

Figure 5.8: Lines of constant incompressible turbine efficiency and constant modified power density.

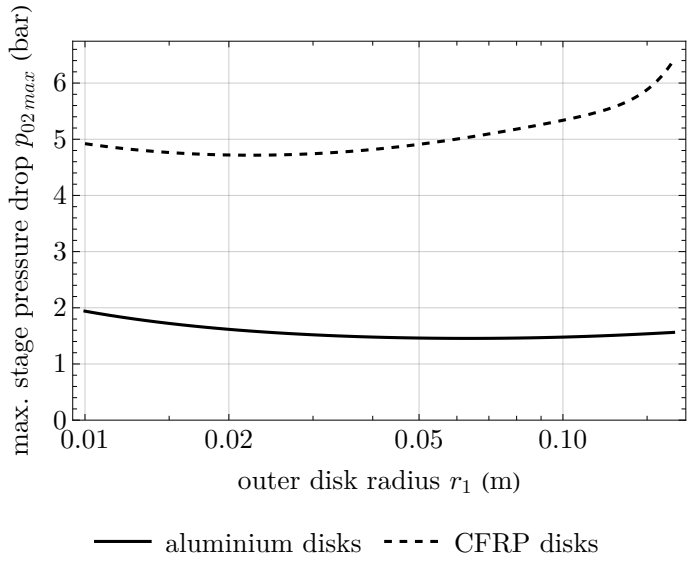

Figure 5.9: Maximum achievable stage pressure drop at the Reynolds and Taylor number limit as a function of outer disk radius for different disk materials.

medium		air	water	
mass flow	$\dot{m}$	0.1	10	$\mathrm{kg\,s^{-1}}$
max. outlet velocity	u_{3max}	68	3	$\mathrm{m\,s^{-1}}$
stage pressure drop	p_{02}	1	5	bar

Table 5.3: Sample design boundary conditions.

medium		air		water		
disk material		Aluminium	CFRP	Aluminium	CFRP	
min. outer radius	r_{1min}	0.0397		0.0652		m
max. Reynolds number	Re_{max}	46.6		5038		
max. Taylor number	Ta_{max}	738	2204	18486	55183	
max. stage pressure drop	Δp_{02max}	1.48	4.82	-	-	bar

Table 5.4: Sample parameter limits.

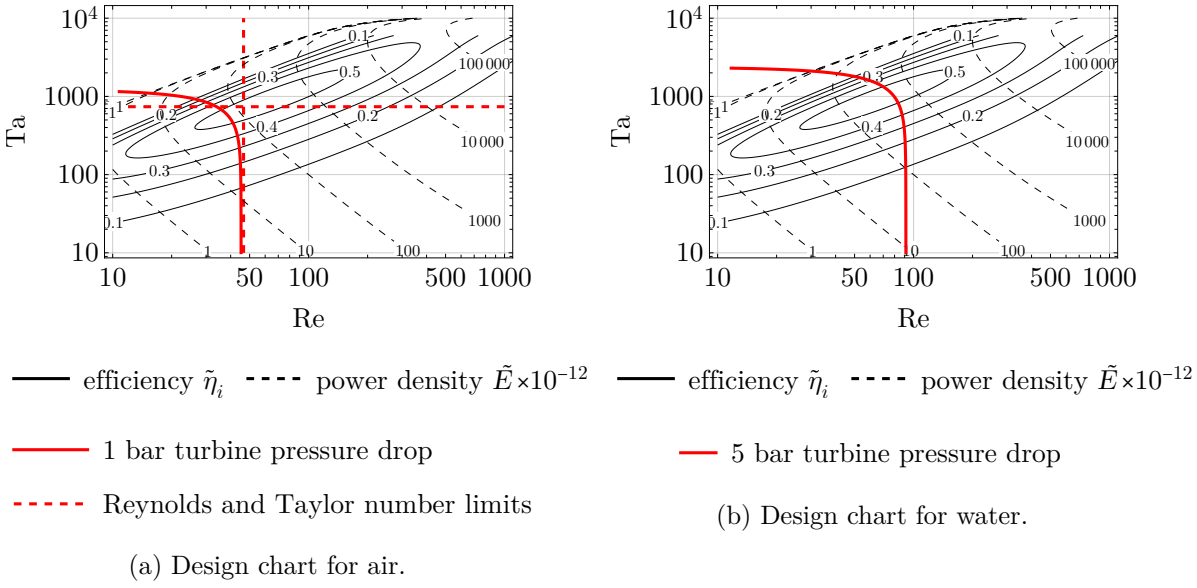

(a) Design chart for air.

(b) Design chart for water.

Figure 5.10: Example design charts with limits based on the sample data from tables 5.3 and 5.4.

efficiency of $\tilde{\eta}_i = 0.53$ on the 1 bar pressure contour is at a Reynolds number of 39 and at a Taylor number of 569. For the water turbine, the optimal efficiency at design pressure drop of 5 bar is at Re= 77 and Ta= 1089 and $\tilde{\eta}_i = 0.54$.

In these examples, the pressure contour at the desired stage pressure drop already intersects the region of highest turbine efficiency, which makes it easy to select a good turbine design. If this is not the case, and the pressure contour is located towards the lower left of the efficiency optimum, the contour can be shifted towards the upper right of the chart by increasing the outer disk radius. This however comes at the cost of lower dimensional power density e (see equation 5.9). If the pressure contour at the desired design pressure drop is located towards the upper right of the efficiency optimum, or even past the Reynolds and Taylor number limits, it is advisable to divide the pressure drop between multiple turbine stages, so that the individual stages can be operated at a lower pressure drop and thus better efficiency. Once an operating point is selected, additional turbine parameters like the power output and the required number of disk gaps can be calculated, as well as off-design turbine performance.

5.5.4 Modify assumptions and iterate

With Reynolds number, Taylor number and outer disk radius selected, the previously estimated turbine parameters can be optimized one by one. Figure 5.11 visualizes this for the previously given sample designs for air and water. These charts can be used to generate a new set of estimates for the next iteration of the design process.

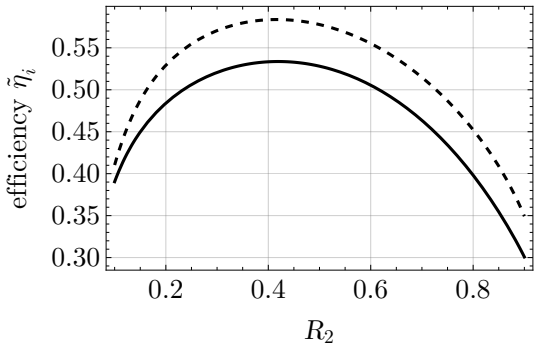

(a) Radius ratio. Efficiency maxima are around $R_2 = 0.42$ for both air and water.

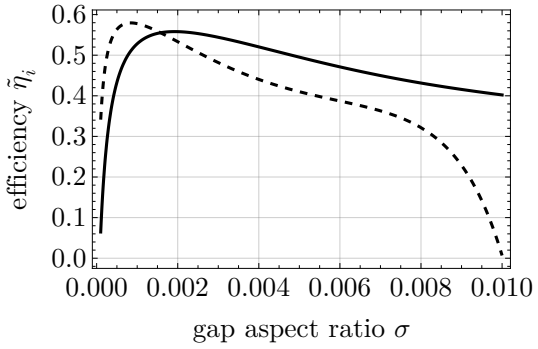

(b) Gap Aspect Ratio. Efficiency maxima are around $\sigma = 0.0019$ and $\sigma = 0.00084$ for air and water respectively.

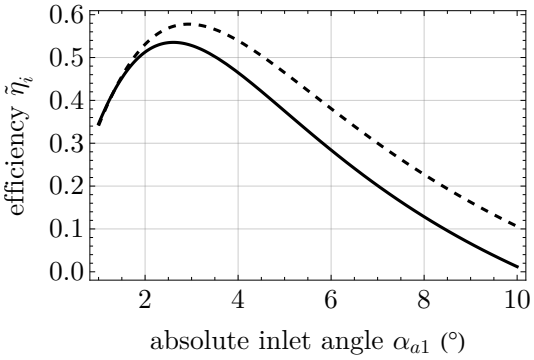

(c) Absolute inlet angle. Efficiency maxima are around $\alpha_a = 2.6$ and $\alpha_a = 2.9$ for air and water respectively.

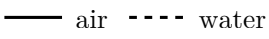

Figure 5.11: Optimization of previously estimated design parameters for the air and water sample designs.

Depending on the choice of operating point, the design parameters might not converge to a certain set of values. For example, if the designer keeps choosing the point with the highest efficiency, the design will drift towards lower and lower Reynolds numbers, which goes hand in hand with lower and lower energy densities. So ultimately, a compromise has to be found, that satisfies application requirements, parameter limits and optimization goals.

Chapter 6

Conclusion

By now, through this work and all previous research on Tesla turbines, it has been shown that there are reliable modelling approaches, experience in Tesla turbine operation and methods for preliminary optimization of turbine parameters. Based on this, Tesla turbine performance can be reliably predicted and the Tesla turbine can be considered for any new application, that requires a low-cost, small-scale expander.

6.1 Summary

Existing literature on Tesla turbines was summarized, especially the variety of rotor modelling approaches that are made possible by the simple rotor geometry. Comparisons of some analytical models to experimental and numerical data showed, that the models are applicable in the laminar and transitional region but naturally get unreliable for turbulent flow. Through stability analysis results that were confirmed by direct numerical simulation, a good estimate for the stability boundary can be obtained, which helps guide the choice of modelling approach. For someone new to the field of Tesla turbines it is probably easiest to set up a rotor model using conventional numerical fluid simulation software to obtain some performance estimates. If however an in-depth optimization of turbine parameters is required, implementing an analytical turbine model allows for a more efficient design process.

The experimental test facility that was set up in the course of this work is one of the largest Tesla turbines built in recent years, with a power output of over 5 kW and an isentropic efficiency of up to 49 %. Further efficiency optimization is certainly possible. The turbine configuration with the thinnest disks and the smallest disk spacing gave the highest turbine efficiency and power output in the experiment. Nozzle counts of one, two and four were compared, as well as different shapes of nozzles. A number of four nozzles gave the best results. Loss measurements gave some insight into the source and magnitude of some turbine losses. The space between rotor and stator was determined to be a major source of turbine losses, together with outlet kinetic energy, losses inside the rotor, windage and leakage. For reducing interspace and windage losses, it is important to optimize the clearances between rotor and stator. Larger clearances lead to less dissipation between rotating and stationary parts. Nevertheless, for reducing interspace losses, i.e. losses inside the radial clearance between rotor and stator, it is favourable to have small clearance in order to prevent high-speed fluid from the nozzle exits leak into the axial clearance and bypass the rotor.

The conclusions from theoretical and experimental analyses were finally condensed into practical advice for turbine designers, to help them assess tesla turbine performance and

benchmark it against other turbine types. The most important turbine parameters were determined to be the disk inner and outer radii, disk spacing, disk thickness, Reynolds number, Taylor number and rotor inlet angle. Rough estimates for these parameters can be read from the provided design charts. The routine can be modified to account for specific application requirements and other modelling approaches. Implementing the design routine and experimenting with it helps to build a feeling for the impact of the individual design parameters on turbine performance. Efficient turbines tend to have a large rotor diameter, small radial mass flow, high rotational speed and a rotor inlet angle close to the tangential direction. However, optimizing for efficiency alone doesn't give a good turbine design since efficient machines are large and have a small power output that might get eaten up by turbine losses like bearing or windage loss. A good turbine design always implies a tradeoff between efficiency and power density.

6.2 Further research

Although analytical modelling of the rotor flow is well developed, it is still possible for new approaches to simplifying and solving the Navier Stokes equations to be found. A potential for further theoretical research lies in the understanding of turbulence and transition of the inter-disk flow. Because of the large variety in rotating disk flow configurations, the studies that specifically target the Tesla turbine configuration are sparse so far and the connection between experimental and theoretical studies on flow regime is not yet fully clarified.

Regarding practical turbines, the full potential of the Tesla turbine has not been demonstrated yet. The test facility that was set up during this study can be further developed and used to further analyse turbine parameters. The study of nozzle count and shape was done using a rotor design which later turned out to be inferior, so analysis of nozzle designs with a more optimal rotor configuration could yield more insight. The number of nozzles could be increased to obtain a full admission Tesla turbine. Height, inner diameter and outer diameter of the rotor were not taken into account so far. New approaches to sealing can be implemented. The design of the stator, plenum and outlet structures could be analysed systematically. Finally, it would be possible to modify the test facility to pump operation, using an appropriate stator design and the motor that was already in use for turbine loss measurements.

The turbine design routine is a starting point for further development. So far the loss modelling that is employed is oversimplified, especially for the stator. Compressibility effects could be taken into account, as well as effects from partial admission. Models for turbulent rotor flow can be implemented. Improvement of performance prediction accuracy could also be achieved by dedicating modelling efforts towards peripheral turbine components like plenum or volute and the outlet structures.

Appendix A

Further test equipment specifications

A.1 Air supply

Pressurized air is supplied by a BOGE SLDF 75-3 screw compressor with a rated power of 55 kW and a maximum output pressure of 11 bara. The air is dried and filtered before entering the 2 m^3 supply tank. A heating element is in place to heat up the air stream, however the heater wasn't in use for all test runs reported here. The compressor is set to keep the pressure in the supply tank between 9 bara and 11 bara and automatically adapts the delivered quantity of air to the withdrawn quantity. For mass flows above approximately 160 $g\,s^{-1}$, the pressure in the supply tank decreases over time, because the compressor cannot provide enough mass flow.

A.2 Eddy current brake

The Magtrol 2WB43 eddy current brake acts as a sink for turbine power and is cooled by tap water. Its rated power is 3 kW, but higher power consumption is possible, given sufficient cooling. The maximum rated torque and rotational speed are 3 N m and 50 000 min^{-1}. Torque measurement is achieved through strain gauges attached to the housing of the brake, rotational speed is measured through an internal optical sensor giving 30 pulses per rotation. Magtrol [2022] specifies a torque accuracy of less than $\pm 0.5\,\%$ full scale, which translates to ± 0.015 N m. The residual torque of the unloaded brake is given as 0.03 N m. The brake is partly visible in figure 4.3. A Magtrol DSP7001 control unit is connected to the brake and controls its rotational speed by adjusting the resistive torque of the brake. Torque values are filtered with an internal filter with a cutoff frequency of 2 Hz. Torque and rotational speed values are supplied directly to the PC via an RS-232 data connection.

A.3 Mass flow measurement

After a 2.4 m straight pipe, which acts as calming section, there is a Bronkhorst IN-FLOW F-106CI-ABD-03-V flow meter which measures air mass flow. It has an integrated controller which is directly connected to a Samson electropneumatic control valve. The desired mass flow set value is transmitted to the flow meter, which in turn directly controls the control valve accordingly. The maximum rated volume flow for the flow meter is 215 $g\,s^{-1}$

of air. Its accuracy is specified as ±1 % full scale which corresponds to a maximum error of $\pm 2.15\,\mathrm{g\,s^{-1}}$. During setup of the test facility, the flow meter was calibrated externally.

A.4 Pressure measurement

There are two types of absolute pressure sensors in operation: 10 Baumer PBSN-1.3.B22.-A.A2.14.06.2.1 and 2 setra ASM1010BA2M2C20A00. Both types have ranges from 0 bara to 10 bara and have an accuracy of ±0.5 % and ±0.05 % full scale respectively, which corresponds to ±0.05 bar and ±0.005 bar. The sensors are connected either through 2 mm inner diameter polyurethane tubing with push-in fittings or connected directly to their respective measuring point.

To determine the actual accuracy of the relative pressure measurement of turbine inlet and outlet pressure measurement, the respective sensors are compared to a Wika CPG 1000 digital pressure gauge with an accuracy of ±0.05% full scale and a measuring range from 0 barg to 7 barg, which results in an absolute measurement error of ±0.0035 bar. The sensors are connected to the calibration device and a handheld pump to generate pressures across the region of interest up to about 2.5 barg. Figure A.1 gives an overview over the calibration data. After correcting for the mean deviation, the remaining maximum fluctuation of the measurements is ±0.015 bar and ±0.016 bar for $\bar{p}_0$ and $\bar{p}_2$. Adding the maximum error of the calibration device results in a maximum error of the relative pressure measurement of $\Delta p_{0r} = \Delta p_{2r} = \pm 0.02$ bar.

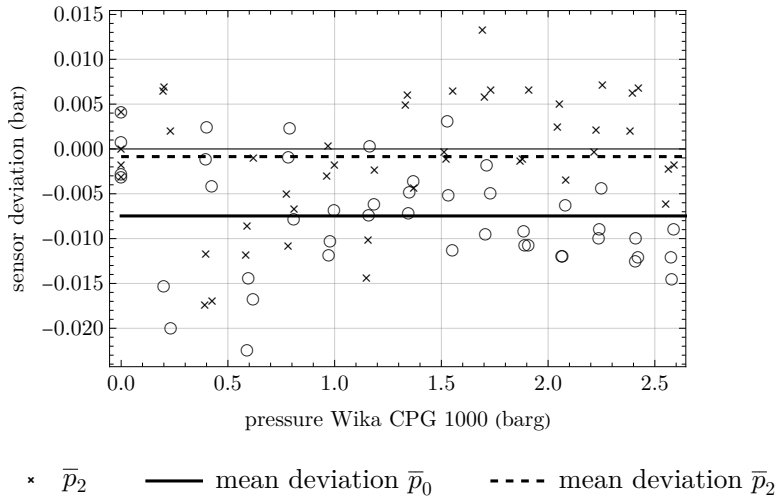

Figure A.1: Pressure calibration data for $\bar{p}_0$ and $\bar{p}_2$.

A.5 Temperature measurement

Temperatures are measured with type K thermocouples with an accuracy of ±2 °C. Prior to installation, all thermocouples are checked using a calibration oven.

A.6 Data acquisition hardware and control cabinet

Data acquisition is managed by a National Instruments cRIO-9022 controller together with the input/output modules listed in table A.1. The cRIO controller runs a custom

module	function	used for
NI 9205	voltage input ±10 V	pressure, mass flow, motor torque
NI 9213	thermocouple input	thermocouples
NI 9263	voltage output ±10 V	mass flow set value, motor set speed
NI 9402	digital input/output	motor speed (pulse count)

Table A.1: National Instruments cRIO modules.

LabVIEW [National Instruments, 2019] data acquisition program which consists of a loop that collects data from the measurement equipment in precise 100 ms intervals. Through an Ethernet connection, data is sent to a PC for storage and visualization. Speed and mass flow set values are received from the PC and distributed to the respective controllers. The accuracy of the NI 9205 voltage input module is specified as ±6.23 mV. The cRIO controller, together with other electrical equipment is located in a control cabinet shown in figure A.2. For the basic electrical layout, see figure A.3.

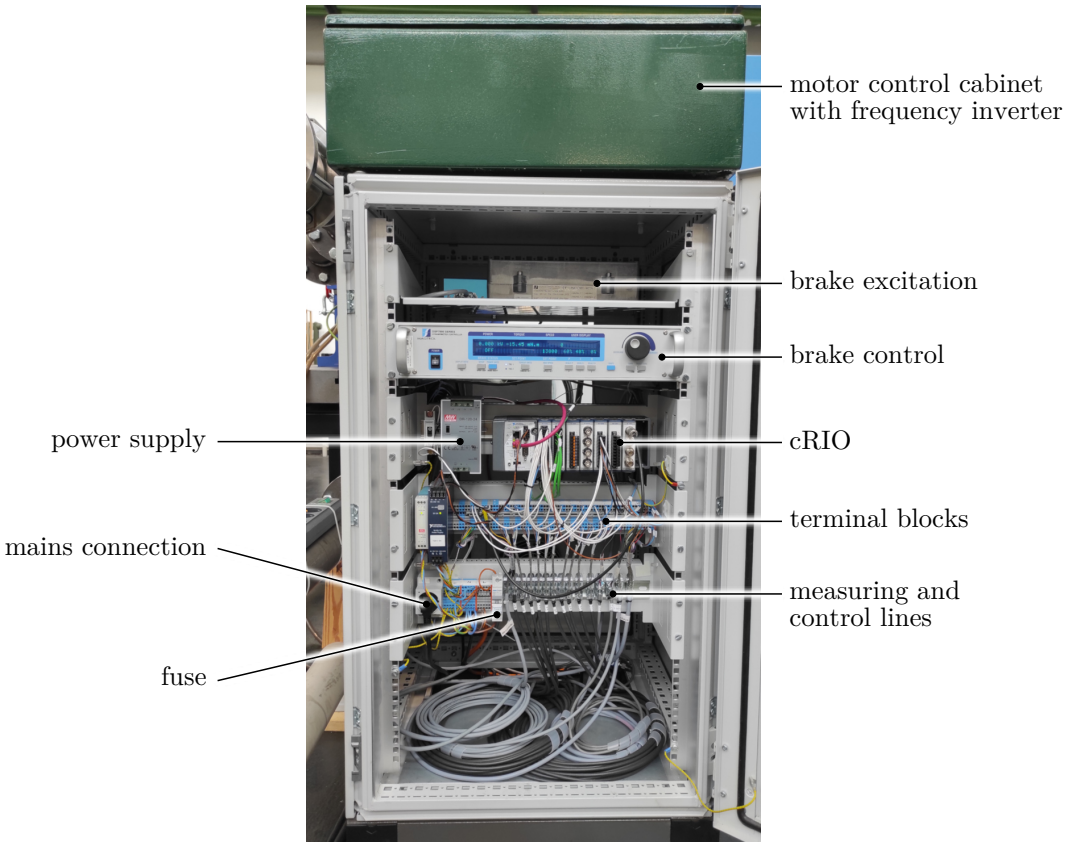

Figure A.2: Control cabinet overview.

A.7 User interface

The test facility can be operated from a PC running a custom LabVIEW [National Instruments, 2019] program, see figure A.4. All received measurement values are displayed and written into a CSV file for postprocessing. Set values for rotational speed and mass flow can be specified manually. The program can also be set to automatically run descending mass flow intervals of specified size and duration at constant rotational speed. In case

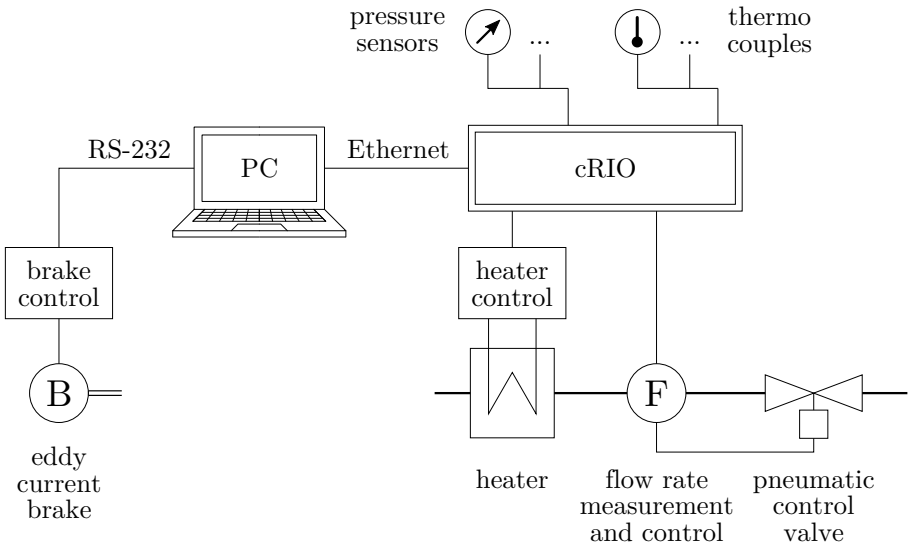

Figure A.3: Electrical layout of the test facility.

the mass flow exceeds the maximum possible supplied amount from the compressor, the pressure in the air tank decreases. When the pressure in the air tank drops below 7 bara, the program automatically decreases the mass flow to a small value and waits for the supply tank pressure to recover before continuing the mass flow intervals.

A.8 Test procedure

The test facility is used to map out turbine performance in dependence of mass flow and rotational speed for different turbine design configurations. Rotational speed is varied in steps of $2000\,\mathrm{min}^{-1}$, up to a maximum speed of $20\,000\,\mathrm{min}^{-1}$ and $18\,000\,\mathrm{min}^{-1}$ for aluminium and steel disks respectively. The mass flow range runs in steps of $5\,\mathrm{g\,s}^{-1}$ or less, starting from the minimum mass flow required to maintain the desired rotational speed. The upper mass flow limit is determined by plenum pressure. For too high mass flows, the disks eventually start rubbing on the housing because they are forced apart by the air stream. Each combination of mass flow and rotational speed is held constant for approximately 5 min to determine a single data point in the performance map. One performance map typically consists of 200-300 points.

The step-by-step procedure of a test run is as follows:

1. turbine start up and about 10 min of run-in time at variable rotational speeds and mass flows
2. accelerate turbine to maximum rotational speed
3. lower mass flow rate until rotational speed is just maintained, this determines the lower bound of mass flow and plenum pressure at the current rotational speed
4. increase mass flow until plenum pressure is about 1.5 bar above the lower bound, this determines the upper bound of mass flow and plenum pressure
5. hold these conditions for 5 min
6. lower mass flow by one step

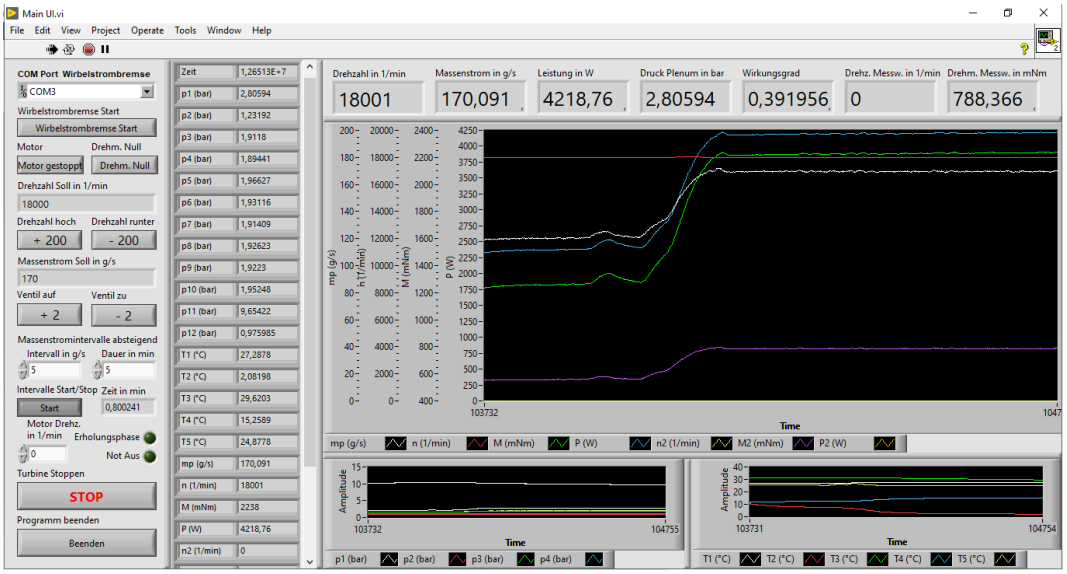

Figure A.4: User interface.

7. go to step 5 and repeat until lower mass flow bound is reached
8. lower rotational speed by one step
9. go to step 3 and repeat until rotational speed reaches zero.

A.9 Modification of the test bench for turbine loss measurement

For measuring friction, windage and leakage losses, the eddy current brake is replaced with a 7 kW Kemmerich HM90E-140-EL asynchronous motor to drive the turbine rotor, combined with an HBM T21WN torque transducer for torque and rotational speed measurement in the ranges of 1 N m and 20 000 min^{-1}. The expected measurement error is less than 0.5 % full scale or 0.005 N m and 100 min^{-1}. Figure A.5 shows the motor and torque transducer. The motor is controlled by a Toshiba VF-S15 frequency inverter. Rotational speed of the setup is limited by the inverter to 15 000 min^{-1}. To allow for controlling the small mass flows required for leakage measurement, the control valve is replaced by a smaller one. For windage and leakage loss measurement, the turbine rotor can be replaced by a solid aluminium dummy with a height of 30 mm, see figure A.6.

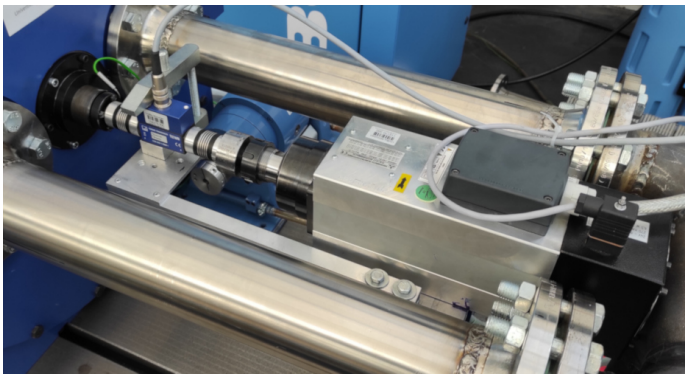

Figure A.5: Mounted motor and torque transducer.

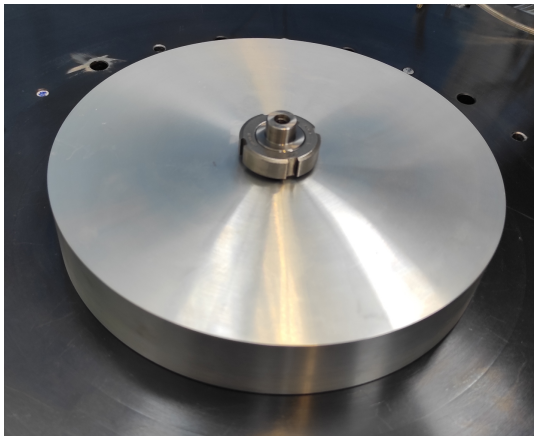

Figure A.6: Solid aluminium rotor dummy.

Appendix B

Turbine performance maps

The following figures B.1 to B.22 show all measured performance maps.

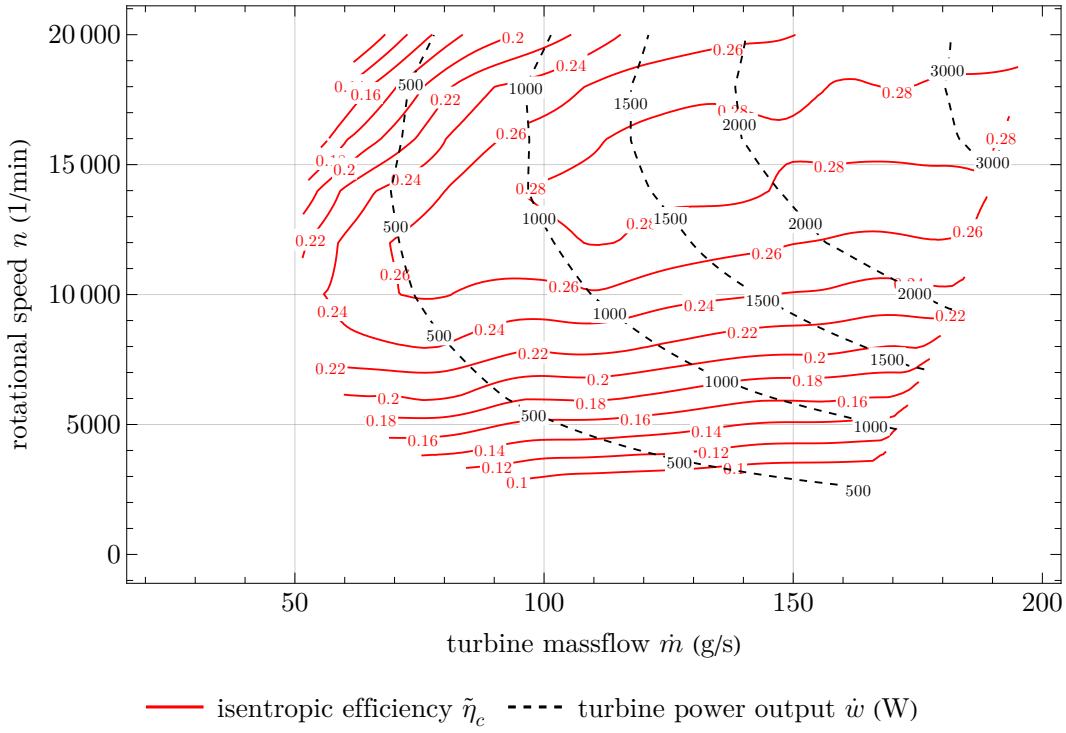

Figure B.1: Turbine performance map at 2-12-4 nozzle configuration and a rotor with 24 0.8 mm thick disks and two 3 mm end disks with a spacing of 0.2 mm between the disks.

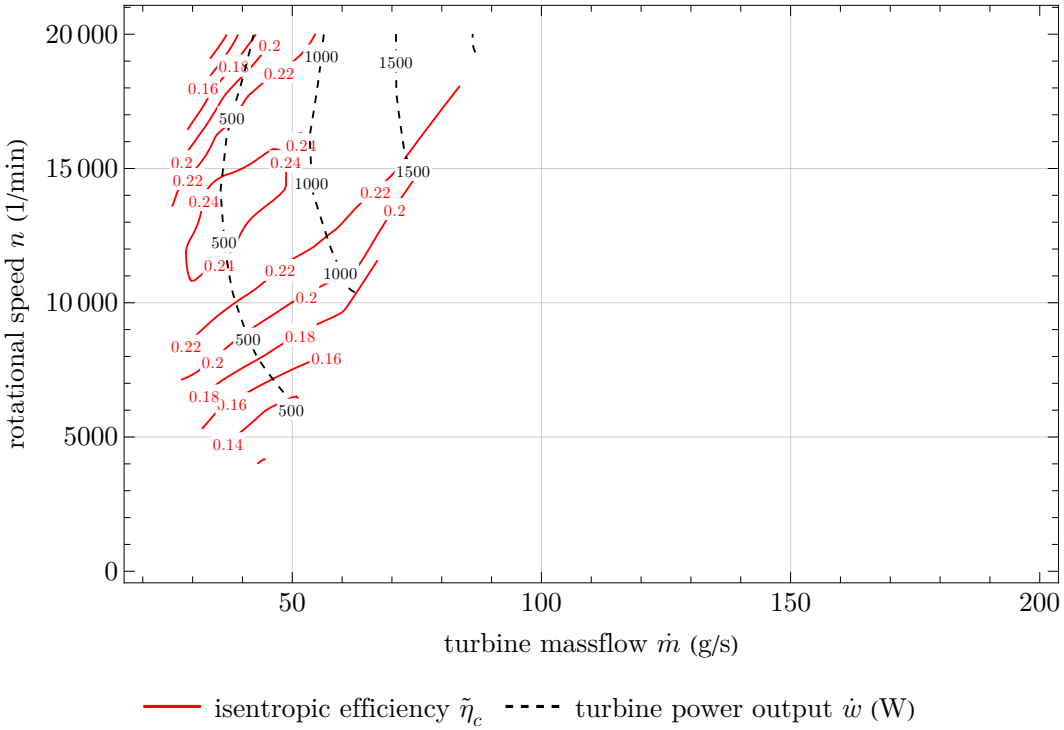

Figure B.2: Turbine performance map at 5-8-1 nozzle configuration and a rotor with 24 0.8 mm thick disks and two 3 mm end disks with a spacing of 0.2 mm between the disks.

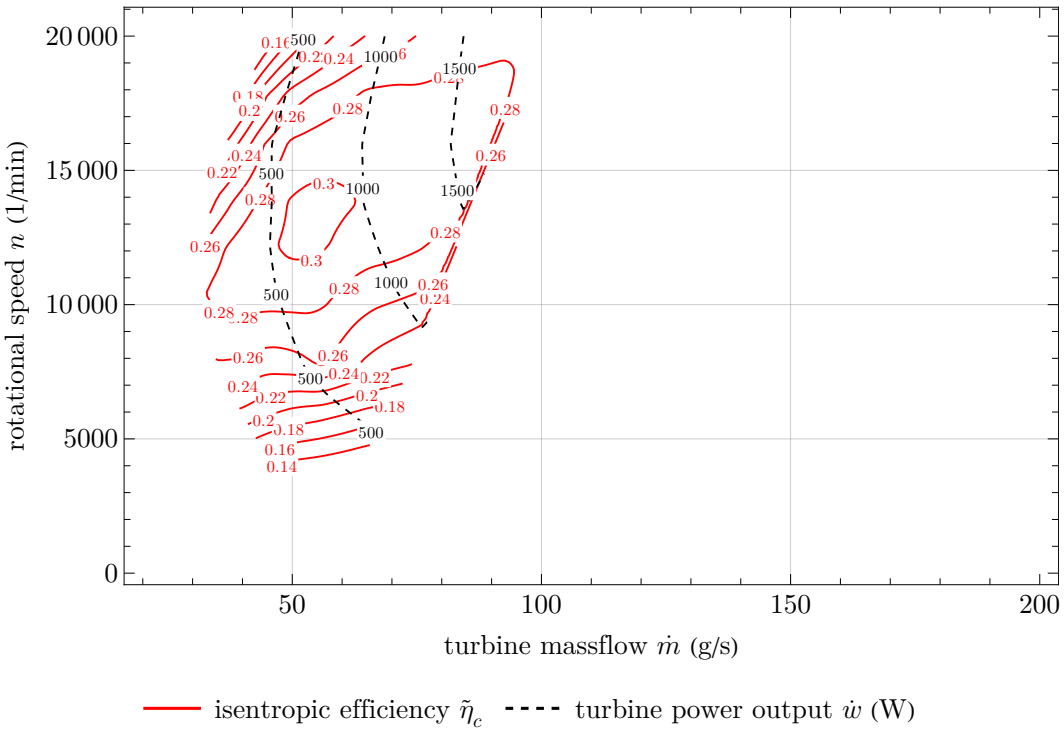

Figure B.3: Turbine performance map at 5-8-2 nozzle configuration and a rotor with 24 0.8 mm thick disks and two 3 mm end disks with a spacing of 0.2 mm between the disks.

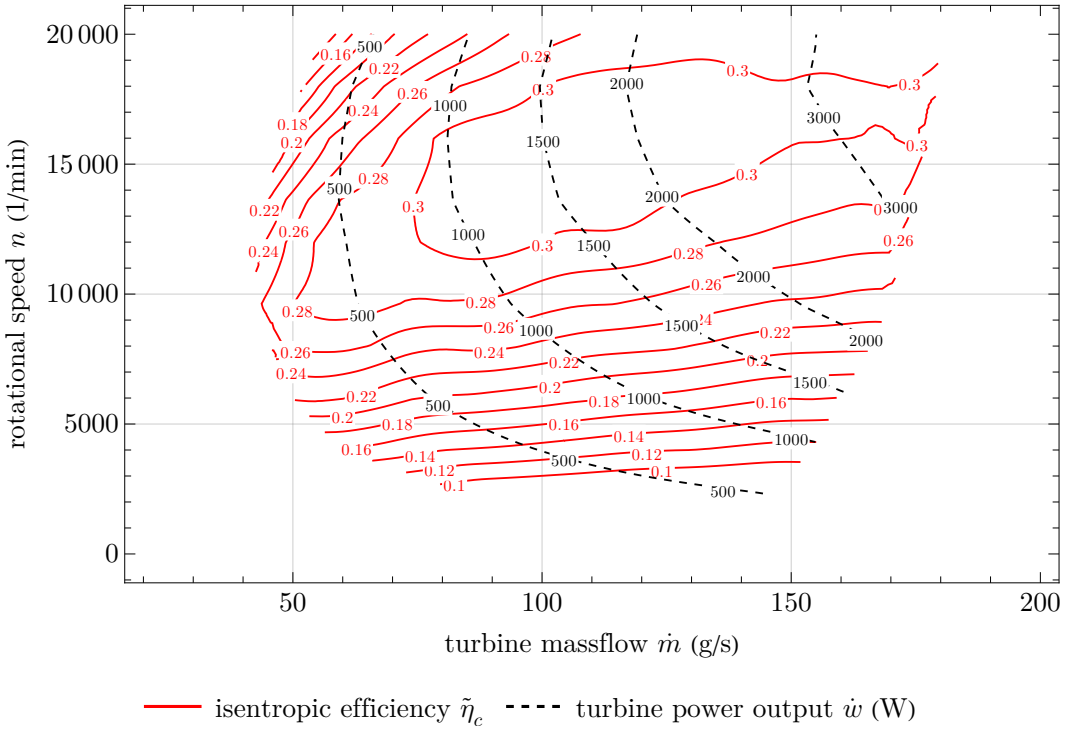

Figure B.4: Turbine performance map at 5-8-4 nozzle configuration and a rotor with 24 0.8 mm thick disks and two 3 mm end disks with a spacing of 0.2 mm between the disks.

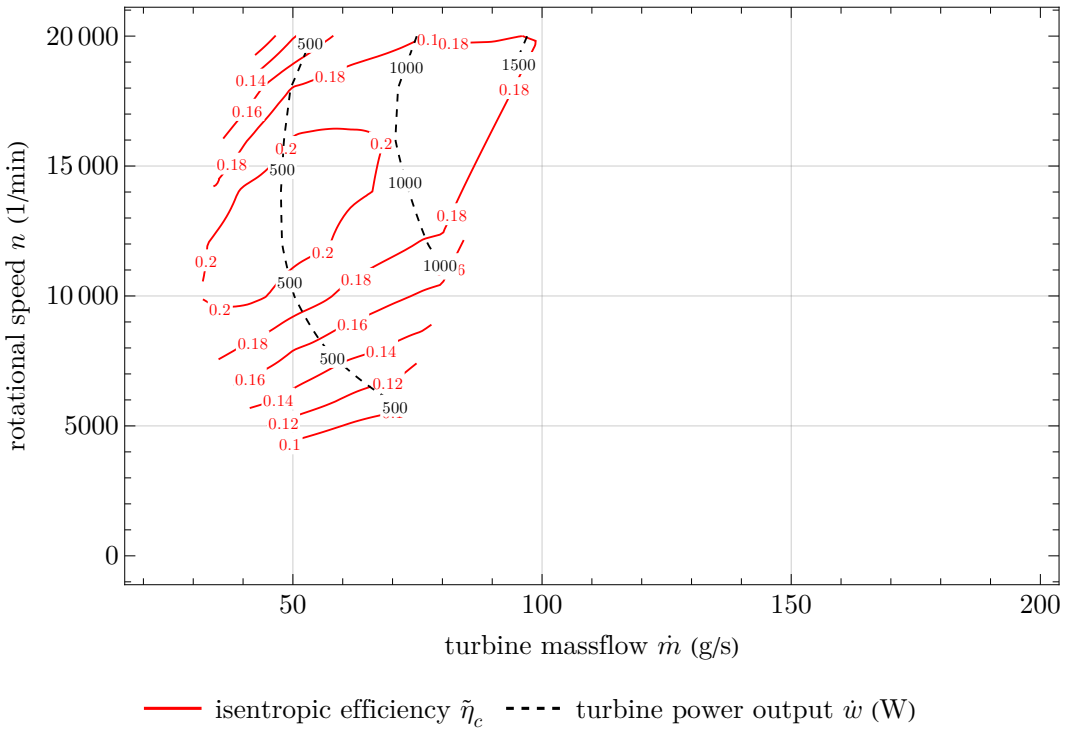

Figure B.5: Turbine performance map at 5-12-1 nozzle configuration and a rotor with 24 0.8 mm thick disks and two 3 mm end disks with a spacing of 0.2 mm between the disks.

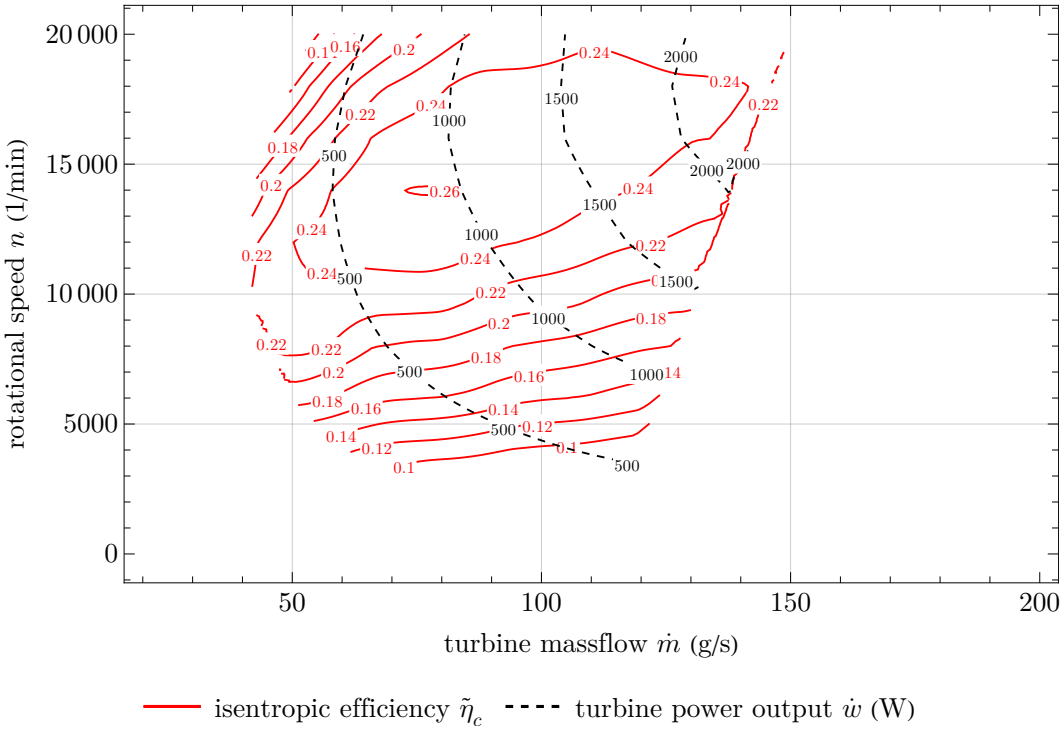

Figure B.6: Turbine performance map at 5-12-2 nozzle configuration and a rotor with 24 0.8 mm thick disks and two 3 mm end disks with a spacing of 0.2 mm between the disks.

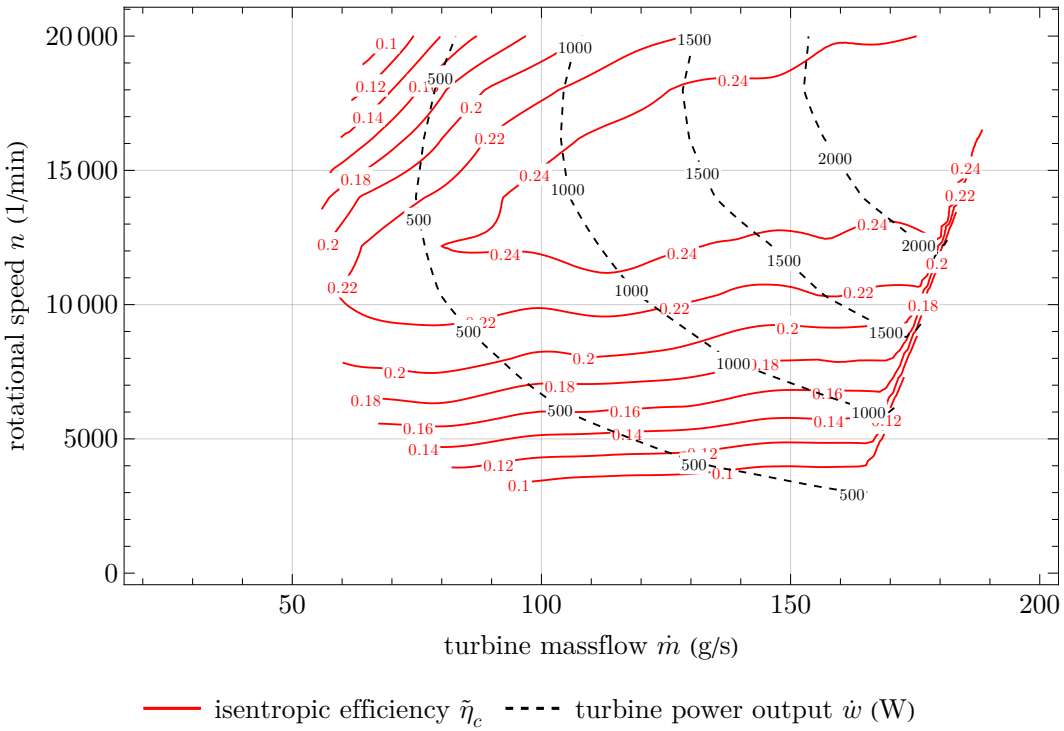

Figure B.7: Turbine performance map at 5-12-4 nozzle configuration and a rotor with 24 0.8 mm thick disks and two 3 mm end disks with a spacing of 0.2 mm between the disks.

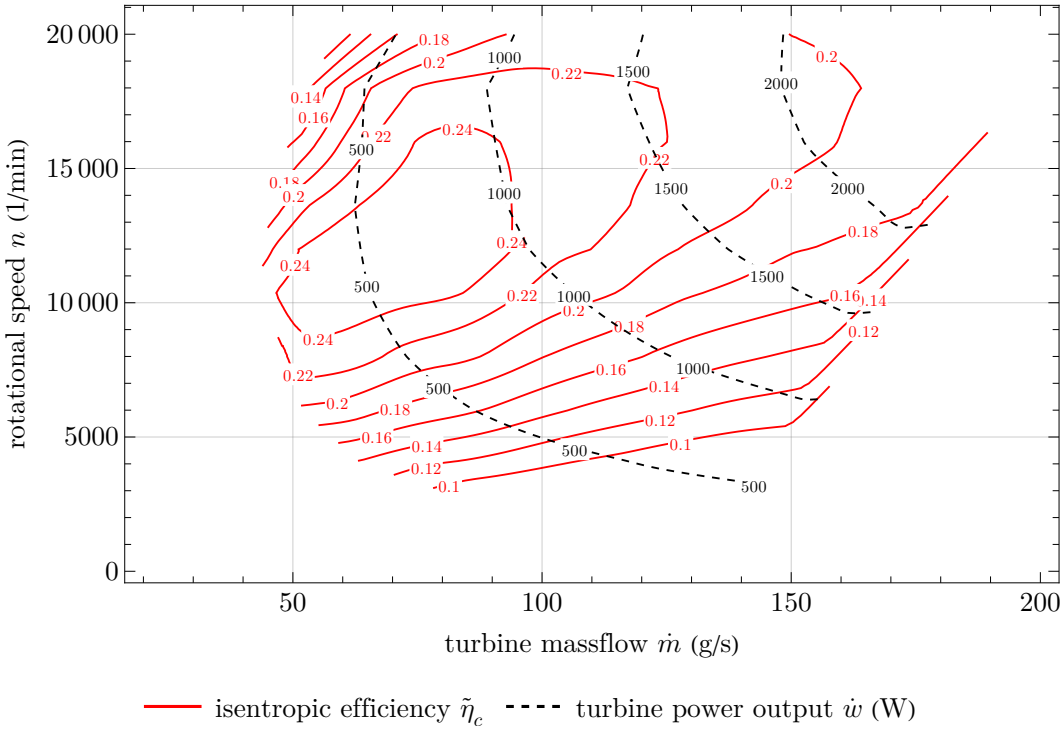

Figure B.8: Turbine performance map at 15-5-4 nozzle configuration and a rotor with 24 0.8 mm thick disks and two 3 mm end disks with a spacing of 0.2 mm between the disks.

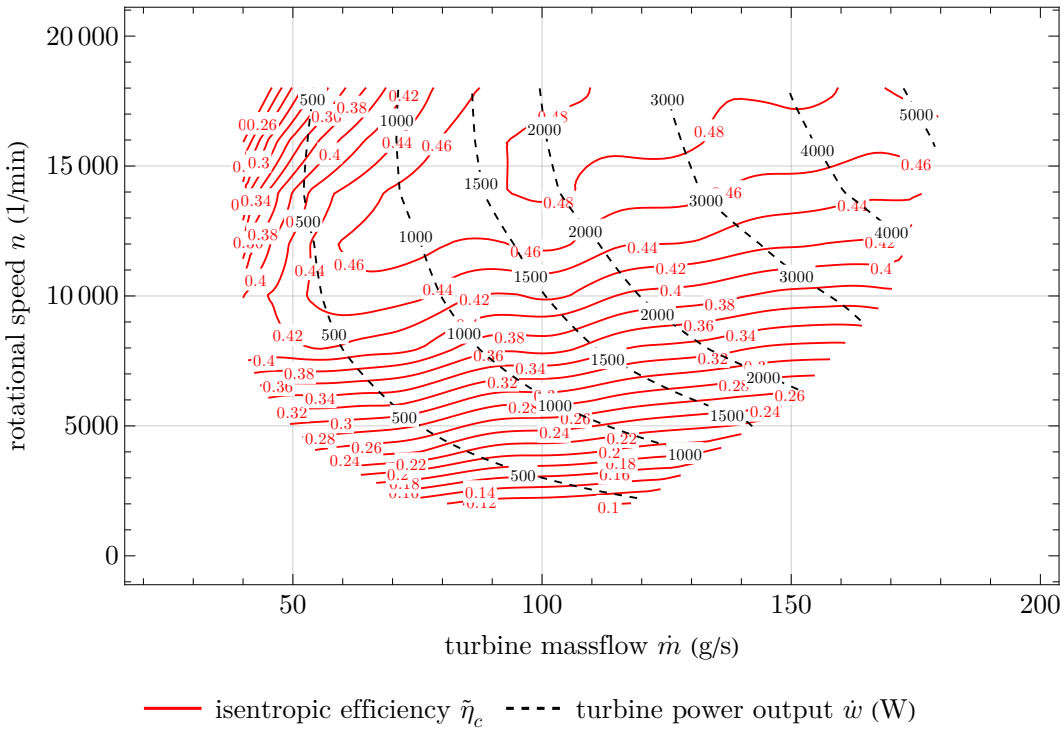

Figure B.9: Turbine performance map at 5-8-4 nozzle configuration and a rotor with 64 0.2 mm thick disks and two 3 mm end disks with a spacing of 0.2 mm between the disks.

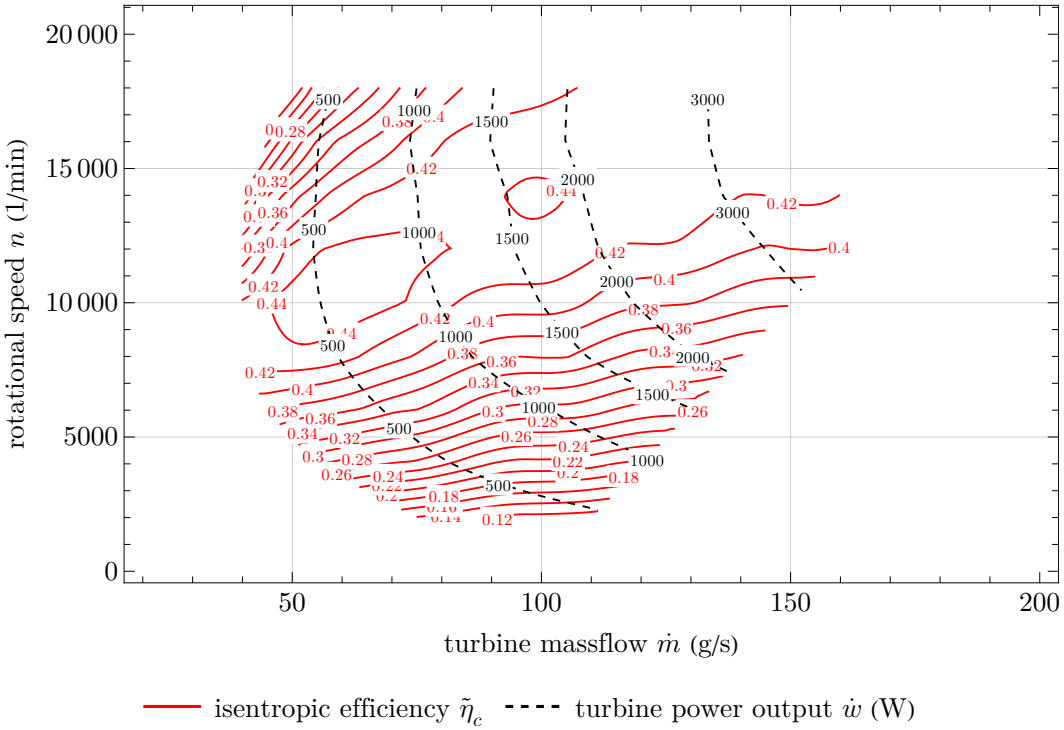

Figure B.10: Turbine performance map at 5-8-4 nozzle configuration and a rotor with 35 0.2 mm thick disks and two 3 mm end disks with a spacing of 0.5 mm between the disks.

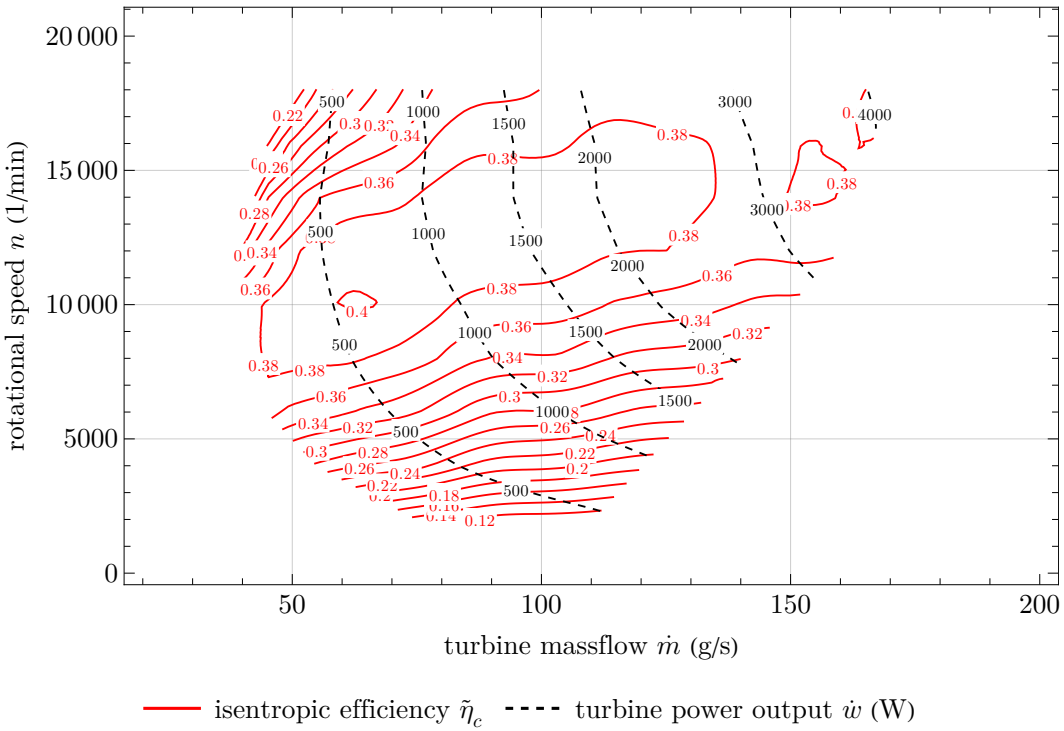

Figure B.11: Turbine performance map at 5-8-4 nozzle configuration and a rotor with 25 0.2 mm thick disks and two 3 mm end disks with a spacing of 0.8 mm between the disks.

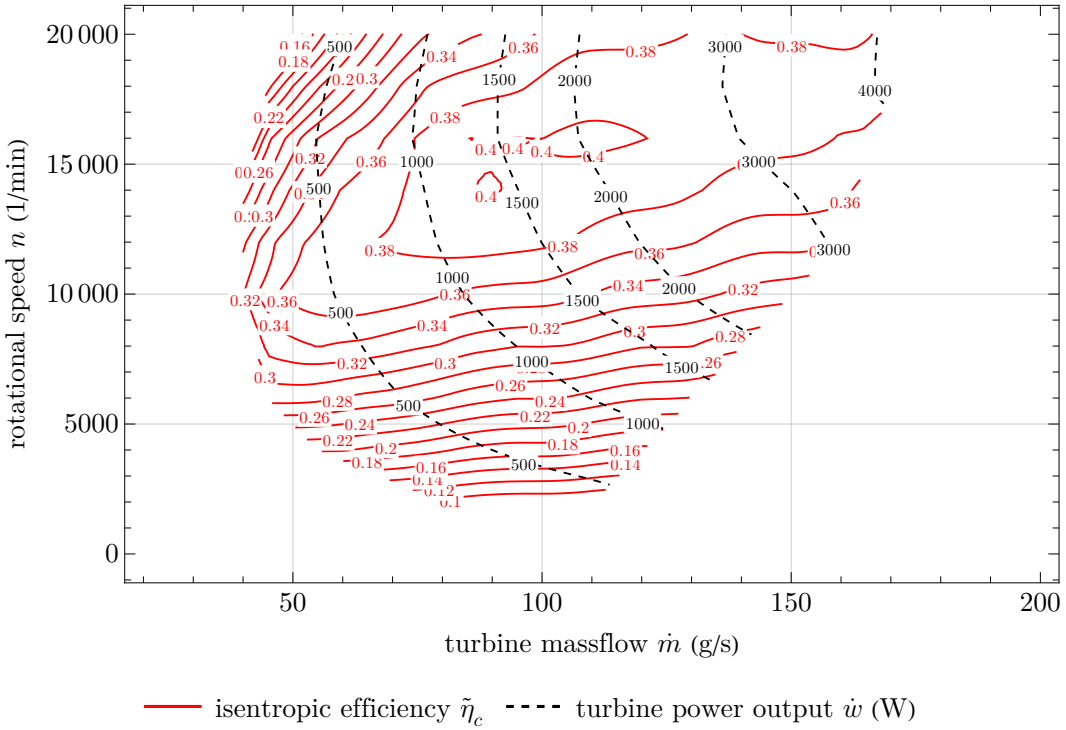

Figure B.12: Turbine performance map at 5-8-4 nozzle configuration and a rotor with 36 0.5 mm thick disks and two 3 mm end disks with a spacing of 0.2 mm between the disks.

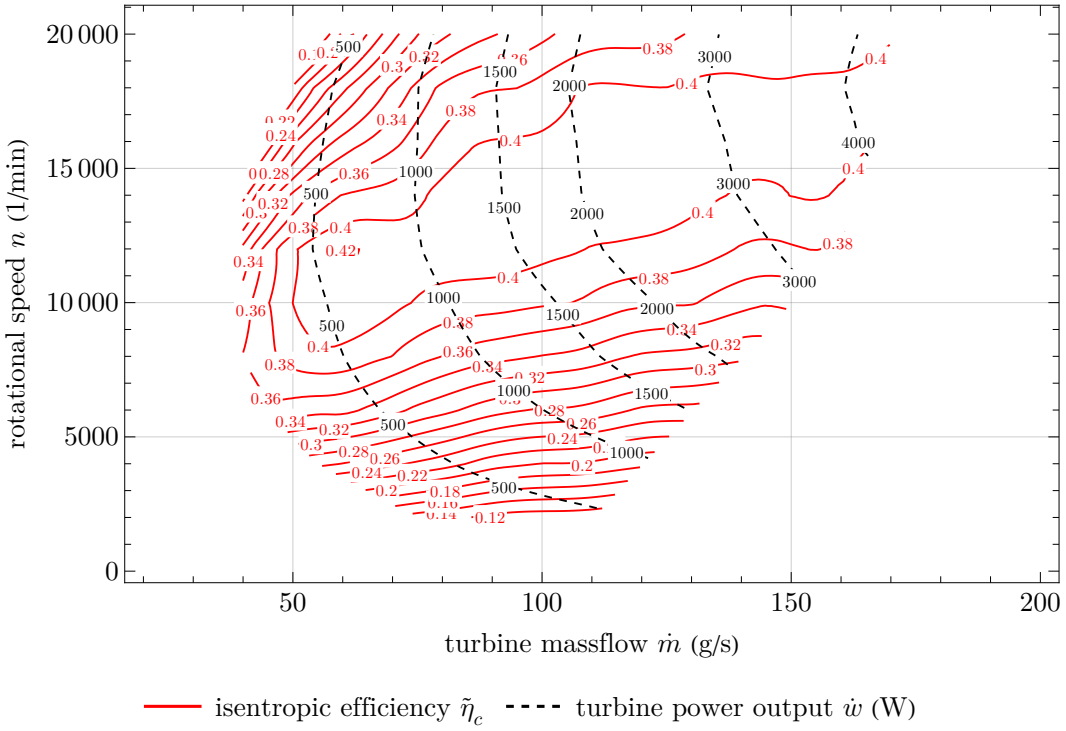

Figure B.13: Turbine performance map at 5-8-4 nozzle configuration and a rotor with 25 0.5 mm thick disks and two 3 mm end disks with a spacing of 0.5 mm between the disks.

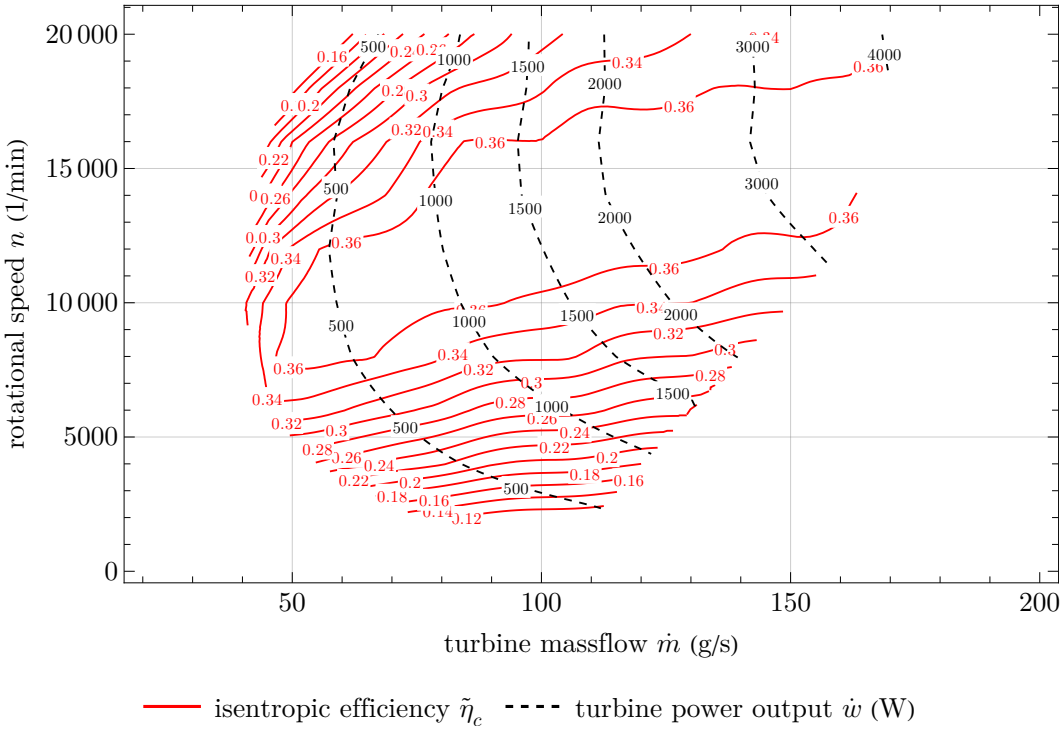

Figure B.14: Turbine performance map at 5-8-4 nozzle configuration and a rotor with 19 0.5 mm thick disks and two 3 mm end disks with a spacing of 0.8 mm between the disks.

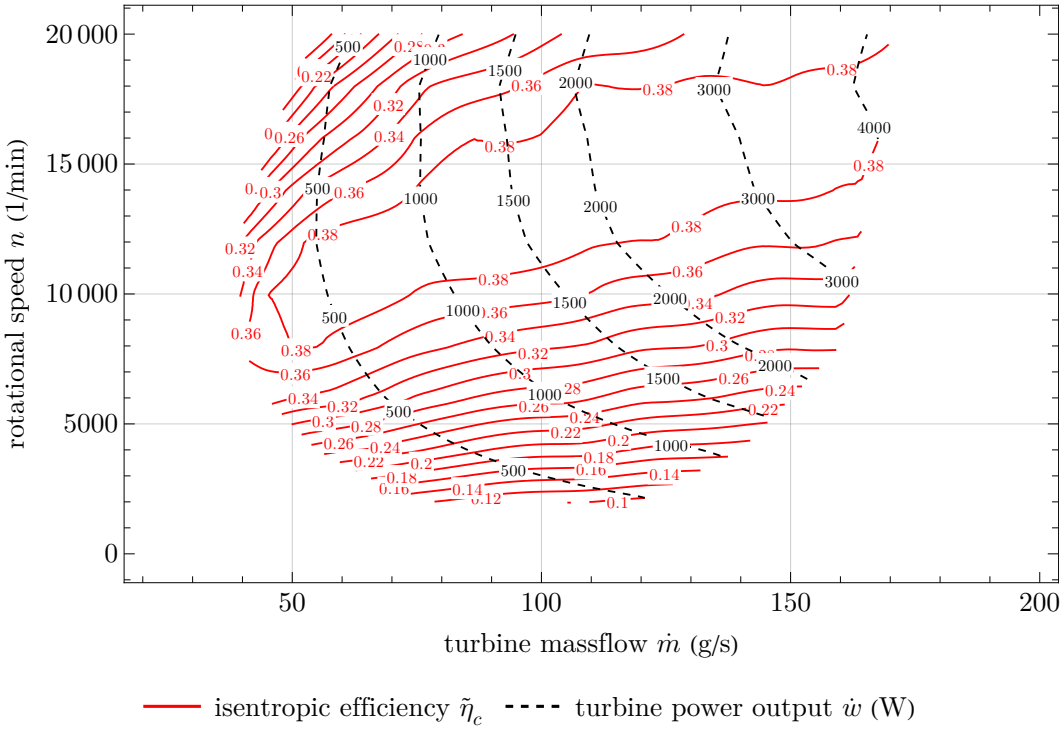

Figure B.15: Turbine performance map at 5-8-4 nozzle configuration and a rotor with 18 0.8 mm thick disks and two 3 mm end disks with a spacing of 0.5 mm between the disks.

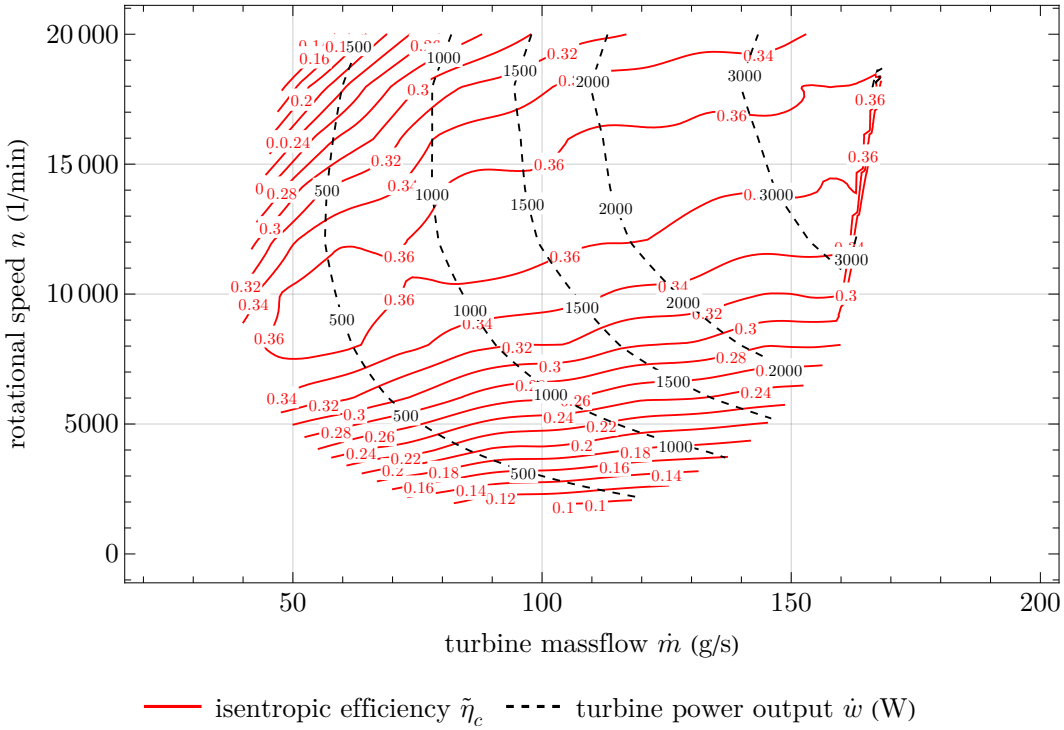

Figure B.16: Turbine performance map at 5-8-4 nozzle configuration and a rotor with 15 0.8 mm thick disks and two 3 mm end disks with a spacing of 0.8 mm between the disks.

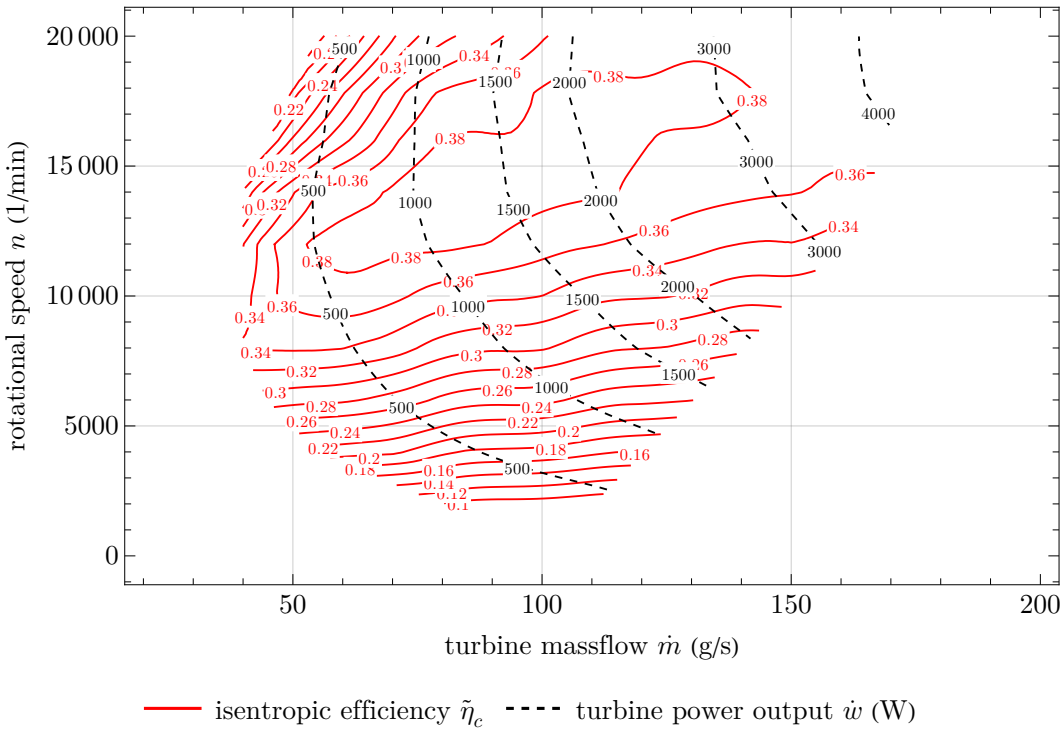

Figure B.17: Turbine performance map at 5-8-4 nozzle configuration and a rotor with 24 0.8 mm thick disks and two 3 mm end disks with a spacing of 0.2 mm between the disks. The outer edges of the 0.8 mm disks have a 15° bevel.

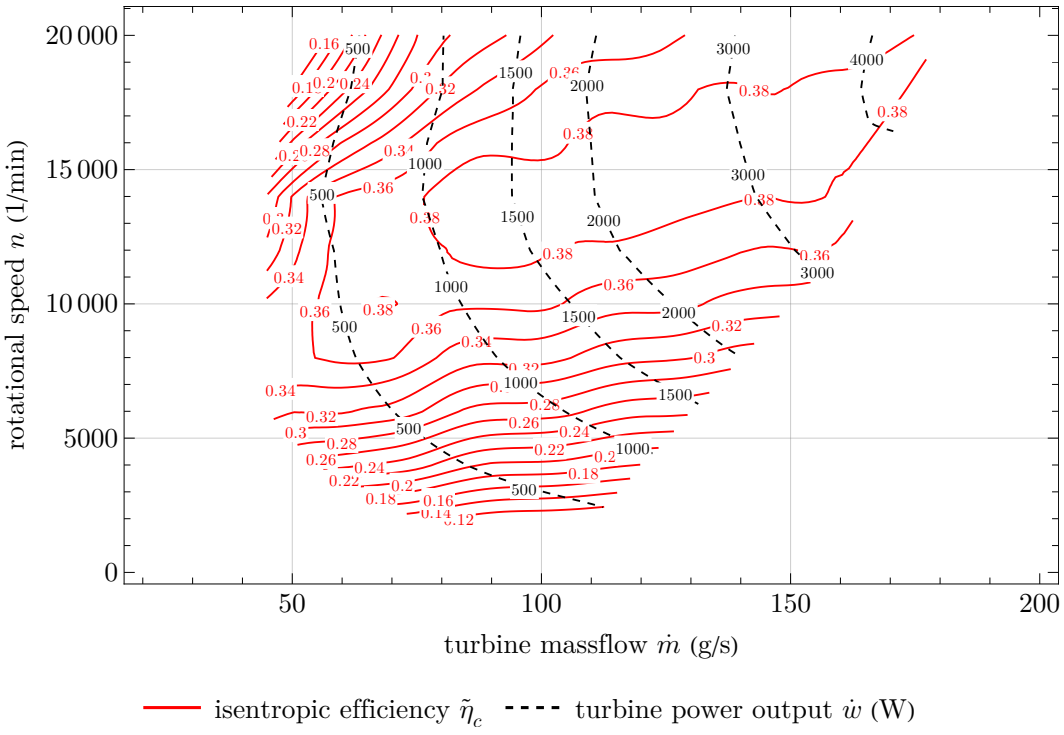

Figure B.18: Turbine performance map at 5-8-4 nozzle configuration and a rotor with 18 0.8 mm thick disks and two 3 mm end disks with a spacing of 0.5 mm between the disks. The outer edges of the 0.8 mm disks have a 15° bevel.

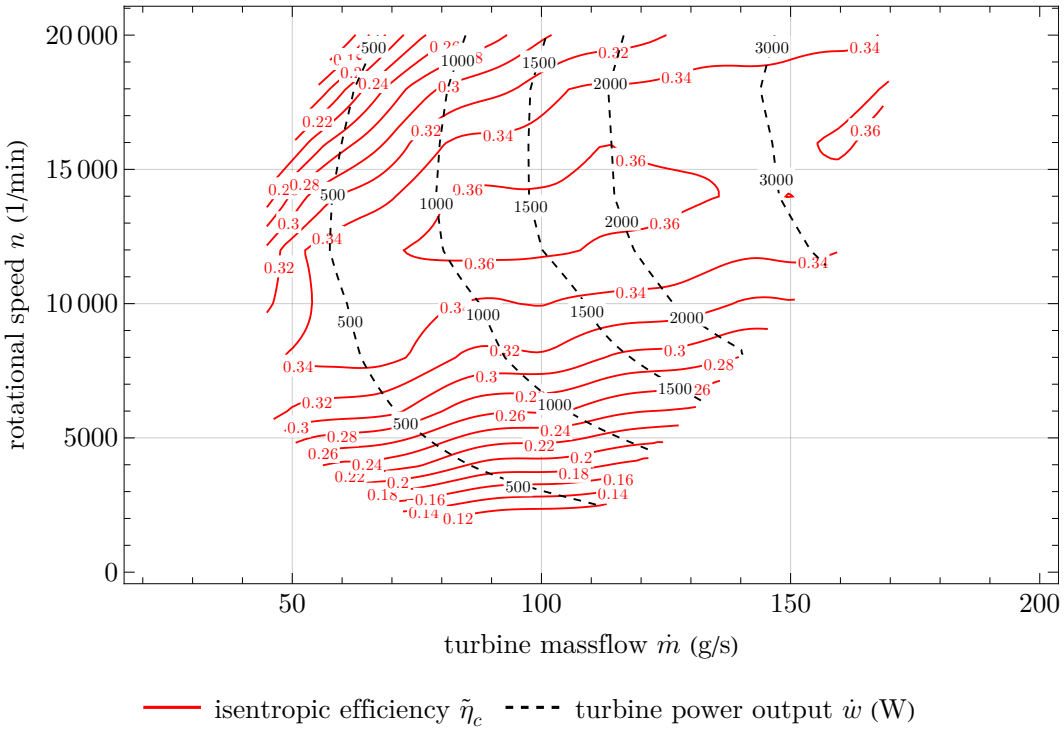

Figure B.19: Turbine performance map at 5-8-4 nozzle configuration and a rotor with 15 0.8 mm thick disks and two 3 mm end disks with a spacing of 0.8 mm between the disks. The outer edges of the 0.8 mm disks have a 15° bevel.

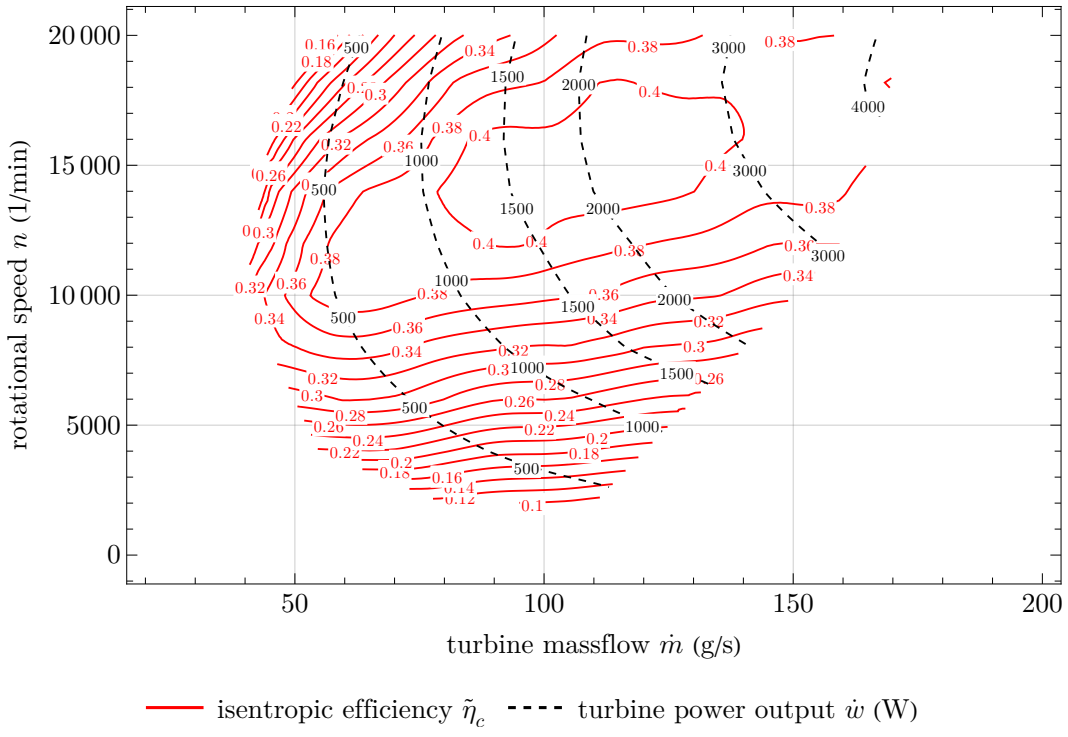

Figure B.20: Turbine performance map at 5-8-4 nozzle configuration and a rotor with 36 0.5 mm thick disks and two 3 mm end disks with a spacing of 0.2 mm between the disks. The surface of the disks is roughened concentrically with coarse sandpaper.

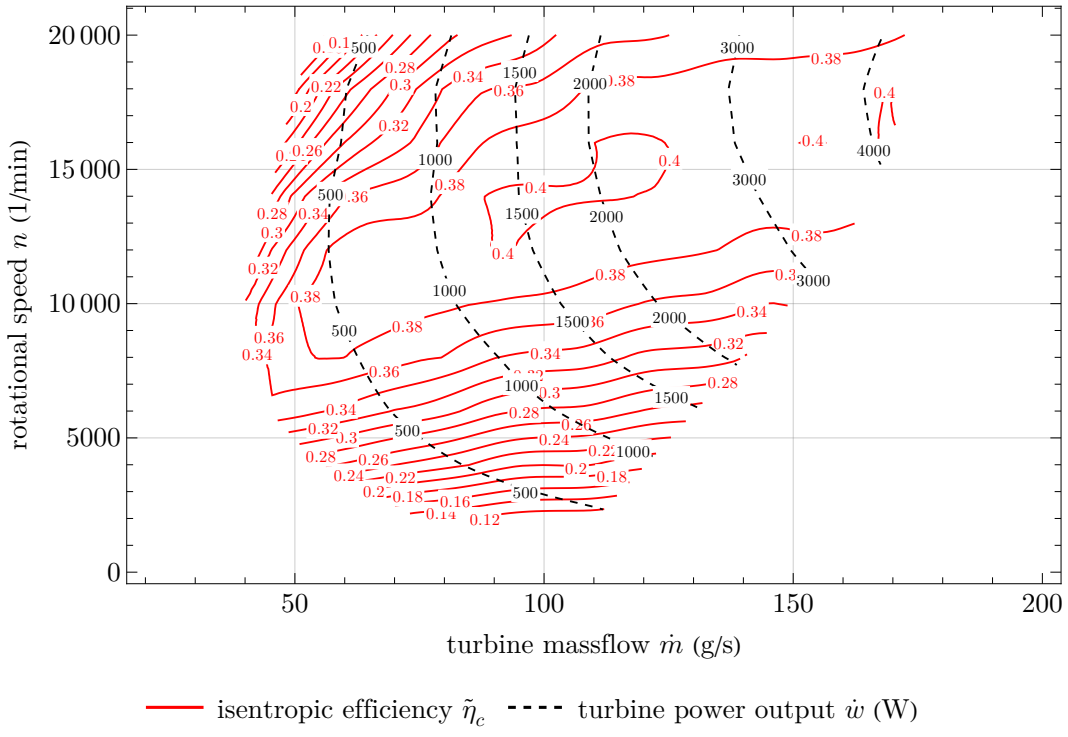

Figure B.21: Turbine performance map at 5-8-4 nozzle configuration and a rotor with 24 0.5 mm thick disks and two 3 mm end disks with a spacing of 0.5 mm between the disks. The surface of the disks is roughened concentrically with coarse sandpaper.

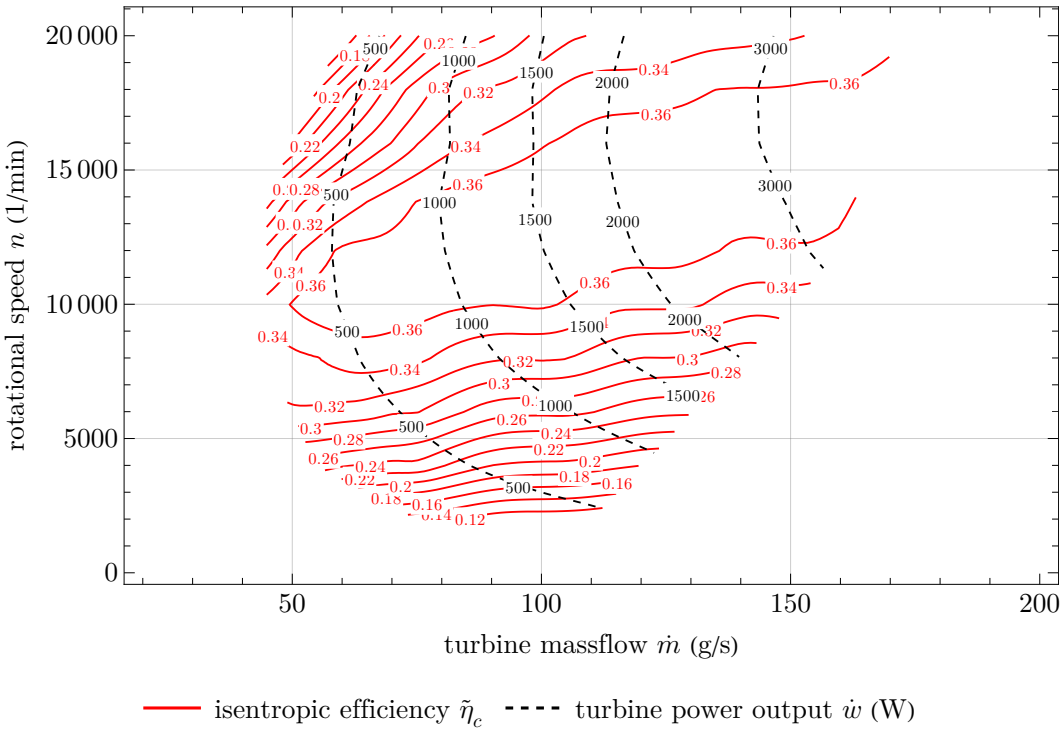

Figure B.22: Turbine performance map at 5-8-4 nozzle configuration and a rotor with 19 0.5 mm thick disks and two 3 mm end disks with a spacing of 0.8 mm between the disks. The surface of the disks is roughened concentrically with coarse sandpaper.

Bibliography

R. Adams and W. Rice. Experimental investigation of the flow between corotating disks. *Journal of Applied Mechanics*, 37(3):844–849, 1970.

A. Aghagoli and M. Sorin. CFD modelling and exergy analysis of a heat pump cycle with Tesla turbine using CO2 as a working fluid. *Applied Thermal Engineering*, 178:115587, 2020. ISSN 1359-4311. doi: 10.1016/j.applthermaleng.2020.115587. URL `https://www.sciencedirect.com/science/article/pii/S1359431120330696`.

Jeffrey Allen. A model for fluid flow between parallel, co-rotating annular disks. *Masters thesis, University of Dayton, Ohio*, 1990. doi: 10.2514/6.1989-838.

Mubarak S. Alrabie, Faisal N. Altamimi, Muhammad H. Altarrgemy, Fatemeh Hadi, Muhammad K. Akbar, and Matthew J. Traum. Method to design a hydro Tesla turbine for sensitivity to varying laminar reynolds number modulated by changing working fluid viscosity. In *ASME 2017 11th International Conference on Energy Sustainability*, Energy Sustainability, June 2017. doi: 10.1115/ES2017-3442. V001T07A004.

Jibsam Andres and Michael Loretero. Performance of Tesla turbine using open flow water source. *International Journal of Engineering Research and Technology*, 12(12):2191–2199, 2019.

ANSYS Inc. ANSYS CFX, release 19.0. 2018.

E. Appelquist, P. Schlatter, P. H. Alfredsson, and R. J. Lingwood. Transition to turbulence in the rotating-disk boundary-layer flow with stationary vortices. *Journal of Fluid Mechanics*, 836:43–71, 2018a. doi: 10.1017/jfm.2017.771.

E. Appelquist, P. Schlatter, P.H. Alfredsson, and R.J. Lingwood. Turbulence in the rotating-disk boundary layer investigated through direct numerical simulations. *European Journal of Mechanics - B/Fluids*, 70:6–18, 2018b. ISSN 0997-7546. doi: 10.1016/j.euromechflu.2018.01.008.

James Hal Armstrong. An investigation of the performance of a modified Tesla turbine. Master's thesis, Georgia Institute of Technology, 1952.

Autodesk. Autodesk Inventor 2022. *Build 26.0.15300*, 2022.

Pawel Baginski and Lukasz Jedrzejewski. The strength and dynamic analysis of the prototype of Tesla turbine. *Diagnostyka*, 16(3):17–24, 2015.

Seungjoon Baik, Hyeon Tae Kim, and Jeong Ik Lee. Preliminary test of friction disk type turbine for S-CO2 cycle application. In *Proceedings of the KNS 2016 spring meeting*, Korea, Republic of, 2016. KNS. URL `http://inis.iaea.org/search/search.aspx?orig_q=RN:48048557`.

C. E. Bassett. An integral solution for compressible flow through disc turbines. In *10th Intersociety Energy Conversion Engineering Conference, At Newark, Delaware*, 1975.

M. Batista. Steady flow of incompressible fluid between two co-rotating disks. *Applied Mathematical Modelling*, 35:5225–5233, 2011.

E. W. Beans. Performance characteristics of a friction disc turbine. *PhD thesis, Pennsylvania State University*, 1961.

E. W. Beans. Investigation into the performance characteristics of a friction turbine. *Journal of Spacecraft and Rockets*, 9(1):131–134, 1966.

B. E. Boyack and W. Rice. Integral method for flow between corotating disks. *Journal of Basic Engineering*, 93(3):350–354, September 1971. ISSN 0021-9223. doi: 10.1115/1.3425252.

K. E. Boyd and W. Rice. Laminar inward flow of an incompressible fluid between rotating disks with full peripheral admission. *Journal of Applied Mechanics*, 35(2):229–237, 1968.

James Braun, Guillermo Paniagua, and Francois Falempin. Aerothermal optimization of bladeless turbines. *Journal of Engineering for Gas Turbines and Power*, 143(3), March 2021. ISSN 0742-4795. doi: 10.1115/1.4049355. 031023.

M. C. Breiter and K. Pohlhausen. Laminar flow between two parallel rotating disks. *Report No. ARL 62-318. Aeronautical Research Laboratories, Wright-Patterson AFB, Ohio*, 1962.

Van P. Carey. Assessment of Tesla turbine performance for small scale rankine combined heat and power systems. *Journal of Engineering for Gas Turbines and Power*, 132(12), September 2010. ISSN 0742-4795. doi: 10.1115/1.4001356. 122301.

V. M. Chesnokov. Oscillations of a viscous fluid in a thin layer between coaxial rotating disks. *Akademiia Nauk SSSR Izvestiia Mekhanika Zhidkosti i Gaza*, 20:166–169, 1984.

J. W. Chew. A theoretical study of ingress for shrouded rotating disk systems with radial outflow. *Journal of Turbomachinery*, 113(1):91–97, January 1991. ISSN 0889-504X. doi: 10.1115/1.2927742.

L. Ciappi, D. Fiaschi, P.H. Niknam, and L. Talluri. Computational investigation of the flow inside a Tesla turbine rotor. *Energy*, 173:207–217, 2019. ISSN 0360-5442. doi: 10.1016/j.energy.2019.01.158. URL `https://www.sciencedirect.com/science/article/pii/S0360544219301744`.

E. Crespo Del Arco, E. Serre, P. Bontoux, and B. E. Launder. Stability, transition and turbulence in rotating cavities. *Advances in Fluid Mechanics/Adv. Fluid Mech.*, 41: 141–195, 2005.

Ryan Crowell. Generation of electricity utilizing solar hot water collectors and a Tesla turbine. In *ASME 2009 3rd International Conference on Energy Sustainability, Volume 1*, Energy Sustainability, pages 613–620, July 2009. doi: 10.1115/ES2009-90395.

James W. Daily and Ronald E. Nece. Chamber dimension effects on induced flow and frictional resistance of enclosed rotating disks. *Journal of Basic Engineering*, 82:217–230, 1960.

Abhijit Das. Analytical solution to the flow between two coaxial rotating disks using HAM. *Procedia Engineering*, 127:377–382, 2015. ISSN 1877-7058. doi: 10.1016/j.proeng.2015.11.384. URL `https://www.sciencedirect.com/science/article/pii/S1877705815037443`. International Conference On Computational Heat And Mass Transfer (ICCHMT) - 2015.

R. T. Deam, E. Lemma, B. Mace, and R. Collins. On scaling down turbines to millimeter size. *Journal of Engineering for Gas Turbines and Power*, 130(5), June 2008. ISSN 0742-4795. doi: 10.1115/1.2938516. 052301.

Robert J. Deissler. The convective nature of instability in plane Poiseuille flow. *The Physics of Fluids*, 30(8):2303–2305, 1987. doi: 10.1063/1.866118.

Sam W. Delaney. A parametric approach to Tesla turbine design for the organic rankine cycle. Master's thesis, San Diego State University, 2019.

Jacob Pieter Den Hartog. *Mechanical Vibrations*. McGraw-Hill, 1956.

Q. Deng, W. Qi, and Z. Feng. Improvement of a theoretical analysis method for Tesla turbines. *ASME Turbo Expo 2013: Turbine Technical Conference and Exposition, V06CT40A012*, 2013.

G. Dibelius and D. Nendl. *Reibungsturbomaschinen. Forschungsberichte Des Landes Nordrhein-Westfalen*. VS Verlag für Sozialwissenschaften, Wiesbaden, 1973. ISBN 978-3-322-88329-2. doi: 10.1007/978-3-322-88329-2_1.

E. Geoffrey Engelbrecht, Zoitis Giakoumis, Stathis Sidiropoulos, Alexandros Chasoglou, and Ndaona Chokani. Modelling phase change in a novel turbo expander for application to heat pumps and refrigeration cycles. In *E3S Web of Conferences*, volume 1 of *E3S Web of Conferences*, page 03012, September 2019. doi: 10.1051/e3sconf/201911303012.

G. A. Euteneuer and M. Piesche. Betriebsverhalten einer Reibungsturbine bei turbulentem Stromfeld und viskosem, inkompressiblem Medium im Spaltelement. *Forsch. Ing.-Wes.*, 44:79–84, 1978.

K. O. Felsch and M. Piesche. Ein Beitrag zur Berechnung der Strömung in einer Tesla-Turbine bei temperaturabhängiger Zähigkeit des Fördermediums. *Ingenieur-Archiv*, 50: 121–129, 1981.

Marco Ferrando, Michael Caminale, Federico Reggio, and Paolo Silvestri. Design and testing of a static rig for Tesla turbine flow visualization. *Turbo Expo: Power for Land, Sea, and Air*, Volume 6: Ceramics and Ceramic Composites; Coal, Biomass, Hydrogen, and Alternative Fuels; Microturbines, Turbochargers, and Small Turbomachines, June 2021. doi: 10.1115/GT2021-59175. V006T19A010.

Daniele Fiaschi and Lorenzo Talluri. Design and off-design analysis of a Tesla turbine utilizing CO_2 as working fluid. In *E3S Web of Conferences*, volume 1 of *E3S Web of Conferences*, page 03008, September 2019. doi: 10.1051/e3sconf/201911303008.

Edson Alves Figueira Júnior, Carlos Hanieri de Freitas Oliveira, Valério Luiz Borges, and Solidônio Rodrigues de Carvalho. Design of bladeless impellers for abrasive fluid pumping. *Journal of the Brazilian Society of Mechanical Sciences and Engineering*, 43 (4):225, 2021. ISSN 1806-3691. doi: 10.1007/s40430-021-02954-1.

J. E. Flaherty and R. C. DiPrima. Effect of a Coriolis force on the stability of plane Poiseuille flow. *The Physics of Fluids*, 21(5):718–726, 1978. doi: 10.1063/1.862289.

Marco Gambini and Michela Vellini. *Turbomachinery*. Springer International Publishing, 2021. doi: 10.1007/978-3-030-51299-6.

P. W. Garrison, D. W. Harvey, and I. Catton. Laminar compressible flow between rotating disks. *Journal of Fluids Engineering*, 98(3):382–388, September 1976. ISSN 0098-2202. doi: 10.1115/1.3448330.

Zoitis Giakoumis, E. Geoffrey Engelbrecht, Alexandros Chasoglou, and Ndaona Chokani. Computational investigation of a multiphase turbo expander for heat pumps and refrigeration cycles. In *Volume 5: Controls, Diagnostics, and Instrumentation; Cycle Innovations; Cycle Innovations: Energy Storage*, Turbo Expo: Power for Land, Sea, and Air, September 2020. doi: 10.1115/GT2020-15683. V005T06A030.

A Guha and B Smiley. Experiment and analysis for an improved design of the inlet and nozzle in Tesla disc turbines. *Proceedings of the Institution of Mechanical Engineers, Part A: Journal of Power and Energy*, 224(2):261–277, 2010. doi: 10.1243/09576509JPE818.

Abhijit Guha and Sayantan Sengupta. The fluid dynamics of the rotating flow in a Tesla disc turbine. *European Journal of Mechanics - B/Fluids*, 37:112–123, 2013. ISSN 0997-7546. doi: 10.1016/j.euromechflu.2012.08.001. URL `https://www.sciencedirect.com/science/article/pii/S099775461200091X`.

Abhijit Guha and Sayantan Sengupta. The physics of pressure variation in microchannels within corotating or static discs. *Physics of Fluids*, 28(10):103601, 2016. doi: 10.1063/1.4963370.

Abhijit Guha and Sayantan Sengupta. A non-dimensional study of the flow through corotating discs and performance optimization of a Tesla disc turbine. *Proceedings of the Institution of Mechanical Engineers, Part A: Journal of Power and Energy*, 231(8):721–738, 2017. doi: 10.1177/0957650917715148.

Anatolij Gusev and Fritz H. Bark. Stability of rotation-modified plane Poiseuille flow. *The Physics of Fluids*, 23(11):2171–2177, 1980. doi: 10.1063/1.862911.

Fatemeh Hadi, Haoping Yang, and Matthew J. Traum. Assessment of performance of Tesla turbine in water distribution systems for energy harvesting. *Journal of Energy Resources Technology*, 143(4), August 2020. ISSN 0195-0738. doi: 10.1115/1.4048018.042101.

Kai Han, Jianjun Luo, Jian Chen, Baodong Chen, Liang Xu, Yawei Feng, Wei Tang, and Zhong Lin Wang. Self-powered ammonia synthesis under ambient conditions via N2 discharge driven by Tesla turbine triboelectric nanogenerators. *Microsystems & Nanoengineering*, 7(1):7, 2021. ISSN 2055-7434. doi: 10.1038/s41378-020-00235-w.

Benjamín Herrmann-Priesnitz, Williams R. Calderón-Muñoz, Eduardo A. Salas, Alejandro Vargas-Uscategui, Manuel A. Duarte-Mermoud, and Diego A. Torres. Hydrodynamic structure of the boundary layers in a rotating cylindrical cavity with radial inflow. *Physics of Fluids*, 28(3):033601, 2016. doi: 10.1063/1.4943860.

Kris Holland. Design, construction and testing of a Tesla turbine. Master's thesis, Laurentian University, Sudbury, Ontario, Canada, 2015.

G P Hoya and A Guha. The design of a test rig and study of the performance and efficiency of a Tesla disc turbine. *Proceedings of the Institution of Mechanical Engineers, Part A: Journal of Power and Energy*, 223(4):451–465, 2009. doi: 10.1243/09576509JPE664.

Bo Hu, Dieter Brillert, Hans Josef Dohmen, and Friedrich-Karl Benra. Investigation on the flow in a rotor-stator cavity with centripetal through-flow. *International Journal of Turbomachinery, Propulsion and Power*, 2(4), 2017. ISSN 2504-186X. doi: 10.3390/ijtpp2040018. URL `https://www.mdpi.com/2504-186X/2/4/18`.

I. E. Idel'chik. *Handbook of Hydraulic Resistance, Coefficients of Local Resistance and Friction (translated from Russian)*. U.S. Department of Commerce, Clearinghouse for Federal Scientific and Technical Information Springfield, 1966.

Lukasz Jedrzejewski and Piotr Lampart. Tesla friction-type micro turbine for small-scale cogeneration. *RED. ZAGR. ANGIELSKI*, 2:132–137, 2011.

Fenzhu Ji, Yangping Bao, Yu Zhou, Farong Du, Hongji Zhu, Shuai Zhao, Guo Li, Xuefeng Zhu, and Shuiting Ding. Investigation on performance and implementation of Tesla turbine in engine waste heat recovery. *Energy Conversion and Management*, 179:326–338, 2019. ISSN 0196-8904. doi: 10.1016/j.enconman.2018.10.071. URL `https://www.sciencedirect.com/science/article/pii/S0196890418311993`.

Huiqing Jin, Wei-Yang Lu, April Nissen, Kevin Nelson, and Timothy Briggs. Mechanical properties of woven composites at ambient temperature. August 2018. doi: 10.2172/1463448. URL `https://www.osti.gov/biblio/1463448`.

Magnus Jonsson, Adrian Zurbuchen, Andreas Haeberlin, Alois Pfenniger, and Rolf Vogel. Vascular turbine powering a cardiac pacemaker: An in-vivo case study. *Experimental and clinical cardiology*, 20:2000–2003, March 2014.

Muhammad Ali Kamran and Shahryar Manzoor. Effect of nozzle angle, turbine inlets and mass flow rate on the performance of a bladeless turbine. *Proceedings of the Institution of Mechanical Engineers, Part A: Journal of Power and Energy*, 234(8):1101–1107, 2020. doi: 10.1177/0957650919893539.

Th. V. Kármán. Über laminare und turbulente Reibung. *Journal of Applied Mathematics and Mechanics / Zeitschrift für Angewandte Mathematik und Mechanik*, 1(4):233–252, 1921.

S. Klingl, S. Lecheler, and M. Pfitzner. Linear stability investigations on the inward flow between closely spaced co-rotating disks. *European Journal of Mechanics - B/Fluids*, 84:455–469, 2020. ISSN 0997-7546. doi: 10.1016/j.euromechflu.2020.07.007.

S. Klingl, S. Lecheler, and M. Pfitzner. Absolute and convective stability of flow between closely spaced co-rotating disks with imposed throughflow. *European Journal of Mechanics - B/Fluids*, 91:226–232, 2022. ISSN 0997-7546. doi: 10.1016/j.euromechflu.2021.10.012.

S. Klingl, S. Lecheler, and M. Pfitzner. Direct numerical simulation of laminar, transitional and turbulent radially inward flow between closely spaced corotating disks. *European Journal of Mechanics - B/Fluids*, 105:119–137, 2024. ISSN 0997-7546. doi: https://doi.org/10.1016/j.euromechflu.2024.01.007. URL `https://www.sciencedirect.com/science/article/pii/S0997754624000153`.

Vedavalli Krishnan. *Design and Fabrication of cm-Scale Tesla Turbines*. PhD thesis, University of California, Berkeley, May 2015.

P. Lampart and L. Jedrzejewski. Investigations of aerodynamics of Tesla blade-less microturbines. *Journal of Theoretical and Applied Mechanics*, 49:477–499, 2011.

Piotr Lampart, Krzysztof Kosowski, Marian Piwowarski, and Lukasz Jedrzejewski. Design analysis of Tesla micro-turbine operating on a low-boiling medium. *Polish Maritime Research - POL MARIT RES*, 16:28–33, January 2009. doi: 10.2478/v10012-008-0041-5.

Brian Launder, Sébastien Poncet, and Eric Serre. Laminar, transitional, and turbulent flows in rotor-stator cavities. *Annual Review of Fluid Mechanics*, 42(1):229–248, 2010. doi: 10.1146/annurev-fluid-121108-145514.

E. Lemma, R. T. Deam, D. Tonchich, and R. Collins. Characterisation of a small viscous flow turbine. *Experimental Thermal and Fluid Science*, 33(1):96–105, 2008.

Bu-Yang Li, Nan-Sheng Liu, and Xi-Yun Lu. Direct numerical simulation of wall-normal rotating turbulent channel flow with heat transfer. *International Journal of Heat and Mass Transfer*, 49(5):1162–1175, 2006. ISSN 0017-9310. doi: 10.1016/j.ijheatmasstransfer.2005.08.030. URL `https://www.sciencedirect.com/science/article/pii/S0017931005005545`.

Ruixiong Li, Huanran Wang, Erren Yao, Meng Li, and Weigang Nan. Experimental study on bladeless turbine using incompressible working medium. *Advances in Mechanical Engineering*, 9(1):1687814016686935, 2017. doi: 10.1177/1687814016686935.

R. J. Lingwood. Absolute instability of the boundary layer on a rotating disk. *Journal of Fluid Mechanics*, 299:17–33, 1995. doi: 10.1017/S0022112095003405.

R. J. Lingwood. Absolute instability of the Ekman layer and related rotating flows. *Journal of Fluid Mechanics*, 331:405–428, 1997. doi: 10.1017/S0022112096004144.

Roberto Lisker and Udo Hellwig. The application of a thin liquid film at the outlet of a Tesla turbine. *International Journal of Advanced Research in Innovative Discoveries in Engineering and Applications*, 2(4):1–8, 2017.

Roberto Lisker, Udo Hellwig, and Franz-Xaver Wildenauer. Entwicklung und Leistungsbestimmung einer 2,2 kW Tesla Turbine. *Wissenschaftliche Beiträge 2015*, 19:61–66, 2015.

Roberto Lisker, Udo Hellwig, and Franz-Xaver Wildenauer. Thin film condensation in a Tesla turbine. *Wissenschaftliche Beiträge 2017*, 21:71–76, 2017.

Kurt Löffler. *Die Berechnung von rotierenden Scheiben und Schalen*. Springer, 1961.

Magtrol. WB series eddy-current dynamometers. *data sheet*, 2022. URL `https://www.magtrol.com/product/eddy-current-dynamometers-wb-series/`.

G. Manfrida, L. Pacini, and L. Talluri. An upgraded Tesla turbine concept for ORC applications. *Energy*, 158:33–40, 2018. ISSN 0360-5442. doi: 10.1016/j.energy.2018.05.181. URL `https://www.sciencedirect.com/science/article/pii/S0360544218310259`.

L. Matsch and W. Rice. Flow at low Reynolds number with partial admission between rotating disks. *Journal of Applied Mechanics*, 34(3):768–770, September 1967a. ISSN 0021-8936. doi: 10.1115/1.3607779.

L. Matsch and W. Rice. An asymptotic solution for laminar flow of an incompressible fluid between rotating disks. *Journal of Applied Mechanics*, 35(1):155–159, 1968.

Lee Matsch and Warren Rice. Potential flow between two parallel circular disks with partial admission. *Journal of Applied Mechanics*, 34(1):239–240, March 1967b. ISSN 0021-8936. doi: 10.1115/1.3607643.

K. W. McAlister and W. Rice. Throughflows between rotating surfaces of revolution, having similarity solutions. *Journal of Applied Mechanics*, 37(4):924–930, December 1970. ISSN 0021-8936. doi: 10.1115/1.3408719.

A.T. McDonald, R.W. Fox, and R.V. Van Dewoestine. Effects of swirling inlet flow on pressure recovery in conical diffusers. *AIAA Journal*, 9(10):2014–2018, 1971.

A. Mehdizadeh and M. Oberlack. Analytical and numerical investigations of laminar and turbulent Poiseuille–Ekman flow at different rotation rates. *Physics of Fluids*, 22(10): 105104, 2010. doi: 10.1063/1.3488039.

Amirfarhang Mehdizadeh. *Direct Numerical Simulation, Lie Group Analysis and Modeling of a Turbulent Channel Flow with Wall-Normal Rotation*. PhD thesis, Technische Universität, Darmstadt, März 2010. URL `http://tuprints.ulb.tu-darmstadt.de/2092/`.

Gerald Miller and Rainer Fink. Analysis of optimal design configurations for a multiple disk centrifugal blood pump. *Artificial Organs*, 23(6):559–565, June 1999. doi: 10.1046/j.1525-1594.1999.06403.x.

Tomohito Miura and Jiro Mizushima. Stability of flow between two corotating disks in an enclosure. *Physics of Fluids*, 19(6):068106, 2007. doi: 10.1063/1.2747543.

H. D. Murphy, F. W. Chambers, and D. M. Mceligot. Laterally converging flow. part 1. mean flow. *Journal of Fluid Mechanics*, 127:379–401, 1983. doi: 10.1017/S0022112083002785.

Vikranth H. Nagaraja, Soikat Ghosh Moulic, Jennifer V. D'souza, M. Limesh, Peter Walters, and Jeroen H. M. Bergmann. A novel respiratory control and actuation system for upper-limb prosthesis users: Clinical evaluation study. *IEEE Access*, 10:128764–128778, 2022. doi: 10.1109/ACCESS.2022.3226697.

National Instruments. LabView version 19.0.1f3. 2019.

David Navarro-Alarcon, Luiza Labazanova, Man Kiu Chow, and Kwun Wang Ng. Can a Tesla turbine be utilised as a non-magnetic actuator for MRI-guided robotic interventions? In *2021 IEEE International Conference on Robotics and Biomimetics (ROBIO)*, pages 1735–1742, 2021. doi: 10.1109/ROBIO54168.2021.9739336.

Nek5000. Version 19.0. 28.12.2019. *Argonne National Laboratory, Illinois*, 2019. URL `https://nek5000.mcs.anl.gov`.

D. Nendl. Reibungsturbine. *VDI-Berichte*, 193:287–293, 1973.

D. Nendl. Dreidimensionale laminare Instabilitäten bei ebenen Wänden. *ZAMM - Journal of Applied Mathematics and Mechanics / Zeitschrift für Angewandte Mathematik und Mechanik*, 56(S1):T211–T213, 1976. doi: 10.1002/zamm.19765613089.

Carlo Alberto Niccolini Marmont Du Haut Champ, Paolo Silvestri, and Federico Reggio. Experimental validation of a rotor-bearings system model for Tesla turbines resonances prediction. *Turbo Expo: Power for Land, Sea, and Air*, Volume 4: Cycle Innovations; Cycle Innovations: Energy Storage, June 2022. doi: 10.1115/GT2022-81710. V004T06A015.

Pouriya H. Niknam, Lorenzo Talluri, Lorenzo Ciappi, and Daniele Fiaschi. Numerical assessment of a two-phase Tesla turbine: Parametric analysis. *Applied Thermal Engineering*, 197:117364, 2021. ISSN 1359-4311. doi: 10.1016/j.applthermaleng.2021.117364. URL `https://www.sciencedirect.com/science/article/pii/S1359431121007997`.

M. Nishioka, S. Iid A, and Y. Ichikawa. An experimental investigation of the stability of plane Poiseuille flow. *Journal of Fluid Mechanics*, 72(4):731–751, 1975. doi: 10.1017/S0022112075003254.

Konstantinos Ntatsis, Anastasia Chatziangelidou, Theofilos Efstathiadis, Vasilis G. Gkoutzamanis, Paolo Silvestri, and Anestis I. Kalfas. CFD analysis of a Tesla turboexpander using single phase steam. In *Proceedings of Global Power and Propulsion Society*, 2019.

Herbert Oertel and Ludwig Prandtl, editors. *Prandtl - Führer durch die Strömungslehre*. Springer Reference Technik. Springer Vieweg, Wiesbaden, 14. auflage edition, 2017. ISBN 9783658086268.

Herbert Jr. Oertel and Jan Delfs. *Strömungsmechanische Instabilitäten*. Springer, Berlin, Heidelberg, 1996. ISBN 978-3-540-56984-8. doi: 10.1007/978-3-642-60931-2.

Steven A. Orszag. Accurate solution of the Orr–Sommerfeld stability equation. *Journal of Fluid Mechanics*, 50(4):689–703, 1971. doi: 10.1017/S0022112071002842.

Nikhil Patel and Darren D. Schmidt. Biomass boundary layer turbine power system. In *2002 International Joint Power Generation Conference*, International Joint Power Generation Conference, pages 931–934, June 2002. doi: 10.1115/IJPGC2002-26035.

L. L. Pater, E. Crowther, and W. Rice. Flow regime definition for flow between corotating disks. *Journal of Fluids Engineering*, 96(1):29–34, March 1974. ISSN 0098-2202. doi: 10.1115/1.3447090.

Larry Lamann Pater. *Transition of Inward Flow between Closely Spaced Corotating Disks*. PhD thesis, Arizona State University, 1973.

Daniel Pfeffer. *Druckluftbetriebene Kleinturbinen für mobile Anwendungen*. PhD thesis, Technische Universität, Darmstadt, 2020. URL `http://tuprints.ulb.tu-darmstadt.de/9644/`.

Guilherme M. Placco and Lamartine N. F. Guimarães. Power analysis on a 70-mm rotor Tesla turbine. *Journal of Energy Resources Technology*, 142(3), September 2019. ISSN 0195-0738. doi: 10.1115/1.4044569. 031202.

S. Poncet, M. P. Chauve, and P. Le Gal. Turbulent rotating disk flow with inward throughflow. *Journal of Fluid Mechanics*, 522:253–262, 2005. doi: 10.1017/S0022112004002046.

Romuald Puzyrewski and Krzysztof Tesch. 1D model callibration on the basis of 3D calculations for Tesla turbine. *TASK Quarterly*, 14(iss. 3):67–78, 2010.

Wenjiao Qi, Qinghua Deng, Zhenping Feng, and Qi Yuan. Influence of disc spacing distance on the aerodynamic performance and flow field of Tesla turbines. In *Volume 8: Microturbines, Turbochargers and Small Turbomachines; Steam Turbines*, Turbo Expo: Power for Land, Sea, and Air, June 2016. doi: 10.1115/GT2016-57971. V008T23A035.

Wenjiao Qi, Qinghua Deng, Zhinan Chi, Lehao Hu, Qi Yuan, and Zhenping Feng. Influence of disc tip geometry on the aerodynamic performance and flow characteristics of multichannel Tesla turbines. *Energies*, 12(3), 2019a. ISSN 1996-1073. doi: 10.3390/en12030572. URL `https://www.mdpi.com/1996-1073/12/3/572`.

Wenjiao Qi, Qinghua Deng, Yu Jiang, Zhenping Feng, and Qi Yuan. Aerodynamic performance and flow characteristics analysis of Tesla turbines with different nozzle and outlet geometries. *Proceedings of the Institution of Mechanical Engineers, Part A: Journal of Power and Energy*, 233(3):358–378, 2019b. doi: 10.1177/0957650918785312.

Wenjiao Qi, Qinghua Deng, Yu Jiang, Qi Yuan, and Zhenping Feng. Disc thickness and spacing distance impacts on flow characteristics of multichannel Tesla turbines. *Energies*, 12(1), 2019c. ISSN 1996-1073. doi: 10.3390/en12010044. URL `https://www.mdpi.com/1996-1073/12/1/44`.

Wenjiao Qi, Qinghua Deng, Shuxia Yuan, and Bing Chen. Advantages of the aerodynamic performance of micro-Tesla turbines. *Energy Science & Engineering*, 11(5):1734–1752, 2023. doi: 10.1002/ese3.1417.

Anthony Randriamampianina, Roland Schiestel, and Michael Wilson. Spatio-temporal behaviour in an enclosed corotating disk pair. *Journal of Fluid Mechanics*, 434:39–64, 2001. doi: 10.1017/s0022112001003433.

Jung Raunak, Raunak Pandey, Sanam Pudasaini, Saurav Dhakal, Rangeet Uprety, and Hari Neopane. Design and computational analysis of 1 kW Tesla turbine. *International Journal of Scientific and Research Publications*, 4(11), November 2014.

Avinash Renuke and Alberto Traverso. Performance assessment of Tesla expander using 3D numerical simulation. *Journal of Engineering for Gas Turbines and Power*, page 111006, September 2022. ISSN 0742-4795. doi: 10.1115/1.4055486.

Avinash Renuke, Alberto Traverso, and Matteo Pascenti. Experimental campaign tests on a Tesla micro-expanders. In *E3S Web of Conferences*, volume 1 of *E3S Web of Conferences*, page 03015, September 2019. doi: 10.1051/e3sconf/201911303015.

Avinash Renuke, Alberto Vannoni, Matteo Pascenti, and Alberto Traverso. Experimental and numerical investigation of small-scale Tesla turbines. *Journal of Engineering for Gas Turbines and Power*, 141(12):121011, November 2019. ISSN 0742-4795. doi: 10.1115/1.4044999. 121011.

Avinash Renuke, Federico Reggio, Paolo Silvestri, Alberto Traverso, and Matteo Pascenti. Experimental investigation on a 3 kW air Tesla expander with high speed generator. volume Volume 5: Controls, Diagnostics, and Instrumentation; Cycle Innovations; Cycle Innovations: Energy Storage of *Turbo Expo: Power for Land, Sea, and Air*, 09 2020. doi: 10.1115/GT2020-14572. URL `https://doi.org/10.1115/GT2020-14572`. V005T06A006.

W. Rice. An analytical and experimental investigation of multiple-disk turbines. *Journal for Engineering for Power*, 87(1):29–36, 1965.

Upendar Rohatgi and Eli Reshotko. Analysis of laminar flow between stationary and rotating disks with inflow. *NASA Contractor Reports*, February 1974.

V. D. Romanin. *Theory and Performance of Tesla Turbines.* PhD thesis, University of California, Berkeley, 2012.

V. D. Romanin and V. P. Carey. An integral perturbation model of flow and momentum transport in rotating microchannels with smooth or microstructured wall surfaces. *Physics of Fluids*, 23(8):082003, 2011.

Vince Romanin, Van P. Carey, and Zack Norwood. Strategies for performance enhancement of Tesla turbines for combined heat and power applications. In *ASME 2010 4th International Conference on Energy Sustainability, Volume 2*, Energy Sustainability, pages 57–64, May 2010. doi: 10.1115/ES2010-90251.

K Rusin, W Wróblewski, and M Strozik. Experimental and numerical investigations of Tesla turbine. *Journal of Physics: Conference Series*, 1101:012029, October 2018a. doi: 10.1088/1742-6596/1101/1/012029.

Krzysztof Rusin. The influence of outlet system geometry on tesla turbine working parameters. *Acta Innovations*, pages 58–67, 2017. URL `https://api.semanticscholar.org/CorpusID:204291600`.

Krzysztof Rusin, Włodzimierz Wróblewski, and Sebastian Rulik. The evaluation of numerical methods for determining the efficiency of Tesla turbine operation. *Journal of Mechanical Science and Technology*, 32(12):5711–5721, 2018b. ISSN 1976-3824. doi: 10.1007/s12206-018-1118-4.

Krzysztof Rusin, Włodzimierz Wróblewski, and Michał Strozik. Comparison of methods for the determination of Tesla turbine performance. *Journal of Theoretical and Applied Mechanics*, 57(3):563–575, 2019. ISSN 1429-2955. doi: 10.15632/jtam-pl/109602.

Krzysztof Rusin, Emad Hasani Malekshah, Włodzimierz Wróblewski, and Sebastian Rulik. Improvement of the semi-analytical model of a Tesla disc turbine by the correction of the velocity profile. Volume 10B: Turbomachinery — Axial Flow Turbine Aerodynamics; Deposition, Erosion, Fouling, and Icing; Radial Turbomachinery Aerodynamics, June 2022. doi: 10.1115/GT2022-83879. V10BT35A016.

P. I. San'kov and E. M. Smirnov. Asymptotic solution of the Navier-Stokes equations for radial fluid flow in the gap between two rotating disks. *Journal of Applied Mechanics and Technical Physics*, 24(1):8–12, 1983. ISSN 1573-8620. doi: 10.1007/BF00914469.

Hermann Schlichting and Klaus Gersten. *Boundary Layer Theory.* Springer Berlin Heidelberg, Berlin, Heidelberg, 2017. ISBN 978-3-662-52919-5. doi: 10.1007/978-3-662-52919-5_3.

Peter J. Schmid and Dan S. Henningson. *Stability and Transition in Shear Flows.* Springer New York, New York, NY, 2001. ISBN 978-1-4613-0185-1. doi: 10.1007/978-1-4613-0185-1_9.

C. Schosser. Experimental and numerical investigations and optimisation of Tesla-radial turbines. *Dissertation, Universität der Bundeswehr, München*, 2016.

C. Schosser and M. Pfitzner. A numerical study of the three-dimensional incompressible rotor airflow within a Tesla turbine. *Proceedings of Conference on Modelling Fluid Flow CMFF'15, Budapest, Hungary*, 2015.

C. Schosser, S. Klingl, S. Lecheler, T. Fuchs, R. Hain, C. Kähler, and M. Pfitzner. Comprehensive investigation of the flow in a narrow gap between co-rotating disks. *European Journal of Mechanics - B/Fluids*, 78:50–61, 2019. ISSN 0997-7546. doi: 10.1016/j.euromechflu.2019.05.014.

Constantin Schosser, Stefan Lecheler, and Michael Pfitzner. Analytical and numerical solutions of the rotor flow in Tesla turbines. *Periodica Polytechnica Mechanical Engineering*, 61(1):12–22, 2017. doi: 10.3311/PPme.9000. URL `https://pp.bme.hu/me/article/view/9000`.

Scientific American. The Tesla steam turbine. *Scientific American*, 105(14):296–297, 1911. doi: 10.1038/scientificamerican09301911-296.

E. Semin. Gas turbine without blades (in russian, translated to english via https://www.deepl.com). *Technica Molodezhi*, (5), 1962.

S. Sengupta and A. Guha. A theory of Tesla disc turbines. *Proceedings of the Institution of Mechanical Engineers, Part A: Journal of Power and Energy*, 226(5):650–663, 2012.

S. Sengupta and A. Guha. Analytical and computational solutions for three-dimensional flow-field and relative pathlines for the rotating flow in a Tesla disc turbine. *Computers & Fluids*, 88:344–353, 2013.

Sayantan Sengupta and Abhijit Guha. Inflow-rotor interaction in Tesla disc turbines: Effects of discrete inflows, finite disc thickness, and radial clearance on the fluid dynamics and performance of the turbine. *Proceedings of the Institution of Mechanical Engineers, Part A: Journal of Power and Energy*, 232(8):971–991, 2018. doi: 10.1177/0957650918764156.

Yahya Sheikhnejad, João Simões, and Nelson Martins. Introducing Tesla turbine to enhance energy efficiency of refrigeration cycle. *Energy Reports*, 6:358–363, 2020. ISSN 2352-4847. doi: 10.1016/j.egyr.2019.08.073. URL `https://www.sciencedirect.com/science/article/pii/S2352484719306092`. The 6th International Conference on Energy and Environment Research - Energy and environment: challenges towards circular economy.

A. Singh, B.D. Vyas, and U.S. Powle. Investigations on inward flow between two stationary parallel disks. *International Journal of Heat and Fluid Flow*, 20(4):395–401, 1999. ISSN 0142-727X. doi: 10.1016/S0142-727X(98)10058-9. URL `https://www.sciencedirect.com/science/article/pii/S0142727X98100589`.

Achhaibar Singh. Theoretical investigation on inflow between two rotating disks. *Journal of Fluids Engineering*, 139(11):111202, August 2017. ISSN 0098-2202. doi: 10.1115/1.4037058. 111202.

Achhaibar Singh and D. K. Singh. An investigation on the forced convection heat transfer in the gap of two rotating disks with laminar inflow. *Heat Transfer*, 50(7):6964–6983, 2021. doi: 10.1002/htj.22212.

Jian Song, Chun wei Gu, and Xue song Li. Performance estimation of Tesla turbine applied in small scale organic rankine cycle (orc) system. *Applied Thermal Engineering*, 110:318–326, 2017. ISSN 1359-4311. doi: 10.1016/j.applthermaleng.2016.08.168. URL https://www.sciencedirect.com/science/article/pii/S1359431116315277.

Jian Song, Xiao dong Ren, Xue song Li, Chun wei Gu, and Ming ming Zhang. One-dimensional model analysis and performance assessment of Tesla turbine. *Applied Thermal Engineering*, 134:546–554, 2018. ISSN 1359-4311. doi: 10.1016/j.applthermaleng.2018.02.019. URL https://www.sciencedirect.com/science/article/pii/S1359431117353346.

R. Steidel and H. Weiss. Performance test of a bladeless turbine for geothermal applications. Technical report, United States, 1976. URL https://www.osti.gov/servlets/purl/7363794.

L. Talluri, D. Fiaschi, G. Neri, and L. Ciappi. Design and optimization of a Tesla turbine for ORC applications. *Applied Energy*, 226:300–319, 2018. ISSN 0306-2619. doi: 10.1016/j.apenergy.2018.05.057. URL https://www.sciencedirect.com/science/article/pii/S0306261918307670.

L. Talluri, P. Niknam, A. Copeta, M. Amato, P. Iora, S. Uberti, C. Invernizzi, G. Di Marcoberardino, L. Pacini, G. Manfrida, and D. Fiaschi. A revised Tesla turbine concept for 2-phase applications. In *E3S Web of Conferences*, volume 238 of *E3S Web of Conferences*, page 10006, October 2021. doi: 10.1051/e3sconf/202123810006.

Lorenzo Talluri. *Micro Turbo Expander Design for Small Scale ORC: Tesla Turbine*. PhD thesis, Università degli Studi di Firenze, 2019.

Lorenzo Talluri, Olivier Dumont, Giampaolo Manfrida, Vincent Lemort, and Daniele Fiaschi. Geometry definition and performance assessment of Tesla turbines for ORC. *Energy*, 211:118570, 2020. ISSN 0360-5442. doi: 10.1016/j.energy.2020.118570. URL https://www.sciencedirect.com/science/article/pii/S0360544220316789.

Nikola Tesla. Turbine, patent no. us1061206. *New York*, 1913.

Vassilios Theofilis. Global linear instability. *Annual Review of Fluid Mechanics*, 43(1): 319–352, 2011. doi: 10.1146/annurev-fluid-122109-160705.

C. R. Truman, W. Rice, and D. F. Jankowski. Laminar throughflow of varying-quality steam between co-rotating disks. *Journal of Fluids Engineering*, 100(2):194–200, 1978.

C. R. Truman, W. Rice, and D. F. Jankowski. Laminar throughflow of a fluid containing particles between corotating disks. *Journal of Fluids Engineering*, 101:87–92, 1979.

Y. S. Tsai, Y. M. Chang, Y. J. Chang, and Y. M. Chen. Phase-resolved PIV measurements of the flow between a pair of co-rotating disks in a cylindrical enclosure. *Journal of Fluids and Structures*, 23(2):191–206, 2007.

Ewa Tuliszka-Sznitko and Alexander J. Zielinski. Numerical investigation of transitional flow in co- and counter-rotating annular cavity. *Journal of Theoretical and Applied Mechanics*, 44:405–420, 2006.

Nuno Vinha, Guillermo Paniagua, Jorge Sousa, and Bayindir H. Saracoglu. Axial bladeless turbine suitable for high supersonic flows. *Journal of Propulsion and Power*, 32(4):975–983, 2016. doi: 10.2514/1.B35818.

A. Whitfield and N. C. Baines. *Design of Radial Turbomachines*. Longman Scientific & Technical, 1990.

Herbert Wittel, Dieter Jannasch, Joachim Voßiek, and Christian Spura. *Roloff/Matek Maschinenelemente*. Springer Fachmedien Wiesbaden, 2017. doi: 10.1007/978-3-658-17896-3.

Wolfram Research, Inc. Mathematica, version 13.1, 2022. URL `https://www.wolfram.com/mathematica`. Champaign, IL.

R. Wollkind and R. C. DiPrima. Effect of a Coriolis force on the stability of plane Poiseuille flow. *The Physics of Fluids*, 16(12):2045–2051, 1973. doi: 10.1063/1.1694263.

Eunok Yim, J.-M. Chomaz, D. Martinand, and E. Serre. Transition to turbulence in the rotating disk boundary layer of a rotor–stator cavity. *Journal of Fluid Mechanics*, 848: 631–647, 2018. doi: 10.1017/jfm.2018.239.

Dan Zhao, Chenzhen Ji, C. Teo, and Shihuai Li. Performance of small-scale bladeless electromagnetic energy harvesters driven by water or air. *Energy*, 74:99–108, 2014. ISSN 0360-5442. doi: 10.1016/j.energy.2014.04.004. URL `https://www.sciencedirect.com/science/article/pii/S0360544214004174`.